VNIVERSITAT DE VALÈNCIA

PhD program in Chemistry

Hybrid materials based on conductive polymers for energy harvesting

José Francisco Serrano Claumarchirant

Supervisor: Clara María Gómez Clari

July 2022

Dra Dña. Clara María Gómez Clari, Catedrática de Química Física de la Facultat de Química de la Universitat de València

Certifica:

Que el trabajo que presenta D. José Francisco Serrano Claumarchirant en esta memoria bajo el título “Hybrid materials based on conductive polymers for energy harvesting” ha sido realizado bajo su dirección en el Institut de Ciència dels Materials de la Universitat de València.

Y para que así conste a efectos de su presentación para optar al Grado de Doctor en Química, expide el presente que firma en

Paterna a 25 de julio de 2022

ICMUV
INSTITUT DE CIÈNCIA DELS MATERIALS de la Universitat de València

Fdo: Clara M Gómez Clari

“Dicen que el saber no ocupa lugar, pero eso será porque no han visto mis estanterías.”

“It is said that knowledge does not take up space, but that will be because they have not seen my shelves.”

Juan de la Cruz Claumarchirant Sarrión

Abstract

One of the objectives established by the UN for Sustainable Development 2030 is aligned with obtaining energy that is more affordable and less polluting. Due to the increase in energy demand to power our society, renewable energy sources have been prioritized to reduce carbon footprint. However, this increase in energy demand should be combined with an improved energy efficiency due to the fact that 95% of the energy produced is wasted. Much of the energy is lost as heat; therefore, thermoelectric generators can help to harvest some of the wasted energy since they can generate an electrical potential from a thermal gradient. The efficiency of thermoelectric materials is given by the Figure of Merit, *Z*T, which depends on the Seebeck coefficient, electrical conductivity, thermal conductivity, and temperature. Currently, inorganic thermoelectric materials are the most efficient. However, the vast majority of the precursors used to obtain them are scarce and polluting, which goes against Sustainable Development 2030. As an alternative, organic materials, such as conductive polymers, offer advantages such as abundance, low cost, flexibility, and low thermal conductivity. However, the thermoelectric efficiency of these materials is very low compared to their inorganic counterparts. Looking at this scenario, this thesis focuses on developing and characterizing hybrid organic/inorganic thermoelectric materials as a strategy to improve the thermoelectric efficiency of conductive polymers. Hybrid layered materials based on PEDOT with carbon nanotubes (CNT) or SnS:Ag have been produced by Layer-by-Layer deposition and electrodeposition, respectively. Thermoelectric fabrics coated with conductive polymers (PEDOT, polypyrrole, and polyaniline) have also been prepared by electrodeposition. Finally, a method has been developed to obtain thermoelectric films based on mixtures of polythiophene with polymeric matrices of PMMA and polyurethane. Furthermore, this thesis shows the development of two textile-based thermoelectric generators and the development of a hybrid thermoelectric generator that combines the properties of a thermoelectric material with a plasmonic material.

Resumen

Uno de los objetivos establecidos por la ONU para el Desarrollo Sostenible 2030 está alineado con la obtención de energía más asequible y menos contaminante. Debido al aumento de la demanda de energía para alimentar a nuestra sociedad, se han priorizado las fuentes de energía renovable para reducir la huella de carbono. Sin embargo, este aumento de la demanda energética debe combinarse con una mejora de la eficiencia energética debido a que el 95% de la energía producida se desperdicia. Gran parte de la energía se pierde en forma de calor; por lo tanto, los generadores termoeléctricos pueden ayudar a aprovechar parte de la energía desperdiciada, ya que pueden generar un potencial eléctrico a partir de un gradiente térmico. La eficiencia de los materiales termoeléctricos viene dada por la Figura de Mérito, ZT, que depende del coeficiente de Seebeck, la conductividad eléctrica, la conductividad térmica y la temperatura. Actualmente, los materiales termoeléctricos inorgánicos son los más eficientes. Sin embargo, la gran mayoría de los precursores que se utilizan para obtenerlos son escasos y contaminantes, lo que va en contra del Desarrollo Sostenible 2030. Como alternativa, los materiales orgánicos, como los polímeros conductores, ofrecen ventajas como abundancia, bajo coste, flexibilidad y baja conductividad térmica. Sin embargo, la eficiencia termoeléctrica de estos materiales es muy baja en comparación con sus equivalentes inorgánicos. Por todo ello, esta tesis se enfoca en desarrollar y caracterizar materiales termoeléctricos híbridos orgánicos/inorgánicos como una estrategia para mejorar la eficiencia termoeléctrica de los polímeros conductores. Se han producido materiales laminados híbridos basados en PEDOT con nanotubos de carbono (CNT) o SnS:Ag mediante deposición capa a capa y electrodeposición, respectivamente. También se han preparado por electrodeposición tejidos termoeléctricos recubiertos con polímeros conductores (PEDOT, polipirrol y polianilina). Finalmente, se ha desarrollado un método para la obtención de películas termoeléctricas basadas en mezclas de politiofeno con matrices poliméricas de PMMA y poliuretano. Además, esta tesis muestra el desarrollo de dos generadores termoeléctricos de base textil y el desarrollo de un generador termoeléctrico híbrido que combina las propiedades de un material termoeléctrico con un material plasmónico.

Resum

Un dels objectius establits per l'ONU per al Desenvolupament Sostenible 2030 està alineat amb l'obtenció d'energia més assequible i menys contaminant. A causa de l'augment de la demanda d'energia per a alimentar a la nostra societat, s'han prioritzat les fonts d'energia renovable per a reduir la petjada de carboni. Ara bé, aquest augment de la demanda energètica ha de combinar-se amb una millora de l'eficiència energètica pel fet que el 95% de l'energia produïda es malgasta. Gran part de l'energia es perd en forma de calor; per tant, els generadors termoelèctrics poden ajudar a aprofitar part de l'energia malgastada, ja que poden generar un potencial elèctric a partir d'un gradient tèrmic. L'eficiència dels materials termoelèctrics ve donada per la Figura de Mèrit, ZT, que depén del coeficient de Seebeck, la conductivitat elèctrica, la conductivitat tèrmica i la temperatura. Actualment, els materials termoelèctrics inorgànics són els més eficients. No obstant això, la gran majoria dels precursors que s'utilitzen per a obtindre'ls són escassos i contaminants, la qual cosa va en contra del Desenvolupament Sostenible 2030. Com a alternativa, els materials orgànics, com els polímers conductors, ofereixen avantatges com a abundància, sota cost, flexibilitat i baixa conductivitat tèrmica. En canvi, l'eficiència termoelèctrica d'aquests materials és molt baixa en comparació amb els seus equivalents inorgànics. Per tot això, aquesta tesi s'enfoca a desenvolupar i caracteritzar materials termoelèctrics híbrids orgànics/inorgànics com una estratègia per a millorar l'eficiència termoelèctrica dels polímers conductors. S'han produït materials laminats híbrids basats en PEDOT amb nanotubs de carboni (CNT) o SnS:Ag mitjançant deposició capa a capa i electrodeposició, respectivament. També s'han preparat per electrodeposició teixits termoelèctrics recoberts amb polímers conductors (PEDOT, polipirrol i polianilina). Finalment, s'ha desenvolupat un mètode per a l'obtenció de películas termoelèctriques basades en mescles de politiofè amb matrius polimèriques de PMMA i poliuretà A més, aquesta tesi mostra el desenvolupament de dos generadors termoelèctrics de base tèxtil i el desenvolupament d'un generador termoelèctric híbrid que combina les propietats d'un material termoelèctric amb un material plasmònic.

Acknowledgments

Writing the thesis means stopping along the way, looking back, and collecting all the information from recent years. This new perspective has allowed me to remember the moments I lived and realize the number of people who have helped me to be here today.

First, I would like to thank my thesis director, Clara Gómez, who has been like a scientific mother congratulating me on my successes and encouraging me in the most challenging moments. Furthermore, I have worked with great scientists and better people. Therefore, I would also like to thank the help received by Andrés Cantarero in the thermoelectric characterization of the samples; to Rafael Muñoz-Espí for his invaluable help in the development of colloidal systems and the writing of articles with their formal aspects; Rafael Abargues, for his help in the development of the hybrid thermoelectric/plasmonic system; and to Mario Culebras, who has been like my big brother, always willing to help me with everything.

I would also like to thank the help received by researchers from other universities, such as María and Marta from the Polytechnic University of Valencia in the characterization of thermoelectric fabrics through dielectric spectroscopy and mechanical dynamic analysis; Sebas and Kai from the Materials Science Institute of Barcelona for the measurements on the thermal conductivity of thin films; and Chungyeon Cho of Wonkwang University (South Korea) for Hall effect measurements.

During these years, I have been lucky enough to share a laboratory, lunch, and coffee with Toni, Ana María, Juanfran, Inés, Lola, Asmaa, Ali Nasiri, Amparo, Jaume, Rodolfo, Valeriano, Alejandro, Pablo, Ismael, Cristina, and Sheila. Furthermore, I have applied the principle "*Mens sana in corpore sano*" with Jamal and Pedro, sharing some mountain routes. In addition, we are all aware of how lucky we are to have Mª Ángeles, Amparo, and David Vie (SuperDavid) for their willingness to help us with everything we need. Finally, I would also like to take the opportunity to thank Pilar for cleaning the offices and laboratories.

This doctoral thesis has been possible thanks to funding from the Ministerio de Universidades through the Formación de Profesorado Universitario scholarship (FPU17/01414). Thanks to this scholarship, I have collaborated in teaching activities in the Physical Chemistry I and II Laboratories under the supervision of Iolanda and Inma,

respectively. Thank you very much for the help received in developing my teaching tasks in the best possible way. In addition, with the FPU scholarship, I applied for complementary aid to carry out a doctoral stay (EST19/00037) at the Royal Institute of Technology (KTH) in the group directed by Muhammet Toprak. I want to thank him and my lab colleagues Bejan, Hazal, Adem, Rabia, and Gianmarco for the warm welcome they gave me.

I would like to thank Teresa, Juan, and Vicente their affection and interest from the end of my high school studies until today.

One of the pillars of my life is friends. Many thanks to Rubén, Valeriano, Pedro, Carlos, María, Pedro Berrocal, and José María for helping me disconnect from the thesis. I would also like to thank the Colla de Dolçaina i Tabalet "Dolçanna", especially Mª Dolores, Antonio; and my dolçaina teachers Cristina and Xavi, for teaching me how to open space-time fissures with the dolçaina through which I could momentarily evade writing my thesis and thus return to it with renewed energy.

Another of the pillars of my life is family, and, in my case, I am lucky to have two. I will always be eternally grateful to Juan, Lola, Isabel, Juan, Francisco, Encarna, Tita Juani, and Tio Paco for the welcome you gave me from the first moment I appeared in your lives. And how can I forget Isabela, who always welcomes me with an ear-to-ear smile and ready to have fun. But the fundamental pillar has been my family. None of this would have been possible without the sacrifice of my parents, Pepe and Consuelo, who with limited resources, worked hard to give my sister Maria and me a musical education and university studies. They are the leading promoters of our dreams. To my sister María and Germán, who had always shown interest in the thesis progress and, above all, where and when they can visit me during my research stay. I would also like to thank the support, motivation, and affection received by my grandparents Juan, Consuelo, Pepe, and Matilde, who always told me: *"Study hard, the countryside is no longer valid"*. To all my "aunts", uncles, and cousins, especially to my uncle Javi, who gave me a room to sleep in during the first three years of my degree and has always been there for everything we have needed.

Finally, I thank Lola for her support and love during the thesis. She has always been the first to congratulate me on successes and offer me a shoulder to rest on to put all my thoughts in order when I was overwhelmed. I am so fortunate to share my life with her.

Agradecimientos

Escribir la tesis supone hacer un alto en el camino, mirar hacia atrás y recopilar toda la información de los últimos años. Esta nueva perspectiva me ha permitido recordar cada uno de los momentos vividos y darme cuenta de la cantidad de gente que me ha ayudado de un modo u otro a estar hoy aquí.

En primer lugar, me gustaría dar las gracias a mi directora de tesis, Clara Gómez, la cual ha sido como una madre científica felicitándome en los éxitos conseguidos y alentándome en los momentos más difíciles. Junto con Clara he tenido la suerte de trabajar con grandes científicos y mejores personas. Por ello me gustaría agradecer también la ayuda recibida por Andrés Cantarero en la caracterización termoeléctrica de las muestras; a Rafael Muñoz-Espí, por su inestimable ayuda en el desarrollo de los sistemas coloidales y la redacción de artículos con sus aspectos formales; a Rafael Abargues, por su ayuda en el desarrollo del sistema híbrido termoeléctrico/plasmónico; y a Mario Culebras, el cual ha sido como un hermano mayor, siempre dispuesto a ayudarme en todo.

También me gustaría agradecer la ayuda recibida por investigadores de otras universidades como María y Marta de la Universidad Politécnica de Valencia en la caracterización de las telas termoeléctricas mediante espectroscopia dieléctrica y análisis dinámico mecánico; Sebas y Kai del Instituto de Ciència de Materials de Barcelona por las medidas en la conductividad térmica de películas delgadas; y a Chungyeon Cho de la Universidad Wonkwang (Corea del Sur) por las medidas de efecto Hall.

Durante estos años he tenido la suerte de compartir laboratorio, comidas y cafés con Toni, Ana María, Juanfran, Inés, Lola, Asmaa, Ali Nasiri, Amparo, Jaume, Rodolfo, Valeriano, Alejandro, Pablo, Ismael, Cristina y Sheila. Con Jamal y Pedro he aplicado la máxima *"Mens sana in corpore sano"* compartiendo algunas rutas de montaña. Además, creo que todos somos conscientes de la suerte de contar con Mª Ángeles, Amparo y David Vie (SuperDavid) por su predisponibilidad para ayudarnos en todo lo que necesitamos. También me gustaría aprovechar estas líneas para agradecer a Pilar la limpieza de despachos y laboratorios.

Esta tesis doctoral ha sido posible gracias a la financiación por parte del Ministerio de Universidades a través de las Ayudas para la Formación de Profesorado Universitario (FPU17/01414). Gracias a esta beca he podido colaborar en actividades docentes en los

Laboratorios de Química Física I y II bajo la supervisión de Iolanda e Inma, respectivamente. Muchas gracias a ambas por la ayuda recibida para poder desarrollar mis tareas docentes de la mejor manera posible. Además, con la beca FPU pude optar a las ayudas complementarias para realizar una estancia doctoral (EST19/00037) en el Real Instituto de Tecnología (KTH) en el grupo dirigido por Muhammet Toprak. Me gustaría darle las gracias a él y a mis compañeros de laboratorio Bejan, Hazal, Adem, Rabia y Gianmarco por la calurosa acogida que me proporcionaron.

Me gustaría agradecer a Teresa, Juan y Vicente el cariño y el interés que han mostrado desde la finalización de mis estudios de bachillerato hasta el día de hoy.

Uno de los pilares de mi vida son los amigos. Muchas gracias a Rubén, Valeriano, Pedro, Carlos, María, Pedro Berrocal y José María por ayudarme a desconectar de la tesis. También quisiera agradecer a la Colla de Dolçaina i Tabal "Dolçanna", en especial a Mª Dolores, Antonio; y a mis profesores de dolçaina Cristina y Xavi, por enseñarme a abrir fisuras espaciotemporales con la dolçaina a través de las cuales evadirme momentáneamente de la escritura de la tesis y así, retomarla con energías renovadas.

Otro de los pilares de mi vida es la familia y, en mi caso, tengo la suerte de tener dos. Siempre voy a estar eternamente agradecido a Juan, Lola, Isabel, Juan, Francisco, Encarna, la Tita Juani y el tío Paco por la acogida que me brindasteis desde el primer momento en que aparecí en vuestras vidas. Y como olvidarme de Isabela, la cual siempre me recibe con una sonrisa de oreja a oreja y dispuesta a jugar. Pero el pilar fundamental ha sido mi familia. Nada de esto hubiera sido posible sin el sacrificio de mis padres, Pepe y Consuelo, los cuales con unos recursos limitados se esforzaron en darnos a mi hermana María y a mi una educación musical y estudios universitarios. Ellos son los principales promotores de nuestros sueños. A mi hermana María y Germán, que siempre han mostrado interés en los avances de la tesis y, sobre todo, a dónde y cuándo iba de estancia para venir a visitarme. También me gustaría agradecer el apoyo, motivación y cariño recibido por mis abuelos Juan, Consuelo, Pepe y Matilde, los cuales siempre me decían: *"Estudia mante, que el campo ya no se vale"*. A todas mis "tías", tíos y primos, y en especial a mi tío Javi, que me dio una habitación donde dormir durante los tres primeros años de carrera y siempre ha estado ahí para todo lo que hemos necesitado.

Por último, me gustaría agradecer a Lola todo su apoyo y cariño durante la tesis. Ella siempre ha sido la primera en felicitarme ante los éxitos y la primera en ofrecerme un hombro sobre el que descansar para poner todos mis pensamientos en orden cuando me veía agobiado. Verdaderamente tengo mucha suerte de contar con ella en mi vida.

Dedicado a todos aquellos que de una forma u otra han puesto su granito de arena en esta tesis

Dedicated to all those who, in some way, have contributed to this thesis

Contents

Contents

Chapter 1

General introduction

Content

This chapter briefly introduces the energy problem we are facing and how we can provide a solution through the use of thermoelectric materials. In addition, the present chapter provides a complete description of the state-of-the-art of conductive polymers as thermoelectric materials.

1.1 Motivation

One of the objectives of the United Nations (UN) for Sustainable Development 2030 is to obtain energy that is affordable and non-polluting. For this reason, improvements in energy efficiency and green energy sources are strongly recommended as optimal solutions to reduce carbon dioxide emissions and thus reduce the carbon footprint of our society.[1] Carbon emissions have quadrupled since 1950 and currently contribute around 80% of greenhouse gas emissions. As a result of this change, the global climate is facing changes in global rain trends and a reduction in the polar ice caps.[2] With the impact of global climate changes becoming more severe, governments are trying to reduce carbon emission levels and achieve sustainable development in their countries by using renewable energy sources. They harness natural resources such as sunlight, rain, geothermal heat, and waves to produce clean energy without greenhouse gas emissions.[3,4] The electricity generation results (Figure 1.1a) indicate that the trend is becoming more sustainable as the commitment to renewable energies increases yearly. However, the most consumed primary energy sources worldwide continue to be oil and its derivatives (83.15%), and only 5.7% of the global energy consumed comes from renewable energy sources.

In addition, as shown in **Figure 1.1b**, energy consumption fell in 2020 by around 4.5% compared to the previous year due to the crisis caused by Covid-19. However, energy consumption is expected to increase in the coming years, according to the International Energy Agency (IEA). It is vitally important that this increase in energy demand by society goes hand in hand with improving energy efficiency to meet the UN sustainable objectives. Only in this way it will be possible to achieve Net Zero Emissions by the 2050 Scenario over 2020-2030.[5]

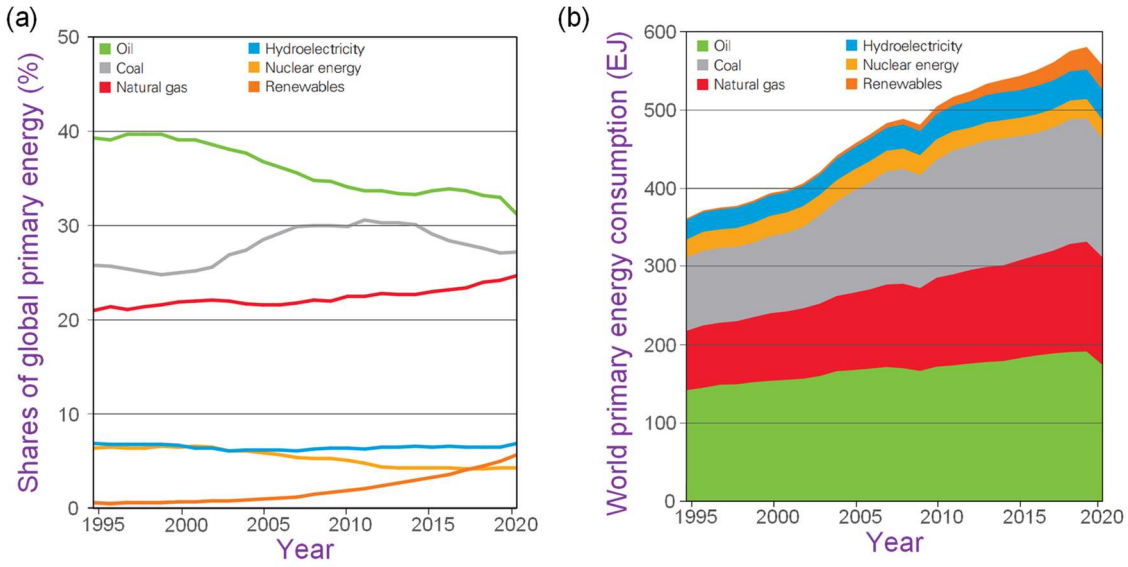

Figure 1.1 (a) Shares of global primary energy per year. (b) World primary energy consumption per year. Images reproduced from BP Statistical Review of World Energy, London 2021. Copyright BP p.l.c., 2022.

Energy efficiency must be improved because, as shown graphically in **Figure 1.2**, 62% of the fuel used to generate energy is lost as heat. Moreover, energy is lost as heat in power plants during energy conversion processes, and only 5% of the energy is used in homes. Therefore, finding ways to recover all this wasted energy is imperative. Some of this lost energy can be retrieved by harvesting energy and turning it into electrical power. The three main phenomena that can recover energy are: piezoelectricity, which can convert mechanical stretching into electrical current, [6,7] triboelectricity, which can produce electrical power through frictional contact between different materials, and [8,9] thermoelectricity, which can recover electrical energy from heat losses. In recent years, this latter phenomenon has become the most promising way to improve energy efficiency since it is a property in semiconductors that can convert a temperature gradient into an electrical current and vice versa.[10,11]

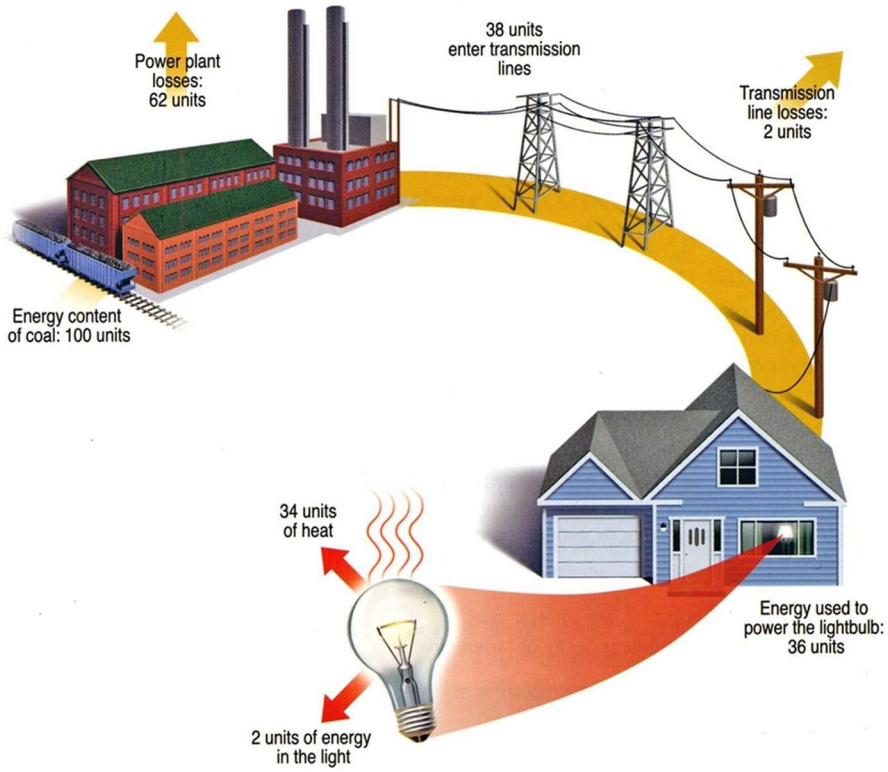

Figure 1.2 Scheme of the energy losses. The image is reproduced from Northeast Clean Heat and Power Initiative. Copyright NECHPI, 2018.

1.2 Thermoelectricity

Thermoelectricity is the ability of certain conductive or semiconductor materials to produce an electrical potential from a thermal gradient or vice versa. In general, any phenomenon that involves an exchange of heat and electric potential can be considered a thermoelectric effect. There are three reversible thermoelectric effects: Seebeck, Peltier, and Thomson effects. Furthermore, the performance of a thermoelectric device always remains below the Carnot efficiency due to the presence of irreversible processes such as Joule heating and thermal conduction.[12]

1.2.1 Thermoelectric effects

The Seebeck effect was discovered by the physicist Thomas Johann Seebeck in 1820 during his experimental investigations on the relationship between electricity and heat.[13]

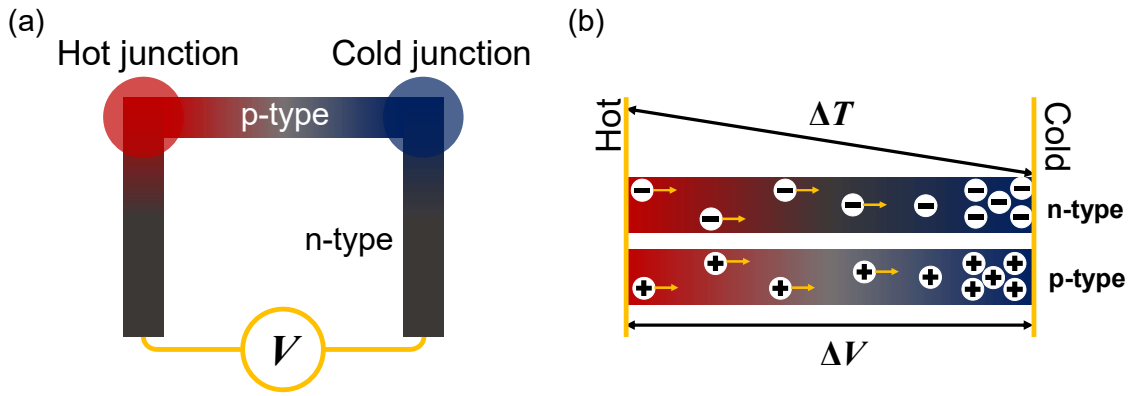

Figure 1.3 (a) Seebeck effect in a circuit of two dissimilar materials. (b) Temperature gradient effect on the charge carrier diffusion for p- and n-type semiconductors.

He corroborated this phenomenon utilizing a circuit formed by two different conductors, which were connected electrically in series but thermally in parallel, as shown in **Figure 1.3(a)**. If a temperature T_1 is applied to the joint between these two materials and a temperature T_2 is applied to the other joint, being $T_1<T_2$, a thermal gradient is generated that causes an electromotive force, ΔV, which is given following equation:[12]

$$\Delta V = -S\,\Delta T \qquad \textbf{(1.1)}$$

This electromotive force is proportional to the thermal gradient, and the proportionality coefficient is known as the Seebeck coefficient or thermopower. When a temperature gradient is established, the charge carriers available for conductive the material begin to diffuse from the higher energy (hot) region to the cooler area of the conductor, as shown in **Figure 1.3(b)**. This process continues until equilibrium is reached, characterized by a stable Seebeck voltage. At the junction between two dissimilar materials, the charge carriers of the conductor with higher electron density will tend to diffuse over the region of the lower density of the other conductor. If most of the charge carriers are holes, the Seebeck coefficient will be positive, and it will be a p-type material. In contrast, if the charge carriers are electrons, the Seebeck coefficient will be negative, and the material will be n-type. Therefore, the voltage difference obtained depends on the nature of the material (p- or n-type) and the thermal gradient.

The Peltier effect was discovered in 1834 by Jean Peltier. He explained this effect with the same experimental set-up as the Seebeck effect. However, a thermal gradient was not established between the junctions of the materials, and instead, a current was passed through the thermoelectric junction. As this current passed, a thermal gradient was spontaneously generated at the intersections of the dissimilar materials (**Figure 1.4**).[14]

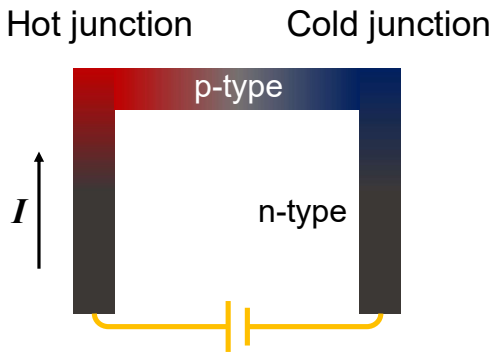

Figure 1.4 Peltier effect in a circuit of two dissimilar materials.

At a constant temperature, the Peltier coefficient of a material is given by:

$$\pi = \frac{q}{I} \tag{1.2}$$

where I is the electrical current and π is the Peltier coefficient, and q is the rate of heating. The Peltier coefficient sign is analogous to the Seebeck coefficient and therefore depends on the nature of the material. If it is a p-type material, the coefficient will be positive; if it is an n-type material, the coefficient will be negative. The Peltier effect can be interpreted in the following way: when an electric field interacts with n-type material, the electrons migrate towards the positive side, releasing the energy in the form of heat. In contrast, when the material interacting with the electric field is p-type, the holes move to the negative side in opposition to the current flow. In addition, reversing the polarity of the electrical current will also change the direction of heat transfer.

The last of the three thermoelectric effects was discovered by Thomson in 1851. Essentially, the Thompson effect relates the heat generated or absorbed due to the passage of current along a portion of conductive material where there is a temperature difference, as shown in **Equation (1.3)**:

$$q = \beta\, I\, \Delta T \tag{1.3}$$

where β is the Thomson coefficient. Like the Seebeck or Peltier coefficients, the Thomson coefficient can be positive or negative depending on the nature of the conductive material. The Thomson effect can be neglected in thermoelectric devices, but must be taken into account when a detailed calculation is required.[12,15]

Two irreversible processes tend to reduce the performance of a thermoelectric material. These are Joule heating and heat conduction effects. These processes prevent reaching the thermodynamic equilibrium of a device, known as Carnot efficiency.[12]

Joule heating inevitably takes place due to the presence of current density. Therefore, this process is not desirable in the case of thermoelectric materials since it causes heat dissipation, giving rise to the so-called ohmic loss.

On the other hand, a conductor subjected to a temperature gradient always shows an increase in the temperature at the cold end as a result of heat conduction, which is expressed by:

$$q = -A\,\kappa\,\frac{dT}{dx} \tag{1.4}$$

where A is the cross-section area of the conductor and κ is the thermal conductivity of the material. The loss of thermoelectric efficiency due to heat conduction is directly proportional to the thermal conductivity. Therefore, materials with low thermal conductivity are required for efficient energy conversion.

1.2.2 Thermoelectric efficiency

A thermoelectric generator consists of a p-type and n-type semiconductor connected electrically in series and thermally in parallel (**Figure 1.5**). A thermoelectric generator is a device that converts heat to electricity or vice versa and which obeys the laws of thermodynamics.

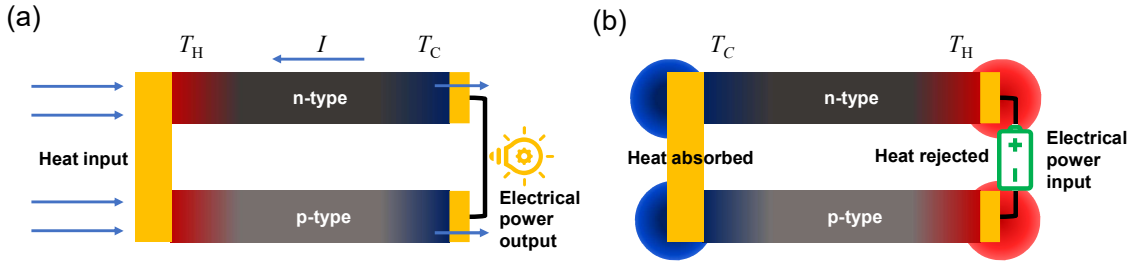

Figure 1.5 (a) Thermoelectric generator. (b) Thermoelectric refrigerator.

Considering an ideal thermoelectric generator with no losses or heat conduction in a first approximation, the efficiency of the generator will be the ratio between the electrical power delivered to the load to the heat absorbed at the hot junction as expressed by the following:

$$\phi = \frac{\text{energy supplied to the load}}{\text{heat energy absorbed at hot junction}} \tag{1.5}$$

If we assume that the electrical conductivity, thermal conductivity, and Seebeck coefficient are constant throughout the module and that the contact resistances at the hot and cold junctions are negligible compared to the sum of the module resistance, the generator efficiency, ϕ, can be expressed by:

$$\phi = \frac{I^2 R}{S\, I\, T_{\mathrm{H}} + \lambda'(T_{\mathrm{H}} - T_{\mathrm{C}}) - \frac{1}{2} I^2 R} \tag{1.6}$$

where λ' is the thermal conductance of both materials connected in parallel, and *R* is the resistance of the module. However, in real thermoelectric materials, the electrical conductivity (σ), the thermal conductivity (κ), and the Seebeck coefficient (*S*) depend on temperature. In addition, heat losses must be considered. Therefore, the maximum thermoelectric efficiency can be expressed in terms of the Carnot efficiency as:

$$\phi_{\max} = \eta_{\mathrm{C}}\, \gamma \tag{1.7}$$

where η_{C} is the Carnot efficiency:

$$\eta_{\mathrm{C}} = \frac{T_{\mathrm{H}} - T_{\mathrm{C}}}{T_{\mathrm{H}}} \tag{1.8}$$

and γ, which takes into account the mentioned parameters of the materials:

$$\gamma = \frac{\sqrt{1 + ZT_{av}} - 1}{\sqrt{1 + ZT_{av}} + \frac{T_{\mathrm{C}}}{T_{\mathrm{H}}}} \tag{1.9}$$

being T_{av}

$$T_{av} = \frac{T_{\mathrm{H}} + T_{\mathrm{C}}}{2} \tag{1.10}$$

and Z the figure of merit:

$$Z = \frac{S^2 \sigma}{\kappa} \tag{1.11}$$

Therefore, the thermoelectric efficiency can be expressed as a function of the figure of merit and temperature. Furthermore, we must take into account that thermal conductivity has an electronic contribution (κ_e) which is predominant in metals and a phononic contribution (κ_p) which is important in semiconductors. Therefore, the dimensionless figure of merit would be as follows:

$$ZT = \frac{S^2 \sigma}{\kappa_e + \kappa_p} T \tag{1.12}$$

On the other hand, if we want to compare materials whose electronic and phonon contributions to thermal conductivity are similar, it is typically used the power factor (*PF*):

$$PF = S^2\sigma \tag{1.13}$$

Equation (1.7) shows that the maximum efficiency of a thermoelectric generator depends on the Carnot efficiency and the figure of merit. In **Figure 1.6**, which represents the conversion efficiency as a function of the working temperature and the figure of merit, it can be seen that the higher the temperature, the higher the degree of conversion due to the Carnot efficiency is directly proportional to the thermal gradient. Therefore, a high thermal gradient is desirable to obtain good energy conversion yields. However, this is not always possible since there are cases in which reaching these temperature differences is difficult either by the application being worked on or by the material used.

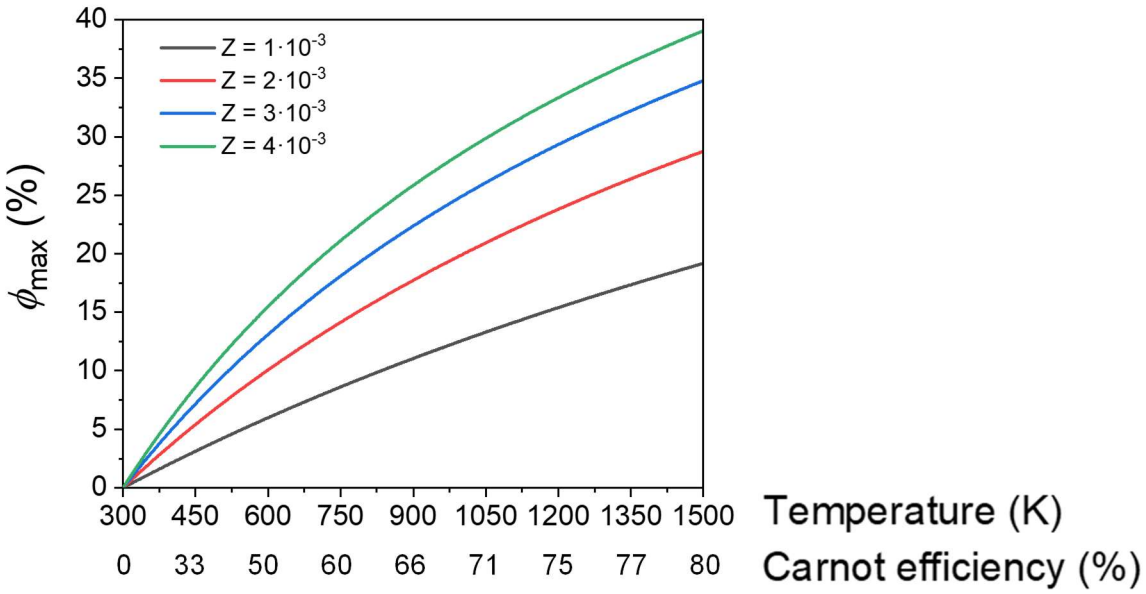

Figure 1.6 Thermoelectric efficiency as a function of temperature and thermocouple material figure of merit. Cold junction at 300 K.

For example, inorganic materials can withstand high temperatures, but a high thermal gradient would only be possible in applications with extreme conditions. On the other hand, organic materials do not withstand high temperatures as they begin to decompose. In conclusion, thermoelectric efficiency is the parameter to be optimized in thermoelectric materials. Therefore, attention should focus on maximizing the figure of merit.

1.2.3 Thermoelectric materials

According to the definition of the Figure of Merit, an excellent thermoelectric material will have a high Seebeck coefficient, a high electrical conductivity, and a low thermal conductivity.[16,17] These three parameters are a function of the concentration of free charge carriers. For example, **Figure 1.7** shows how the electrical conductivity increases with the concentration of charge carriers while the Seebeck coefficient decreases. Furthermore, the electronic contribution to the thermal conductivity increases with the charge carrier concentration, while the phononic contribution is unaffected. Therefore, the efficiency of thermoelectric materials is conditioned by the concentration of charge carriers.

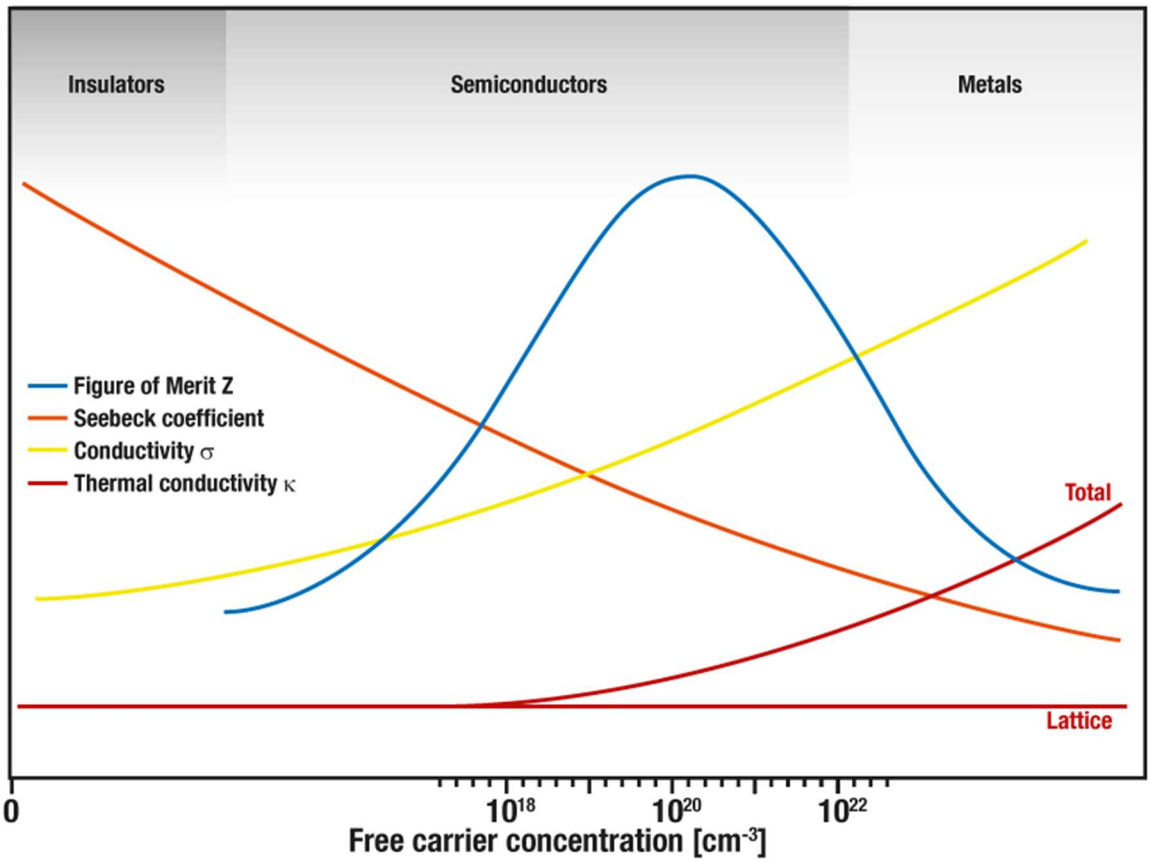

Figure 1.7 Seebeck coefficient, electrical conductivity, thermal conductivity, and Figure of Merit as a function of free carrier concentration. Image reproduced from Linseis. Copyright Linseis GmbH, 2022.

Insulating materials have a low concentration of charge carriers, and therefore, the Seebeck coefficient is very high. Furthermore, the electrical and thermal conductivity are very low with a low concentration of charge carriers. Therefore, these materials are unsuitable for thermoelectric applications due to their low electrical conductivity. On the other hand, metals have high electrical conductivity, but their Seebeck coefficients are too

low to be considered suitable thermoelectric materials. Finally, semiconductors are the most appropriate materials to meet high *Z*T value requirements. However, the semiconductors should be doped to adjust the concentration of charge carriers that can give an optimum *Z*T value.

The Figure of Merit of a thermoelectric material depends on the temperature. However, not all materials have the same dependence of *Z*T on temperature, and for this reason, thermoelectric materials can be divided into three groups according to the operating temperature range, as shown in **Figure 1.8**.

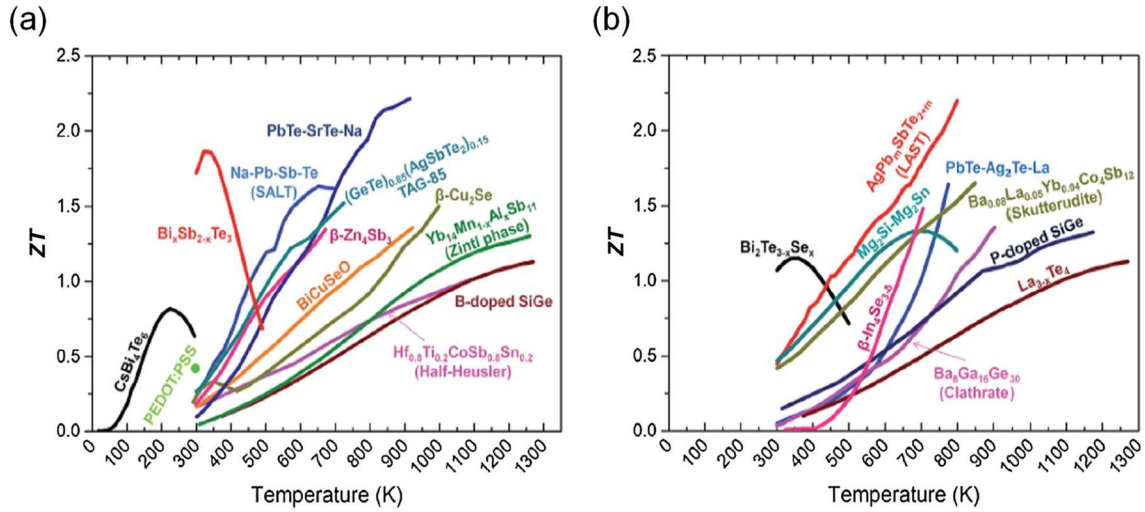

Figure 1.8 Performance of (a) p-type and (b) n-type thermoelectric materials as a function of temperature. Reprinted with permission from Rull-Bravo et al.[18] Copyright 2015, The Royal Society of Chemistry.

The first group consists of alloys based on bismuth combined with antimony, tellurium, and selenium, which have a maximum *Z*T in the temperature range between room temperature and 450 K. The second group comprises materials based on lead telluride, which have maximum thermoelectric efficiency at temperatures up to 850 K. Lastly, materials based on silicon-germanium alloys reach their maximum *Z*T value at high temperatures, close to 1300 K.[12]

Although the materials presented above continue to be the most widely used for commercial applications, significant advances have been made in synthesizing new materials and structures with improved thermoelectric performance. It has sought to improve the Figure of Merit by reducing the lattice thermal conductivity. One way to achieve this goal is through so-called phonon-glass electron-crystal strategy, whereby the material should conduct heat as glass but electricity as a crystal. The result of this research are materials such as skutterudites and clathrates.[19–22]

Another strategy to improve thermoelectric efficiency by reducing lattice thermal conductivity is based on the use of materials with low-dimensional structures. Hicks and Dresselhaus, in 1993, demonstrated the potential use of quantum wells to improve the Figure of Merit.[23] As a result of this work, materials such as Bi_2Te_3/Sb_2Te_3, PbSeTe, or SiGe achieved *Z*T values around 2.[24–26]

However, these inorganic materials have several drawbacks, such as the high production cost, toxicity of some of the elements used, and the scarcity of raw materials.[27,28] All of these drawbacks make inorganic thermoelectric materials not suitable from the point of view of sustainable energy development. For this reason, many studies have focused on the search for efficient thermoelectric materials that are friendly to the environment.[28] One of the potential candidates for room temperature applications are organic semiconductors, particularly conductive polymers, due to their abundance, low cost, flexibility, and easy modification.

1.3 Conductive polymers

Conductive polymers are a particular class of polymers that have the ability to carry electric charges along their π-conjugated chain. In general, polymers are chemical compounds based on carbon, in which all the available electrons are strongly linked by σ bonds, which gives them insulating properties. However, conductive polymers present σ bonds, where the electrons are strongly bonded, and a conjugated π bond, where the electrons are delocalized along the polymer chains.[29] Higher π-electronic delocalization allows higher electron mobility along the polymer backbone, which is achieved when the conjugated chain has a large number of repeating units. However, the chains of conductive polymers tend to interact with each other creating spaghetti-like structures making it practically impossible to achieve long-range order. In fact, conductive polymers are generally shorter than insulating polymers and are often amorphous. Furthermore, its solubility is very low unless specific side-chain groups are introduced. However, in the last decade conductive polymers have attracted the attention of researchers as thermoelectric materials for energy harvesting using low-grade heat (below 100 ºC). **Figure 1.9(a)** shows the evolution of the number of publications and citations of conductive polymers for thermoelectric applications in the last 50 years, according to the Web of Science. The classical conjugated

systems, **Figure 1.9(b)**, include polyaniline (PANI), polypyrrole, polythiophene (PTh), poly(3,4-ethylenedioxythiophene) (PEDOT), and their derivatives.[30–32]

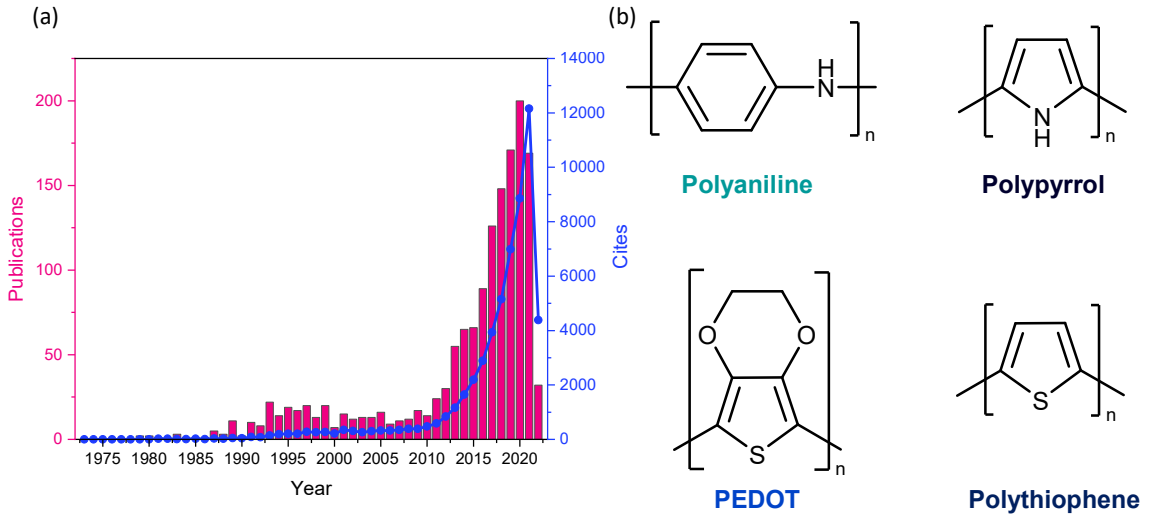

Figure 1.9 (a) Publications and cites of conductive polymers for thermoelectric applications during the last 50 years. Data from Web of Science. (b) Chemical structure of the classical conductive polymers.

1.3.1 Synthesis of conductive polymers

In general, p-type conductive polymers are obtained by oxidative polymerization. This type of polymerization is carried out by oxidation of the monomer in the presence of an oxidizing salt or by electrochemical oxidation of the monomer on a working electrode (electropolymerization). In both cases, the polymerization mechanism is similar. As an example, **Figure 1.10** shows the oxidative polymerization mechanism of EDOT in the presence of iron (III) p-toluenesulfonate proposed in a study carried out at Bayer AG.[33]

The overall polymerization process can be split into two steps. In the first step occurs the oxidative polymerization of EDOT to neutral. During this process, the oxidizing agent extracts electrons from the double bonds of the monomer, forming radical cations, which quickly dimerize. The oxidizing agent continues to form radical cations, which react with each other, progressively increasing the length of the polymer chain.

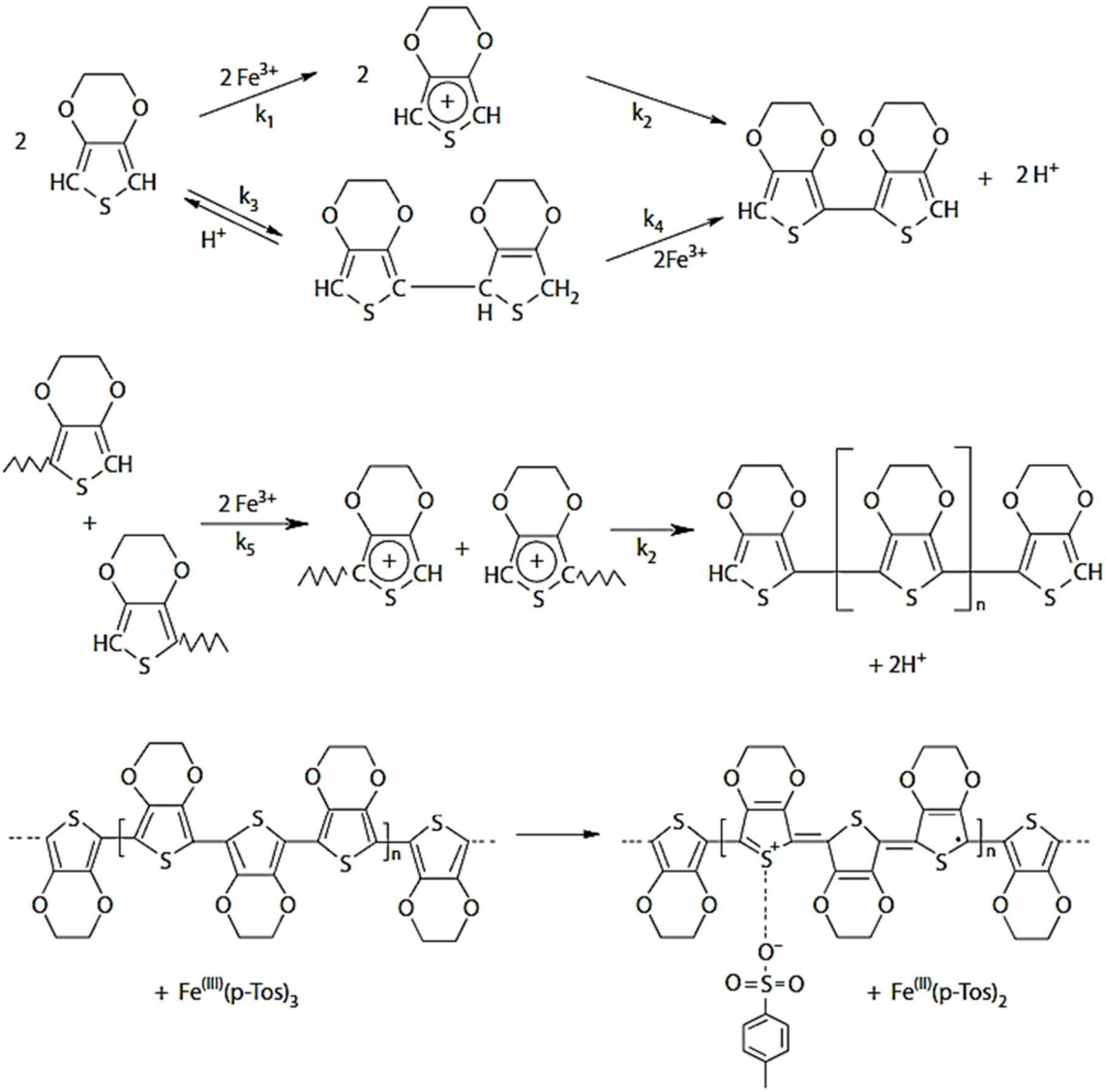

Figure 1.10 Proposed reaction mechanism for the oxidation of EDOT to PEDOT. Reprinted with permission.[34] Copyright 2011, Taylor and Francis Group, LLC.

In the second stage, the neutral polymeric chain of PEDOT is doped by the excess oxidant as it continues to oxidize the polymeric chain forming cationic structures. In the first place, after doping, polaronic states are obtained, characterized by the presence of a positive charge every 3-4 monomers. Next, these polaronic states are further oxidized to the stable and highly conductive polaronic state, characterized by two positive charges every 3-4 monomers.[35] Finally, the anions associated with the oxidizing salt are incorporated into each positive charge within the polymeric structure, acting as counterions.

1.3.2 Doping of conductive polymers

The main requirement for a polymer to be conductive is the presence of a π-conjugated chain. However, the band gaps of conductive polymers in their neutral state are in the range of 1 to 3 eV,[36] which are typical values of semiconductor or even insulating materials. Therefore, it is necessary to dope the conjugated polymers to acquire metal-like electronic properties. Unlike inorganic materials, where doping involves the substitution of an atom, doping in conjugated polymers is due to oxidation (p-type doping) or reduction (n-type doping) processes. Another difference concerning the doping of inorganic materials is that conductive polymers can reach doping levels greater than 50%, exceeding inorganic ones by several orders of magnitude.[37]

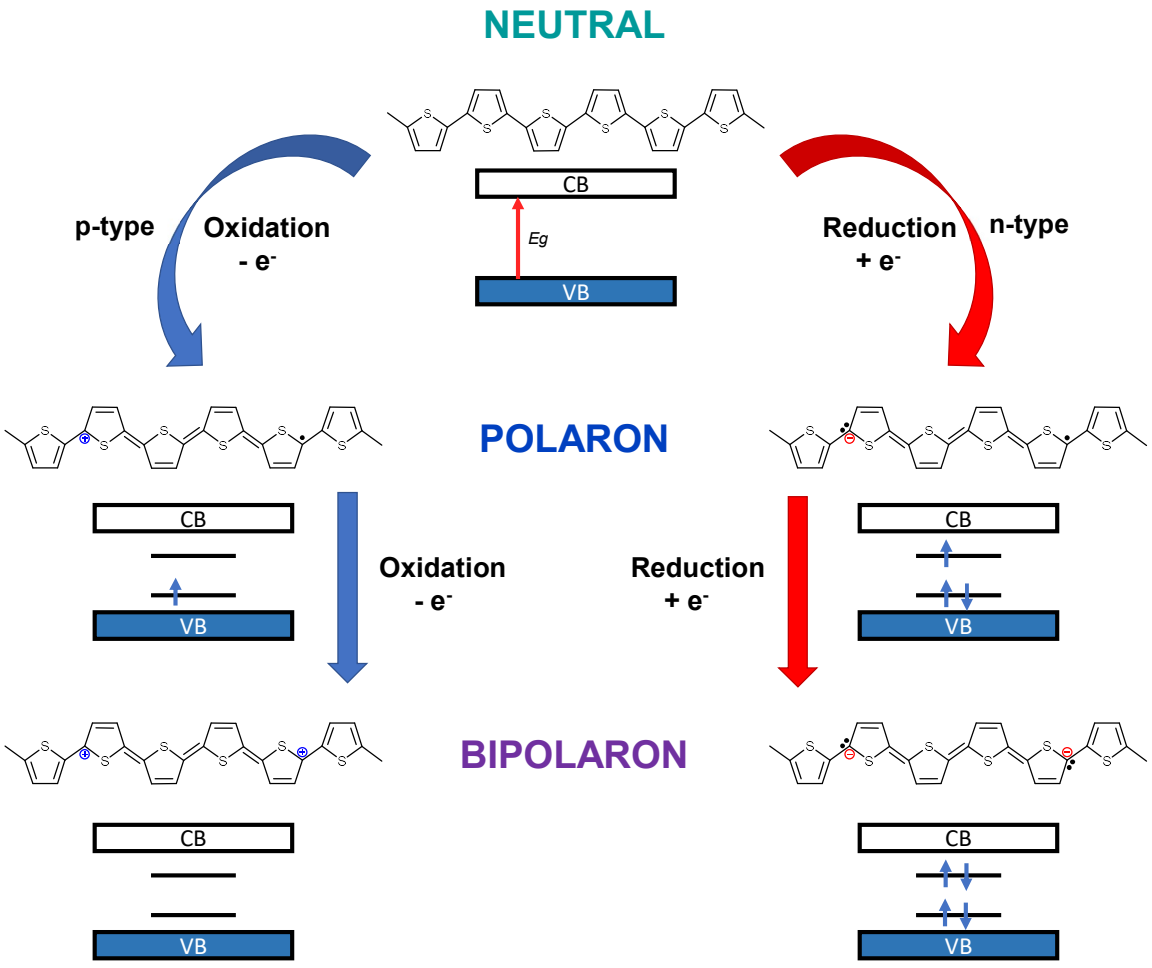

Figure 1.11 Schematic doping process of polythiophene by oxidation and reduction.

As we have seen in **Figure 1.10**, doping can be achieved by oxidation (reduction) by removing (adding) an electron from (to) a conjugated polymer in its neutral state, thus obtaining a polaron which forces the chemical structure to change from benzoic to quinoid.

The polaron is an excitation of a single charge that can be positive or negative, depending on whether it is obtained by oxidation or reduction, which extends between three or four monomer units depending on the chemical structure of the polymer. Its presence in p-type conductive polymers causes a semi-occupied electronic level above the valence band (VB) and a new antibonding level below the conduction band (CB). However, in the case of n-type conductive polymers, the electron level above VB is fully occupied, and the energy level below CB is half occupied. Next, an elimination (addition) of an electron on the polaronic structure of the conductive polymer leads to obtaining a bipolaron. The bipolaron is an excited state with two positive or negative charges and, like the polaron, spans between three or four monomer units. In this case, its presence in p-type conductive polymers causes the intermediate level that was previously semi-occupied to be empty. For the case of n-type conductive polymers, the two electronic levels located between the VB and the CB are fully occupied. **Figure 1.11** schematizes the doping of a polythiophene polymeric chain by oxidation and reduction. Finally, the charges generated during the doping process are stabilized by counterions (anions or cations) to maintain the electroneutrality of the material.

The level of doping can be controlled in two main ways. The simplest form is chemical doping, in which the polymer is exposed to a solution or vapor of the dopant, producing the redox reaction.[38] Consequently, the concentration of charge carriers increases and the electrical conductivity improves, even reaching values close to metals.[39] However, the number of doping agents capable of producing the redox reaction is limited. In addition, samples doped by this method usually reach high doping levels, because is not easy to obtain intermediate doping levels.[40] Another way to control the level of doping is electrochemical doping. This method consists of applying an electric current between the conductive polymer and the electrode while the electrolyte ions diffuse to maintain the electroneutrality of the conductive polymer. In the case of n-doping, the polymer is reduced, and cations from the electrolyte penetrate the conductive polymer. In contrast, a p-doping, the polymer is oxidized, and the anions balance the charge of the conductive polymer. This method offers better control over the doping level, which is related to the applied potential.

1.3.3 Charge transport in conductive polymers

Most conductive polymers are amorphous, and only polymers with high conductivity have a higher degree of crystallinity.[41] This high degree of polymer chain disorder implies a deep charge localization. Therefore, these systems are characterized by low conductivity and charge carrier mobility even at high doping levels (high charge carrier concentrations).

In general, charge transport in conductive polymers is dominated by three effects that determine the electrical conduction: 1) propagation of a charge carrier along the polymer chain; 2) transfer between polymer chains through jumps; 3) tunneling between conductive segments spaced by amorphous regions. As discussed above, the delocalization of π electrons along the polymer chain is insufficient for good charge transport due to charge localization by its amorphous structure. Therefore, although the jump transfer integral between polymer chains represents a tiny part of charge transport, such interchain coupling is essential.[42] In this way, the jump of charge carriers from one chain to another is promoted, preventing carriers from being trapped by defects in the polymer chain. However, using side chains in conjugated polymers to improve their solubility hinders the transfer of charge carriers between the different polymer chains by reducing the intermolecular overlap of the chains.[43] Another critical aspect to consider in charge transport in conductive polymers is their molecular weight. A low molecular weight polymer has a shorter chain length, allowing it to adopt a crystalline structure more easily than high molecular weight polymers. This crystalline structure allows a greater delocalization of charge carriers along the polymer chain, which would improve charge transport. However, the mobility of the charge carriers is lower because the crystals formed are not connected to each other. On the contrary, in high molecular weight polymers, by having a longer polymeric chain, they can attach different regions of the material despite the possible interruptions of conjugation due to defects in the chain.[44]

1.3.4 Improving thermoelectric properties of conductive polymers

Section 1.2 of this chapter mentions that conductive polymers are good candidates for thermoelectric applications because the energy sector is looking for environmentally friendly materials. In addition, conductive polymers provide other benefits. From an environmental point of view, conductive polymers are mainly composed of carbon, which

is an abundant, low cost and non-toxic element. Those properties imply that obtaining thermoelectric materials based on conductive polymers is much more sustainable than traditional inorganic materials. Furthermore, from a chemical point of view, conductive polymers can be easily modified to provide additional functionalities, and also, the flexible properties are useful for printing large areas.[45–47] In addition, conductive polymers often have a thermal conductivity (0.1 – 1 W m^{-1} K^{-1}) below the thermal conductivity of metals and inorganic semiconductors.[48] All these advantages make conductive polymers the ideal candidates for the next generation of thermoelectric materials because it is possible to obtain low-cost and large-area flexible devices for low-grade heat energy harvesting. However, despite the significant increase in the thermoelectric efficiency of conductive polymers in the last decade, the Figure of Merit remains much lower than the *Z*T of inorganic materials. Therefore, it is necessary to find new strategies to improve the efficiency of conductive polymers. Three strategies are presented below: 1) optimization of the doping level, 2) improvement of the ordering of the polymeric chains, 3) obtaining hybrid organic-inorganic materials.

1.3.4.1 Optimization of the doping level

As mentioned before, conductive polymers need to be doped to have carriers that conduct electricity. The doping with an effective dopant can control the concentration of charge carriers (n) and, therefore, the electrical conductivity of conductive polymers. However, increasing charge carrier concentration has opposite effects on the Seebeck coefficient according to the following equations:

$$\sigma = ne\mu \tag{1.14}$$

$$S = \frac{8\pi^2 k_B^2}{3eh^2} m^* T \left(\frac{\pi}{3n}\right)^{2/3} \tag{1.15}$$

where n is the charge carrier concentration, e is the electric charge, μ is the charge carrier mobility, k_B is Boltzmann's constant, h is Planck's constant, and m^* is the effective carrier mass.

From equations **(1.14)** and **(1.15)**, it is deduced that with increasing the dopant concentration, n increases, leading to enhance electrical transport and decreasing the Seebeck coefficient. Considering the expression of the Figure of Merit, **Equation (1.12)**, an effective doping of conductive polymers for thermoelectric applications should carefully control the concentration of charge carriers to achieve a maximum value of Figure of Merit, and also the Power Factor, **Equation (1.13)**, as shown in **Figure 1.7**. In order to

achieve this goal, it is necessary to select the appropriate dopant, as well as the required amount and synthetic parameters such as temperature and time. Sometimes it is even needed to use multiple dopants to tune the n, revealing that effective doping is a complex task and, therefore, a myriad of works have focused on this.[49–54]

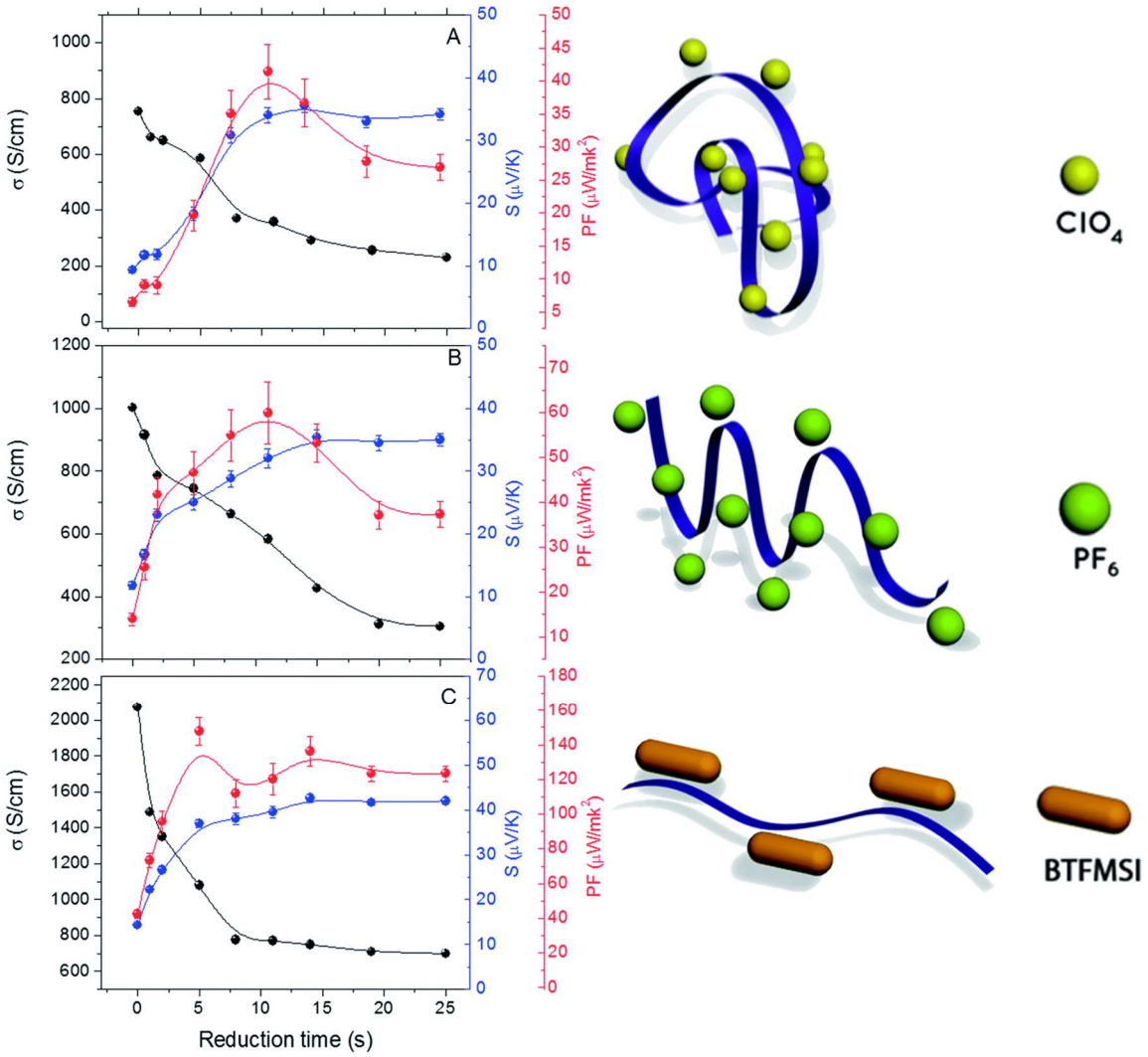

Figure 1.12 TE performances of PEDOT films with ClO_4, PF_6, and BTFMSI as dopants. Reproduced with permission.[55] Copyright 2014, Royal Society of Chemistry.

For example, Culebras et al.[55] prepared PEDOT films by electrodeposition with different counterions (ClO_4^-, PF_6^-, $BTFMSI^-$) to optimize the level of doping by reducing those films with hydrazine. Power Factor values were higher than the initial samples (**Figure 1.12**). In addition, they observed that the size of the dopants also affects the electrical conductivity. In particular, the PEDOT:BTFMSI film had the highest electrical conductivity because, being the largest counterion, it modified the structure of the PEDOT polymer chain, as is schematically represented in **Figure 1.12**.

1.3.4.2 Controlling polymeric chain ordering

This second strategy is based on improving the crystalline arrangement of the conductive polymer microstructure and eliminating the insulating phases through post-treatments. In this case, a redox reaction does not occur, and, therefore, the concentration of charge carriers (n) is not modified. However, the mobility of charge carriers (μ) along the polymer chain is improved, as is observed in **Figure 1.13 (a)**. One of the most common examples is the chemical treatment of PEDOT:PSS films with solvents such as ethylene glycol,[56] DMSO,[57] methanol,[58] DMF,[59] or sulfuric acid.[60] These compounds can remove the insulating phases of PSS, leading to a higher μ and σ (**Figure 1.13 (b)**). This increase in electrical conductivity without modifying the concentration of charge carriers makes it possible to preserve the Seebeck coefficient and, therefore, improve the ZT (**Figure 1.13 (c)**).

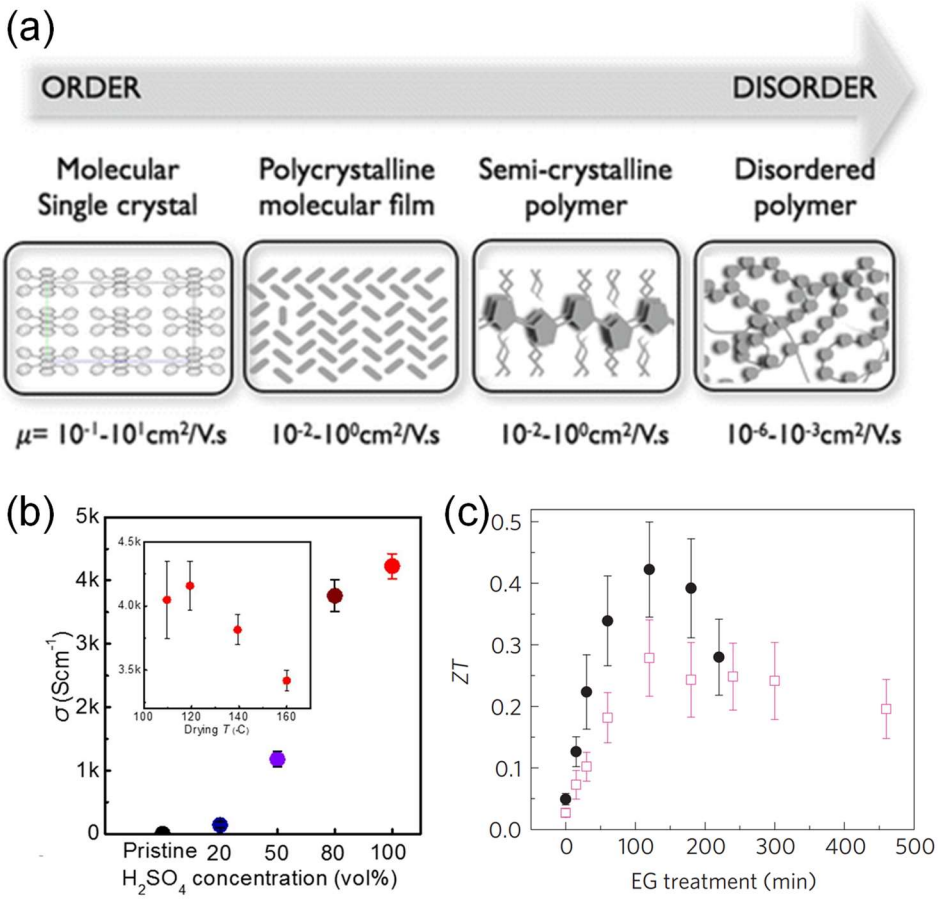

Figure 1.13 (a) Organic field-effect transistor mobility correlates with structural order. Reprinted with permission.[61] Copyright 2014, Springer-Verlag Berlin Heidelberg. (b) Electrical conductivity of PEDOT:PSS films as a function of the concentration of H_2SO_4 solvent. Reprinted with permission.[60] Copyright 2013, WILEY-VCH Verlag GmbH & Co. KGaA, Weinheim. (c) ZT properties of PEDOT:PSS films after ethylene glycol post-treatment. Reprinted with permission.[56] Copyright 2013, Macmillan Publishers Limited.

There are other methods of improving crystal order, such as mechanical stretching of conductive polymer films, through which an increase in electrical conductivity is produced without damaging the Seebeck coefficient.[62] Additionally, it is possible to apply annealing post-treatments whereby well-aligned microstructures and highly crystallized domains are formed in the conductive polymer film.[63]

1.3.4.3 Hybrid materials

The third strategy to increase the efficiency of conductive polymers consists of the combination of conductive polymers with inorganic fillers. In this way, it is expected that both materials' synergistic combinations will lead to obtaining an organic-inorganic hybrid material with improved thermoelectric properties. In fact, adding new interfaces in the conductive polymer matrix tends to block the low-energy charge carriers due to the filtering effect, which translates into an increase in the Seebeck coefficient of the conductive polymer.[64,65] Normally, inorganic materials and highly conductive carbonaceous materials have high thermal conductivity, but when combined with conductive polymers, the thermal conductivity of the final material is reduced by phonon scattering at the interface.[66]

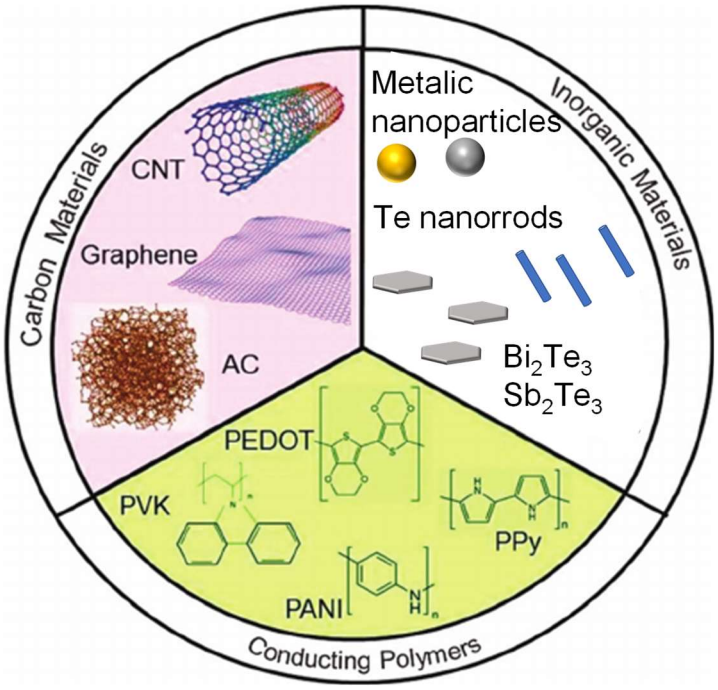

Figure 1.14 Schematic diagram of the components used in hybrid thermoelectric materials.

Organic-inorganic hybrid thermoelectric materials have been based on combining conductive polymers with inorganic fillers made of carbonaceous materials or inorganic semiconductors, as shown in **Figure 1.14**. Among carbonaceous materials, SWCNT,[67]

MWCNT,[68], and graphene,[69] among others, have been used in thermoelectricity. These materials have high electrical conductivity and are easily dispersible in aqueous media. On the other hand, inorganic semiconductors have exceptional thermoelectric properties that optimize polymeric composite films. However, these fillers tend to aggregate during the solidification process. The most used inorganic semiconductors, among others, are tellurium (Te),[70] bismuth telluride (Bi_2Te_3),[71] or tin selenide (SnSe).[72]

1.4 Objectives and structure of the thesis

The main objective of this thesis has been to elaborate hybrid thermoelectric materials based on conductive polymers to improve their thermoelectric efficiency. This main objective is divided into the following sub-objectives:

1. Synthesis and preparation of hybrid thermoelectric materials based on PEDOT with carbon nanotubes and SnS:Ag.
2. Synthesis and development of thermoelectric fabrics coated with MWCNT/conductive polymers to obtain wearable thermoelectric materials.
3. Manufacture of a thermoelectric generator based on the fabrics obtained.
4. Optimization of the *in-situ* polymerization of terthiophene mixtures with different polymeric matrices and oxidizing agents.
5. Elaboration of a hybrid plasmonic/TEG system to harvest thermal energy from sunlight.

Each chapter of this thesis, except for the general introduction (Chapter 1), characterization techniques (Chapter 2), and general conclusions (Chapter 6), are organized with the same scheme: an introductory part that reviews the fundamental concepts of the chapter, followed by the results and discussion of the experiments carried out and, finally, the main conclusions of the chapter.

Chapter 3 focuses on obtaining hybrid layered materials based on PEDOT with carbon nanotubes (CNT) or SnS:Ag. The first series of experiments describe the formation and thermoelectric characterization of PEDOT/CNT hybrid materials obtained by Layer-by-Layer (LbL) deposition of PEDOT nanoparticles functionalized with a cationic polyelectrolyte (PDADMAC) and various types of nanotubes of carbon (MWCNT, DWCNT, SWCNT) functionalized with an anionic surfactant (DOC). The second work

focuses on obtaining and characterizing hybrid layered PEDOT/SnS:Ag films obtained by electrodeposition.

Chapter 4 uses electrosynthesis to prepare thermoelectric fabrics coated with conductive polymers (PEDOT, PPy, PANI). The first part of this chapter describes the strategy utilized to cover felt textiles with conductive polymers by electrosynthesis. The second part of the chapter focuses on the conductive polymer that offers the best thermoelectric properties of the previous section (PEDOT) to deposit it in different textiles (cotton and felt) and build a thermoelectric device with both fabrics. Finally, in the last part of the chapter, after selecting the PEDOT-coated textile that offers a higher power output, the counterions of the PEDOT polymer chains are modified, and another thermoelectric device is made.

Chapter 5 shows the optimization of the *in-situ* polymerization of terthiophene (3T) within polymeric matrices (PMMA and polyurethane) with different oxidizing agents ($AgClO_4$, $Cu(ClO_4)_2$). In the first part of this chapter, the 3T polymerization conditions are optimized within the PMMA matrix using $AgClO_4$ as an oxidant. With these conditions, in the second part of the chapter, the polymeric matrix of PMMA is changed for that of polyurethane (PU), and a systematic study of the polythiophene (PT) films obtained with both oxidants is made. Finally, in the last part of this chapter, due to the presence of silver nanoparticles in the PT/PU/$AgClO_4$ film, the plasmonic heating effect of these metallic nanoparticles after irradiating the film with a solar simulator is studied. The reached temperature difference is minimal; therefore, a plasmonic layer was added to the thermoelectric film, getting a more significant thermal gradient. With this hybrid plasmon/thermoelectric system, a thermoelectric generator was designed that could recover energy from solar light.

References

(1) Zakari, A.; Khan, I.; Tan, D.; Alvarado, R.; Dagar, V. Energy Efficiency and Sustainable Development Goals (SDGs). *Energy* **2022**, *239*, 122365. https://doi.org/https://doi.org/10.1016/j.energy.2021.122365.

(2) Chong, C. T.; Fan, Y. Van; Lee, C. T.; Klemeš, J. J. Post COVID-19 ENERGY Sustainability and Carbon Emissions Neutrality. *Energy* **2022**, *241*, 122801. https://doi.org/https://doi.org/10.1016/j.energy.2021.122801.

(3) Arévalo, P.; Cano, A.; Jurado, F. Mitigation of Carbon Footprint with 100% Renewable Energy System by 2050: The Case of Galapagos Islands. *Energy* **2022**, *245*, 123247. https://doi.org/https://doi.org/10.1016/j.energy.2022.123247.

(4) Fell, H.; Gilbert, A.; Jenkins, J. D.; Mildenberger, M. Nuclear Power and Renewable Energy Are Both Associated with National Decarbonization. *Nat. Energy* **2022**, *7* (1), 25–29. https://doi.org/10.1038/s41560-021-00964-w.

(5) Nastasi, B.; Markovska, N.; Puksec, T.; Duić, N.; Foley, A. Renewable and Sustainable Energy Challenges to Face for the Achievement of Sustainable Development Goals. *Renew. Sustain. Energy Rev.* **2022**, *157*, 112071. https://doi.org/https://doi.org/10.1016/j.rser.2022.112071.

(6) Maria Joseph Raj, N. P.; KS, A.; Khandelwal, G.; Kim, S.-J. Method for Fabricating Highly Crystalline Polyvinylidene Fluoride for Piezoelectric Energy-Harvesting and Vibration Sensor Applications. *Sustain. Energy Fuels* **2022**, *6* (3), 674–681. https://doi.org/10.1039/D1SE01139A.

(7) Di Li; Wang, C.; Cui, X.; Chen, D.; Fei, C.; Yang, Y. Recent Progress and Development of Interface Integrated Circuits for Piezoelectric Energy Harvesting. *Nano Energy* **2022**, *94*, 106938. https://doi.org/https://doi.org/10.1016/j.nanoen.2022.106938.

(8) Jin, Z.; Zhao, F.; Lei, Y.; Wang, Y.-C. Hydrogel-Based Triboelectric Devices for Energy-Harvesting and Wearable Sensing Applications. *Nano Energy* **2022**, *95*,

106988. https://doi.org/https://doi.org/10.1016/j.nanoen.2022.106988.

(9) Li, X.; Gao, Q.; Cao, Y.; Yang, Y.; Liu, S.; Wang, Z. L.; Cheng, T. Optimization Strategy of Wind Energy Harvesting via Triboelectric-Electromagnetic Flexible Cooperation. *Appl. Energy* **2022**, *307*, 118311. https://doi.org/https://doi.org/10.1016/j.apenergy.2021.118311.

(10) Ando Junior, O. H.; Maran, A. L. O.; Henao, N. C. A Review of the Development and Applications of Thermoelectric Microgenerators for Energy Harvesting. *Renew. Sustain. Energy Rev.* **2018**, *91*, 376–393. https://doi.org/https://doi.org/10.1016/j.rser.2018.03.052.

(11) Heubner, C.; Liebmann, T.; Schneider, M.; Michaelis, A. Intercalation Electrochemistry for Thermoelectric Energy Harvesting from Temperature Fluctuations. *Chem. Commun.* **2022**, *58* (8), 1203–1206. https://doi.org/10.1039/D1CC06121F.

(12) *Thermoelectrics Handbook: Macro to Nano*; Rowe, D. M., Ed.; CRC Press. Taylor & Francis Group: Boca Raton, 2006. https://doi.org/10.1201/9781420038903.

(13) Seebeck, T. J. Magnetic Polarization of Metals and Minerals. *Abhandlungen der Dtsch. Akad. der Wissenschaften zu Berlin* **1822**, 289–346.

(14) Jordan, F. W. The Thomson and Peltier Effects. *Nature* **1911**, *86* (2168), 380. https://doi.org/10.1038/086380a0.

(15) Starling, S. G. Demonstration of Peltier and Thomson Effects. *Nature* **1911**, *85* (2155), 512. https://doi.org/10.1038/085512a0.

(16) Snyder, G. J.; Toberer, E. S. Complex Thermoelectric Materials. *Nat. Mater.* **2008**, *7*, 105–114.

(17) Tritt, T. *Advances in Thermoelectric Materials I*; ISSN; Elsevier Science, 2000.

(18) Rull-Bravo, M.; Moure, A.; Fernández, J. F.; Martín-González, M. Skutterudites as Thermoelectric Materials: Revisited. *RSC Adv.* **2015**, *5* (52), 41653–41667. https://doi.org/10.1039/C5RA03942H.

(19) Nolas, G. S.; Morelli, D. T.; Tritt, T. M. Skutterudites: A Phonon-Glass-Electron Crystal Approach to Advanced Thermoelectric Energy Conversion Applications. *Annu. Rev. Mater. Sci.* **1999**, *29* (1), 89–116. https://doi.org/10.1146/annurev.matsci.29.1.89.

(20) Shi, X.; Yang, J.; Salvador, J. R.; Chi, M.; Cho, J. Y.; Wang, H.; Bai, S.; Yang, J.; Zhang, W.; Chen, L. Multiple-Filled Skutterudites: High Thermoelectric Figure of Merit through Separately Optimizing Electrical and Thermal Transports. *J. Am.*

Chem. Soc. **2011**, *133* (20), 7837–7846. https://doi.org/10.1021/ja111199y.

(21) Christensen, M.; Johnsen, S.; Iversen, B. B. Thermoelectric Clathrates of Type I. *Dalt. Trans.* **2010**, *39* (4), 978–992. https://doi.org/10.1039/B916400F.

(22) Takabatake, T.; Suekuni, K.; Nakayama, T.; Kaneshita, E. Phonon-Glass Electron-Crystal Thermoelectric Clathrates: Experiments and Theory. *Rev. Mod. Phys.* **2014**, *86* (2), 669–716. https://doi.org/10.1103/RevModPhys.86.669.

(23) Hicks, L. D.; Dresselhaus, M. S. Effect of Quantum-Well Structures on the Thermoelectric Figure of Merit. *Phys. Rev. B* **1993**, *47*, 12727 – 12731.

(24) Poudel, B.; Hao, Q.; Ma, Y.; Lan, Y.; Minnich, A.; Yu, B.; Yan, X.; Wang, D.; Muto, A.; Vashaee, D.; Chen, X.; Liu, J.; Dresselhaus, M. S.; Chen, G.; Ren, Z. High-Thermoelectric Performance of Nanostructured Bismuth Antimony Telluride Bulk Alloys. *Science (80-.).* **2008**, *320* (5876), 634–638. https://doi.org/10.1126/science.1156446.

(25) Harman, T. C.; Taylor, P. J.; Walsh, M. P.; LaForge, B. E. Quantum Dot Superlattice Thermoelectric Materials and Devices. *Science (80-.).* **2002**, *297* (5590), 2229–2232. https://doi.org/10.1126/science.1072886.

(26) Venkatasubramanian, R.; Siivola, E.; Colpitts, T.; O'Quinn, B. Thin-Film Thermoelectric Devices with High Room-Temperature Figures of Merit. *Nature* **2001**, *413* (6856), 597–602. https://doi.org/10.1038/35098012.

(27) Soleimani, Z.; Zoras, S.; Ceranic, B.; Shahzad, S.; Cui, Y. The Cradle to Gate Life-Cycle Assessment of Thermoelectric Materials: A Comparison of Inorganic, Organic and Hybrid Types. *Sustain. Energy Technol. Assessments* **2021**, *44*, 101073. https://doi.org/https://doi.org/10.1016/j.seta.2021.101073.

(28) Zhang, Y.; Heo, Y.-J.; Park, M.; Park, S.-J. Recent Advances in Organic Thermoelectric Materials: Principle Mechanisms and Emerging Carbon-Based Green Energy Materials. *Polymers (Basel).* **2019**, *11* (1). https://doi.org/10.3390/polym11010167.

(29) Heeger, A. J. Semiconducting and Metallic Polymers: The Fourth Generation of Polymeric Materials. *J. Phys. Chem. B* **2001**, *105* (36), 8475–8491. https://doi.org/10.1021/jp011611w.

(30) Bubnova, O.; Khan, Z. U.; Malti, A.; Braun, S.; Fahlman, M.; Berggren, M.; Crispin, X. Optimization of the Thermoelectric Figure of Merit in the Conducting Polymer Poly(3,4-Ethylenedioxythiophene). *Nat. Mater.* **2011**, *10* (6), 429–433. https://doi.org/10.1038/nmat3012.

(31) Zhang, Q.; Sun, Y.; Xu, W.; Zhu, D. Thermoelectric Energy from Flexible P3HT Films Doped with a Ferric Salt of Triflimide Anions. *Energy Environ. Sci.* **2012**, *5* (11), 9639. https://doi.org/10.1039/c2ee23006b.

(32) Nath, C.; Kumar, A.; Kuo, Y.-K.; Okram, G. S. High Thermoelectric Figure of Merit in Nanocrystalline Polyaniline at Low Temperatures. *Appl. Phys. Lett.* **2014**, *105* (13), 133108. https://doi.org/10.1063/1.4897146.

(33) Kirchmeyer, S.; Reuter, K.; Simpson, J. Poly(3.4-Ethylenedioxythiophene) - Scientific Importance, Remarkable Properties, and Applications. In *Handbook of Conducting Polymers*; Skotheim, T. A., Reynolds, J., Eds.; CRC Press. Taylor & Francis Group: New York, 2007. https://doi.org/10.1201/b12346.

(34) Elschner, A.; Kirchmeyer, S.; Lovenich, W.; Merker, U.; Reuter, K. *PEDOT: Principles and Applications of an Intrinsically Conductive Polymer*; CRC Press, 2010.

(35) Brédas, J. L.; Wudl, F.; Heeger, A. J. Polarons and Bipolarons in Doped Polythiophene: A Theoretical Investigation. *Solid State Commun.* **1987**, *63* (7), 577–580. https://doi.org/https://doi.org/10.1016/0038-1098(87)90856-8.

(36) Fahlman, M.; Salaneck, W. R. Surfaces and Interfaces in Polymer-Based Electronics. *Surf. Sci.* **2002**, *500* (1–3), 904–922. https://doi.org/10.1016/S0039-6028(01)01554-0.

(37) Reiss, H. Theoretical Analysis of Protonic Acid Doping of the Emeraldine Form of Polyaniline. *J. Phys. Chem.* **1988**, *92* (12), 3657–3662. https://doi.org/10.1021/j100323a064.

(38) MacDiarmid, A. G. "Synthetic Metals": A Novel Role for Organic Polymers (Nobel Lecture). *Angew. Chemie Int. Ed.* **2001**, *40* (14), 2581–2590. https://doi.org/https://doi.org/10.1002/1521-3773(20010716)40:14<2581::AID-ANIE2581>3.0.CO;2-2.

(39) MacDiarmid, A. G.; Mammone, R. J.; Kaner, R. B.; Porter, Lord. The Concept of 'Doping' of Conducting Polymers: The Role of Reduction Potentials. *Philos. Trans. R. Soc. London. Ser. A, Math. Phys. Sci.* **1985**, *314* (1528), 3–15. https://doi.org/10.1098/rsta.1985.0004.

(40) Heeger, A. J. Semiconducting and Metallic Polymers: The Fourth Generation of Polymeric Materials (Nobel Lecture). *Angew. Chemie Int. Ed.* **2001**, *40* (14), 2591–2611. https://doi.org/https://doi.org/10.1002/1521-3773(20010716)40:14<2591::AID-ANIE2591>3.0.CO;2-0.

(41) Kaiser, A. B. Systematic Conductivity Behavior in Conducting Polymers: Effects of Heterogeneous Disorder. *Adv. Mater.* **2001**, *13* (12–13), 927–941. https://doi.org/https://doi.org/10.1002/1521-4095(200107)13:12/13<927::AID-ADMA927>3.0.CO;2-B.

(42) Kim, N.; Lee, B. H.; Choi, D.; Kim, G.; Kim, H.; Kim, J.-R.; Lee, J.; Kahng, Y. H.; Lee, K. Role of Interchain Coupling in the Metallic State of Conducting Polymers. *Phys. Rev. Lett.* **2012**, *109* (10), 106405. https://doi.org/10.1103/PhysRevLett.109.106405.

(43) Kline, R. J.; McGehee, M. D. Morphology and Charge Transport in Conjugated Polymers. *J. Macromol. Sci. Part C Polym. Rev.* **2006**, *46* (1), 27–45. https://doi.org/10.1080/15321790500471194.

(44) Levy, O.; Stroud, D. Macroscopic Disorder and the Metal - Insulator Transition in Conducting Polymers. *J. Phys. Condens. Matter* **1997**, *9* (45), L599–L605. https://doi.org/10.1088/0953-8984/9/45/002.

(45) Li, X.; Liu, C.; Zhou, W.; Duan, X.; Du, Y.; Xu, J.; Li, C.; Liu, J.; Jia, Y.; Liu, P.; Jiang, Q.; Luo, C.; Liu, C.; Jiang, F. Roles of Polyethylenimine Ethoxylated in Efficiently Tuning the Thermoelectric Performance of Poly(3,4-Ethylenedioxythiophene)-Rich Nanocrystal Films. *ACS Appl. Mater. Interfaces* **2019**, *11* (8), 8138–8147. https://doi.org/10.1021/acsami.9b00298.

(46) Fan, Z.; Du, D.; Guan, X.; Ouyang, J. Polymer Films with Ultrahigh Thermoelectric Properties Arising from Significant Seebeck Coefficient Enhancement by Ion Accumulation on Surface. *Nano Energy* **2018**, *51*, 481–488. https://doi.org/10.1016/j.nanoen.2018.07.002.

(47) Jiang, Y.; Dong, X.; Sun, L.; Liu, T.; Qin, F.; Xie, C.; Jiang, P.; Hu, L.; Lu, X.; Zhou, X.; Meng, W.; Li, N.; Brabec, C. J.; Zhou, Y. An Alcohol-Dispersed Conducting Polymer Complex for Fully Printable Organic Solar Cells with Improved Stability. *Nat. Energy* **2022**, *7* (4), 352–359. https://doi.org/10.1038/s41560-022-00997-9.

(48) Cappai, A.; Antidormi, A.; Bosin, A.; Narducci, D.; Colombo, L.; Melis, C. Impact of Synthetic Conditions on the Anisotropic Thermal Conductivity of Poly(3,4-Ethylenedioxythiophene) (PEDOT): A Molecular Dynamics Investigation. *Phys. Rev. Mater.* **2020**, *4* (3), 035401. https://doi.org/10.1103/PhysRevMaterials.4.035401.

(49) Zhao, W.; Ding, J.; Zou, Y.; Di, C.; Zhu, D. Chemical Doping of Organic

Semiconductors for Thermoelectric Applications. *Chem. Soc. Rev.* **2020**, *49* (20), 7210–7228. https://doi.org/10.1039/D0CS00204F.

(50) Patel, S. N.; Glaudell, A. M.; Kiefer, D.; Chabinyc, M. L. Increasing the Thermoelectric Power Factor of a Semiconducting Polymer by Doping from the Vapor Phase. *ACS Macro Lett.* **2016**, *5* (3), 268–272. https://doi.org/10.1021/acsmacrolett.5b00887.

(51) Yurash, B.; Cao, D. X.; Brus, V. V.; Leifert, D.; Wang, M.; Dixon, A.; Seifrid, M.; Mansour, A. E.; Lungwitz, D.; Liu, T.; Santiago, P. J.; Graham, K. R.; Koch, N.; Bazan, G. C.; Nguyen, T.-Q. Towards Understanding the Doping Mechanism of Organic Semiconductors by Lewis Acids. *Nat. Mater.* **2019**, *18* (12), 1327–1334. https://doi.org/10.1038/s41563-019-0479-0.

(52) Pingel, P.; Neher, D. Comprehensive Picture of P-Type Doping of P3HT with the Molecular Acceptor F4TCNQ. *Phys. Rev. B* **2013**, *87* (11), 115209. https://doi.org/10.1103/PhysRevB.87.115209.

(53) Rivnay, J.; Inal, S.; Salleo, A.; Owens, R. M.; Berggren, M.; Malliaras, G. G. Organic Electrochemical Transistors. *Nat. Rev. Mater.* **2018**, *3* (2), 17086. https://doi.org/10.1038/natrevmats.2017.86.

(54) Zhang, F.; Zang, Y.; Huang, D.; Di, C.; Gao, X.; Sirringhaus, H.; Zhu, D. Modulated Thermoelectric Properties of Organic Semiconductors Using Field-Effect Transistors. *Adv. Funct. Mater.* **2015**, *25* (20), 3004–3012. https://doi.org/10.1002/adfm.201404397.

(55) Culebras, M.; Gómez, C. M.; Cantarero, A. Enhanced Thermoelectric Performance of PEDOT with Different Counterions Optimized by Chemical Reduction. *J. Mater. Chem. A* **2014**, *2* (26), 10109–10115. https://doi.org/10.1039/C4TA01012D.

(56) Kim, G.-H.; Shao, L.; Zhang, K.; Pipe, K. P. Engineered Doping of Organic Semiconductors for Enhanced Thermoelectric Efficiency. *Nat. Mater.* **2013**, *12* (8), 719–723. https://doi.org/10.1038/nmat3635.

(57) Luo, J.; Billep, D.; Waechtler, T.; Otto, T.; Toader, M.; Gordan, O.; Sheremet, E.; Martin, J.; Hietschold, M.; Zahn, D. R. T.; Gessner, T. Enhancement of the Thermoelectric Properties of PEDOT:PSS Thin Films by Post-Treatment. *J. Mater. Chem. A* **2013**, *1* (26), 7576. https://doi.org/10.1039/c3ta11209h.

(58) Mengistie, D. A.; Chen, C.-H.; Boopathi, K. M.; Pranoto, F. W.; Li, L.-J.; Chu, C.-W. Enhanced Thermoelectric Performance of PEDOT:PSS Flexible Bulky Papers by Treatment with Secondary Dopants. *ACS Appl. Mater. Interfaces* **2015**, *7* (1), 94–

100. https://doi.org/10.1021/am507032e.

(59) Fan, Z.; Du, D.; Yu, Z.; Li, P.; Xia, Y.; Ouyang, J. Significant Enhancement in the Thermoelectric Properties of PEDOT:PSS Films through a Treatment with Organic Solutions of Inorganic Salts. *ACS Appl. Mater. Interfaces* **2016**, *8* (35), 23204–23211. https://doi.org/10.1021/acsami.6b07234.

(60) Kim, N.; Kee, S.; Lee, S. H.; Lee, B. H.; Kahng, Y. H.; Jo, Y.-R.; Kim, B.-J.; Lee, K. Highly Conductive PEDOT:PSS Nanofibrils Induced by Solution-Processed Crystallization. *Adv. Mater.* **2014**, *26* (14), 2268–2272. https://doi.org/10.1002/adma.201304611.

(61) Atahan-Evrenk, Ş.; Aspuru-Guzik, A. Prediction and Theoretical Characterization of P-Type Organic Semiconductor Crystals for Field-Effect Transistor Applications BT - Prediction and Calculation of Crystal Structures: Methods and Applications; Atahan-Evrenk, S., Aspuru-Guzik, A., Eds.; Springer International Publishing: Cham, 2014; pp 95–138. https://doi.org/10.1007/128_2013_526.

(62) Hiroshige, Y.; Ookawa, M.; Toshima, N. High Thermoelectric Performance of Poly(2,5-Dimethoxyphenylenevinylene) and Its Derivatives. *Synth. Met.* **2006**, *156* (21–24), 1341–1347. https://doi.org/10.1016/j.synthmet.2006.10.004.

(63) Ito, H.; Harada, T.; Tanaka, H.; Kuroda, S. Critical Regime for the Insulator–Metal Transition in Highly Ordered Conjugated Polymers Gated with Ionic Liquid. *Jpn. J. Appl. Phys.* **2016**, *55* (3S2), 03DC08. https://doi.org/10.7567/JJAP.55.03DC08.

(64) Shi, W.; Qu, S.; Chen, H.; Chen, Y.; Yao, Q.; Chen, L. One-step Synthesis and Enhanced Thermoelectric Properties of Polymer–Quantum Dot Composite Films. *Angew. Chemie* **2018**, *130* (27), 8169–8174. https://doi.org/10.1002/ange.201802681.

(65) He, M.; Ge, J.; Lin, Z.; Feng, X.; Wang, X.; Lu, H.; Yang, Y.; Qiu, F. Thermopower Enhancement in Conducting Polymer Nanocomposites via Carrier Energy Scattering at the Organic–Inorganic Semiconductor Interface. *Energy Environ. Sci.* **2012**, *5* (8), 8351. https://doi.org/10.1039/c2ee21803h.

(66) Xu, S.; Shi, X.-L.; Dargusch, M.; Di, C.; Zou, J.; Chen, Z.-G. Conducting Polymer-Based Flexible Thermoelectric Materials and Devices: From Mechanisms to Applications. *Prog. Mater. Sci.* **2021**, *121*, 100840. https://doi.org/10.1016/j.pmatsci.2021.100840.

(67) Yao, Q.; Wang, Q.; Wang, L.; Chen, L. Abnormally Enhanced Thermoelectric Transport Properties of SWNT/PANI Hybrid Films by the Strengthened PANI

Molecular Ordering. *Energy Environ. Sci.* **2014**, *7* (11), 3801–3807. https://doi.org/10.1039/C4EE01905A.

(68) Meng, C.; Liu, C.; Fan, S. A Promising Approach to Enhanced Thermoelectric Properties Using Carbon Nanotube Networks. *Adv. Mater.* **2010**, *22* (4), 535–539. https://doi.org/10.1002/adma.200902221.

(69) Xu, K.; Chen, G.; Qiu, D. In Situ Chemical Oxidative Polymerization Preparation of Poly(3,4-Ethylenedioxythiophene)/Graphene Nanocomposites with Enhanced Thermoelectric Performance. *Chem. - An Asian J.* **2015**, *10* (5), 1225–1231. https://doi.org/10.1002/asia.201500066.

(70) See, K. C.; Feser, J. P.; Chen, C. E.; Majumdar, A.; Urban, J. J.; Segalman, R. A. Water-Processable Polymer−Nanocrystal Hybrids for Thermoelectrics. *Nano Lett.* **2010**, *10* (11), 4664–4667. https://doi.org/10.1021/nl102880k.

(71) Wang, L.; Zhang, Z.; Liu, Y.; Wang, B.; Fang, L.; Qiu, J.; Zhang, K.; Wang, S. Exceptional Thermoelectric Properties of Flexible Organic−inorganic Hybrids with Monodispersed and Periodic Nanophase. *Nat. Commun.* **2018**, *9* (1), 3817. https://doi.org/10.1038/s41467-018-06251-9.

(72) Ju, H.; Kim, J. Chemically Exfoliated SnSe Nanosheets and Their SnSe/Poly(3,4-Ethylenedioxythiophene):Poly(Styrenesulfonate) Composite Films for Polymer Based Thermoelectric Applications. *ACS Nano* **2016**, *10* (6), 5730–5739. https://doi.org/10.1021/acsnano.5b07355.

Chapter 2

Characterization techniques

Content

This chapter explains the characterization techniques used to determine the properties of the materials synthesized in this work. The vast majority of the characterization carried out corresponds to thermoelectric, mechanical, structural, and morphological analysis.

2.1 Electrical conductivity

Determining electrical conductivity involves measuring electrical resistance, a simple measurement for most materials. The four-probe method is typically used where an electrical current is passed between two current leads, and the voltage is recorded using two other voltage leads. In this way, the contribution of the leads or contacts in the measurement of the sample voltage is eliminated. However, measuring electrical resistance in thermoelectric materials, generally, semiconductors, poses several challenges. On the one hand, making good electrical contacts is complicated in most thermoelectric materials due to the formation of oxide layers on the surface, frequently forming p-n junctions and resulting in nonohmic voltages producing errors in the measurement of electrical resistivity. This is not our case since conductive polymers are generally p-type semiconductors in which oxide layers do not form on the surface. On the other hand, the measurement of electrical resistance in thin films presents more diffusion problems than in bulk samples.[1]

There are specific techniques for measuring electrical resistivity in thin films or samples with an arbitrary shape. One of them was developed by van der Pauw in the late 1950s[2,3], and corrections were added in later years.[4–6] In this technique, the electrical conductivity is obtained from the measurement of four-point resistance in two different geometries of the contact arrangement, as shown in **Figure 2.1(a)**. For the first resistance measurement, a current I_{AB} was driven from two contacts, A and B. The potential difference V_{CD} between the other contacts, C and D, was measured, obtaining the resistance R_1. The second resistance, R_2, was determined by driving the current from A to C, I_{AC}, and measuring the voltage between B and D, V_{BD}. According to the Ohm law, the voltage and

current values were plotted, giving a linear trend as shown in **Figure 2.1(b)**. The electrical conductivity of the sample was obtained by solving the van der Pauw equation:[2]

$$e^{-\pi d R_1 \sigma} + e^{-\pi d R_2 \sigma} = 1 \qquad \textbf{(2.1)}$$

where d is the sample thickness previously measured, and σ is the electrical conductivity. A Keithley 2400 Source Meter was used as a driving source and voltage measurer.

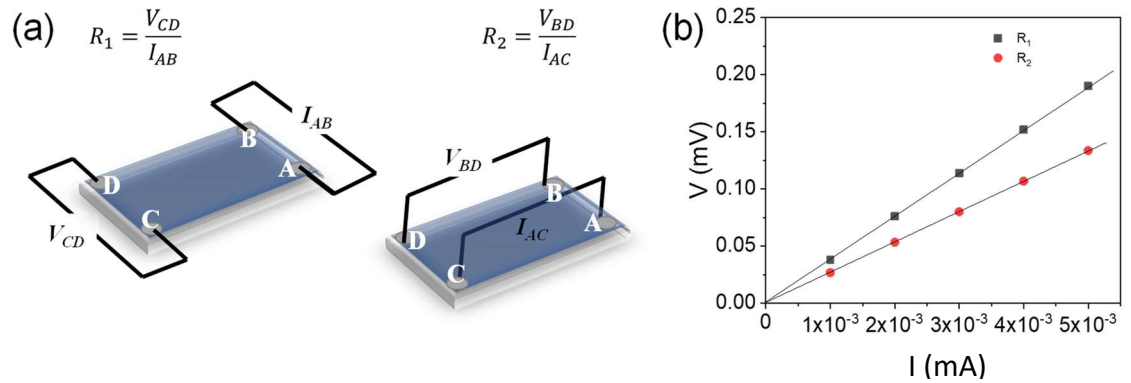

Figure 2.1 (a) Contacts configurations to measure electrical resistance R_1 and R_2. (b) Voltage as a function of the current to determine R_1 and R_2.

2.2 Seebeck coefficient

The Seebeck effect is the development of an electromotive force across the material in response to the imposition of a thermal gradient. The ratio of the electromotive force to the temperature difference is called the Seebeck coefficient, S.[1] The Seebeck coefficient or thermopower is an intrinsic property related to the electronic structure of the material. Thermopower provides information about the sign of the charge carrier. Its temperature dependence is difficult to interpret because many other contributions, such as phonon-drag, can be combined with the simple diffusion of thermopower (linear in T) typical of metals. Seebeck coefficient does not depend on the sample geometry (as electrical resistance does) and is given by measuring the ratio of the sample voltage to the temperature difference, **Equation (2.2)**. The precision in the measurements of the Seebeck coefficient relies on determining the temperatures precisely at the position of the voltage probes. Therefore, the thermocouples should be placed as close to the voltage contacts as possible without electronically contacting the sample for accurate measurements. Another way to measure

the thermal gradient is to use two independent thermocouples. This configuration can use one leg of each thermocouple as the sample voltage lead. Therefore, the thermocouples must have good thermal and electrical contact with the sample. Although this technique provides reliable results, unfortunately, this method often requires the use of new thermocouples for each measurement, making it impractical. Therefore, it is desirable to use permanent thermocouples that only require thermal anchoring with the sample using contact adhesives for faster sample throughput.

For the measurement of the Seebeck coefficient, there are mainly two procedures. The first consists of setting the temperature of the sample at one end and gradually varying the temperature at the other end until a slight thermal gradient is reached across the sample. The voltage is recorded as a function of the thermal gradient, and the slope gives the Seebeck coefficient. The second one sets a small thermal gradient across the sample and varies the temperature while keeping the gradient constant. In this case, the voltage at each temperature is measured, and, knowing the thermal gradient, the Seebeck coefficient is calculated.

In this thesis, the Seebeck coefficient has been determined using a homemade device. This device consists of one Peltier as a heater and one copper block cooled by water flow which acts as a cooler. The sample is placed between these moduli, creating a temperature difference, and the resulting voltage is recorded. The Seebeck coefficient can be determined as the ratio between the electrical potential, ΔV, and the temperature difference, ΔT:

$$S = -\frac{\Delta V}{\Delta T} \qquad \textbf{(2.2)}$$

A Lakeshore 340 and two PT100 sensors previously calibrated temperature control the temperature. To record the potential data, an Agilent 34401A Multimeter was employed. Both instruments are controlled together using LabView Software. **Figure 2.2(a)** shows a schematic of the homemade setup developed for the Seebeck coefficient measurements. The voltage as a function of the thermal gradient was plotted, giving a linear trend **Figure 2.2(b)** according to the typical diffusion of the thermopower of the metals. Additionally, the copper block can be substituted for another Peltier to measure the Seebeck coefficient at different temperatures than ambient, between 0 ºC to 140 ºC.

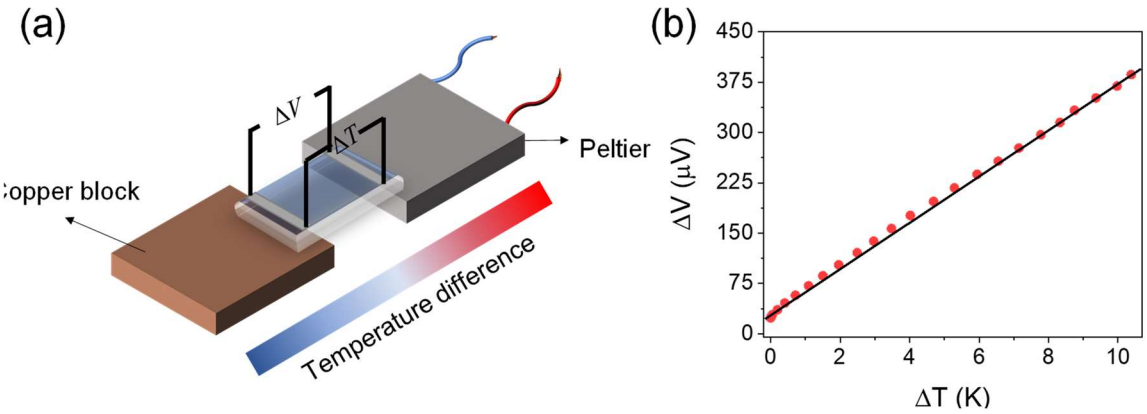

Figure 2.2 (a) Scheme of the homemade setup to measure Seebeck coefficient. (b) Seebeck voltage as a function of the temperature difference.

2.3 Film thickness

To determine the dimensions of the sample, it is necessary to know its thickness since, as we have seen previously in the van der Pauw equation, **Equation (2.1)** is one of the parameters to calculate the electrical conductivity. Therefore, tiny cuts were made on the film's surface without damaging the substrate, and the thickness was measured with the Dektak 150 profilometer. The values used to determine electrical and thermal conductivity represent an average of at least five measurements per film.

2.4 Power output

Thermoelectric modules can convert heat into electricity when working in Seebeck mode. Electrical power generated by a module depends on the number of units and their configuration in the module, the thermoelectric properties, the properties of the contact layers, and the temperature difference reached across the sample. In general, the output voltage and the output current depend inversely on the element's length.[1] Therefore, for a particular temperature difference and unit length, the ratio of current/area and voltage/number of the elements should be optimized to reach the maximum power output, *P*, which is expressed with the following Equation:

$$P = \frac{\Delta V^2}{R_L} \qquad \textbf{(2.3)}$$

where V is the voltage across the contacts and R_L is the load resistance.

The research group has designed a setup to control the loaded resistance and the output voltage measured with the Agilent 34401A digital multimeter, **Figure 2.3(a)**. The thermoelectric generators with a determined thermal gradient were placed and connected to the device designed to supply the resistance for the output power measurements, also connected to the multimeter. Resistance is gradually being loaded to the thermoelectric generator while simultaneously measuring the output voltage so that the output voltage is recorded as a function of the loaded resistance, **Figure 2.3(b)**. Then, applying **Equation (2.3),** the output power is obtained.

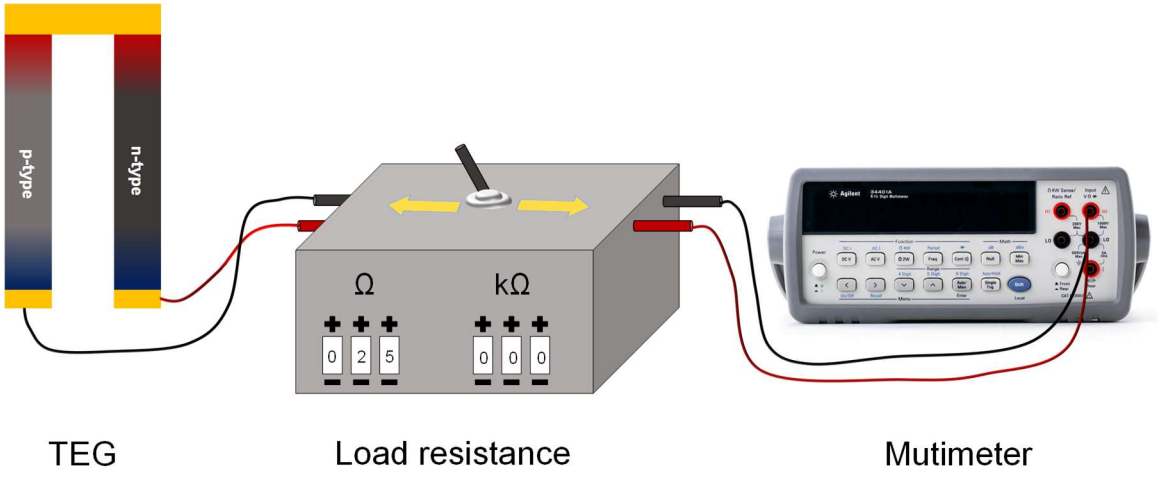

Figure 2.3 Homemade setup designed to measure the output power.

2.5 Thermal conductivity

Two different techniques were used to measure the thermal conductivity of the samples. On the one hand, the frequency-domain thermoreflectance was used for thin films. However, this technique is unsuitable for materials with a rough surfaces such as fabrics. Therefore, the thermal conductivity of the fabrics was carried out by the axial heat flow method.

2.5.1 Axial heat flow method

The axial heat flow technique is a steady-state method for determining thermal conductivity.[7] The operating principle is based on the deduction of the heat flux by measuring a temperature drop in thermal resistance. The sample is placed between two plates at different temperatures, and a heat flux sensor is used to obtain the heat flux through the sample. The heat flux, Q, is determined by measuring the electrical potential drop across the sample following the specific expression recommended by the manufacturer:

$$Q = \frac{V}{S\left(1 + 0.002(T - 20)\right)} \tag{2.4}$$

where V is the output voltage obtained by the heat flux sensor, S is the sensor sensibility, and T is the absolute temperature.

The temperature of the plates is adjusted to a desired constant value. Steady-state conditions are reached when the heat flow is equal at each point in the system. Once the thermal equilibrium is reached, the thermal conductivity is determined with the Fourier-Biot expression:[8,9]

$$Q = -\kappa\, A\, \frac{\Delta T}{\Delta x} \tag{2.5}$$

where Q is the heat flux, measured in W m^{-2}, κ is the thermal conductivity of the material, A is the heat transfer area, ΔT is the temperature difference across the sample, and Δx is the distance of heat transfer (the thickness of the sample).

This method is suitable for measuring the thermal conductivity of insulating materials and polymers (κ < 0.3 W m^{-1} K^{-1}) with a measurement uncertainty of around 3%.[10]

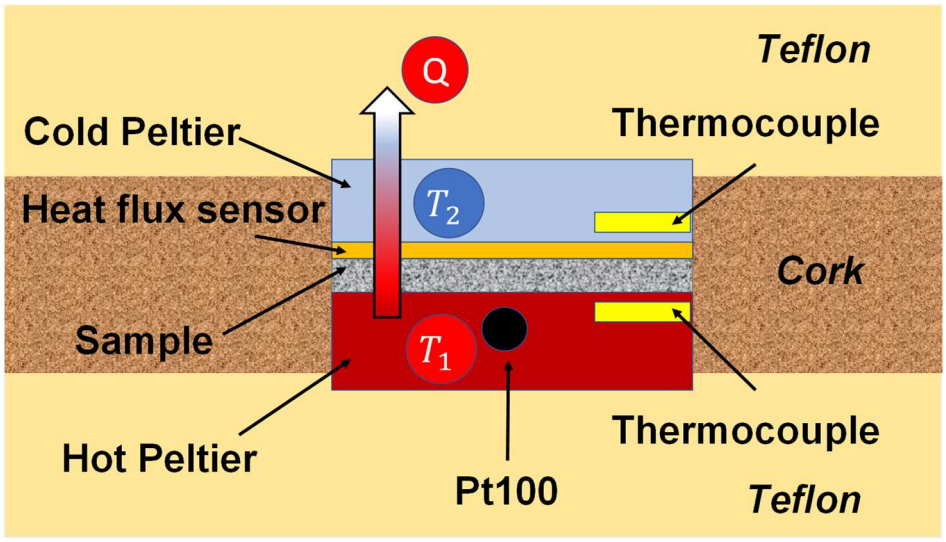

Figure 2.4 Scheme of the homemade setup for thermal conductivity of textiles.

A homemade setup was built to measure the thermal conductivity of the fabrics. As shown in **Figure 2.4**, two surface thermocouple self-adhering of Omega company were used to measure the temperature difference between the hot and cold parts, and an FHF04 heat flux sensor with an accuracy of 10.88 μV W^{-1} m^2 was used to measure the heat flux through the sample. The heat flux was monitored by the voltage changes detected by the sensor and recorded by the Agilent 344420A digital multimeter, and the heat flux sensor measured the temperature.

The hot part was kept at a constant temperature simulating body temperature (308 K) using an omega model CN7500 temperature controller connected to the Peltier TEC1-12706 and a Pt100 temperature sensor. Besides, for simulation of ambient temperature (cold part), Peltier ATS-TEC30-36-017 was used.

The heat flux was determined with **Equation (2.4)**, and the thermal conductivity of the fabrics was calculated with **Equation (2.5)**, using the previously obtained heat flux value.[11,12] All samples were stored at 50% humidity for 24 hours and tested at a pressure of 10 kPa.

2.5.2 Frequency-domain thermoreflectance method

The thermoreflectance technique is a transient thermal measurement technique that can measure both in-plane and cross-plane thermal conductivity of thin films.[13,14]

In thermoreflectance measurements, a modulated laser heat source (pump laser) locally heats the sample, while a second laser (probe laser) detects the local temperature variation by reflectance change at the sample surface, **Figure 2.5(a)**. The energy from the harmonic modulated pump is absorbed in the surface, resulting in a fluctuation in temperature, ΔT. The change in temperature causes a variation in the optical constants of the surface, leading to a change in reflectivity, ΔR. This is known as the thermoreflectance effect. The transducer covers the sample with an optically thick (>60nm) metallic film to ensure that the laser is optically absorbed on the surface. In the transducer, the thermal reflectance coefficient C_{TR} is defined by:

$$C_{TR} = \frac{\Delta R}{\Delta T} \tag{2.6}$$

The phase measured in the probe signal is made up of three signals: the thermal phase, which contains the information we want to determine; the phase of the path of the beams; and the phase of the instrument:

$$\varphi_{measured} = \varphi_{thermal} + \varphi_{path} + \varphi_{instrument} \quad \textbf{(2.7)}$$

In order to make sure the measured phase only contains information on the thermal properties of the sample, it is necessary to suppress the contribution of the other two phases. The phase difference caused by the optical path can be considered negligible because the light speed is very high, and the modulation frequency range used in the experiment is not that high. The detectors, instruments, and cables produce the instrumental phase difference and are frequency dependent. By calibrating at each frequency point using the reflection of the pump laser, it is possible to determine the instrumental phase difference. This correction factor is subtracted from subsequent measurements so that $\varphi_{measured} = \varphi_{thermal}$.

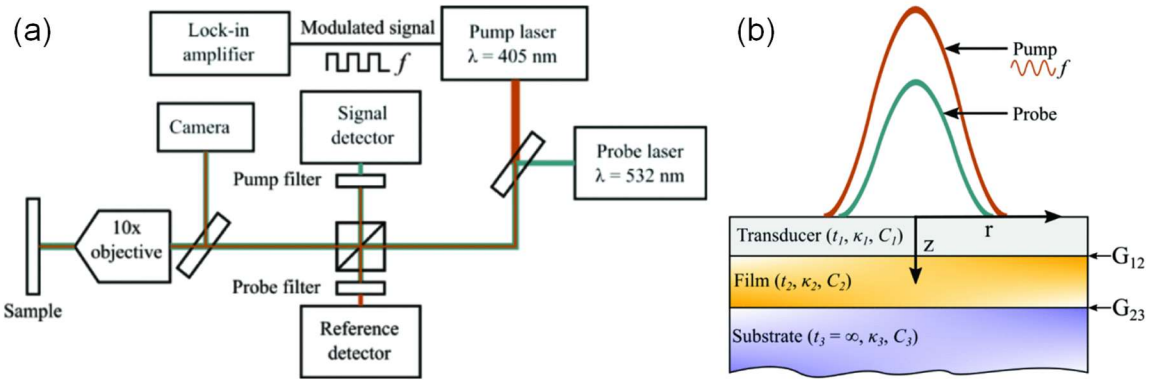

Figure 2.5 (a) Schematic diagram of a typical frequency-domain thermoreflectance setup. (b) Schematic measurement of the thin film sample. Reproduced with permission.[14] Copyright 2022 IEEE.

With this configuration, a frequency vs phase shift curve is obtained. This curve is fitted with a thermal model curve, using the thermal conductivity of the sample as the fitting parameter. **Figure 2.5(b)** schematically shows the measurement process illustrating the relevant sample properties: thermal conductivity (κ_n), volume heat capacity (C_n), thickness (t_n), and thermal boundary conductance between adjacent layers $(G_{n,n+1})$.

2.6 Dielectric relaxation spectroscopy

Dielectric Relaxation Spectroscopy, DRS, is a technique that analyzes the interaction of the sample with a time-dependent electric field and allows to determine the electrical properties of the material since these are related to the physical and chemical properties of the sample. The Dielectric Relaxation Spectroscopy technique is based on applying an

external electric field to the sample so that the molecular dipole systems present are altered until the electric field disappears. Then, the molecular dipoles return to equilibrium and allow obtaining information about the spontaneous fluctuations of the material. The dipoles' reorientation and the charged particles' translational diffusion in the oscillating electric field are the basis of this technique's analysis. Therefore, the DRS technique measures the changes in different physical properties of polar material, such as polarization, permittivity, and conductivity, as a function of the temperature and the frequency of the external electric field.[15]

Dielectric spectroscopy has been used to determine the electrical conductivity of the fabrics using a Novocontrol Broadband dielectric spectrometer (Hundsagen, Germany), integrated by an SR lock-in amplifier with an Alpha dielectric interface in the frequency range 10^{-2} to 10^{6} Hz. The samples were placed under a steady flow inert N_2 atmosphere to avoid moisture uptake during all measurements. Disc-shaped samples of 10 mm diameter and an approximate thickness of 0.12 mm were mounted in the dielectric cell between two parallel cylindrical gold-plated electrodes. The sample thickness was accurately determined with a micrometer screw. Isothermal measurements (room temperature) were carried out at forty-four frequencies between $5 \cdot 10^{-2}$ and $3 \cdot 10^{6}$ Hz. The experimental uncertainty was less than 5% in all cases.

2.7 Differential scanning calorimetry

Differential scanning calorimetry (DSC) is a thermoanalytical technique in which the difference in the amount of heat required to increase the temperature of a sample and the reference is measured as a function of temperature. The sample and reference are maintained at nearly the same temperature throughout the experiment. Generally, the temperature program for a DSC analysis is designed such that the sample holder temperature increases linearly as a function of time. Before the DSC experiment started, the sample and reference pans were in equilibrium (same temperature), and when the measurement started, the heating block would be heated at a linear rate. Therefore, the sample and reference pans will also be heated. Due to the additional mass of the sampling calorimeter, the heat capacity is higher than the reference one, which is empty. This fact induces a temperature lag in the sampling calorimeter and assuming the pan masses are identical, the temperature difference between the sample and reference will be proportional

to the heat capacity. This temperature difference developed between the sample and the reference pans allows the calculation of the heat flow and the measurements of several characteristic properties from the sample, such as fusion and crystallization events as well as glass transition temperatures.[16]

A TA Instruments DSC Q20 calibrated with indium and refrigerated with a cooling system was employed to analyze all the samples in this thesis. In this module, the sample and reference pans sit on raised platforms with a constantan disk at their base. The temperature sensors are placed on the underside of each platform (see **Figure 2.6**). The ΔT output from the sample and reference temperature sensors are connected to an amplifier to increase their signal strength.

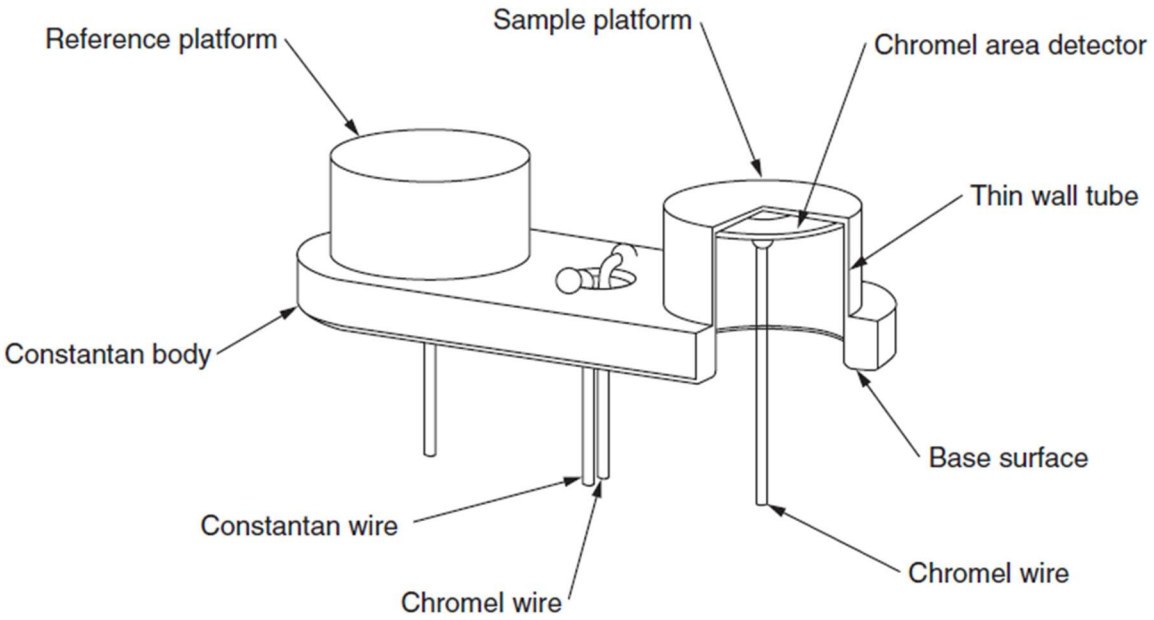

Figure 2.6 DSC sensor assembly for the TA Instrument Q20. Reproduced with permission.[17] Copyright 2002, Elsevier Science B.V.

The DSC tests were performed under a 20 mL min^{-1} flow of nitrogen to avoid the oxidation of the samples. The measurements were conducted in crimpled non-hermetic aluminum pans, using an empty crimpled aluminum pan as the reference calorimeter. In order to obtain a defined peak and high resolution, it recommends that the contact surface between the calorimeter and the sample be high. For that reason, the fabrics were cut in disc shapes like the pans with a total mass of around 5 mg. DSC thermograms were obtained from 0 to 300 ºC under a nitrogen atmosphere. Two scans were performed. In the first one, the sample was heated at a rate of 10 ºC min^{-1} until 300 ºC, then was kept at this

temperature for 10 minutes. The sample was then cooled at 50 °C min^{-1} to 0 °C. In the second cycle, samples were heated at 10 °C min^{-1} to 300 °C.

Glass transition temperature (T_g), melting temperature (T_m), and melting enthalpy (ΔH) were determined using TRIOS software. In DSC measurements, T_g can be observed by a step in the baseline of the measurement curve. It is characterized by its midpoint. The melting process appears as an endothermic peak, whose maximum value is associated with the T_m. The melting enthalpy is determined by integrating this peak.

2.8 Thermogravimetric analysis

The thermogravimetric analysis (TGA) is a method of thermal analysis that consists of monitoring the mass of the sample as a function of temperature (dynamic mode) or as a function of time, keeping constant the temperature (isothermal mode) in a controlled atmosphere.[16] Depending on the purge gas flowing through the balance, we can create an inert atmosphere (nitrogen, argon, or helium), oxidizing atmosphere (air, oxygen), or a reducing atmosphere (8-10 % hydrogen in nitrogen). This measurement provides information about physical phenomena, such as phase transitions, absorption, adsorption, and desorption; as well as chemical phenomena, including chemisorptions, thermal decomposition, and solid-gas reactions (e.g., oxidation or reduction).[18]

Polymers generally exhibit mass loss as a function of temperature or time at a certain temperature. This mass loss can have three main regions. Usually, the first region corresponds to the volatile components such as absorbed moisture, residual solvents, low-molecular-mass additives, or oligomers, which generally evaporate between ambient and 300 ºC. The second region corresponds to the reaction products, typically between 100 ºC and 250 ºC. Finally, the last region corresponds to the generation of volatile degradation products resulting from chain scission that require temperatures above 200 ºC but not more than 800 ºC. These mass loss processes are useful for obtaining information about the composition and thermal stability.[16]

TGA measurements were performed on a TGA 550 from TA Instruments using platinum pans under a 50 mL min^{-1} flow of air. Depending on the material analyzed, different conditions were employed.

2.9 Dynamic mechanical analysis

Dynamic mechanical analysis (DMA) is a technique used to study the mechanical properties of polymers as a function of time and temperature. The DMA measures the mechanical stiffness (modulus) and energy absorption by subjecting the sample to oscillating mechanical stress or strain within the linear viscoelastic region. There is a difference between the oscillatory stress or strain applied to the sample strain or stress measured, allowing one to determine the complex modulus (E^*). The phase angle δ represents this difference. The materials respond to the applied stress or strain by dissipating the input energy in a viscous flow (non-reversible response), storing the energy elastically (reversible response), or using a combination of both.[16] Once the complex modulus has been obtained, and the measurements of δ have been made, the storage modulus (E') and the loss modulus (E'') can be determined (see equations **(2.8) to (2.10)**).

$$E^* = \frac{stress}{strain} \quad \textbf{(2.8)}$$

$$E' = E^* \cos\delta \quad \textbf{(2.9)}$$

$$E'' = E^* \sin\delta \quad \textbf{(2.10)}$$

$$\tan\delta = \frac{E''}{E'} \quad \textbf{(2.11)}$$

These new parameters allow a better understanding of the material since the storage modulus is related to the stiffness of the sample. The loss modulus is associated with the viscous component and, therefore, the ability to dissipate mechanical energy through molecular motion. Another standard parameter is the phase angle tangent, or $\tan\delta$, which provides information about the relationship between the elastic and inelastic components, **Equation (2.11)**. Depending on the application, these parameters can be determined based on time, temperature, frequency, or amplitude.

DMA is used to study molecular relaxation processes in polymers and determine inherent mechanical or flow properties as a function of time and temperature. The temperature of the sample or the frequency of the stress are often varied, leading to variations in the complex modulus; this approach can be used to locate the glass transition temperature of the material and identify transitions corresponding to other molecular motions.[19]

DMA measurements have been used to evaluate the effect on the viscoelastic stiffness of the different coatings applied to the thermoelectric fabrics. Measures were performed

using the tension mode geometry on a DMA 2980 from TA Instruments. The sample is placed in tension between a fixed and moveable clamp. Rectangular samples of dimensions close to (20 x 10x1) mm^3 were used. The experimental conditions were temperature range from 35 to 150 ºC at a heating rate of 3 ºC min^{-1} with a frequency of 1.0 Hz and an amplitude of 20.0 µm (linear viscoelastic region).

2.10 Bending and torsion tests

Bending and torsion tests have gained importance in recent years in the development of wearable electronics, in which the material needs to be flexible. Therefore, it is important to measure the flexible properties to check the performance of wearable devices.

Three homemade setups were designed to analyze the flexibility of synthesized materials on the thermoelectric properties. In all three tests, flexibility was evaluated following the variation of the normalized electrical conductivity as a function of the tests. Bending tests were carried out in two modes.[20,21] The first one consists of bending the film 3000 times on a cylinder of known radius, the electrical conductivity was evaluated every 100 bends, **Figure 2.7(a)**. The second one evaluates the electrical conductivity as a function of the bending radius, **Figure 2.7(b)**. Finally, the torsion tests, **Figure 2.7(c)**, were carried out on the fabrics between torsion angles of 0 and 360 º, measuring the electrical conductivity every 30 º.

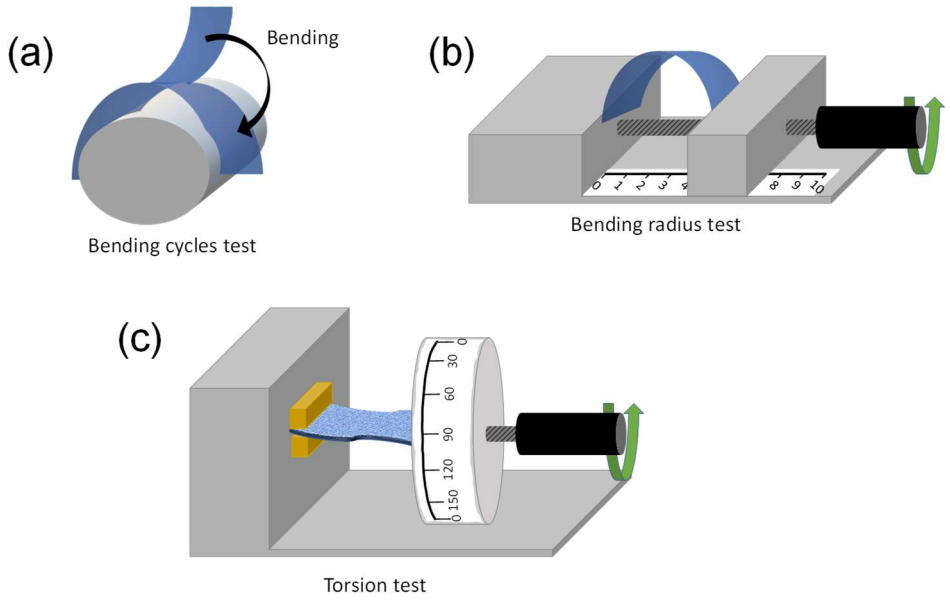

Figure 2.7 (a) Bending test as a function of the number of cycles. (b) Bending test as a function of the radius. (c) Torsion test as a function of torsion angle.

2.11 X-Ray diffraction analysis

X-ray diffraction is an analytical technique used to identify the phases of a crystalline material and provides information on the dimensions of the unit cell. That technique is based on the wave interference of a monochromatic X-ray light beam with the sample.[22] When the X-ray beam falls upon the sample, the interaction can be constructive if Bragg's law holds:

$$n\lambda = 2d \sin\theta \qquad \textbf{(2.12)}$$

where d is the distance between the atomic layers in the crystal and λ is the wavelength of the monochromatic X-ray beam.

The X-Ray diffraction analysis was performed to identify the presence of crystalline phases using a Bruker D8 Advance A25 diffractometer. Samples were scanned at 6 º min^{-1} using Cu K_α radiation at a filament voltage of 40 kV and a current of 20 mA. The diffraction scans were collected between 5 º and 90 º.

2.12 Raman spectroscopy

Light can interact with molecules through elastic and inelastic mechanisms. In the event of an elastic collision between light and molecules, a scattering with the same energy as the incident light occurs. On the contrary, when the collision is inelastic, the light scattered can have higher or lower energy than the incident light. As a result of this inelastic collision, there is a shift in the frequency of the scattered light called the Raman Effect. This effect is based on molecular deformation in an electric field determined by molecular polarizability. Therefore, for a sample to be Raman active, its polarizability must change during vibration. In this way, Raman spectroscopy provides information on molecular vibration and is very useful for sample identification. In Raman spectroscopy, the sample is excited with a monochromatic light beam, and the scattered light is collected by optics and filtered to obtain the Raman spectrum.[23]

Raman scattering measurements were carried out at room temperature in a backscattering configuration using a Horiba MTB XPlora spectrometer coupled to a confocal microscope. An Ar/Kr laser provided the excitation line of 514.53 nm focused

onto the sample using a 100x microscope objective. With this technique, we can identify the vibrational modes of carbon nanotubes and conducting polymers.

2.13 X-Ray photoelectron spectroscopy

X-ray photoelectron spectroscopy is an analytical technique that provides information on the composition and oxidation state of the surface of materials. Soft X-rays penetrate to the core levels of the atoms present in the molecules, causing ionization and the emission of core electrons.

The XPS spectrum is generated by plotting the intensity of photoelectrons as a function of binding energy. The binding energy can be determined by measuring the kinetic energy of the emitted photoelectrons since the X-ray energy is the sum of the kinetic energy of the emitted photoelectrons and the binding energy of the core electron.

X-Ray photoelectron spectroscopy (XPS) was performed using a Kratos AXIS ULTRA spectrometer at room temperature equipped with a micro-focused (20 mA, 15 kV) monochromatic Al-K_α X-Ray source (1486.58 eV). The spectrophotometer was calibrated using C_{1s} line at 284.8 eV. For survey spectra, the pass energy was 160 eV with a step of 1.0 eV, a dwell of 50 ms, and three sweeps. For narrow regions, the pass energy was 20 eV with a step of 0.05 eV, a dwell of 100 ms, and 8 – 18 sweeps. With this technique, we can extract information about the oxidation state of the surface atoms and the bonds they form between them.

2.14 UV-Vis-NIR spectroscopy

Ultraviolet-visible-near-infrared (UV-Vis-NIR) spectroscopy is a spectroscopic technique that determines the light absorbed at a given wavelength within the UV-Vis-NIR range. In this region, absorption processes are related to molecular electronic transitions.[24] The UV-Vis-NIR spectroscopy gives us information about the oxidation state of the conducting polymers due to the absorption bands associated with the conjugated double-bonds, polaronic, and bipolaronic states.[25] Also, UV-Vis-NIR spectroscopy helps to identify the presence of plasmonic bands.[26]

The UV-Vis-NIR spectroscopy was carried out in a double beam JASCO V-730 spectrophotometer covering different ranges. In the case of nanoparticle suspensions, quartz buckets were employed in the range of 300 to 1100 nm. For the case of polymer films, the film accessory was used in the range of 300 to 2000 nm. In both cases the measurement was performed without an integrating sphere.

2.15 Scanning electron microscopy

Scanning electron microscopy (SEM) is based on detecting secondary electrons emitted by the surface of the sample when it interacts with the electron beam. These secondary electrons are detected thanks to a sideway detector located above the sample, making it possible to obtain three-dimensional images of the sample.

SEM was performed in a Hitachi S4800 microscope at an accelerating voltage of 10 kV and a working distance of 15 mm. Tiny sample pieces were placed in the sample holder with carbon adhesive tape and were metalized with Au-Pd coating before observation. In the less conductive samples, it was necessary to cover part of the surface with silver paint and contact it with carbon tape to allow better dispersion of the incident electrons. In addition, the equipment has incorporated an RX Bruker retro-dispersed X-Ray for microanalysis at a working distance of 8 mm.

2.16 Transmission electron microscopy

Transmission electron microscopy (TEM) is an imaging technique that detects transmitted electrons when an electron beam falls on the sample.

TEM images were taken with two different equipment. The first one was JEOL JEM-1010 of 100 kV coupled with a digital camera AMT XR80 with 8 Mpx. The second one was HITACHI HT7800 with 120 kV of high contrast, incorporating a digital camera CMOS EMSIS XAROSA of 20 Mpx.

The samples for cross-section analysis were prepared by embedding a small piece of coated PET in Durcupan^{TM} ACM resin (Sigma Aldrich, Germany), cured overnight, and then cutting the cross-section using an Ultra 45º diamond knife. Finally, samples were

integrated on copper grids. "Image J" software was used to analyze TEM images. The number of particles analyzed was not less than 100.

High-resolution transmission electron microscopy (HRTEM) was performed in an FEI Tecnai G2 F20 S-TWIN of 200 kV with a resolution of 0.24 mm. It is equipped with a CCD GATAN camera digital micrograph and software for image acquisition and treatment. With this equipment is possible to take HRTEM images, electron diffraction patterns, and use spectroscopic techniques such as EDS and Mapping. It also includes a "Double-Tilt" sample holder, allowing a complete sample orientation.

2.17 Dynamic Light Scattering

Dynamic light scattering (DLS) is a technique that uses the Brownian motion of particles in a colloidal dispersion to correlate with particle size and size distribution.[27] DLS equipment employs a beam of monochromatic light that scatters in all directions when it comes into contact with the particles of a dispersion. The intensity of scattered light is recorded with a detector. Since the particles are in motion, the detector will see a difference between the intensity of the scattered and incident light. In addition, the diffusion of the particles in the medium depends significantly on the particle size and, therefore, will determine the variation between the intensity of scattered and incident light.

DLS measurements were performed to determine the hydrodynamic radius (particle size) of the PEDOT nanoparticles synthesized in Chapter 3. The average particle size was determined using dynamic light scattering at 107° with a Zetasizer Nano ZS using solutions diluted to 0.1% by volume.

2.18 ζ-potential

The ζ-potential is the potential difference between the dispersion medium and the stationary layer of fluid attached to the dispersed particle. This potential difference is due to the content of the net electric charge located within the region delimited by the sliding plane. Therefore, this technique is used to determine the charge of the particles. To measure the ζ-potential, an oscillating flow of electrolyte solution is created through the sample.

The sensors in the cuvette monitor the changes produced so that the equipment's software calculates the ζ-potential.

ζ-potential measurements were performed to determine the surface charge of PEDOT nanoparticles and carbon nanotubes in Chapter 3. The ζ-potential was determined using a Zetasizer Nano ZS. The solutions were diluted to 0.1% by volume with 0.1 mM KCl to keep the ionic strength constant.

References

(1) *Thermoelectrics Handbook: Macro to Nano*; Rowe, D. M., Ed.; CRC Press. Taylor & Francis Group: Boca Raton, 2006. https://doi.org/10.1201/9781420038903.

(2) van der Pauw, L. J. A Method of Measuring Specific Resistivity and Hall Effect of Discs of Arbitrary Shape. *Philips Res. Reports* **1958**, *13*, 1–9.

(3) van der Pauw, L. J. Determination of Resistivity Tensor and Hall Tensor of Anisotropic Conductors. *Philips Res. Reports* **1961**, *16*, 187.

(4) Wasscher, J. D. Note on Four Point Resistivity Measurements on Anisotropic Conductors. *Philips Res. Reports* **1961**, *16*, 301.

(5) Koon, D. W.; Bahl, A. A.; Duncan, E. O. Measurement of Contact Placement Errors in the van Der Pauw Technique. *Rev. Sci. Instrum.* **1989**, *60* (2), 275–276. https://doi.org/10.1063/1.1140423.

(6) Koon, D. W. Effect of Contact Size and Placement, and of Resistive Inhomogeneities on van Der Pauw Measurements. *Rev. Sci. Instrum.* **1989**, *60* (2), 271–274. https://doi.org/10.1063/1.1140422.

(7) Xing, C.; Folsom, C.; Jensen, C.; Ban, H.; Marshall, D. W. A Correction Scheme for Thermal Conductivity Measurement Using the Comparative Cut-Bar Technique Based on 3D Numerical Simulation. *Meas. Sci. Technol.* **2014**, *25* (5), 55602. https://doi.org/10.1088/0957-0233/25/5/055602.

(8) Yüksel, N.; Avcı, A.; Kılıç, M. The Effective Thermal Conductivity of Insulation Materials Reinforced with Aluminium Foil at Low Temperatures. *Heat Mass Transf.* **2012**, *48* (9), 1569–1574. https://doi.org/10.1007/s00231-012-1001-2.

(9) Yüksel, N. The Review of Some Commonly Used Methods and Techniques to Measure the Thermal Conductivity of Insulation Materials. In *Insulation Materials in Context of Sustainability*; InTech, 2016. https://doi.org/10.5772/64157.

(10) *Springer Handbook of Materials Measurement Methods*; Czichos, H., Saito, T., Smith, L., Eds.; Springer Berlin Heidelberg: Berlin, Heidelberg, 2006.

https://doi.org/10.1007/978-3-540-30300-8.

(11) Liu, D.; Li, Y.-Z.; Li, Y.; Lee, K.-M. A Novel Temperature Based Flat-Plate Heat Flux Sensor for High Accuracy Measurement. In *2009 IEEE/ASME International Conference on Advanced Intelligent Mechatronics*; 2009; pp 1242–1247. https://doi.org/10.1109/AIM.2009.5229762.

(12) Shen, H.; Xie, K.; Shi, H.; Yan, X.; Tu, L.; Xu, Y.; Wang, J. Analysis of Heat Transfer Characteristics in Textiles and Factors Affecting Thermal Properties by Modeling. *Text. Res. J.* **2019**, *89* (21–22), 4681–4690. https://doi.org/10.1177/0040517519842790.

(13) Schmidt, A. J.; Cheaito, R.; Chiesa, M. A Frequency-Domain Thermoreflectance Method for the Characterization of Thermal Properties. *Rev. Sci. Instrum.* **2009**, *80* (9), 094901. https://doi.org/10.1063/1.3212673.

(14) Sandell, S.; Maire, J.; Chavez-Angel, E.; Sotomayor Torres, C. M.; He, J. A Frequency-Domain Thermoreflectance Method for Measuring the Thermal Boundary Conductance of a Metal-Polymer System. In *2020 IEEE 8th Electronics System-Integration Technology Conference (ESTC)*; IEEE, 2020; pp 1–5. https://doi.org/10.1109/ESTC48849.2020.9229862.

(15) *Broadband Dielectric Spectroscopy*, 1st ed.; Kremer, F., Schönhals, A., Eds.; Springer: Berlin, Heidelberg, 2003. https://doi.org/10.1007/978-3-642-56120-7.

(16) *Thermal Analysis of Polymers: Fundamentals and Applications*; Menczel, J. D., Prime, R. B., Eds.; Wiley & Sons Ltd, 2009.

(17) Danley, R. L. New Heat Flux DSC Measurement Technique. *Thermochim. Acta* **2002**, *395* (1), 201–208. https://doi.org/https://doi.org/10.1016/S0040-6031(02)00212-5.

(18) Coats, A. W.; Redfern, J. P. Thermogravimetric Analysis. A Review. *Analyst* **1963**, *88* (1053), 906–924. https://doi.org/10.1039/AN9638800906.

(19) Ferry, J. D. Some Reflections on the Early Development of Polymer Dynamics: Viscoelasticity, Dielectric Dispersion, and Self-Diffusion. *Macromolecules* **1991**, *24* (19), 5237–5245. https://doi.org/10.1021/ma00019a001.

(20) Kim, T.; Kim, J.-H.; Kang, T. E.; Lee, C.; Kang, H.; Shin, M.; Wang, C.; Ma, B.; Jeong, U.; Kim, T.-S.; Kim, B. J. Flexible, Highly Efficient All-Polymer Solar Cells. *Nat. Commun.* **2015**, *6* (1), 8547. https://doi.org/10.1038/ncomms9547.

(21) Liu, Y.; Yin, L.; Zhang, W.; Wang, J.; Hou, S.; Wu, Z.; Zhang, Z.; Chen, C.; Li, X.; Ji, H.; Zhang, Q.; Liu, Z.; Cao, F. A Wearable Real-Time Power Supply with a

Mg3Bi2-Based Thermoelectric Module. *Cell Reports Phys. Sci.* **2021**, *2* (5), 100412. https://doi.org/10.1016/j.xcrp.2021.100412.

(22) Suryanarayana, C.; Norton, M. G. *X-Ray Diffraction: A Practical Approach*; Artech House Telecommunications; Springer US, 1998.

(23) McCreery, R. L. Raman Spectroscopy of Surfaces. In *Raman Spectroscopy for Chemical Analysis*; John Wiley & Sons, Ltd, 2000; pp 373–413. https://doi.org/https://doi.org/10.1002/0471721646.ch13.

(24) Perkampus, H. H. *UV-VIS Spectroscopy and Its Applications*; Springer: Heidelberg, Berlin, 1992. https://doi.org/10.1007/978-3-642-77477-5.

(25) Zozoulenko, I.; Singh, A.; Singh, S. K.; Gueskine, V.; Crispin, X.; Berggren, M. Polarons, Bipolarons, And Absorption Spectroscopy of PEDOT. *ACS Appl. Polym. Mater.* **2019**, *1* (1), 83–94. https://doi.org/10.1021/acsapm.8b00061.

(26) Jin, R.; Charles Cao, Y.; Hao, E.; Métraux, G. S.; Schatz, G. C.; Mirkin, C. A. Controlling Anisotropic Nanoparticle Growth through Plasmon Excitation. *Nature* **2003**, *425* (6957), 487–490. https://doi.org/10.1038/nature02020.

(27) Schärtl, W. *Light Scattering from Polymer Solutions and Nanoparticle Dispersions*; Springer Laboratory; Springer Berlin Heidelberg, 2007.

Chapter 3

Hybrid layered thermoelectric materials

Content

This chapter shows the thermoelectric properties of hybrid layered thermoelectric materials based on PEDOT to increase thermoelectric efficiency. First, the introduction explains the use of hybrid materials to improve the thermoelectric efficiency of conductive polymers and two techniques for obtaining layered hybrid materials (Layer-by-Layer and electrochemical deposition). Then, two studies show the improvement of the thermoelectric efficiency of PEDOT through the formation of hybrid layered materials. In the first of them, PEDOT/CNT hybrid films are obtained by Layer-by-Layer by using PEDOT nanoparticles as building blocks. The second study obtains a layered hybrid material by electrodeposition of PEDOT and SnS:Ag.

3.1 Introduction

As it can be deduced from the expression of the Figure of Merit, for a thermoelectric material to have a high performance, it must have high electrical conductivity, a high Seebeck coefficient, and low thermal conductivity. Meeting all these requirements in a single material is especially challenging due to the correlation between these properties, determined by the electronic structure (band gap, band shape, and band degeneracy near the Fermi level) and the scattering of the charge carriers (electrons or holes).[1] One strategy to improve the thermoelectric efficiency of conductive polymers is the formation of hybrid organic-inorganic materials. The key to hybrid materials lies in the synergistic combination of conductive polymers with low thermal conductivity and inorganic materials with high Seebeck coefficient and electrical conductivity. More importantly, polymer and inorganic fillers have different electron densities and wavefunctions, resulting in an energy mismatch at the polymer-filler interface that induces an energy filtering effect.[2,3] This potential barrier interface can selectively scatter low-energy charge carriers and allow high-energy charge carriers to pass, **Figure 3.1**. However, this energy filtering effect will decrease the electrical conductivity due to carrier loss. In contrast, this effect will improve the Seebeck coefficient because high energy charge carriers contribute more to the Seebeck coefficient.[4] Since the Seebeck coefficient is a quadratic term in the expression of the Power Factor,

selecting two materials with a sufficiently high energy barrier increases the thermoelectric efficiency of the polymer-filler hybrid material.

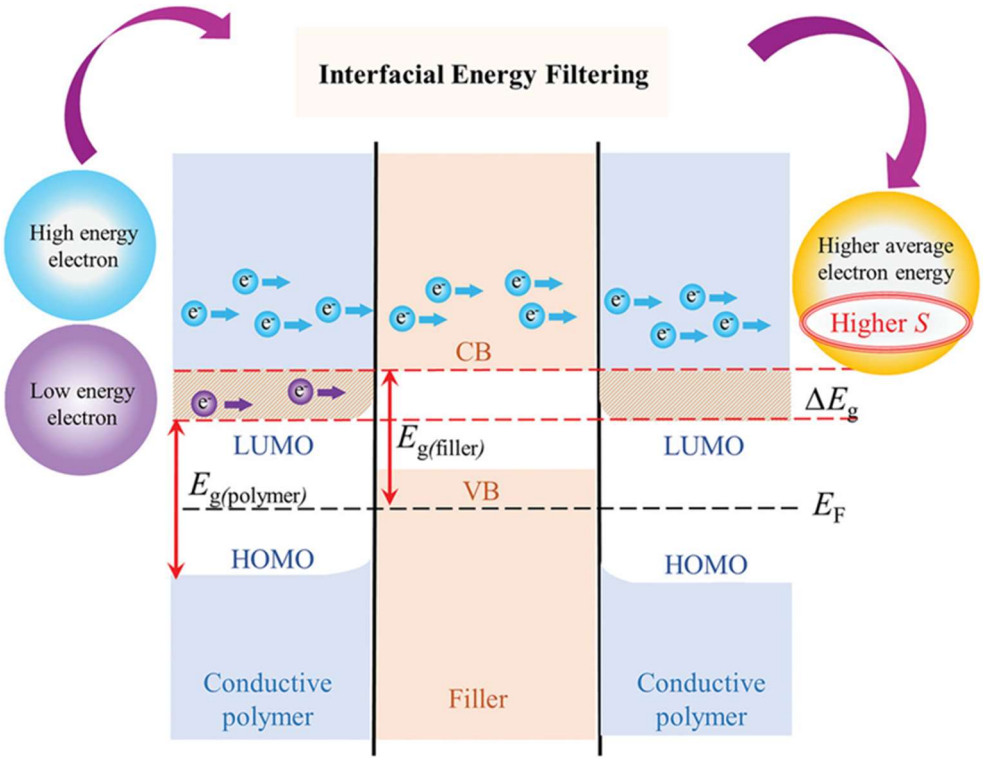

Figure 3.1 Schematic illustration of the energy-filtering effect at the interface between the conductive polymer and the filler. Reprinted with permission.[5] Copyright 2019, WILEY-VCH Verlag GmbH & Co. KGaA, Weinheim.

Therefore, hybrid thermoelectric materials based on conductive polymers offer a new route to decouple the interconnected thermoelectric parameters. The main strategies have been the combination of conductive polymers with carbonaceous materials (MWCNT, DWCNT, SWCNT, Graphene, Graphene oxide) or inorganic semiconductors (Bi_2Te_3, Sb_2Te_3, Cu_2S, Cu_2Se, SnSe, SnS).[5]

3.1.1 Hybrid thermoelectric materials based on conductive polymers and carbon nanotubes

Carbon nanotubes (CNT) are composed of carbon atoms arranged in a cylindrical hexagonal lattice with the same structure that would be acquired if a sheet of graphene were rolled up on itself, obtaining single-walled carbon nanotubes (SWCNT). However, when the carbon nanotube includes concentric tubes of different diameters, it is known as a multi-walled carbon nanotube (MWCNT). In both cases, its properties will be determined by the electronic structure of the nanotube since it can be semiconducting or metallic,

depending on the roll-up vector. If we consider, for example, a SWCNT, the magnitude and chiral angle (α) of the roll-up vector to the zig-zag axis can be defined by the Hamada indices (*n, m*), as shown in **Figure 3.2(a)**. These indices determine the electronic properties of nanotubes since for a nanotube to be metallic (m-SWCNT), the difference *n*–*m* must be a multiple of three, otherwise, it will be a semiconductor (s-SWCNT).

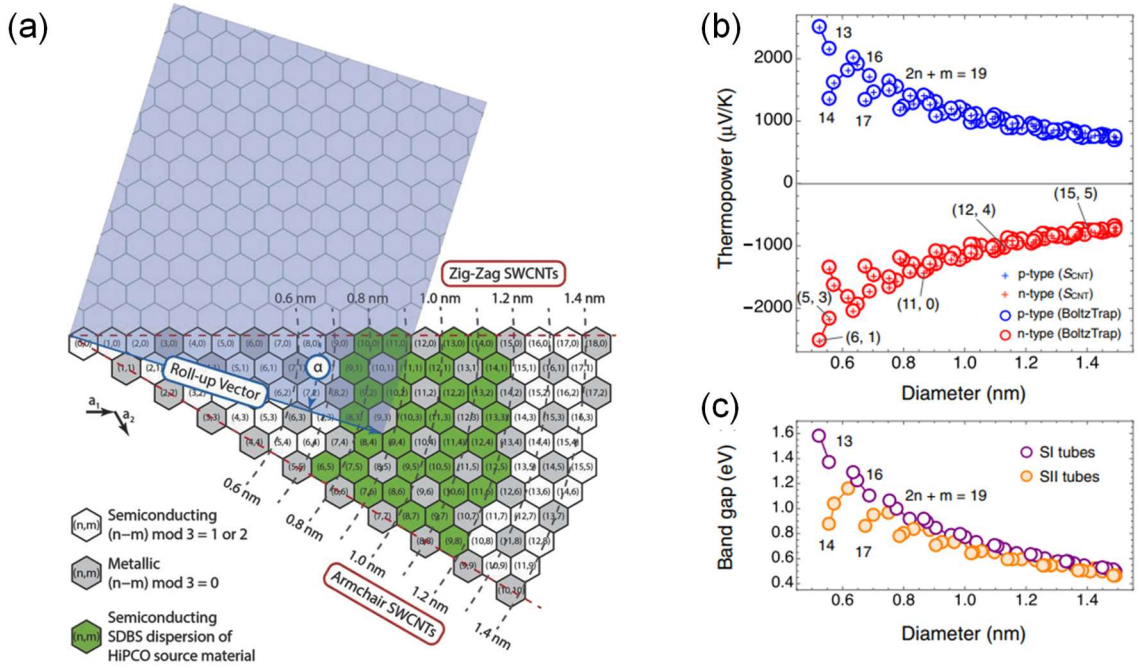

Figure 3.2 (a) Scheme of SWCNT formation from a graphene layer with different Hamada indices. Reprinted with permission.[6] Copyright 2018, WILEY-VCH Verlag GmbH & Co. KGaA, Weinheim. (b) Seebeck coefficient values of s-SWCNT as a function of SWCNT diameter. (c) SWCNT band gap evolution as a function of SWCNT diameter. Reprinted with permission.[7] Copyright 2015, American Physical Society.

The Seebeck coefficient and electrical conductivity are closely related to the electronic structure and, in the case of SWCNTs, depend on the Hamada indices. m-SWCNTs have high electrical conductivity, but their Seebeck coefficient is around 10 – 20 μV K^{-1}. On the other hand, s-SWCNTs have a Seebeck coefficient between 80 – 160 μV K^{-1}, but the electrical conductivity is very low.[8,9] However, after adequate doping, s-SWCNTs can achieve significantly higher electrical conductivity than m-SWCNTs,[10] opening the possibility of obtaining s-SWCNTs with good thermoelectric performance. In addition, another parameter to consider is the diameter of the nanotube. A theoretical study, **Figure 3.2(b)**, shows a decrease in the Seebeck coefficient with increasing SWCNT diameter due to an increase in charge carrier mobility. This effect is also observed in the band gap evolution, **Figure 3.2(c)**. Therefore, it is expected that the electrical conductivity increases as the diameter of the nanotube increases.[7,11]

In the case of MWCNTs, the thermoelectric properties will depend on the electronic structure of each of the concentric nanotubes. For example, in the case of double-walled nanotubes (DWCNTs), there are four permutations of inner@outer combinations: semi@semi, metal@metal, semi@metal, and metal@semi.[12] It is expected that those DWCNTs with a suitably doped semi@semi combination have better thermoelectric properties than the rest of the combinations. However, if we extrapolate these permutations to carbon nanotubes with a higher number of concentric tubes, the probability that all of them have a semiconductor nature decreases drastically; therefore, the MWCNTs have worse thermoelectric performance.

One of the main advantages of combining conductive polymers and carbon nanotubes is the reduction of the thermal conductivity of the final composite. For example, Meng et al.[13] demonstrated a reduction of thermal conductivity of the 20 wt. % PANI/CNT composite through the *in-situ* polymerization of polyaniline (PANI) on carbon nanotubes. The thermal conductivity values of the composite reached values close to the pristine PANI ones while maintaining good electrical conductivity and Seebeck coefficient. Another advantage offered by this type of hybrid thermoelectric materials is the possibility of decoupling electrical conductivity and the Seebeck coefficient. For example, Moriarty et al.[14] demonstrated that the barriers found at the SWCNT/PEDOT:PSS interface block the passage of low-energy charge carriers and only allow the passage of high-energy charge carriers shown in Figure 3.3**(a)**. This effect translates into an increase in conductivity from 500 S cm^{-1} to 4000 S cm^{-1}, with increasing SWCNT content, while the Seebeck coefficient remains practically unchanged, around 20 μV K^{-1} (Figure 3.3**(b)**). In addition, the phonon scattering in the interface between CNT–PEDOT will reduce the thermal conductivity. Finally, the Power Factor (**Figure 3.3(c)**) reaches a maximum value of 120 μW m^{-1} K^{-2}.

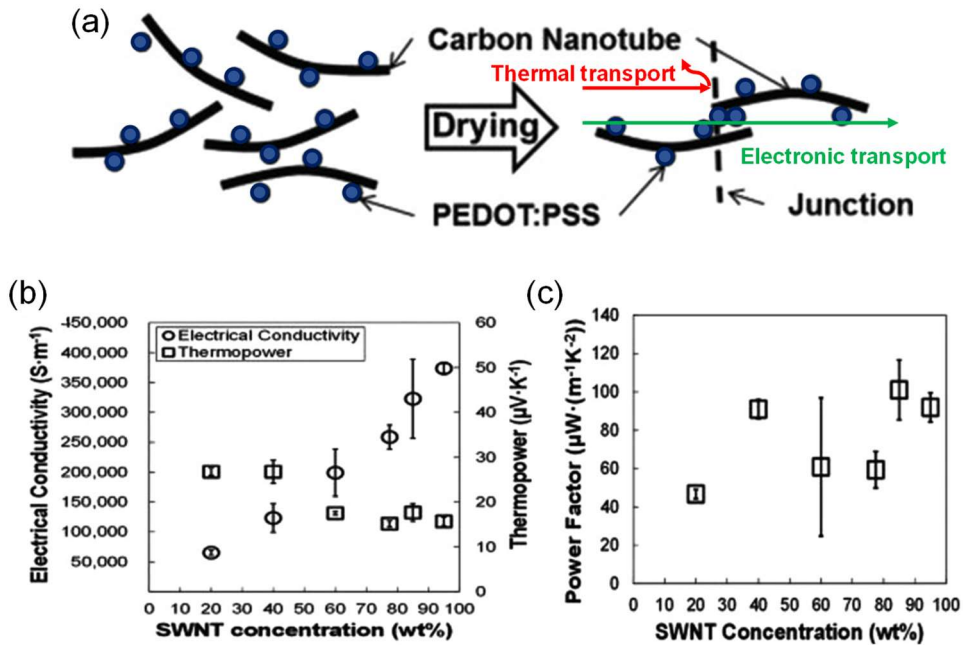

Figure 3.3 (a) Scheme of the electrically conductive junction between carbon nanotubes and PEDOT:PSS. (b) Electrical conductivity, thermopower, and (c) Power Factor of SWCNT/PEDOT:PSS films as a function of SWCNT wt. %. Reprinted with permission.[14] Copyright 2012, Wiley Periodicals, Inc.

Finally, another positive influence of the synthesis of hybrid materials based on conductive polymers with carbon nanotubes is the increase in the Power Factor due to the π–π interaction between the aromatic rings of the conductive polymers and the CNTs. This interaction causes a greater ordering of the conductive polymers around the nanotube, favoring the delocalization of the polarons. This, in turn, increases carrier mobility and simultaneously improves the electrical conductivity and Seebeck coefficient of conductive polymers.[15,16]

3.1.2 Hybrid thermoelectric materials based on conductive polymers and chalcogenides

The most used inorganic semiconductors in thermoelectricity are chalcogenides, which have high thermoelectric efficiencies, reaching ZT values ≥ 2.[17,18] Therefore, these materials are excellent candidates for forming hybrid materials based on conductive polymers since they have a high Seebeck coefficient and high electrical conductivity. In addition, incorporating conductive polymers with semiconductor nanoparticles would reduce the thermal conductivity of the material due to phonon scattering in the polymer–nanoparticle interface,[19,20] and increase the Seebeck coefficient due to the energy-filtering

effect,[2] allowing a higher thermoelectric efficiency than the pristine conductive polymer. On the other hand, conductive polymers offer mechanical properties that inorganic semiconductors do not have since they are mostly rigid and brittle. In this way, it is possible to obtain flexible and more efficient hybrid thermoelectric materials based on conductive polymers. For example, Ou et al.[21] developed a hybrid material by mixing *in-situ* an ink containing Bi_2Te_3 (Sb_2Te_3) nanoparticles with another ink containing PEDOT:PSS. The resulting ink was deposited by an aerosol-jet printer on a flexible substrate, as shown in **Figure 3.4(a)**. They studied the thermoelectric properties of the films as a function of the content of Bi_2Te_3 (Sb_2Te_3) nanoparticles, obtaining a maximum Power Factor of 30 $\mu W\ m^{-1}\ K^{-2}$ with a content of 85 wt% of Sb_2Te_3. In addition, the flexibility tests showed that both the electrical resistance of the films and the Seebeck coefficient remained approximately stable **Figure 3.4(b)**.

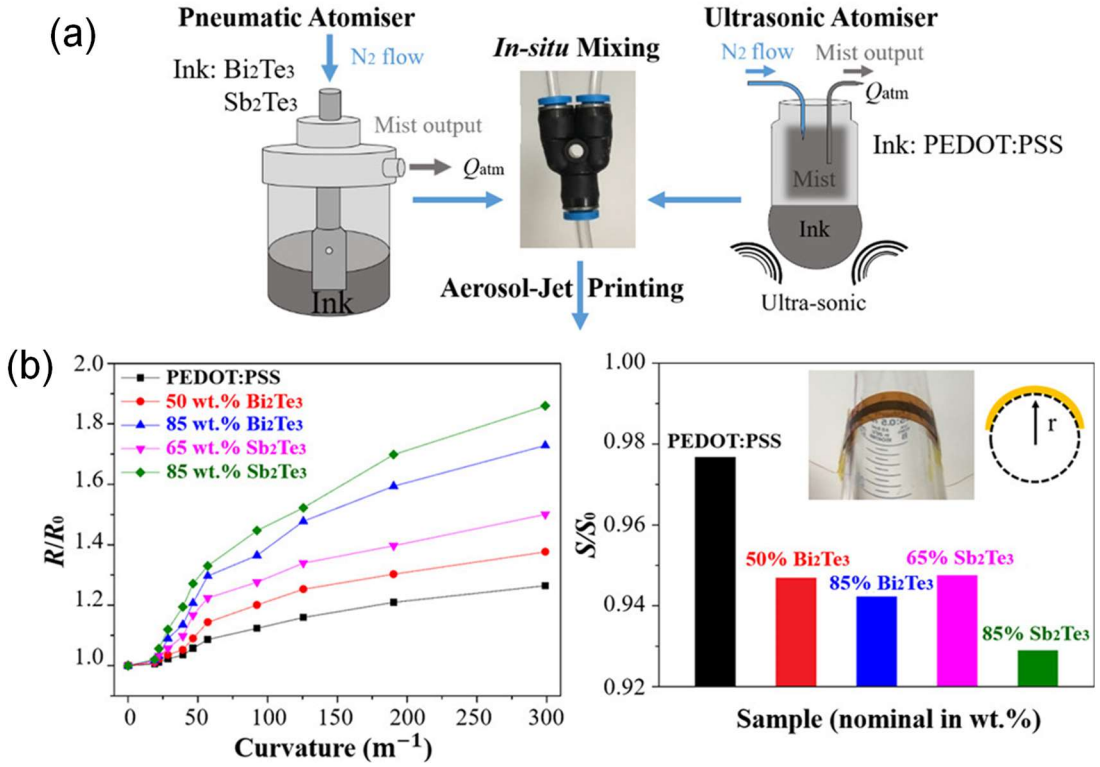

Figure 3.4 (a) Schematic process of Aerosol-Jet printing. (b) Flexibility test of Bi_2Te_3 (Sb_2Te_3)/PEDOT:PSS films. Reprinted with permission.[21] Copyright 2018, American Chemical Society.

We et al.[22] prepared a thermoelectric generator based on a Bi_2Te_3/Sb_2Te_3 composite with PEDOT:PSS. In this case, the inorganic material was first deposited by screen printing on a flexible substrate, and a thermal treatment was carried out in an N_2 atmosphere to obtain the best thermoelectric properties. The Bi_2Te_3 (Sb_2Te_3) films were coated with PEDOT:PSS, which penetrated through the resulting porous structure after annealing.

Finally, the authors made a thermoelectric generator combining 15 p–n pairs with these materials, showing an output voltage of 12.5 mV at a ΔT of 5 K.

However, the classical inorganic semiconductors most commonly used (Bi_2Te_3, Sb_2Te_3, PbTe) are expensive, scarce, and toxic. For this reason, in recent years, there has been a commitment to developing other highly efficient and environmentally friendly chalcogenides based on abundant and low-toxicity materials (SnS, SnSe, Cu_2S, Cu_2Se).[23–28] In addition, hybrid materials based on conductive polymers and more environmentally friendly inorganic semiconductors have been recently studied. For example, Ju et al.[29] exfoliated SnSe nanosheets homogeneously distributed on a PEDOT:PSS matrix. The PEDOT:PSS/SnSe nanocomposite showed a maximum Power Factor with a weight content of 20 wt. % SnSe with a very low thermal conductivity, leading to a Figure of Merit of 0.32, **Figure 3.5(a)**. Another work carried out by Ju et al.[30] developed a PANI:DBSA/SnS hybrid compound whose maximum Power Factor was 80 μW m^{-1} K^{-2}.

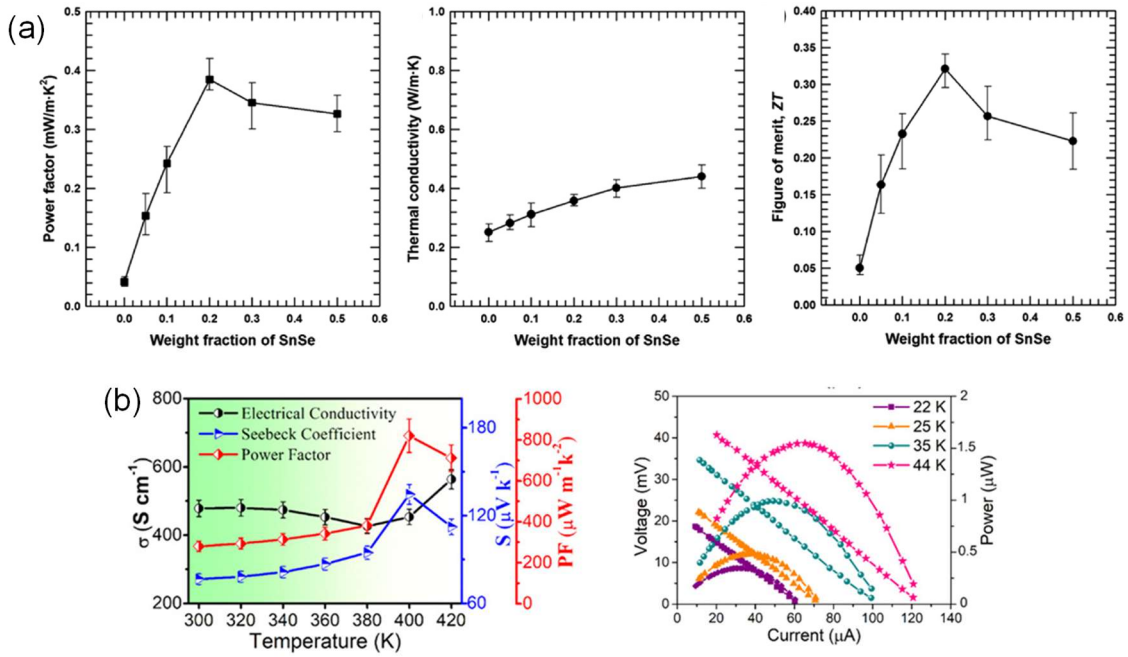

Figure 3.5 (a) Power Factor, thermal conductivity, and ZT as a function of weight fraction of SnSe in a PEDOT:PSS matrix. Reprinted with permission.[29] Copyright 2016, American Chemical Society. (b) Thermoelectric properties and TEG output power of PEDOT:PSS/Cu_2Se hybrid material. Reprinted with permission.[31] Copyright 2021, American Chemical Society.

By vacuum filtration, Liu et al.[32] synthesized a flexible and self-supporting PEDOT:PSS/Cu_2S composite. The electrical conductivity of the composite decreased with the increase in Cu_2S content, while the Seebeck coefficient increased, reaching a maximum Power Factor of 56.15 μW m^{-1} K^{-2} with a content of 10 wt. % Cu_2S. Finally, Lu et al.[31]

prepared a flexible PEDOT:PSS/Cu_2Se nanocomposite on a nylon membrane by vacuum filtering and hot pressing, obtaining a Power Factor of 820 μW m^{-1} K^{-2}. They also developed a thermoelectric generator, obtaining an output power of 1.55 μW with a thermal gradient of 44 K, **Figure 3.5(b)**.

3.1.3 Methods to prepare hybrid layered thermoelectric materials

The synthesis of hybrid thermoelectric materials consists of creating a homogeneous dispersion of nanofillers in the polymeric matrix. There are different methods of obtaining hybrid materials. One consists of the colloidal dispersion of the nanofillers in a dispersion containing the conductive polymer. Another method consists of colloidally dispersing the nanofillers in a solution containing the conductive polymer monomer and adding the oxidizing agent responsible for oxidative polymerization. The main drawback of both methods is the phase segregation phenomena during film formation, which impairs thermoelectric performance.[33] This is why new ways of obtaining hybrid materials have been sought, avoiding phase segregation. An example is the aerosol-jet printing deposition technique in which the dispersions containing the nanofillers and the conductive polymer are mixed simultaneously.[21] Another way is by impregnating a substrate with the conductive polymer, which has been previously coated with nanofillers.[22] However, following the work carried out by Cho et al.[34], there has been a strong interest in synthesizing hybrid layered thermoelectric materials, which can be obtained using Layer-by-Layer and electrodeposition of alternating layers techniques.

3.1.3.1 Layer-by-Layer

The Layer-by-Layer (LbL) deposition technique is a template-assisted assembly method used to obtain multilayer films. These multilayer films are obtained through the sequential exposure of a substrate to dispersions containing the complementary functionalized materials. Therefore, the LbL assembly needs interaction between the successive layers, which can be electrostatic, hydrophobic, charge-transfer, host-guest, or hydrogen bonds.[35,36] In addition, using LbL deposition, the structure of the obtained films and composition can be controlled at the nanometer scale.[37]

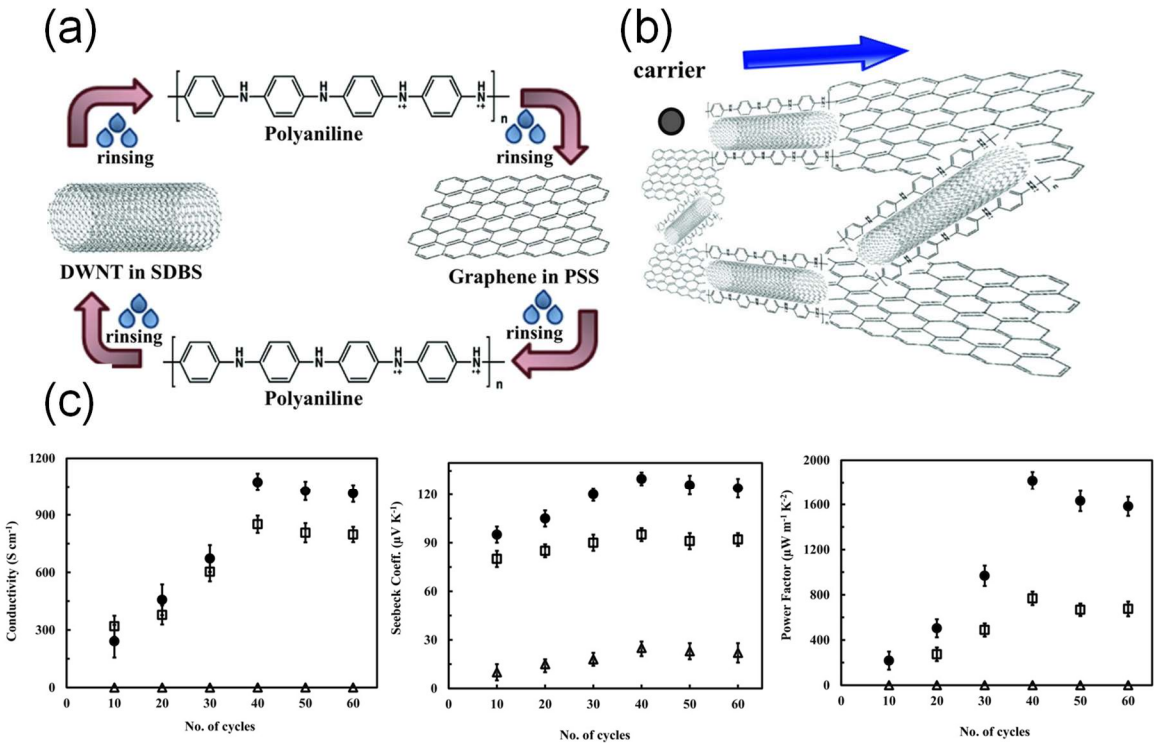

Figure 3.6 (a) Scheme of the LbL assembly procedure. (b) Representation of the charge carrier transport in the PANI/graphene/PANI/DWCNT film. (c) Electrical conductivity, Seebeck coefficient, and Power Factor of PANI/graphene (open triangles), PANI/DWCNT (open squares), and PANI/graphene/PANI/DWCNT (filled circles) as a function of deposited cycles. Reprinted with permission.[34] Copyright 2015, WILEY-VCH Verlag GmbH & Co. KGaA, Weinheim.

Using the Layer-by-Layer deposition technique, excellent results can be obtained, as reported by Cho et al.[34] They obtained a layered hybrid film composed of four layers (PANI/Graphene/PANI/DWCNT), with an electrical conductivity of 1080 S cm^{-1} and a Seebeck coefficient of 130 μV K^{-1}, resulting in a Power Factor of 1825 μW m^{-1} K^{-2}, **Figure 3.6**. This exceptional Power Factor value is attributed to the π–π interaction of PANI with graphene and DWCNT, generating a greater delocalization of charge carriers along the system backbone. As a result of this work, numerous studies have been published in which the LbL technique is used to elaborate multilayer hybrid systems based on conductive polymers and carbon nanotubes.[38–40]

3.1.3.2 Electrochemical deposition

The electrodeposition of inorganic semiconductors is a method to obtain thin films in a sustainable, easily scalable and low-cost way.[41] Electrodeposition is based on applying reduction potentials on the working electrode, which is immersed in a solution containing the precursors of the desired compound. For example, Martín-González et al.[42] synthesized

Bi_2Te_3 by applying reduction potentials to a Pt electrode immersed in a solution of $HTeO_2^+$ and Bi^{3+} in an acid medium. This technique allows obtaining inorganic semiconductors with perfect control over the composition and high thermoelectric efficiency. Due to the advantages of electrodeposition over conventional methods for obtaining inorganic semiconductors (spark plasma sintering, ball-milling, hot pressing, solvothermal synthesis) and the good thermoelectric efficiency values of the materials obtained by electrodeposition, interest has grown in the electrochemical deposition of chalcogenides such as AgSe,[41] SnSe,[43] Bi_2Te_3 nanowires,[44] and CuTe,[45] among others.

However, the deposition of semiconductors requires a conductive working electrode, often gold or platinum. Therefore, transferring the films to a non-conductive substrate is necessary to measure the thermoelectric properties. One way to avoid this problem is to synthesize layered hybrid thermoelectric materials by depositing the conductive polymer on an insulating substrate. This substrate is then used as a working electrode to deposit the inorganic semiconductor.

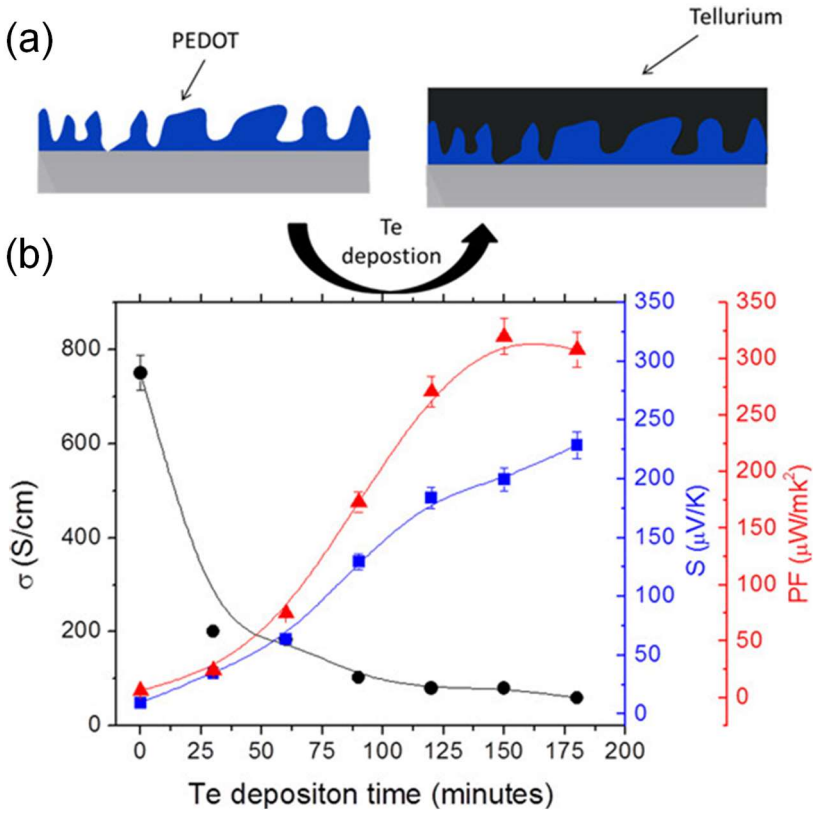

Figure 3.7 (a) Scheme of Te-electrodeposition procedure. (b) Thermoelectric properties of hybrid material as a function of Te deposition time. Reprinted with permission.[46] Copyright 2017, American Chemical Society.

For example, Culebras et al.[46] used a PET-gold working electrode on which they electrodeposited a layer of PEDOT:ClO_4. Then, with treatment with aqua regia, they

eliminated the gold, obtaining a substrate of PET-PEDOT:ClO_4. Finally, they used this substrate as a working electrode and deposited the tellurium on it, **Figure 3.7(a)**. This work studied the thermoelectric properties as a function of tellurium deposition time on the PET-PEDOT:ClO_4 electrode (**Figure 3.7(b)**). The electrical conductivity decreased after tellurium deposition, and the Seebeck coefficient gradually increased. The maximum Power Factor was obtained after 150 minutes of tellurium deposition, reaching a value of 320 $\mu W\ m^{-1}\ K^{-2}$.

3.2 Poly (3,4-ethylenedioxythiophene) nanoparticles as building blocks for hybrid thermoelectric flexible films

3.2.1 Materials

Poly(diallyldimethylammonium chloride) (PDADMAC, 20 wt.% in water), iron(III) p-toluenesulfonate hexahydrate (FeTos), and sodium deoxycholate (DOC, ≥ 97% by titration) were purchased from Sigma-Aldrich. 3, 4-Ethylenedioxytiophene (EDOT) 97% was obtained from Alfa Aesar. Hydrogen peroxide 30 wt.% was purchased from PanReac AppliChem (Barcelona, Spain). Multi-walled carbon nanotubes (MWCNTs, 12–15 nm outer and 4 nm inner wall diameter, > 1 μm length, C ≥ 95 wt%) were obtained from Bayer MaterialScience (Leverkusen, Germany). Double-walled carbon nanotubes (DWCNTs, 2–4 nm outer and 1–3 nm inner wall diameter, > 50 μm length, C > 60%) and single-walled carbon nanotubes (SWCNTs, 1–2 nm wall diameter, 5–30 μm length, C = 90%) were purchased from Nanostructured & Amorphous Materials, Inc. (Houston, TX, USA). Polyethylene terephthalate (PET), with a thickness of 179 μm (trade name ST 505 by DuPont Teijin, purchased from Tekra Corp, New Berlin, WI, USA), was rinsed with deionized water, methanol, and deionized water again, and dried with filtered air before use. Corona treatment (a BD-20C Corona Treater, Electro-Technic Products Inc., Chicago, IL, USA) was used to improve the adhesion of the first layer by oxidizing the polymer surface.

3.2.2 Synthesis of PEDOT:Tos nanoparticles

The synthesis of PEDOT:Tos nanoparticles was carried out by chemical oxidation polymerization in miniemulsion using FeTos as an oxidizer and PDADMAC as a stabilizer, as shown in **Figure 3.8(a)**. The commercial PDADMAC aqueous solution (20 wt.%) was diluted in 40 mL of water, and then EDOT was added and stirred at 800 rpm for 5 min. To obtain the miniemulsion, the mixture was ultrasonicated with a Branson Sonifier 450 (1/2 inch tip, amplitude of 70%, pulse of 90% for 10 min). The polymerization was carried out by slowly adding to the miniemulsion a solution of FeTos in 10 mL of water, according to the proportions shown in **Table 3.1**. Afterward, hydrogen peroxide was added. The samples were purified three times by centrifugation at 13,000 rpm for 20 minutes by discarding the supernatant. Finally, the purified samples were redispersed in 40 mL of water.

Table 3.1 Quantities of reagents used for the preparation of the PEDOT nanoparticles.

Molar Ratio EDOT:FeTos	**1:1**	**1:1.5**	**1:2**
PDADMAC (wt. %)	0.5	0.5	0.5
EDOT (M)	0.037	0.037	0.037
FeTos (M)	0.037	0.056	0.075
H_2O_2 (M)	0.001	0.001	0.001

3.2.3 Film preparation

Carbon nanotubes (0.05 wt.%) were dispersed in an aqueous solution of DOC (0.1 wt.%). The CNT suspensions were placed in an ultrasound bath for 30 minutes, followed by 20 minutes ultrasonication with a Branson Sonifier 450 (1/2 inch tip, 70% amplitude, continuous mode) while cooling in an ice bath. Finally, the suspensions were placed for 30 min in the ultrasound bath. Next, CNT dispersions were centrifuged at 4000 rpm for 5 minutes to discard the nonstabilized CNTs. Once the PEDOT:Tos/PDADMAC and CNT/DOC dispersions were prepared, the Layer-by-Layer (LbL) technique was used to assemble the PEDOT:Tos nanoparticles with the CNTs through electrostatic interaction between the PDADMAC (cationic polyelectrolyte) and DOC (anionic surfactant), **Figure 3.8(b)**. PEDOT:Tos nanoparticles and CNT layers were assembled via dip-coating on a

pre-treated polyethylene terephthalate (PET) substrate to improve film adhesion.[47] PET substrates were immersed in a cationic PEDOT:Tos/PDADMAC suspension for 5 min, followed by three washing steps of dipping in water, immersion in the anionic CNT/DOC suspension for 5 min, and eventually three further steps of washing in water. This process results in one deposition sequence of a PEDOT:Tos/PDADMAC–CNT/DOC bilayer (BL). This cycle was repeated to deposit the desired number of bilayers. Deposited multilayer films were washed and air-dried overnight and then stored in a desiccator prior to further processing or characterization.

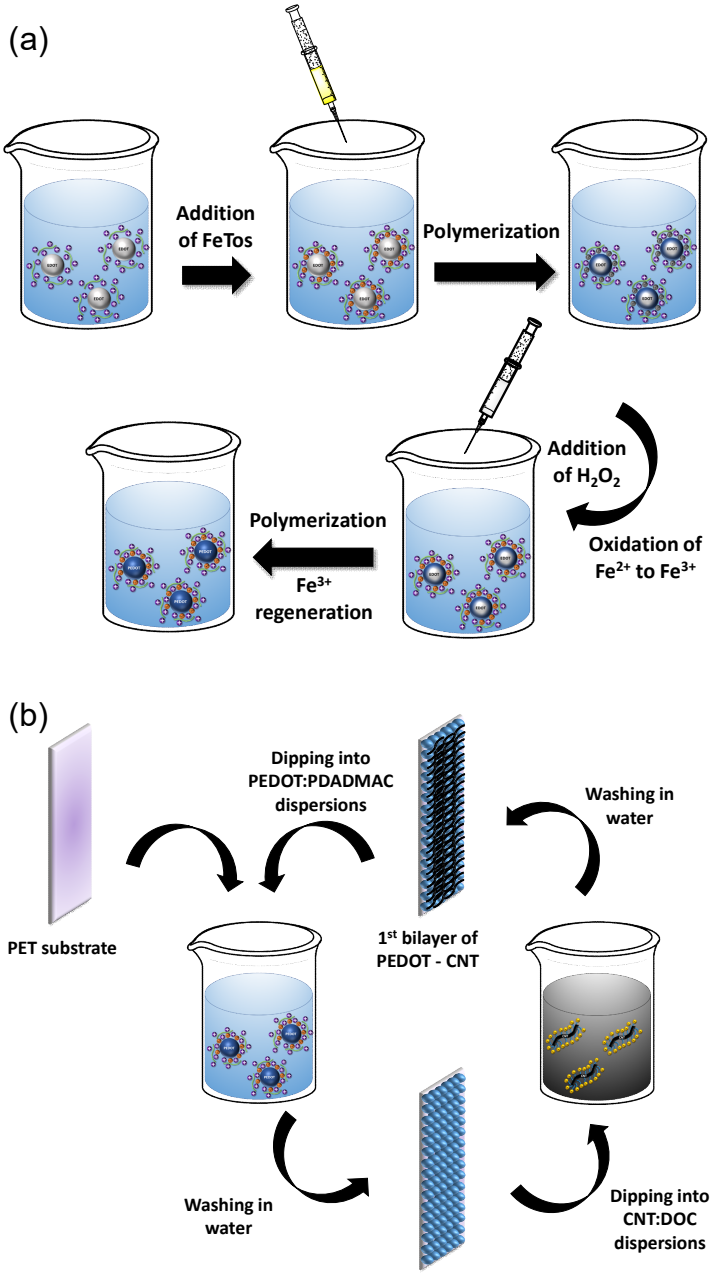

Figure 3.8 (a) Schematic procedure of PEDOT nanoparticles synthesis. (b) Schematic procedure of PEDOT:Tos-CNT LbL assembly.

3.2.4 Morphology of PEDOT:Tos nanoparticles

During the miniemulsion polymerization of EDOT, different stages occur. After ultrasonication, EDOT droplets are stabilized by PDADMAC. The observations suggest that when FeTos is added, iron(III) ions move to the EDOT–water interface and may partially oxidize EDOT to PEDOT, resulting in a PEDOT shell. Consequently, iron (III) ions are reduced to iron(II). Finally, adding hydrogen peroxide oxidizes iron(II) to iron(III), finalizing the oxidation of EDOT to PEDOT. In turn, iron(III) ions are regenerated due to hydrogen peroxide in the medium. The experimental observations also indicate that hydrogen peroxide is essential for maintaining the spherical morphology and preventing droplet coalescence.[48]

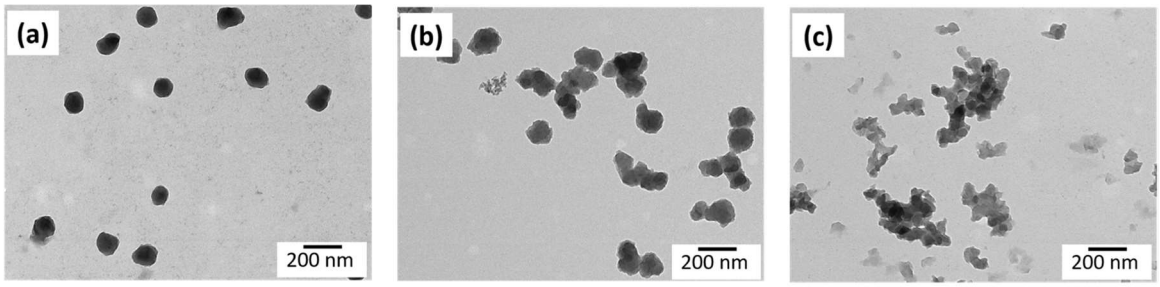

Figure 3.9 TEM images of particles prepared with EDOT:FeTos ratios of (a) 1:1, (b) 1:1.5, and (c) 1:2.

Figure 3.9 shows TEM micrographs of the synthesized nanoparticles. The increase of the molar ratio EDOT:FeTos results in a more significant aggregation of the particles. However, the stability of the suspension was not affected by this partial aggregation, with the samples being stable even after one month. The particle size of the PEDOT nanoparticles was determined by dynamic light scattering (DLS). The sizes of nanoparticles prepared with EDOT:FeTos molar ratios of 1:1, 1:1.5, and 1:2 were 180 ± 10, 260 ± 20, and 490 ± 70 nm, respectively. These results agree with the TEM images (**Figure 3.9**), which indicate a higher formation of aggregates at higher oxidant contents. The statistical treatment of TEM micrographs for the sample obtained at the lowest molar ratio confirms a size distribution centered around 180 nm.

3.2.5 Thermoelectric properties of PEDOT:Tos nanoparticles and carbon nanotubes

Before the LbL assembling of the PEDOT:Tos nanoparticles and the carbon nanotubes, the thermoelectric properties of the PEDOT:Tos nanoparticles were evaluated as a function of the EDOT:FeTos molar ratio. Also, the CNT dispersions were evaluated as a function of the different carbon nanotubes utilized (MWCNT, DWCNT, SWCNT). The respective dispersions were deposited on a substrate and, through the drop-casting method, films of an approximate thickness of (1.5 ± 0.2) μm were obtained. **Figure 3.10** shows the variation of the electrical conductivity, Seebeck coefficient, and Power Factor as a function of the EDOT:FeTos molar ratio and the type of CNTs. As expected, the electrical conductivity increases with the FeTos content since the oxidation level of PEDOT is higher when the EDOT:FeTos molar ratio increases. The Seebeck coefficient is also affected by the oxidant content. Usually, the evolution of the Seebeck coefficient is opposite to the electrical conductivity when the oxidation level of conductive polymers changes.[49–51] However, in this particular case, both parameters, electrical conductivity and Seebeck coefficient, follow the same trend. This fact can be explained by looking at the nanostructure of the particles in the TEM images (**Figure 3.9**). The interconnection degree between particles is more remarkable for an EDOT:FeTos ratio of 1:2 than for 1:1 due to the tendency of the particles to agglomerate and create a more connected path, which improves the charger transport across the film. The electrical conductivity of SWCNTs is higher than for the other CNTs (**Figure 3.10(b)**), which is related to the electronic structure. In the case of DWCNTs, which are a subcategory of MWCNTs, there are four unique permutations of inner@outer wall combinations: semi@semi, metal@metal, semi@metal, and metal@semi.[6] Taking into account that the conductivity of semiconductor nanotubes is smaller, if we extrapolate these combinations to MWCNTs, the probability of having semiconductor nanotubes increases and, therefore, the conductivity decreases.[52–54] The Seebeck coefficient reached a value of 55 μV K^{-1} in agreement with previous work.[55]

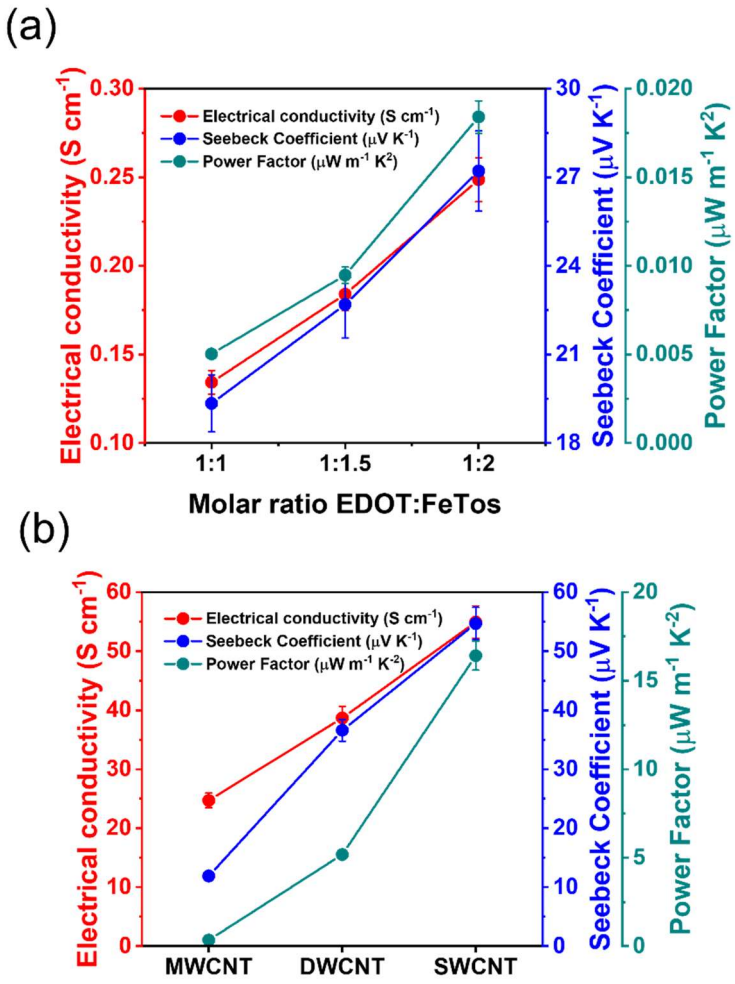

Figure 3.10 Variation of electrical conductivity, Seebeck coefficient, and power factor: (a) as a function of the molar ratio EDOT:FeTos and (b) as a function of the type of carbon nanotubes.

3.2.6 LbL assembly of PEDOT:Tos and CNT

The assembly of PEDOT nanoparticles and CNT layers is controlled by the electrostatic interaction of PDADMAC (cationic polyelectrolyte) and DOC (anionic surfactant). It is thus vital to know the surface charge of the nanoparticles and the CNTs. The zeta potential of the synthesized nanoparticles was (+19.3 ± 0.5) mV. This positive value indicates that PEDOT nanoparticles are positively charged due to the presence of PDADMAC at the surface. The zeta potential was (−29.6 ± 0.3) mV for the CNT dispersion functionalized with DOC. The zeta potential values confirm that the assembly of PEDOT–CNTs bilayers can be carried out through LbL deposition due to the electrostatic interactions of the two components, as shown schematically in **Figure 3.11**.

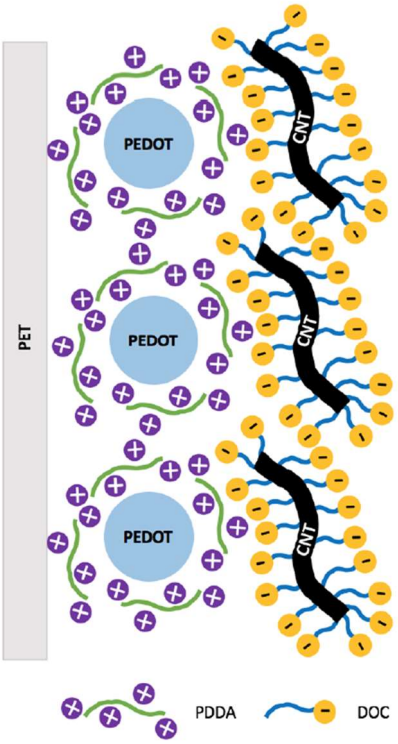

Figure 3.11 Scheme of the electrostatic interaction between PEDOT nanoparticles stabilized with PDADMAC and CNT stabilized with DOC.

PEDOT and CNTs bilayers on the PET surface were obtained by the LbL technique shown in **Figure 3.8(b)**, using MWCNT, DWCNT, and SWCNT dispersions combined with the different EDOT:FeTos molar ratios solutions. The behavior of the samples varying the number of bilayers from 10 to 60 was investigated. **Figure 3.12** shows profilometry measurements to determine the thickness of the samples. At a low number of bilayers (10-30), the thickness of the film increases progressively up to ca. 2 µm. Up to 30 bilayers, the thickness rises rapidly to 3.5–4 µm.

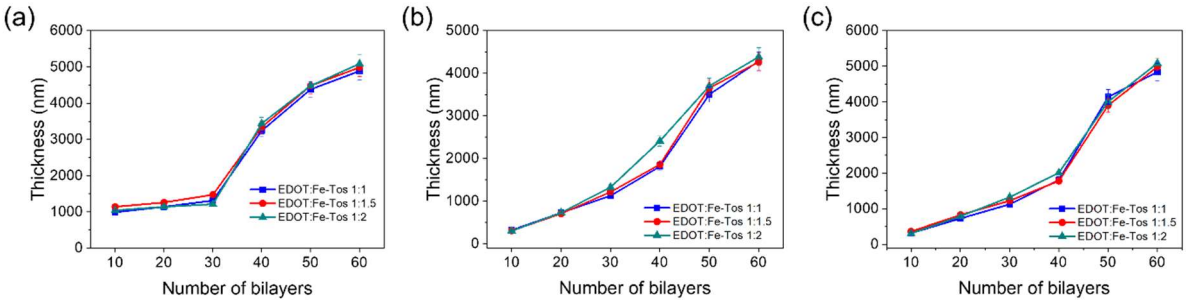

Figure 3.12 Profilometry measurements as a function of the number of bilayers for (a) MWCNT–PEDOT nanoparticles, (b) DWCNT–PEDOT nanoparticles, and (c) SWCNT–PEDOT nanoparticles.

This fact is anomalous and can be explained by an interdiffusion phenomenon between PDADMAC and DOC. Both charged molecules interact with each other due to the high

concentration, forming agglomerates on the film's surface.[56] This observation agrees with the SEM and TEM micrographs of the film cross-sections, presented in **Figure 3.13**.

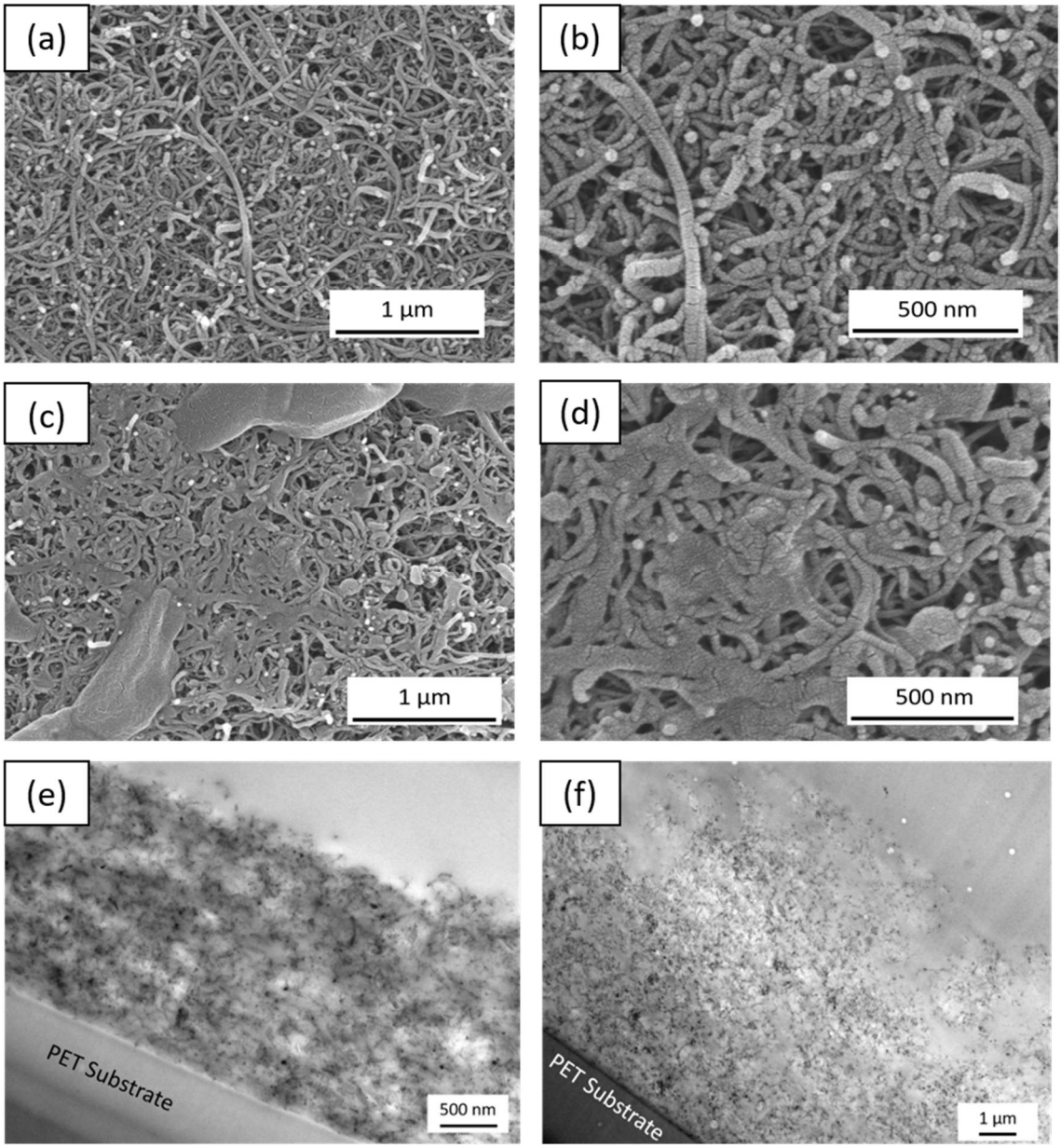

Figure 3.13 (a) and (b) SEM images of 30 BL PEDOT:Tos/MWCNT film. (c) and (d) SEM images of 40 BL PEDOT:Tos/MWCNT film. (e) TEM cross-section micrograph of 30 BL PEDOT:Tos/MWCNT film. (f) TEM cross-section micrograph of 40 BL PEDOT:Tos/MWCNT film.

For 30 bilayers (**Figure 3.13(a)** and **(b)**), PEDOT nanoparticles are uniformly distributed over the MWCNTs fibers due to the electrostatic interactions between PDADMAC and DOC. The morphology of these nanoparticles remains essentially spherical. However, for 40 bilayers (**Figure 3.13(c)** and **(d)**), appears agglomerates on the surface of the films covering the nanotubes. These agglomerates increase the film thickness and the proportion of insulating material at the surface. TEM images of the cross-section

of 30 and 40 bilayer films using MWCNTs (**Figure 3.13(e)** and **(f)**) indicate an interdiffusion phenomenon, with a noticeable increase in the film thickness. **Figure 3.13(f)** shows that the formation of the first layers of MWCNT–PEDOT nanoparticles proceeds uniformly, but when reaching about 2 μm, the film formation is less uniform, with a higher amount of insulating material. Photographs of the films obtained with 10 to 60 bilayers, shown in **Figure 3.14**, demonstrate how the homogeneity of the film is gradually lost with increasing the number of bilayers.

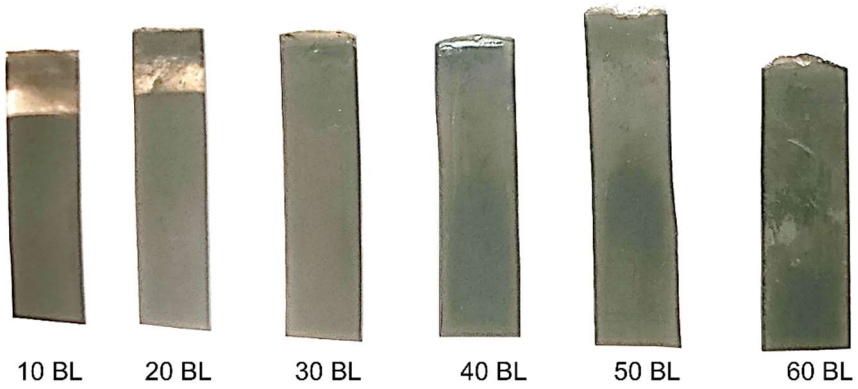

Figure 3.14 Films with a different number of bilayers (BL) of PEDOT–MWCNT.

3.2.7 Thermoelectric properties of PEDOT:Tos/CNT hybrid films

Figure 3.15 shows the thermoelectric parameters of the different systems as a function of the number of bilayers. The electrical conductivity increases until reaching 30 (in the case of MWCNTs) or 40 bilayers (for DWCNTs and SWCNTs). Then, it decreases due to the interdiffusion phenomenon between PDADMAC and DOC, which increases the proportion of insulating material on the film's surface, as already described above. On the other hand, according to the Van der Pauw method for measuring electrical conductivity, increasing the thickness of the film without a notable variation in electrical resistance causes the final electrical conductivity of the composite to decrease.[57] The highest electrical conductivity, with values up to 35 S cm^{-1}, was obtained by using SWCNTs with PEDOT nanoparticles with an EDOT:FeTos molar ratio of 1:2. The Seebeck coefficient has a similar tendency, it increases until 40 bilayers, and then it decreases because the agglomerates of PDADMAC and DOC hinder the passage of the current produced by the difference in temperature. Using SWCNTs with PEDOT nanoparticles at EDOT:FeTos molar ratio of 1:2, the

Seebeck coefficient reached a maximum of 145 μV K^{-1}, higher than water-based polymer emulsion methods containing SWCNTs and PEDOT:PSS.[58]

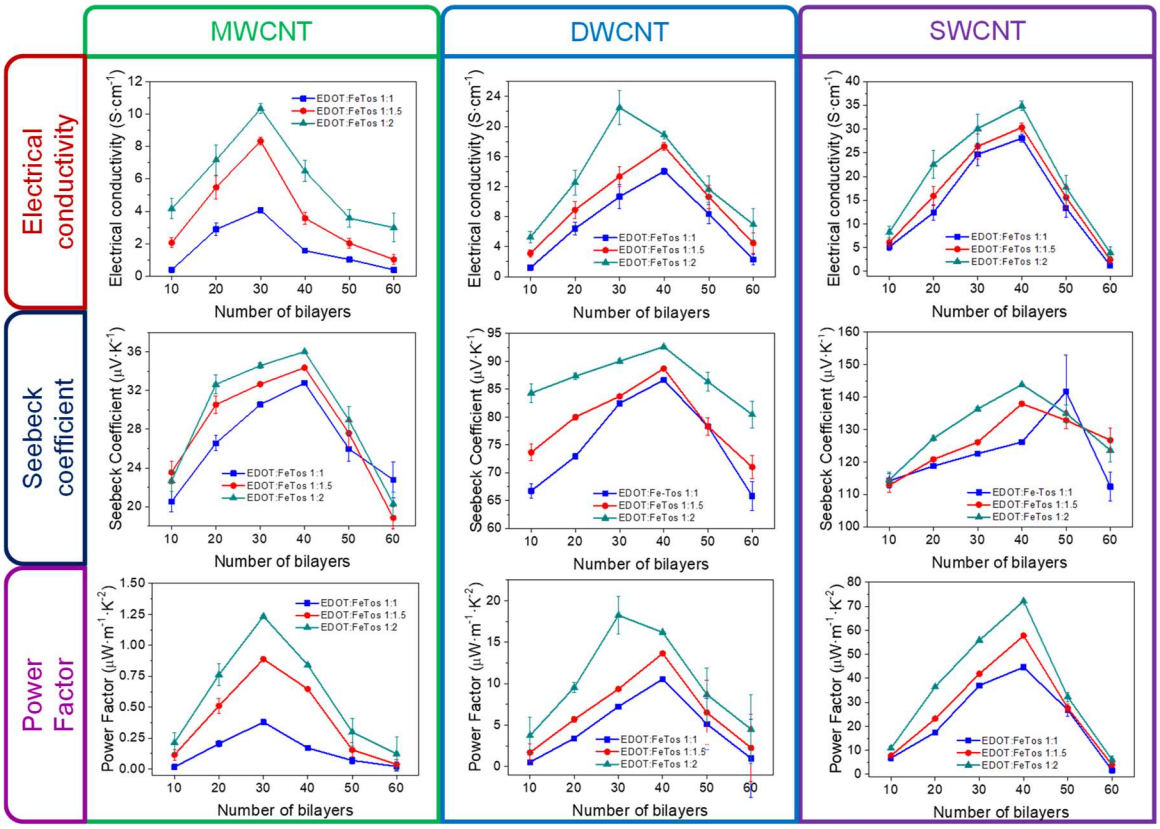

Figure 3.15 Electrical conductivity of films (a) MWCNT–PEDOT nanoparticles, (b) DWCNT–PEDOT nanoparticles, and (c) SWCNT–PEDOT nanoparticles. Seebeck coefficient of (d) MWCNT–PEDOT nanoparticles, (e) DWCNT–PEDOT nanoparticles, and (f) SWCNT–PEDOT nanoparticles. Power Factor of (g) MWCNT–PEDOT nanoparticles, (h) DWCNT–PEDOT nanoparticles, and (i) SWCNT–PEDOT nanoparticles as a function of the number of bilayers.

As the electrical conductivity increases with the number of bilayers, the Seebeck coefficient also increases. This decoupling between the Seebeck coefficient and the electrical conductivity does not occur in conventional thermoelectric bulk materials. The composites with CNT and conductive polymers experience π–π interaction between the aromatic rings of the conductive polymers and the CNTs. This interaction increases carrier mobility and improves the electrical conductivity and Seebeck coefficient of conductive polymers.[58] Finally, the power factor follows the same trend as the electrical conductivity: it increases progressively until 30 (MWCNTs) or 40 bilayers (DWCNTs and SWCNTs) and then sharply decreases. The best power factor was 72 μW m^{-1} K^{-2} with SWCNTs - PEDOT nanoparticles at an EDOT:FeTos molar ratio of 1:2 with 40 bilayers. This value is three orders of magnitude higher than the power factor of pristine PEDOT:Tos

nanoparticles film prepared at the same molar ratio. Interestingly, this value is also higher than previously reported ones for different PEDOT-based materials, including polymer emulsions of PEDOT:PSS/SWCNT/Arabic-gum,[58] PEDOT:PSS/SWCNT deposited by spin-coating,[59] composites by in situ polymerizations of EDOT in the presence of MWCNT and graphene stabilized by PSS,[60] and flexible thermoelectric composite films of polypyrrole and carbon nanotubes.[61]

3.2.8 Flexible properties of PEDOT:Tos/SWCNT

The flexible behavior of PEDOT:Tos/SWCNT films deposited on a PET substrate was determined by measuring the electrical conductivity as a function of the bending number on a 20 mm radius cylinder. **Figure 3.16** shows the variation of the normalized electrical conductivity with the number of bendings of the film with 20 bilayers based on SWCNT and PEDOT nanoparticles with an EDOT: FeTos molar ratio of 1:2. The electrical conductivity remains practically constant, decreasing only 6% after 3000 bends, indicating no layer delamination of the films during the bending. The observations demonstrate that multilayer materials based on carbon nanotubes and nanostructured conductive polymers are suitable for building flexible thermoelectric devices.

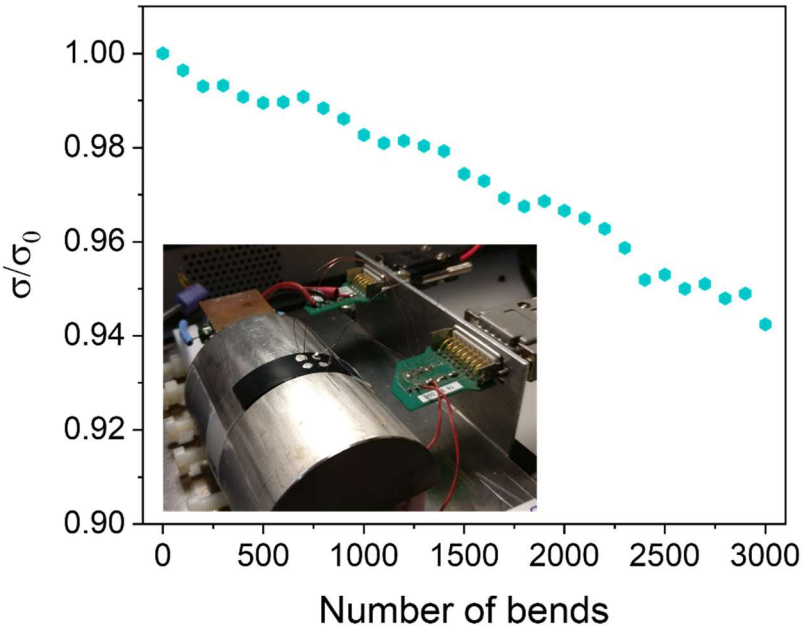

Figure 3.16 Variation of the normalized electrical conductivity (σ_0 is the initial electrical conductivity) as a function of the number of bends with a bending radius of 20 mm for a film with 20 bilayers based on SWCNT and PEDOT nanoparticles. Inset image of the bending test setup.

3.3 Electrochemical synthesis of hybrid layered thermoelectric materials based on PEDOT/SnS doped with Ag

3.3.1 Materials

3,4-ethylenedioxytiophene (EDOT, 97 %) and lithium perchlorate ($LiClO_4$) were purchased from Alfa Aesar, tin (II) sulfate ($SnSO_4$, 97 %) and sodium thiosulfate ($Na_2S_2O_3$, 99 %) were purchased from Acros Organics, silver nitrate ($AgNO_3 \geq 99$ %) was obtained from Sigma-Aldrich and, acetonitrile and sulfuric acid (95 %) were purchased from VWR Chemicals. All the chemicals were used as received, and no further modification or purification was carried out.

3.3.2 Electrochemical deposition of PEDOT

Thin films of PEDOT:ClO_4 were obtained by electrodeposition on a polyethylene terephthalate (PET) substrate. First, a gold layer was deposited on the PET substrate by evaporation in a vacuum chamber (Univex 300 evaporation system) at a pressure of 10^{-5} mbar. The gold films were about 40 nm. Once the PET substrates were coated with gold, the electrochemical deposition of PEDOT:ClO_4 was carried out on the PET-Au substrate in a 3-electrode cell with a 0.01 M EDOT solution, and 0.1 M $LiClO_4$ applying a current of 3 mA for 30 seconds. The working electrode was the PET-gold substrate, the reference electrode was the Ag/AgCl one, and the stainless-steel counter electrode. Next, the electrochemical deposition was performed in an IVIUM n-stat potentiostat. Finally, the gold layer was removed using aqua regia (a mixture of nitric acid and hydrochloric acid, in a molar ratio of 1:3), which is capable of dissolving gold while maintaining the properties of the conductive polymer.[62]

3.3.3 Electrodeposition of SnS:Ag

The electrochemical co-deposition process of SnS:Ag was carried out in an IVIUM n-stat potentiostat using a 3-electrode configuration. The working electrode was the PEDOT film obtained as explained before (**Section 3.3.2**), the reference electrode was Ag/AgCl, and the

counter electrode was stainless steel. The SnS:Ag co-deposition over PEDOT:ClO_4 film was obtained from a solution of 10 mM $SnSO_4$ and 50 mM $Na_2S_2O_3$ at a voltage of -0.92 V versus an Ag/AgCl reference electrode for 7 hours at pH = 2.7.[63–67] Different $AgNO_3$ concentrations were used to optimize the doping of SnS.

During the electrochemical co-deposition of SnS (a binary compound with an atomic ratio of 1:1), the deposition potential of both elements is typically the same, $E_{Sn} = E_S$, with the following reactions occurring at the cathode:

$$Sn^{2+} + 2e^- \rightarrow Sn_{(s)} \quad \textbf{(3.1)}$$

$$S_2O_3^{2-} + 6H^+ + 4e^- \rightarrow 2S_{(s)} + 3H_2O \quad \textbf{(3.2)}$$

$$Sn^{2+} + S + 2e^- \rightarrow SnS_{(s)} \quad \textbf{(3.3)}$$

According to the Nernst equation, the equilibrium deposition potential of Sn and S can be expressed as follows:

$$E_{(Sn^{2+}/Sn)} = E^0_{(Sn^{2+}/Sn)} - \frac{RT}{2F}\ln\frac{1}{(a_{Sn^{2+}})} \quad \textbf{(3.4)}$$

$$E_{(S_2O_3^{2-}/S)} = E^0_{(S_2O_3^{2-}/S)} - \frac{RT}{4F}\ln\frac{1}{(a_{S_2O_3^{2-}})\,(a_{H^+})^6} \quad \textbf{(3.5)}$$

where E^0 is the standard equilibrium potential, and a is the ionic activity of the ions in the bulk solution, which is related to their concentration. To establish the equilibrium potential between Sn and S, we studied different parameters such as ion concentration and pH, resulting in an optimum electrodeposition process of 10 mM of $SnSO_4$ and 50 mM of $Na_2S_2O_3$ at a pH of 2.7. In addition, the temperature for the electrochemical deposition varied from 30 ºC to 50 ºC to establish the optimum synthesis conditions.

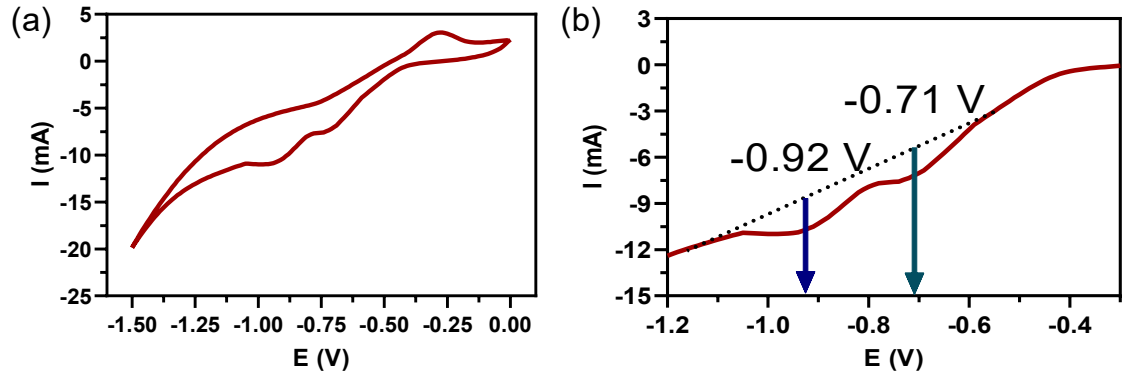

Figure 3.17 (a) Cyclic voltammetry simulating the conditions for the electrodeposition, using PEDOT:ClO_4 as the working electrode and (b) inset of the pics in the cyclic voltammetry.

The study of the redox behavior over a wide range of potential was carried out using cyclic voltammetry. Cyclic scans at 10 mV s^{-1} were carried out in a solution of 10 mM of $SnSO_4$ and 50 mM of $Na_2S_2O_3$ at a pH of 2.7 from 0 to -1.5 V (vs. Ag/AgCl). **Figure 3.17** shows the cyclic voltammetry results used to find the optimum potential for the electrodeposition of SnS:Ag on the PEDOT electrode. First, the potential was in the cathodic direction, and as shown in **Figure 3.17(a)**, the reduction of Sn^{2+} starts at a potential of -0.39 V. Two peaks appear at -0.71 V and -0.92 V due to the active reduction of Sn^{2+}. These ions then react with the S, reduced from $S_2O_3^{2-}$, to produce the SnS film.[63,66,67]

Subsequently, chronoamperometry trials were performed at -0.71 V and -0.92 V for 7 h in a thermostatic bath at 30 ºC using a PEDOT electrode. Results show that at -0.71 V, there was no appreciable co-deposition; therefore, -0.92 V was chosen as the fixed potential to perform chronoamperometric deposition of SnS.

3.3.4 Morphology of PEDOT/SnS:Ag films

Using scanning electron microscopy (SEM), the changes in the surface of the PEDOT film after electrodeposition of SnS with different concentrations of silver were studied.

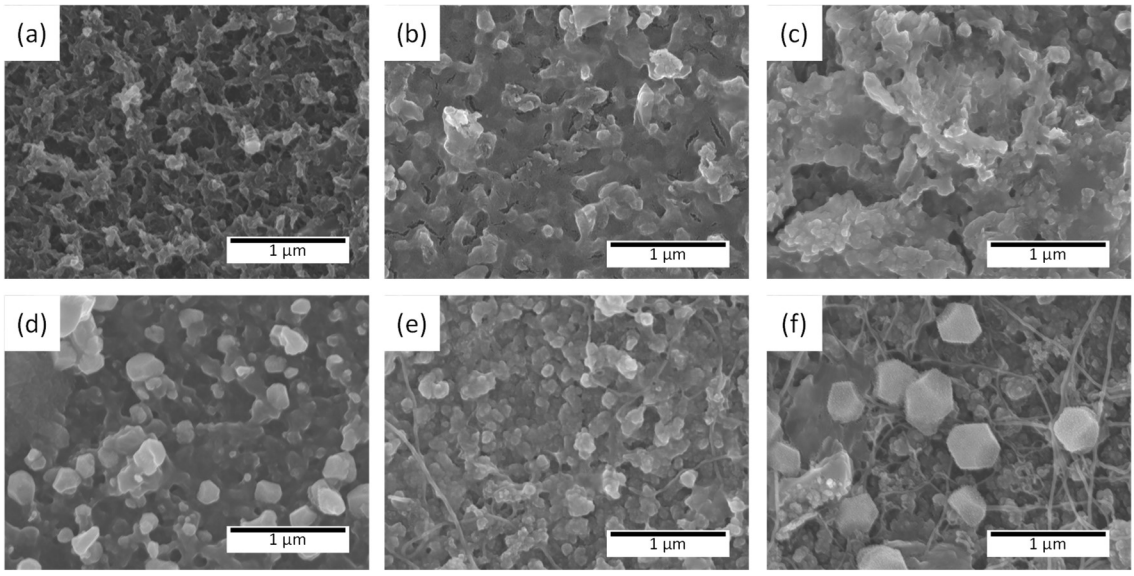

Figure 3.18 SEM micrographs of the samples a) PEDOT:ClO_4, and SnS with different quantities of silver at 30 ºC of b) 0%, c) 0.13%, d) 0.15%, e) 0.17%, f) 0.25%.

Figure 3.18(a) shows the typical cauliflower morphology of PEDOT:ClO_4 obtained by electrodeposition.[62,68] Once SnS is deposited on the PEDOT layer, it is homogeneously distributed on the electrode surface, generating a granular morphology. However, as the

amount of Ag in the solution increases, it is possible to observe hexagonal structures, SnS strands, and small aggregates of silver appear (**Figure 3.18(e)** and **(f)**).

The composition of the SnS strands has been determined utilizing Energy Dispersive Spectroscopy (EDS) microanalysis mapping in an HRTEM (see **Figure 3.19**). **Figure 3.19(a)** shows the TEM micrograph with the microanalysis of the different elements that form part of the strands. Throughout the material, uniform dispersion of the elements S (green), Sn (blue) and Ag (red) is observed, indicating that they are composed of SnS:Ag. The formation of hexagonal crystals at high concentrations of silver (0.25%) is explained by forming the Ag_8SnS_6 phase.[69] This new phase is obtained when the amount of silver ions is high, and they are introduced into the SnS structure.

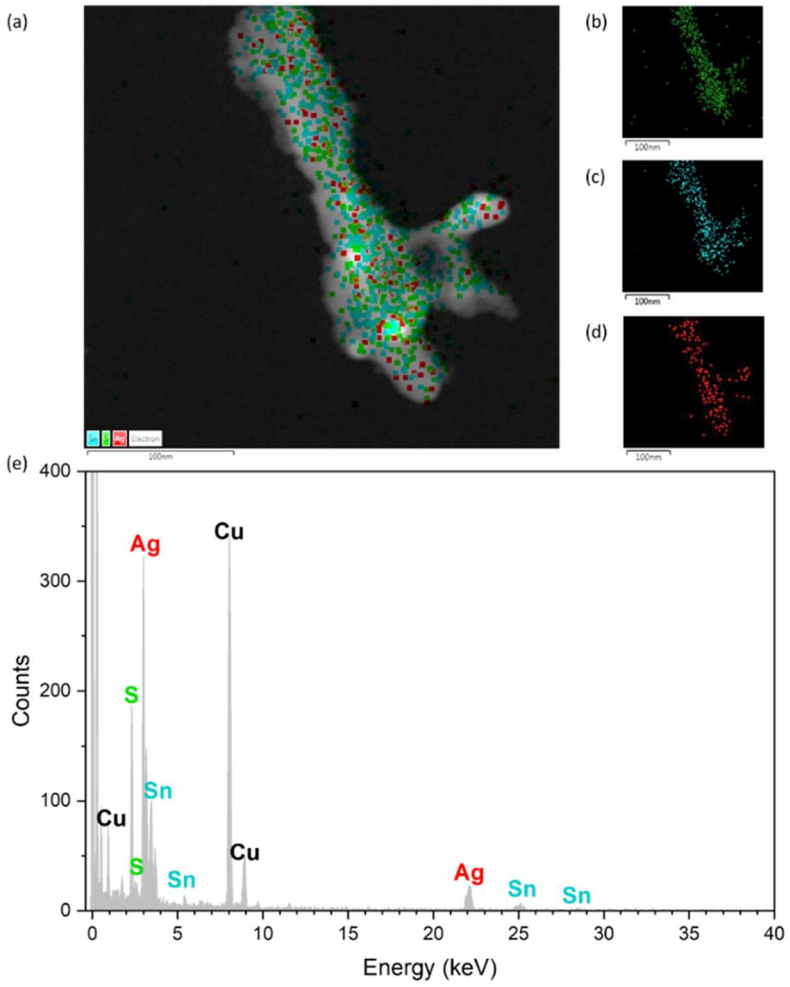

Figure 3.19 (a) Layered mapping image of HRTEM with S, Sn, and Ag atoms (Cu is attributed to the TEM grids). Individual mapping of (b) S, (c) Sn, and (d) Ag atoms. (e) EDS spectra obtained from HRSTEM image.

The electrodeposition conditions (applied potential and temperature) can produce changes in the morphology of the film and, therefore, in the thermoelectric properties. For this reason, a study was conducted depositing SnS:Ag 0.15% on the PEDOT:ClO_4 working

electrode at different temperatures (30 ºC, 40 ºC, and 50 ºC) controlled by a thermostatic bath. The SEM images (**Figure 3.20**) show the different morphologies of the films obtained. The SEM images reveal that increasing the electrodeposition temperature favors the formation of thin SnS strands.[70]

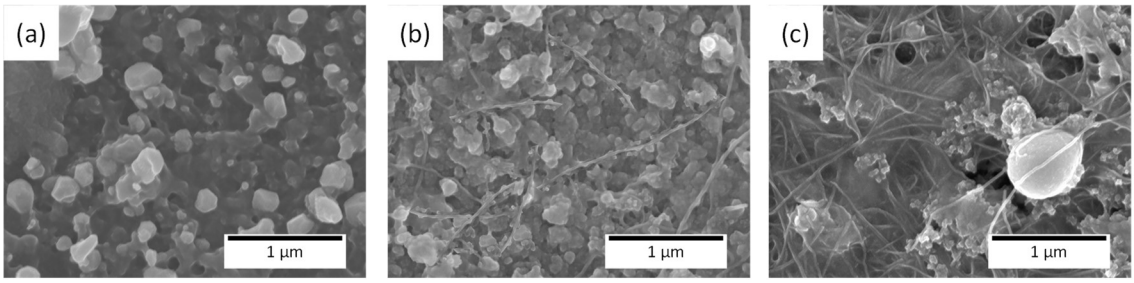

Figure 3.20 SEM micrographs of the samples PEDOT:ClO_4/SnS:Ag 0.15% synthesized at different temperatures (a) 30 °C, (b) 40 °C, and (c) 50 °C.

3.3.5 X-Ray photoelectron spectroscopy analysis

X-ray photoelectron spectroscopy provides information about the composition of PEDOT:ClO_4/SnS:Ag films.

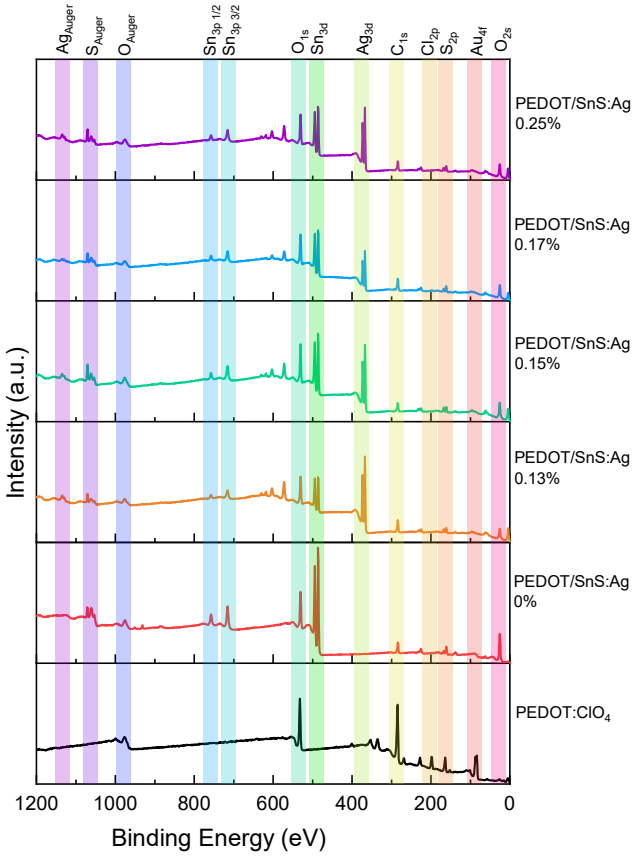

Figure 3.21 XPS survey of the different films obtained in this work.

Figure 3.21 shows XPS survey highlighting the presence of multiple elements, including carbon and gold, attributed to carbon-based contaminants from the atmosphere and traces of gold that were not completely removed with the aqua regia.

The high-resolution XPS spectra of S 2p, Sn 3d, and Ag 3d for PEDOT, undoped, and Ag-doped SnS films are shown in **Figure 3.22**. In addition, **Figure 3.22(a)** shows a schematic of the relative positions of the core levels S 2p, Sn 3d, and Ag 3d and the differences in binding energies. The spectrum of the S 2p for the PEDOT films, **Figure 3.22(b)**, shows the characteristic peaks of thiol groups and thiophene rings of the polymeric chain.[71] For the films with undoped PEDOT/SnS and Ag-doped PEDOT/SnS, the spectra show binding energy of 161.28 eV, which corresponds to the energy of the S^{2-}-Sn^{2+} state. This confirms the presence of the SnS phase. A peak centered at 162.44 eV evidence the presence of silver bonded to sulfur atoms (S^{2-}-Ag^{+}).[72–74] These peaks have an energy difference of 1.16 eV, which agrees with the oxidation state of S^{2-}.[75,76]

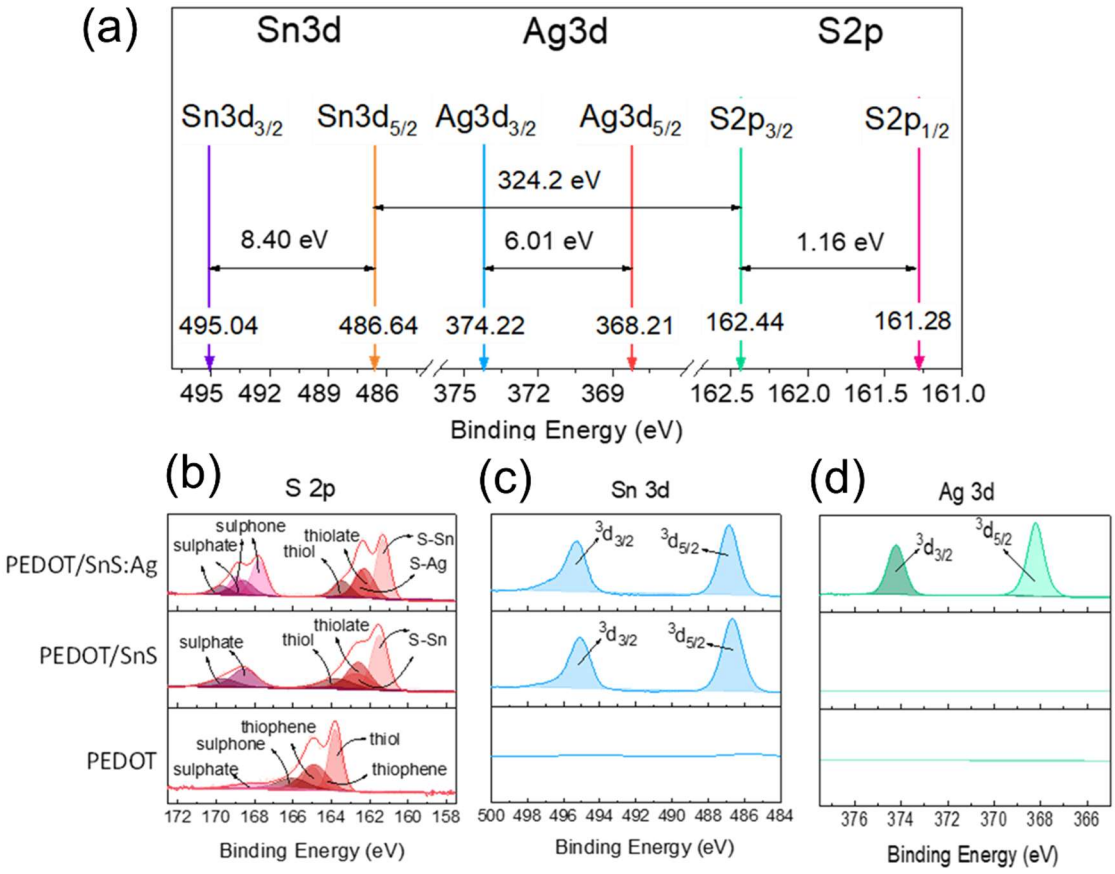

Figure 3.22 (a) Scheme of the relative positions of the core level S 2p, Sn 3d, and Ag 3d. (b)-(d) High-resolution scan of S 2p, Sn 3d, and Ag 3d peaks for the PEDOT, undoped PEDOT:ClO_4/SnS, and Ag-doped PEDOT:ClO_4/SnS films.

The magnified XPS spectra of Sn 3d, **Figure 3.22(c)**, exhibited two signals at 486.64 eV and 495.04 eV, which correspond to the Sn $3d_{5/2}$ and Sn $3d_{3/2}$ energy levels of Sn atoms, respectively. The binding energy between Sn $3d_{5/2}$ and Sn $3d_{3/2}$ is 8.40 eV, indicating the normal state of Sn^{2+} in the film. Therefore, the peaks Sn $3d_{5/2}$ and S $2p_{3/2}$ are related to Sn^{2+} and S^{2-} in SnS, and the binding energy between them is 324.2 eV (see diagram **Figure 3.22(a)**), indicating the formation of an SnS phase.[72,77]

Finally, the films' high-resolution XPS spectra of Ag 3d, **Figure 3.22(d)**, show two signals at 368.21 eV and 374.22 eV, which correspond to Ag 3d5/2 and Ag 3d3/2, respectively. The binding energy between them is 6.01 eV, indicating the presence of silver nanoparticles in the film.[73–75] Furthermore, the high-resolution XPS spectrum at various silver concentrations (see **Figure 3.23**) highlights how the $3d_{5/2}$ Ag peak becomes wider and moves towards lower binding energies, which are consistent with the formation of the Ag_8SnS_6 phase. This phase presents a regular polygonal morphology as observed in the SEM images (**Figure 3.18(f)**).[69] In summary, the magnified XPS spectrum confirms the synthesis of silver-doped tin sulfide on a PEDOT:ClO_4 layer, thereby obtaining a hybrid layered material by electrochemical co-deposition.

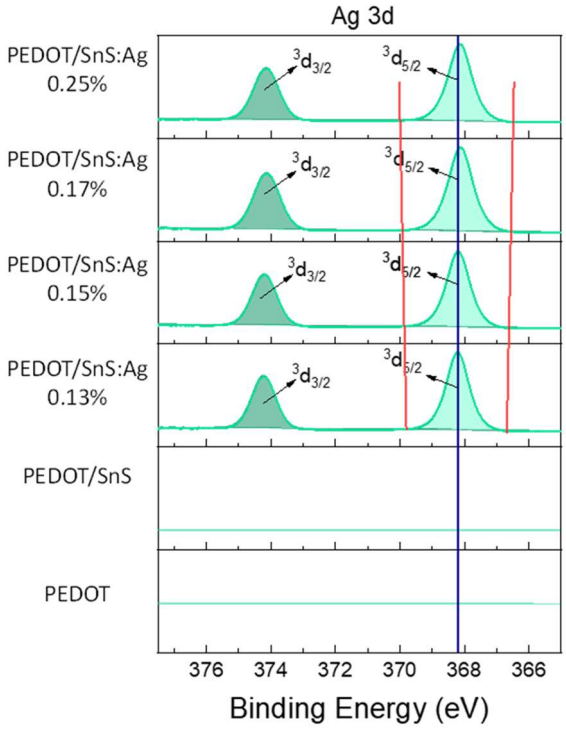

Figure 3.23 High-resolution scan of Ag 3d peaks for the PEDOT, undoped PEDOT/SnS and different Ag-doped PEDOT/SnS films.

3.3.6 Thermoelectric properties of PEDOT/SnS:Ag films

Once the PEDOT:ClO4/SnS:Ag films were synthesized and the composition determined, the electrical conductivity and the Seebeck coefficient were evaluated as a function of the amount of silver and the synthesis temperature. **Figure 3.24** shows the results of the thermoelectric measurements for the samples prepared with different quantities of Ag. The addition of Ag has a significant increase in electrical conductivity because Ag ions act as a charge compensator in the SnS lattice, increasing the hole carrier concentration.[73,78,79] The electrical conductivity of PEDOT (800 S cm^{-1}, **Figure 3.25**) decreased with the addition of the SnS layer since non-doped SnS typically shows low values of electrical conductivity (10^{-4} S cm^{-1}) at room temperature.[27] This supports the hypothesis that the SnS layer dominates the electric transport of the final material. Therefore, when Ag is added during the electrodeposition of SnS over a PEDOT substrate, SnS is doped according to the reaction proposed by Kanatzidis et al.[27]:

$$Ag + S \xrightarrow{SnS} Ag'_{Sn} + S^{x}_{S} + h\cdot \qquad \textbf{(3.6)}$$

Thus, the enhancement of the electrical conductivity with the addition of Ag is attributed to the generation of holes (h ·) during the doping process.

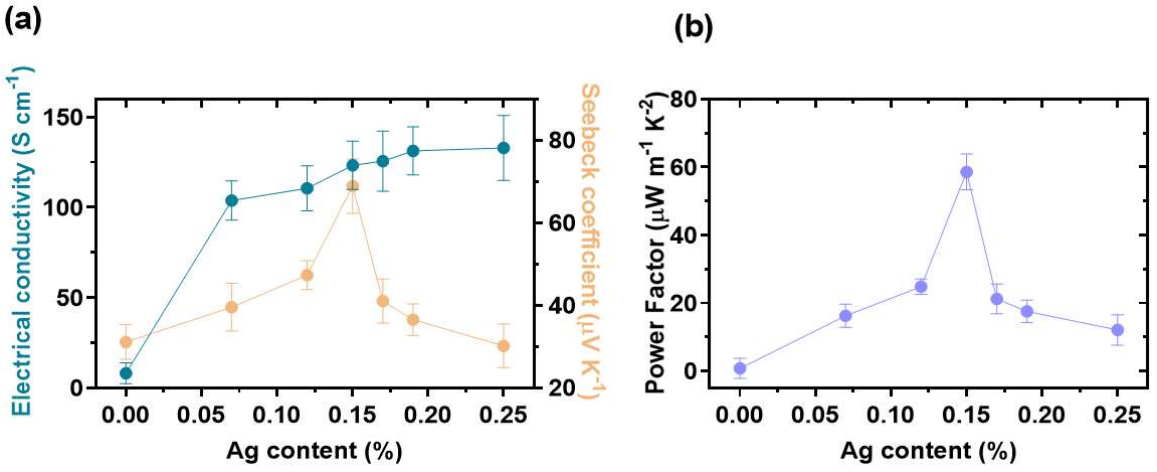

Figure 3.24 (a) Electrical conductivity, Seebeck coefficient, and (b) Power Factor of PEDOT:ClO_4/SnS:Ag films as a function of the Ag content.

In addition, the change in the morphology observed in the SEM images may improve the electric transport in samples. The SnS grain boundaries are thinner; consequently, the scattering of charge carriers is reduced, leading to increased mobility.[73] **Figure 3.24(a)** clearly shows the effect of the Ag doping on the Seebeck coefficient, increasing values to

69 μV K^{-1} when the Ag-dopant concentration in the solution is 0.15%. Without Ag doping, the Seebeck coefficient values are in the order of 30 μV $K^{-1,}$ which indicates that the PEDOT:ClO_4 layer mainly governs the Seebeck coefficient since PEDOT:ClO_4 in a reduced state presents Seebeck values around 33 μV K^{-1} (**Figure 3.25**).

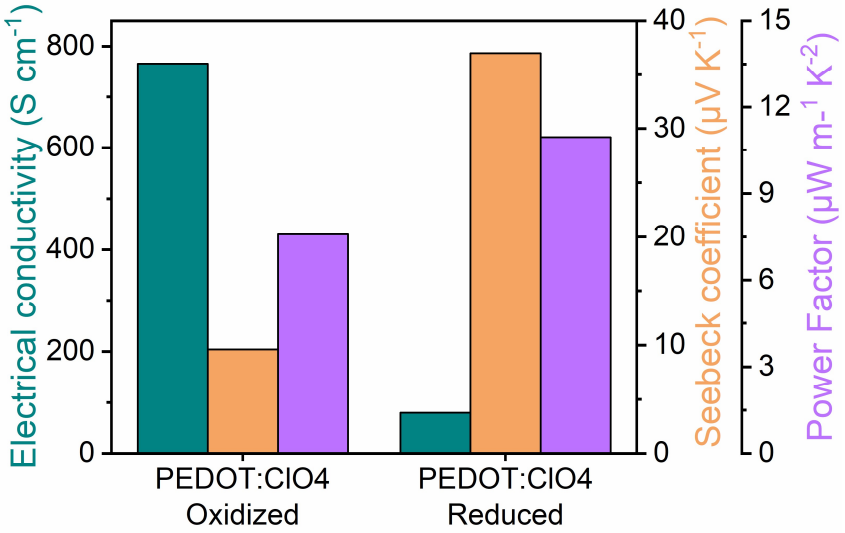

Figure 3.25 Thermoelectric properties of PEDOT:ClO_4 films after removal of Au layer (PEDOT:ClO_4 oxidized) and after electrodeposition of SnS:Ag (PEDOT:ClO_4 reduced).

Typically, SnS shows high Seebeck coefficient values, around 400 μV K^{-1}, which is enhanced by adding low amounts of Ag (>500 μV K^{-1}). The Seebeck coefficient decreases until values of 300 μV K^{-1} at higher amounts of Ag due to the increase of the carrier concentration.[27] This trend is also observed in this study for the samples based on PEDOT:SnS doped with Ag. The maximum value of the Seebeck coefficient reached at 0.15 %. This is explained by the increment of the Ag concentration in the SnS lattice, which can modify the Fermi level energy owing to the heavy-mass band contribution.[27] However, the values of the Seebeck coefficient reached for the samples PEDOT:SnS are not as high as SnS bulk due to the presence of the PEDOT layer. As the PF depends on the conductivity and the Seebeck coefficient, the best results were obtained for the samples with an optimal amount of Ag in the hybrid material (0.15%). The highest PF obtained reached a value of 58.6 μW m^{-1} K^{-2}, a better value than that of SnS doped with silver obtained by solid-state reactions at 300 K.[27] These results evidenced that hybrid materials synthesized by electrochemical methods can contribute to the improvement of the thermoelectric efficiency in organic and inorganic materials without the need for extreme synthesis conditions. In addition, the thermoelectric efficiency of this material is relatively high in terms of the Power Factor compared to SnS bulk material. So this material would be an

interesting alternative to the classical Bi, Pb, and Te based materials that are toxic, low in abundance, and listed as critical raw materials (Bismuth).

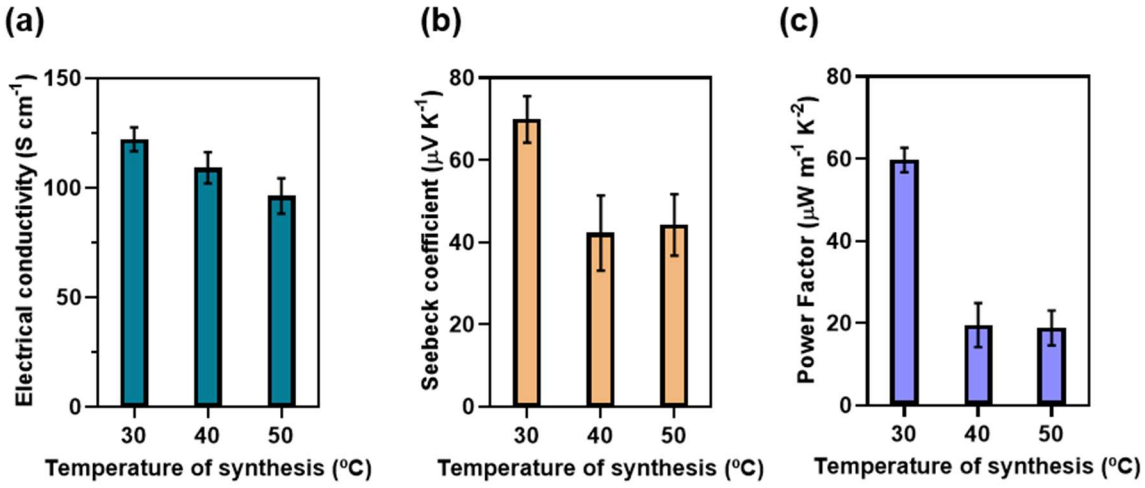

Figure 3.26 (a) Electrical conductivity, (b) Seebeck coefficient and (c) Power Factor of PEDOT:ClO_4/SnS:Ag 0.15% films synthesized at different temperatures.

Figure 3.26(a), (b), and **(c)** show the thermoelectric properties as a function of the temperature of the synthesis. The results show a significant decrease in electrical conductivity. This could be attributed to the different morphologies of the temperature-induced samples. The formation of SnS:Ag strands produce a high degree of heterogeneity of the SnS coating, increasing the grain boundary scattering of charge carriers. Furthermore, an increase in temperature could induce phase changes and consequently reduce the electrical conductivity.[72] An increase in the synthesis temperature causes an increase in the silver content within the SnS structure, forming Ag-related alternative phases. In addition, a decrease in the Seebeck coefficient is observed as a function of the synthesis temperature. Therefore, the highest Power Factor was reached at a synthesis temperature of 30 ºC.

3.3.7 Flexible properties of PEDOT/SnS:Ag films

In order to investigate the reliability of the material under mechanical stress, we have monitored the evolution of the electrical conductivity of the film, PEDOT/SnS:Ag 0.15% synthesized at 30 ºC on a PET substrate. In the first test, the variation of the electrical conductivity of the film after bending with various bending radius has been monitored. In the second test, the evolution of the electrical conductivity has been monitored as a function of the number of bending cycles. **Figure 3.27(a)** indicates no significant changes (less than

5%) in the sheet resistance after bending the film with a different radius. For the bending cycles test, **Figure 3.27(b)**, the film was repeatedly bent up to 3000 cycles with a bending radius of 20 mm. The film also shows a stable electrical conductivity, decreasing around 10% after 3000 bending cycles. Under bending, the mechanical stress is mainly concentrated on the PET substrate,[80], which is well-coated with PEDOT. This helps keep the electrical conductivity nearly constant under mechanical stress. However, the layer of SnS:Ag is not flexible, and after 1800 bindings, it starts to crack. Therefore, the electrical conductivity decreases at a higher rate.

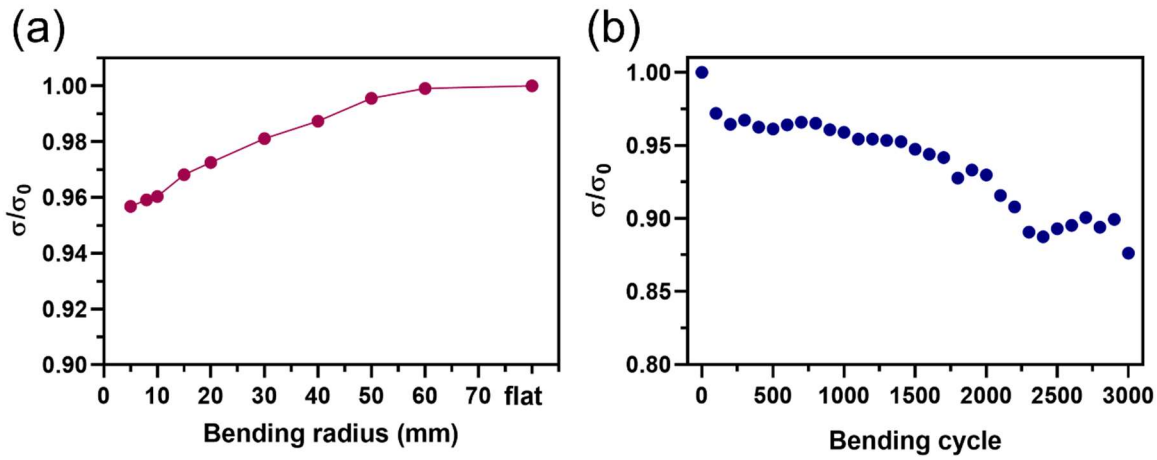

Figure 3.27 Variation of the normalized electrical conductivity (σ_0 is the initial electrical conductivity) as a function of: (a) bending radius, (b) bending cycle with a bending radius of 20 mm for PEDOT:ClO_4/SnS:Ag 0.15% films synthesized at 30 ºC.

These results show a tremendous potential for room-temperature thermoelectric applications since SnS and PEDOT are combined with a low-cost, easy and scalable synthetic route to develop hybrid films with improved thermoelectric efficiency. Furthermore, these hybrid materials adopt the flexible properties of the PEDOT, providing even more added value to the material.

3.4 Conclusions

This chapter describes two methodologies to obtain layered hybrid thermoelectric materials. The first method consists of forming multilayered structures by combining layers of PEDOT:Tos nanoparticles functionalized with a cationic polyelectrolyte (PDADMAC) with layers of carbon nanotubes (MWCNT, DWCNT, SWCNT) functionalized with an

anionic surfactant (DOC). The optimum Power Factor is reached after 30–40 bilayers since, with a higher number of bilayers, an interdiffusion effect creates insulating agglomerates of PDADMAC and DOC. In addition, different carbon nanotubes were used in the multilayered system with PEDOT:Tos nanoparticles. SWCNT with PEDOT:Tos nanoparticles at a 1:2 EDOT:FeTos molar ratio achieved the highest Power Factor, 72 μW m^{-1} K^{-2}, three orders of magnitude higher than the Power Factor of the PEDOT:Tos nanoparticles at the same molar ratio.

The second method is based on the electrodeposition of silver-doped tin sulfide on a PEDOT:ClO_4 working electrode. To optimize the electrochemical doping of SnS with silver, different amounts by weight of silver nitrate were added to the reaction mixture. The morphology of the films is influenced by the addition of Ag and the synthesis temperature. Structural analysis (XPS) and the SEM images indicate the presence of Ag_8SnS_6, which is shown to influence the thermoelectric properties of the films negatively. Electrical conductivity increases as a function of Ag content while the Seebeck coefficient reached the maximum value at an Ag concertation of 0.15% in the electrochemical solution. The maximum power factor observed is 58.6 μW m^{-1} K^{-2}, achieved at 0.15% Ag, four times higher than the pristine PEDOT:ClO_4 film. In addition, PEDOT/SnS:Ag films have good flexibility allowing 1800 bending cycles with a radius of 20 mm with little influence on electrical resistance.

There is no doubt that layered hybrid thermoelectric materials represent an excellent strategy to improve the thermoelectric efficiency of conductive polymers. Furthermore, the results in this chapter represent a clear improvement in hybrid and organic thermoelectric efficiency on sustainable raw materials compared to the state-of-the-art.

References

(1) Jin, H.; Li, J.; Iocozzia, J.; Zeng, X.; Wei, P.; Yang, C.; Li, N.; Liu, Z.; He, J. H.; Zhu, T.; Wang, J.; Lin, Z.; Wang, S. Hybrid Organic–Inorganic Thermoelectric Materials and Devices. *Angew. Chemie Int. Ed.* **2019**, *58* (43), 15206–15226. https://doi.org/10.1002/anie.201901106.

(2) He, M.; Ge, J.; Lin, Z.; Feng, X.; Wang, X.; Lu, H.; Yang, Y.; Qiu, F. Thermopower Enhancement in Conducting Polymer Nanocomposites via Carrier Energy Scattering at the Organic–Inorganic Semiconductor Interface. *Energy Environ. Sci.* **2012**, *5* (8), 8351. https://doi.org/10.1039/c2ee21803h.

(3) Zhou, C.; Dun, C.; Wang, Q.; Wang, K.; Shi, Z.; Carroll, D. L.; Liu, G.; Qiao, G. Nanowires as Building Blocks to Fabricate Flexible Thermoelectric Fabric: The Case of Copper Telluride Nanowires. *ACS Appl. Mater. Interfaces* **2015**, *7* (38), 21015–21020. https://doi.org/10.1021/acsami.5b07144.

(4) Minnich, A. J.; Dresselhaus, M. S.; Ren, Z. F.; Chen, G. Bulk Nanostructured Thermoelectric Materials: Current Research and Future Prospects. *Energy Environ. Sci.* **2009**, *2* (5), 466. https://doi.org/10.1039/b822664b.

(5) Wang, Y.; Yang, L.; Shi, X.; Shi, X.; Chen, L.; Dargusch, M. S.; Zou, J.; Chen, Z. Flexible Thermoelectric Materials and Generators: Challenges and Innovations. *Adv. Mater.* **2019**, *31* (29), 1807916. https://doi.org/10.1002/adma.201807916.

(6) Blackburn, J. L.; Ferguson, A. J.; Cho, C.; Grunlan, J. C. Carbon-Nanotube-Based Thermoelectric Materials and Devices. *Adv. Mater.* **2018**, *30* (11), 1704386. https://doi.org/10.1002/adma.201704386.

(7) Hung, N. T.; Nugraha, A. R. T.; Hasdeo, E. H.; Dresselhaus, M. S.; Saito, R. Diameter Dependence of Thermoelectric Power of Semiconducting Carbon Nanotubes. *Phys. Rev. B* **2015**, *92* (16), 165426. https://doi.org/10.1103/PhysRevB.92.165426.

(8) Piao, M.; Joo, M.-K.; Na, J.; Kim, Y.-J.; Mouis, M.; Ghibaudo, G.; Roth, S.; Kim,

W.-Y.; Jang, H.-K.; Kennedy, G. P.; Dettlaff-Weglikowska, U.; Kim, G.-T. Effect of Intertube Junctions on the Thermoelectric Power of Monodispersed Single Walled Carbon Nanotube Networks. *J. Phys. Chem. C* **2014**, *118* (46), 26454–26461. https://doi.org/10.1021/jp505682f.

(9) Nakai, Y.; Honda, K.; Yanagi, K.; Kataura, H.; Kato, T.; Yamamoto, T.; Maniwa, Y. Giant Seebeck Coefficient in Semiconducting Single-Wall Carbon Nanotube Film. *Appl. Phys. Express* **2014**, *7* (2), 025103. https://doi.org/10.7567/APEX.7.025103.

(10) Jackson, R. K.; Munro, A.; Nebesny, K.; Armstrong, N.; Graham, S. Evaluation of Transparent Carbon Nanotube Networks of Homogeneous Electronic Type. *ACS Nano* **2010**, *4* (3), 1377–1384. https://doi.org/10.1021/nn9010076.

(11) Avery, A. D.; Zhou, B. H.; Lee, J.; Lee, E.-S.; Miller, E. M.; Ihly, R.; Wesenberg, D.; Mistry, K. S.; Guillot, S. L.; Zink, B. L.; Kim, Y.-H.; Blackburn, J. L.; Ferguson, A. J. Tailored Semiconducting Carbon Nanotube Networks with Enhanced Thermoelectric Properties. *Nat. Energy* **2016**, *1* (4), 16033. https://doi.org/10.1038/nenergy.2016.33.

(12) Moore, K. E.; Tune, D. D.; Flavel, B. S. Double-Walled Carbon Nanotube Processing. *Adv. Mater.* **2015**, *27* (20), 3105–3137. https://doi.org/10.1002/adma.201405686.

(13) Meng, C.; Liu, C.; Fan, S. A Promising Approach to Enhanced Thermoelectric Properties Using Carbon Nanotube Networks. *Adv. Mater.* **2010**, *22* (4), 535–539. https://doi.org/10.1002/adma.200902221.

(14) Moriarty, G. P.; De, S.; King, P. J.; Khan, U.; Via, M.; King, J. A.; Coleman, J. N.; Grunlan, J. C. Thermoelectric Behavior of Organic Thin Film Nanocomposites. *J. Polym. Sci. Part B Polym. Phys.* **2013**, *51* (2), 119–123. https://doi.org/10.1002/polb.23186.

(15) Bounioux, C.; Díaz-Chao, P.; Campoy-Quiles, M.; Martín-González, M. S.; Goñi, A. R.; Yerushalmi-Rozen, R.; Müller, C. Thermoelectric Composites of Poly(3-Hexylthiophene) and Carbon Nanotubes with a Large Power Factor. *Energy Environ. Sci.* **2013**, *6* (3), 918. https://doi.org/10.1039/c2ee23406h.

(16) Wang, H.; Yi, S.; Pu, X.; Yu, C. Simultaneously Improving Electrical Conductivity and Thermopower of Polyaniline Composites by Utilizing Carbon Nanotubes as High Mobility Conduits. *ACS Appl. Mater. Interfaces* **2015**, *7* (18), 9589–9597. https://doi.org/10.1021/acsami.5b01149.

(17) Lv, H. Y.; Liu, H. J.; Shi, J.; Tang, X. F.; Uher, C. Optimized Thermoelectric Performance of Bi2Te3 Nanowires. *J. Mater. Chem. A* **2013**, *1* (23), 6831. https://doi.org/10.1039/c3ta10804j.

(18) Venkatasubramanian, R.; Siivola, E.; Colpitts, T.; O'Quinn, B. Thin-Film Thermoelectric Devices with High Room-Temperature Figures of Merit. *Nature* **2001**, *413* (6856), 597–602. https://doi.org/10.1038/35098012.

(19) Liu, B.; Hu, J.; Zhou, J.; Yang, R. Thermoelectric Transport in Nanocomposites. *Materials (Basel).* **2017**, *10* (4), 418. https://doi.org/10.3390/ma10040418.

(20) Kim, C.; Lopez, D. H. Energy Filtering and Phonon Scattering Effects in Bi 2 Te 3 –PEDOT:PSS Composite Resulting in Enhanced n-Type Thermoelectric Performance. *Appl. Phys. Lett.* **2022**, *120* (6), 063903. https://doi.org/10.1063/5.0076952.

(21) Ou, C.; Sangle, A. L.; Datta, A.; Jing, Q.; Busolo, T.; Chalklen, T.; Narayan, V.; Kar-Narayan, S. Fully Printed Organic–Inorganic Nanocomposites for Flexible Thermoelectric Applications. *ACS Appl. Mater. Interfaces* **2018**, *10* (23), 19580–19587. https://doi.org/10.1021/acsami.8b01456.

(22) We, J. H.; Kim, S. J.; Cho, B. J. Hybrid Composite of Screen-Printed Inorganic Thermoelectric Film and Organic Conducting Polymer for Flexible Thermoelectric Power Generator. *Energy* **2014**, *73*, 506–512. https://doi.org/10.1016/j.energy.2014.06.047.

(23) Yu, Y.; Yang, D.; Li, J.; Zhang, M.; Luo, H.; Liang, Q.; Ye, H.; Zhang, Q.; Tang, X.; Wu, J. A Flash Vacuum-Induced Reaction in Preparing High Performance Thermoelectric Cu2S. *Adv. Funct. Mater.* **2022**, *32* (2), 2107284. https://doi.org/https://doi.org/10.1002/adfm.202107284.

(24) Hamawandi, B.; Ballikaya, S.; Råsander, M.; Halim, J.; Vinciguerra, L.; Rosén, J.; Johnsson, M.; S. Toprak, M. Composition Tuning of Nanostructured Binary Copper Selenides through Rapid Chemical Synthesis and Their Thermoelectric Property Evaluation. *Nanomaterials* **2020**, *10* (5). https://doi.org/10.3390/nano10050854.

(25) Byeon, D.; Sobota, R.; Delime-Codrin, K.; Choi, S.; Hirata, K.; Adachi, M.; Kiyama, M.; Matsuura, T.; Yamamoto, Y.; Matsunami, M.; Takeuchi, T. Discovery of Colossal Seebeck Effect in Metallic Cu2Se. *Nat. Commun.* **2019**, *10* (1), 72. https://doi.org/10.1038/s41467-018-07877-5.

(26) Burton, M. R.; Liu, T.; McGettrick, J.; Mehraban, S.; Baker, J.; Pockett, A.; Watson, T.; Fenwick, O.; Carnie, M. J. Thin Film Tin Selenide (SnSe) Thermoelectric

Generators Exhibiting Ultralow Thermal Conductivity. *Adv. Mater.* **2018**, *30* (31), 1801357. https://doi.org/https://doi.org/10.1002/adma.201801357.

(27) Tan, Q.; Zhao, L.-D.; Li, J.-F.; Wu, C.-F.; Wei, T.-R.; Xing, Z.-B.; Kanatzidis, M. G. Thermoelectrics with Earth Abundant Elements: Low Thermal Conductivity and High Thermopower in Doped SnS. *J. Mater. Chem. A* **2014**, *2* (41), 17302–17306. https://doi.org/10.1039/C4TA04462B.

(28) Caballero-Calero, O.; Ares, J. R.; Martín-González, M. Environmentally Friendly Thermoelectric Materials: High Performance from Inorganic Components with Low Toxicity and Abundance in the Earth. *Adv. Sustain. Syst.* **2021**, *5* (11), 2100095. https://doi.org/10.1002/adsu.202100095.

(29) Ju, H.; Kim, J. Chemically Exfoliated SnSe Nanosheets and Their SnSe/Poly(3,4-Ethylenedioxythiophene):Poly(Styrenesulfonate) Composite Films for Polymer Based Thermoelectric Applications. *ACS Nano* **2016**, *10* (6), 5730–5739. https://doi.org/10.1021/acsnano.5b07355.

(30) Ju, H.; Park, D.; Kim, J. Fabrication of Porous SnS Nanosheets and Their Combination with Conductive Polymer for Hybrid Thermoelectric Application. *Chem. Eng. J.* **2019**, *356*, 950–954. https://doi.org/10.1016/j.cej.2018.09.106.

(31) Lu, Y.; Li, X.; Cai, K.; Gao, M.; Zhao, W.; He, J.; Wei, P. Enhanced-Performance PEDOT:PSS/Cu 2 Se-Based Composite Films for Wearable Thermoelectric Power Generators. *ACS Appl. Mater. Interfaces* **2021**, *13* (1), 631–638. https://doi.org/10.1021/acsami.0c18577.

(32) Liu, D.; Yan, Z.; Zhao, Y.; Zhang, Z.; Zhang, B.; Shi, P.; Xue, C. Facile Self-Supporting and Flexible Cu2S/PEDOT:PSS Composite Thermoelectric Film with High Thermoelectric Properties for Body Energy Harvesting. *Results Phys.* **2021**, *31*, 105061. https://doi.org/10.1016/j.rinp.2021.105061.

(33) del Olmo, R.; Mendes, T. C.; Forsyth, M.; Casado, N. Mixed Ionic and Electronic Conducting Binders Containing PEDOT:PSS and Organic Ionic Plastic Crystals toward Carbon-Free Solid-State Battery Cathodes. *J. Mater. Chem. A* **2022**. https://doi.org/10.1039/D1TA09628A.

(34) Cho, C.; Stevens, B.; Hsu, J.; Bureau, R.; Hagen, D. A.; Regev, O.; Yu, C.; Grunlan, J. C. Completely Organic Multilayer Thin Film with Thermoelectric Power Factor Rivaling Inorganic Tellurides. *Adv. Mater.* **2015**, *27* (19), 2996–3001. https://doi.org/10.1002/adma.201405738.

(35) Schlenoff, J. B.; Decher, G. *Multilayer Thin Films: Sequential Assembly of*

Nanocomposite Materials; Wiley, 2006.

(36) Borges, J.; Mano, J. F. Molecular Interactions Driving the Layer-by-Layer Assembly of Multilayers. *Chem. Rev.* **2014**, *114* (18), 8883–8942. https://doi.org/10.1021/cr400531v.

(37) Joo, P.; Jo, K.; Ahn, G.; Voiry, D.; Jeong, H. Y.; Ryu, S.; Chhowalla, M.; Kim, B.-S. Functional Polyelectrolyte Nanospaced MoS 2 Multilayers for Enhanced Photoluminescence. *Nano Lett.* **2014**, *14* (11), 6456–6462. https://doi.org/10.1021/nl502883a.

(38) Cho, C.; Wallace, K. L.; Tzeng, P.; Hsu, J.-H.; Yu, C.; Grunlan, J. C. Outstanding Low Temperature Thermoelectric Power Factor from Completely Organic Thin Films Enabled by Multidimensional Conjugated Nanomaterials. *Adv. Energy Mater.* **2016**, *6* (7), 1502168. https://doi.org/10.1002/aenm.201502168.

(39) Stevens, D. L.; Parra, A.; Grunlan, J. C. Thermoelectric Performance Improvement of Polymer Nanocomposites by Selective Thermal Degradation. *ACS Appl. Energy Mater.* **2019**, *2* (8), 5975–5982. https://doi.org/10.1021/acsaem.9b01079.

(40) Stevens, D. L.; Gamage, G. A.; Ren, Z.; Grunlan, J. C. Salt Doping to Improve Thermoelectric Power Factor of Organic Nanocomposite Thin Films. *RSC Adv.* **2020**, *10* (20), 11800–11807. https://doi.org/10.1039/D0RA00763C.

(41) Manzano, C. V.; Llorente del Olmo, C.; Caballero-Calero, O.; Martín-González, M. High Thermoelectric Efficiency in Electrodeposited Silver Selenide Films: From Pourbaix Diagram to a Flexible Thermoelectric Module. *Sustain. Energy Fuels* **2021**, *5* (18), 4597–4605. https://doi.org/10.1039/D1SE01061A.

(42) Martín-González, M. S.; Prieto, A. L.; Gronsky, R.; Sands, T.; Stacy, A. M. Insights into the Electrodeposition of Bi[Sub 2]Te[Sub 3]. *J. Electrochem. Soc.* **2002**, *149* (11), C546. https://doi.org/10.1149/1.1509459.

(43) Burton, M. R.; Boyle, C. A.; Liu, T.; McGettrick, J.; Nandhakumar, I.; Fenwick, O.; Carnie, M. J. Full Thermoelectric Characterization of Stoichiometric Electrodeposited Thin Film Tin Selenide (SnSe). *ACS Appl. Mater. Interfaces* **2020**, *12* (25), 28232–28238. https://doi.org/10.1021/acsami.0c06026.

(44) Ruiz-Clavijo, A.; Caballero-Calero, O.; Manzano, C. V.; Maeder, X.; Beardo, A.; Cartoixà, X.; Álvarez, F. X.; Martín-González, M. 3D Bi 2 Te 3 Interconnected Nanowire Networks to Increase Thermoelectric Efficiency. *ACS Appl. Energy Mater.* **2021**, *4* (12), 13556–13566. https://doi.org/10.1021/acsaem.1c02129.

(45) Park, J.; Seo, J.; Lim, J.-H.; Yoo, B. Synthesis of Copper Telluride Thin Films by

Electrodeposition and Their Electrical and Thermoelectric Properties. *Front. Chem.* **2022**, *10*. https://doi.org/10.3389/fchem.2022.799305.

(46) Culebras, M.; Igual-Muñoz, A. M.; Rodríguez-Fernández, C.; Gómez-Gómez, M. I.; Gómez, C.; Cantarero, A. Manufacturing Te/PEDOT Films for Thermoelectric Applications. *ACS Appl. Mater. Interfaces* **2017**, *9* (24), 20826–20832. https://doi.org/10.1021/acsami.7b03710.

(47) Naghdi, S.; Rhee, K. Y.; Hui, D.; Park, S. J. A Review of Conductive Metal Nanomaterials as Conductive, Transparent, and Flexible Coatings, Thin Films, and Conductive Fillers: Different Deposition Methods and Applications. *Coatings* **2018**, *8* (8), 278.

(48) Culebras, M.; Serrano-Claumarchirant, J. F.; Sanchis, M. J.; Landfester, K.; Cantarero, A.; Gómez, C. M.; Muñoz-Espí, R. Conducting PEDOT Nanoparticles: Controlling Colloidal Stability and Electrical Properties. *J. Phys. Chem. C* **2018**, *122* (33), 19197–19203. https://doi.org/10.1021/acs.jpcc.8b04981.

(49) Zou, Y.; Huang, D.; Meng, Q.; Di, C.; Zhu, D. Correlation between Seebeck Coefficient and Transport Energy Level in Poly(3-Hexylthiophene). *Org. Electron.* **2018**, *56*, 125–128. https://doi.org/https://doi.org/10.1016/j.orgel.2018.02.008.

(50) Russ, B.; Glaudell, A.; Urban, J. J.; Chabinyc, M. L.; Segalman, R. A. Organic Thermoelectric Materials for Energy Harvesting and Temperature Control. *Nat. Rev. Mater.* **2016**, *1*, 16050. https://doi.org/10.1038/natrevmats.2016.50.

(51) Bubnova, O.; Khan, Z. U.; Malti, A.; Braun, S.; Fahlman, M.; Berggren, M.; Crispin, X. Optimization of the Thermoelectric Figure of Merit in the Conducting Polymer Poly(3,4-Ethylenedioxythiophene). *Nat. Mater.* **2011**, *10*, 429. https://doi.org/10.1038/nmat3012https://www.nature.com/articles/nmat3012#supplementary-information.

(52) Moore, K. E.; Tune, D. D.; Flavel, B. S. Double-Walled Carbon Nanotube Processing. *Adv. Mater.* **2015**, *27* (20), 3105–3137. https://doi.org/10.1002/adma.201405686.

(53) Romero, H. E.; Sumanasekera, G. U.; Mahan, G. D.; Eklund, P. C. Thermoelectric Power of Single-Walled Carbon Nanotube Films. *Phys. Rev. B* **2002**, *65* (20), 205410. https://doi.org/10.1103/PhysRevB.65.205410.

(54) Hayashi, D.; Nakai, Y.; Kyakuno, H.; Yamamoto, T.; Miyata, Y.; Yanagi, K.; Maniwa, Y. Improvement of Thermoelectric Performance of Single-Wall Carbon Nanotubes by Heavy Doping: Effect of One-Dimensional Band Multiplicity. *Appl.*

Phys. Express **2016**, *9* (12), 125103. https://doi.org/10.7567/apex.9.125103.

(55) Tambasov, I. A.; Voronin, A. S.; Evsevskaya, N. P.; Volochaev, M. N.; Fadeev, Y. V; Krylov, A. S.; Aleksandrovskii, A. S.; Luk'yanenko, A. V; Abelyan, S. R.; Tambasova, E. V. Structural and Thermoelectric Properties of Optically Transparent Thin Films Based on Single-Walled Carbon Nanotubes. *Phys. Solid State* **2018**, *60* (12), 2649–2655. https://doi.org/10.1134/S1063783418120296.

(56) Culebras, M.; Cho, C.; Krecker, M.; Smith, R.; Song, Y.; Gómez, C. M.; Cantarero, A.; Grunlan, J. C. High Thermoelectric Power Factor Organic Thin Films through Combination of Nanotube Multilayer Assembly and Electrochemical Polymerization. *ACS Appl. Mater. Interfaces* **2017**, *9* (7), 6306–6313. https://doi.org/10.1021/acsami.6b15327.

(57) van der Pauw, L. J. A Method of Measuring Specific Resistivity and Hall Effect of Discs of Arbitrary Shape. *Philips Res. Reports* **1958**, *13*, 1–9.

(58) Kim, D.; Kim, Y.; Choi, K.; Grunlan, J. C.; Yu, C. Improved Thermoelectric Behavior of Nanotube-Filled Polymer Composites with Poly(3,4-Ethylenedioxythiophene) Poly(Styrenesulfonate). *ACS Nano* **2010**, *4* (1), 513–523. https://doi.org/10.1021/nn9013577.

(59) Song, H.; Liu, C.; Xu, J.; Jiang, Q.; Shi, H. Fabrication of a Layered Nanostructure PEDOT:PSS/SWCNTs Composite and Its Thermoelectric Performance. *RSC Adv.* **2013**, *3* (44), 22065–22071. https://doi.org/10.1039/C3RA42414F.

(60) Hong, C. T.; Lee, W.; Kang, Y. H.; Yoo, Y.; Ryu, J.; Cho, S. Y.; Jang, K.-S. Effective Doping by Spin-Coating and Enhanced Thermoelectric Power Factors in SWCNT/P3HT Hybrid Films. *J. Mater. Chem. A* **2015**, *3* (23), 12314–12319. https://doi.org/10.1039/C5TA02443A.

(61) Li, J.; Du, Y.; Jia, R.; Xu, J.; Shen, S. Z. Flexible Thermoelectric Composite Films of Polypyrrole Nanotubes Coated Paper. *Coatings* **2017**, *7* (12), 211.

(62) Culebras, M.; de Lima Jr., M. M.; Gómez, C.; Cantarero, A. Organic Thermoelectric Modules Produced by Electrochemical Polymerization. *J. Appl. Polym. Sci.* **2017**, *134* (3). https://doi.org/https://doi.org/10.1002/app.43927.

(63) Do, H. W.; Kwon, Y. H.; Cho, H. K. Single Phase Tin Sulfide Films Prepared by One-Bath Electrodeposition. *J. Mater. Sci. Mater. Electron.* **2015**, *26* (11), 8609–8615. https://doi.org/10.1007/s10854-015-3535-9.

(64) Kamel, M. M.; Ibrahim, M. M. Electrochemical Deposition and Characterization of SnS Thin Films. *J. Solid State Electrochem.* **2011**, *15* (4), 683–688.

https://doi.org/10.1007/s10008-010-1136-3.

(65) Supee, A.; Tanaka, Y.; Ichimura, M. Effects of Complexing Agents on Three Steps Pulse Electrodeposited SnS Thin Films. *Mater. Sci. Semicond. Process.* **2015**, *38*, 290–297. https://doi.org/https://doi.org/10.1016/j.mssp.2015.04.028.

(66) Cheng, S.; Chen, Y.; Huang, C.; Chen, G. Characterization of SnS Films Prepared by Constant-Current Electro-Deposition. *Thin Solid Films* **2006**, *500* (1), 96–100. https://doi.org/https://doi.org/10.1016/j.tsf.2005.11.028.

(67) Kafashan, H.; Jamali-Sheini, F.; Ebrahimi-Kahrizsangi, R.; Yousefi, R. Influence of Growth Conditions on the Electrochemical Synthesis of SnS Thin Films and Their Optical Properties. *Int. J. Miner. Metall. Mater.* **2016**, *23* (3), 348–357. https://doi.org/10.1007/s12613-016-1244-x.

(68) Culebras, M.; Gómez, C. M.; Cantarero, A. Enhanced Thermoelectric Performance of PEDOT with Different Counter-Ions Optimized by Chemical Reduction. *J. Mater. Chem. A* **2014**, *2* (26), 10109–10115. https://doi.org/10.1039/C4TA01012D.

(69) An, C.; Tang, K.; Shen, G.; Wang, C.; Huang, L.; Qian, Y. The Synthesis and Characterization of Nanocrystalline Cu- and Ag-Based Multinary Sulfide Semiconductors. *Mater. Res. Bull.* **2003**, *38* (5), 823–830. https://doi.org/https://doi.org/10.1016/S0025-5408(03)00046-1.

(70) Hu, H.; Yang, B.; Zeng, J.; Qian, Y. Morphology Evolution of SnS Nanocrystals: From 3D Urchin-like Architectures to 1D Nanostructures. *Mater. Chem. Phys.* **2004**, *86* (1), 233–237. https://doi.org/10.1016/j.matchemphys.2004.04.001.

(71) Khan, M. A.; Armes, S. P.; Perruchot, C.; Ouamara, H.; Chehimi, M. M.; Greaves, S. J.; Watts, J. F. Surface Characterization of Poly(3,4-Ethylenedioxythiophene)-Coated Latexes by X-Ray Photoelectron Spectroscopy. *Langmuir* **2000**, *16* (9), 4171–4179. https://doi.org/10.1021/la991390+.

(72) Minnam Reddy, V. R.; Gedi, S.; Park, C.; R.w, M.; Ramakrishna, R. R. Development of Sulphurized SnS Thin Film Solar Cells. *Curr. Appl. Phys.* **2015**, *15* (5), 588–598. https://doi.org/10.1016/j.cap.2015.01.022.

(73) Gedi, S.; Minnam Reddy, V. R.; Reddy Kotte, T. R.; Kim, S. H.; Jeon, C. W. Chemically Synthesized Ag-Doped SnS Films for PV Applications. *Ceram. Int.* **2016**, *42* (16), 19027–19035. https://doi.org/10.1016/j.ceramint.2016.09.059.

(74) Jiang, Y.; Yang, Z.; Zhang, P.; Jin, H.; Ding, Y. Natural Assembly of a Ternary Ag-SnS-TiO2 Photocatalyst and Its Photocatalytic Performance under Simulated Sunlight. *RSC Adv.* **2018**, *8* (24), 13408–13416.

https://doi.org/10.1039/c8ra01235k.

(75) Behera, C.; Ghosh, S. P.; Kar, J. P.; Samal, S. L. Facile Synthesis and Enhanced Photocatalytic Activity of Ag-SnS Nanocomposites. *New J. Chem.* **2020**, *44* (27), 11684–11693. https://doi.org/10.1039/d0nj01225d.

(76) Rajwar, B. K.; Sharma, S. K. Structural, Optical and Electrical Properties of Ag-Doped SnS2 Nano-Flowers Synthesized by Solvothermal Method. *Mater. Res. Express* **2019**, *6* (7), 2–12. https://doi.org/10.1088/2053-1591/ab18b4.

(77) Peisert, H.; Chassé, T.; Streubel, P.; Meisel, A.; Szargan, R. Relaxation Energies in XPS and XAES of Solid Sulfur Compounds. *J. Electron Spectros. Relat. Phenomena* **1994**, *68*, 321–328. https://doi.org/https://doi.org/10.1016/0368-2048(94)02129-5.

(78) Devika, M.; NK, R.; Ramesh, K.; KR, G.; ESR, G.; KTR, R. Low Resistive Micrometer-Thick SnS : Ag Films for Optoelectronic Applications. *J. Electrochem. Soc.* **2006**, *153* (8), G727–G733. https://doi.org/10.1149/1.2204870.

(79) Kumar, K. S.; Manohari, A. G.; Dhanapandian, S.; Mahalingam, T. Physical Properties of Spray Pyrolyzed Ag-Doped SnS Thin Films for Opto-Electronic Applications. *Mater. Lett.* **2014**, *131*, 167–170. https://doi.org/https://doi.org/10.1016/j.matlet.2014.05.186.

(80) Kim, S. J.; Lee, H. E.; Choi, H.; Kim, Y.; We, J. H.; Shin, J. S.; Lee, K. J.; Cho, B. J. High-Performance Flexible Thermoelectric Power Generator Using Laser Multiscanning Lift-Off Process. *ACS Nano* **2016**, *10* (12), 10851–10857. https://doi.org/10.1021/acsnano.6b05004.

Chapter 4

Thermoelectric fabrics

Content

This chapter studies the thermoelectric properties of fabrics based on conductive polymers to obtain textile-based wearable thermoelectric generators. The introduction explains the diverse types of wearable thermoelectric generators and various methodologies for coating flexible conductive polymer substrates. Then, three studies optimize the process of coating textiles with conductive polymers. The first analyzes the effect on the thermoelectric properties and thermal stability of the coating of fabrics with different conductive polymers. In the second study, PEDOT:ClO_4 was electrodeposited on felt and cotton fabrics coated with MWCNT, and a thermoelectric generator was prepared with both fabrics. Finally, the thermoelectric and mechanical properties of felt fabric coated with PEDOT and different counterions were studied, and a wearable thermoelectric generator based on PEDOT:BTFMSI coated felt fabrics was developed.

4.1 Introduction

The Internet of Things (IoT) concept has promoted the development of wearable electronics such as smart fabrics and implantable medical devices.[1–3] However, most of these devices use batteries as power sources, subject to periodic recharging and replacement. Therefore, the next challenge is to design new systems to obtain sustainable energy to generate power for portable electronic devices.[4] One way is by harvesting it from the human body, which can be considered a constant and uninterrupted energy source for portable power devices. For example, it is estimated that the daily activities of a 70 kg adult can generate about 100 W of power through breathing, heating, blood transport, and walking.[5] Therefore, getting 1 W of all the energy generated by the human body can be enough to power most portable devices. Triboelectric generators,[6,7] piezoelectric generators,[8] and thermoelectric generators (TEG),[9] have been developed to collect energy from human movement and body heat. The main advantage of TEGs over other energy harvesters is that the dissipation of human heat generates a significant amount of energy per unit area; therefore, wearable TEGs (wTEGs) are suitable for collecting lost thermal energy.[10]

4.1.1 The human body as a heat source for TEG

The ambient temperature varies between -40 to 40 ºC depending on the region, so the maximum temperature difference between the human body (36.5 ºC) and the environment will be 80 ºC.[11] Most human energy is released in the form of heat, so it is reasonable to use thermoelectric generators to harvest thermal energy and convert it into electrical energy. The maximum efficiency of thermal energy harvesting of the human body can be determined from the Carnot efficiency, **Equation (1.8)**. Assuming a normal body temperature (36.5 ºC) and a relatively low ambient temperature (20 ºC), the Carnot efficiency will be 5.3%. However, in a warmer environment (30 ºC), the Carnot efficiency will decrease up to 2.1%. The Carnot efficiency offers the ideal conversion value, but the efficiency of thermoelectric generators under thermal gradients between 5 and 20 ºC oscillates between 0.2% and 0.8%, very far from the value offered by the Carnot efficiency. Reimer et al.[12] estimated that the total heat dissipated by the human body ranges from 60–180 W. However, harvesting all this power would require coating the entire body with thermoelectric generators, limiting their practical use. Therefore, it is more reasonable to design TEGs to occupy a small body part, maximizing efficiency.

Generally, we can consider that the exchange of thermal energy between the human body and the environment occurs through conduction, convection, and radiation. Heat conduction occurs when two bodies or substances are in direct contact. Convection is the heat transmission from the body to the air through a fluid medium such as blood or gases. Finally, radiation or heat dissipation is the most important heat exchange mechanism. Therefore, the design of a thermoelectric generator involves the use of heat dissipation and conduction. By placing the TEG on the human body, the temperature difference (ΔT) between the human body and the environment results in a flow of heat through the generator that generates an intrinsic thermal gradient (ΔT_{TEG}) which, in turn, conducts the production of an output voltage through the Seebeck effect. Therefore, the success of a wearable thermoelectric generator will be based on the maximization of the temperature difference.

Maximizing the intrinsic temperature difference in the thermoelectric generator is a real challenge due to the existence of three thermal resistances that can limit the performance of the TEG. In **Figure 4.1(a)**, the three thermal resistances are schematized. The skin resistance is because the human skin is a thermal insulator that generates a resistance between the TEG and the human body. Contact resistance is due to the roughness

of the skin, which decreases direct contact between the skin and the TEG. Finally, convective resistance occurs between the interface of the TEG and the environment. This resistance usually depends on the air's convection; therefore, a heat sink is often used to increase the efficiency of the convection.[13]

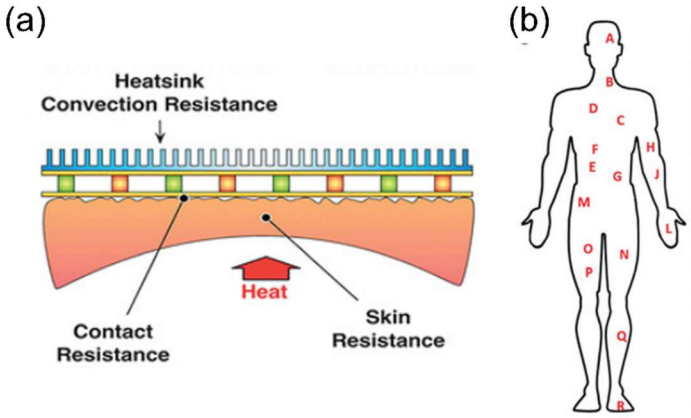

Skin Location	Cold (15°C)	Room (27°C)	Hot (47°C)
Forehead (A)	31.7	35.2	37
Back of Neck (B)	31.2	35.1	36.1
Chest (C)	30.1	34.4	35.8
Upper Back (D)	30.7	34.4	36.3
Lower Back (E)	29.2	33.7	36.6
Upper Abdomen (F)	29.0	33.8	35.7
Lower Abdomen (G)	29.2	34.8	36.2
Tricep (H)	28.0	33.2	36.6
Forearm (J)	26.9	34.0	37.0
Hand (L)	23.7	33.8	36.7
Hip (M)	26.5	32.2	36.8
Side thigh (N)	27.3	33.0	36.5
Front Thigh (O)	29.4	33.7	36.7
Back Thigh (P)	25.5	32.2	36.0
Calf (Q)	25.1	31.6	35.9
Foot (R)	23.2	30.4	36.2

Figure 4.1 (a) Schematic representation of three thermal resistance that impact TEG performance. (b) Human skin temperatures at different body locations. Reprinted with permission.[13] Copyright 2016, The Royal Society of Chemistry.

Another parameter that must be considered for the efficient design of wearable thermoelectric generators is the body position in which the wTEG will be placed since the generation of body heat is related to metabolic activity. Webb et al.[14] measured skin temperature in different body parts, as shown in **Figure 4.1(b)**. The highest temperatures were recorded in the upper part of the human body and the lowest in the lower part. Therefore, skin temperature is essential in optimizing wTEG efficiency since the power output is determined by the temperature difference between the body and the environment.

4.1.2 Wearable thermoelectric generators

Classical thermoelectric materials such as inorganic semiconductors, carbon nanotubes, conductive polymers, 2D materials, and composites have been used to develop wearable thermoelectric generators. Inorganic semiconductors are the materials with the highest ZT values,[15,16] but the need to use low-cost, lightweight, and flexible materials in portable thermoelectric generators has promoted the use of organic materials with low thermal conductivity, high flexibility, and good processability.[17] Other novel thermoelectric materials such as 2D materials and CNTs have also recently come into use due to their transport properties and high Power Factors.[18–20] As previously mentioned, one of the most promising strategies to obtain efficient, low-cost, and flexible thermoelectric materials is

to develop hybrid organic/inorganic materials. In these materials, inorganic fillers are introduced into conductive polymer matrices to produce a synergistic combination between them.[21,22]

Since the human body is not a flat surface, the goal of wearable thermoelectric generators is to collect body heat most efficiently on the skin. Therefore, depending on the application of the wTEG, the integration of the generator in the skin, and the materials used, we can divide the wTEGs into four main categories: rigid, flexible, stretchable, and textile.[23]

4.1.2.1 Rigid wTEG

These types of thermoelectric generators are generally made from conventional bulk TE materials. The first commercial application of a rigid wearable thermoelectric generator (R-wTEG) was in 1980 with the Bulova Thermatron. However, the market success to thermoelectrically powered watches came later after perfecting the electronics of watches. Kishi et al.[24] developed in 1999 a wristwatch with more than 50 pairs of Bi/Te (n-type) and Bi/Sb/Te (p-type) elements that were capable of running on body heat. More recent studies have shown that these types of wearable thermoelectric generators can be used to measure the thermal properties of the human body in the trunk, head, and extremities.[25–27] In addition, these devices show competitive performance in the range of temperatures between 0 to 25 ºC and can replace batteries in low-power portable devices, reaching output power values of 20 μW at 22 ºC.[28] The main drawback of R-wTEGs is that the use of conventional inorganic materials limits their applicability when the body heat source is curved due to the rigidity of these materials.

4.1.2.2 Flexible wTEG

Flexible wearable thermoelectric generators (F-wTEG) emerge as an alternative to R-wTEGs as they allow greater adaptability to the contact between the generator and the skin, thus maximizing heat collection. The main strategy used for the development of F-wTEGs has been the deposition of thermoelectric materials on flexible substrates such as polyimide (PI), polyethylene terephthalate (PET), and polydimethylsiloxane (PDMS).[29–31] These flexible and insulating substrates allow a better adaptation of the thermoelectric generator to arbitrarily shapes heat sources and mass production methods. For example, We et al.[32] developed a high-performance F-wTEG using screen-printed Sb_2Te_3 film and a

PEDOT:PSS hybrid compound, obtaining an output voltage of 12.1 mV with a thermal gradient of 5 K, as shown in **Figure 4.2(a)**. Zeng et al.[33] assembled reduced graphene oxide (rGO) films on PDMS grids to obtain low thermal conductivity while maintaining the high electrical conductivity of rGO. They elaborated a bracelet type F-wTEG with seven legs getting an output power of 4.19 μW g^{-1} with a thermal gradient of 15 K, as shown in **Figure 4.2(b)**. Song et al.[29] made an F-wTEG based on PEDOT:PSS/Te on a polyimide substrate. In the device, a bubble film was used as thermal insulation, obtaining an output voltage of 2.5 mV with a temperature difference of 13.4 K, **Figure 4.2(c)**.

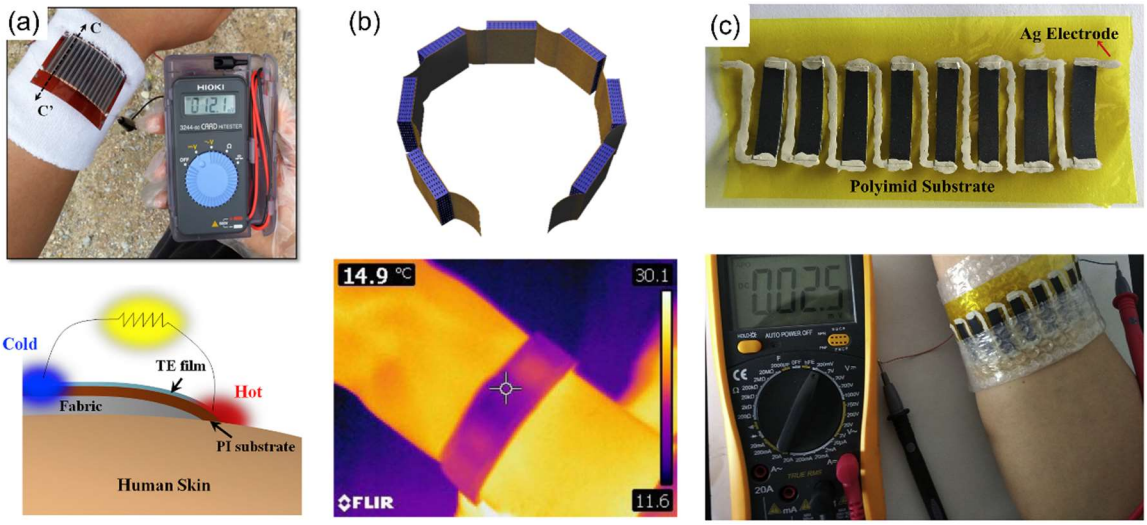

Figure 4.2 (a) Performance demonstration of F-wTEG and schematic TEG cross-section. Reprinted with permission.[32] Copyright 2014, Elsevier Ltd. (b) Scheme of F-wTEG bracelet type and infrared image of the device. Reprinted with permission.[33] Copyright 2018, Elsevier Ltd. (c) PEDOT:PSS/Te F-wTEG and its performance demonstration. Reprinted with permission.[29] Copyright 2017, Elsevier Ltd.

Flexible substrates for thermoelectric generators bring lightness and adaptability to human skin. However, they can cause a loss of wTEG performance due to traction/compression effects at the interface between the TE material and the electrodes during bending.

4.1.2.3 Stretchable wTEG

In contrast to the wearable thermoelectric generators discussed above, the stretchable ones (S-wTEG) have the advantage that they can be used on dynamic surfaces and guarantee better contact between the device and the skin. Therefore, the contact resistance between the device and the skin will be lower. However, it is difficult to obtain a suitable structure for these wearable thermoelectric generators since, to obtain high performance, it is necessary to use rigid inorganic semiconductors. One of the strategies used to address these

limitations is the 3D helical fabrication of stretchable devices since, in this way, the helical structure can withstand greater mechanical stress.[34,35] In addition to the high stretchability (~100%) and stretch stability, air can penetrate through the device to dissipate heat. For example, Xu et al.[35] developed a thermoelectric generator with a helical structure through which he obtained an output voltage of 8.9 mV with a thermal gradient of 16 K, **Figure 4.3(a)**. Yang et al.[36] proposed using stretchable electrodes to favor their use on dynamic surfaces. For this, the S-wTEG consisted of hot-pressed nanolayers of Sb_2Te_3 and Bi_2Te_3 integrated by wavy serpentine interconnections, as shown in **Figure 4.3(b)** and embedded in an Ecoflex elastomer matrix. The device's output power reached 0.15 mW cm^{-2} with a ΔT = 19 K.

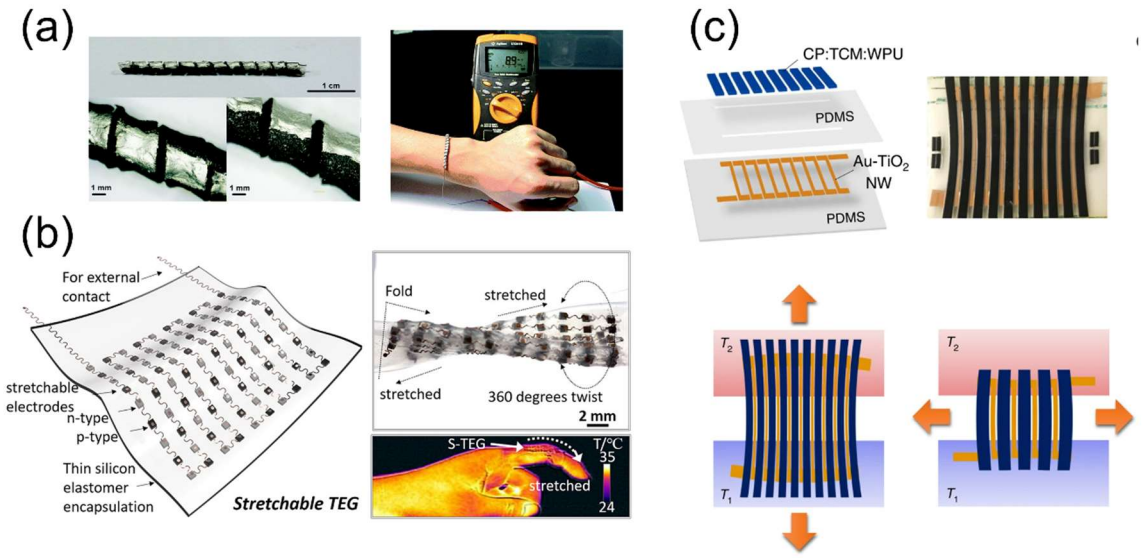

Figure 4.3 (a) Images of stretchable helical TEG. Reprinted with permission.[35] Copyright 2018, The Royal Society of Chemistry. (b) S-wTEG with serpentine interconnection. Reprinted with permission.[36] Copyright 2020, American Chemical Society. (c) PEDOT/WPU/ ionic liquid stretchable wTEG. Reprinted with permission.[37] Copyright 2020, Springer Nature.

Researchers have also investigated the possibility of having intrinsically stretchable thermoelectric generators to obtain a more suitable structure. Kim et al.[37] reported an elastic compound PEDOT/WPU/ionic liquid with high electrical conductivity and stretchability. The open-circuit voltage remained relatively stable up to 40% stretching in both the parallel and perpendicular directions, **Figure 4.3(c)**.

4.1.2.4 Textile wTEG

Textiles have great potential for obtaining wearable thermoelectric generators (T-wTEGs) as they help to improve the portability of TEGs. In general, the advantage of using textiles

to integrate TEGs lies in their comfort, adaptability to movement, and guaranteed heat transfer. However, the application of T-wTEGs is limited by the low-temperature difference (ΔT = 3 – 10 K) available to harvest body heat. Therefore, it is necessary to use inorganic TE materials with high Seebeck coefficients. The main method used to coat textiles with TE materials is screen printing, which is highly compatible with textile processing methods. For example, Kim et al.[38] developed a T-wTEG based on $Bi_{0.5}Sb_{1.5}Te_3$ and $Bi_2Se_{0.3}Te_{2.7}$ using a dispenser printing method, **Figure 4.4(a)**. The device showed a power output of 224 nW with a thermal gradient of 5 K. Lu et al.[39] designed a thermoelectric generator using silk cloth by printing Bi_2Te_3 and Sb_2Te_3 by conventional methods in the textile industry. The prototype consisted of 12 thermocouples and could generate a power output of 15 nW with a thermal gradient of 35 K.

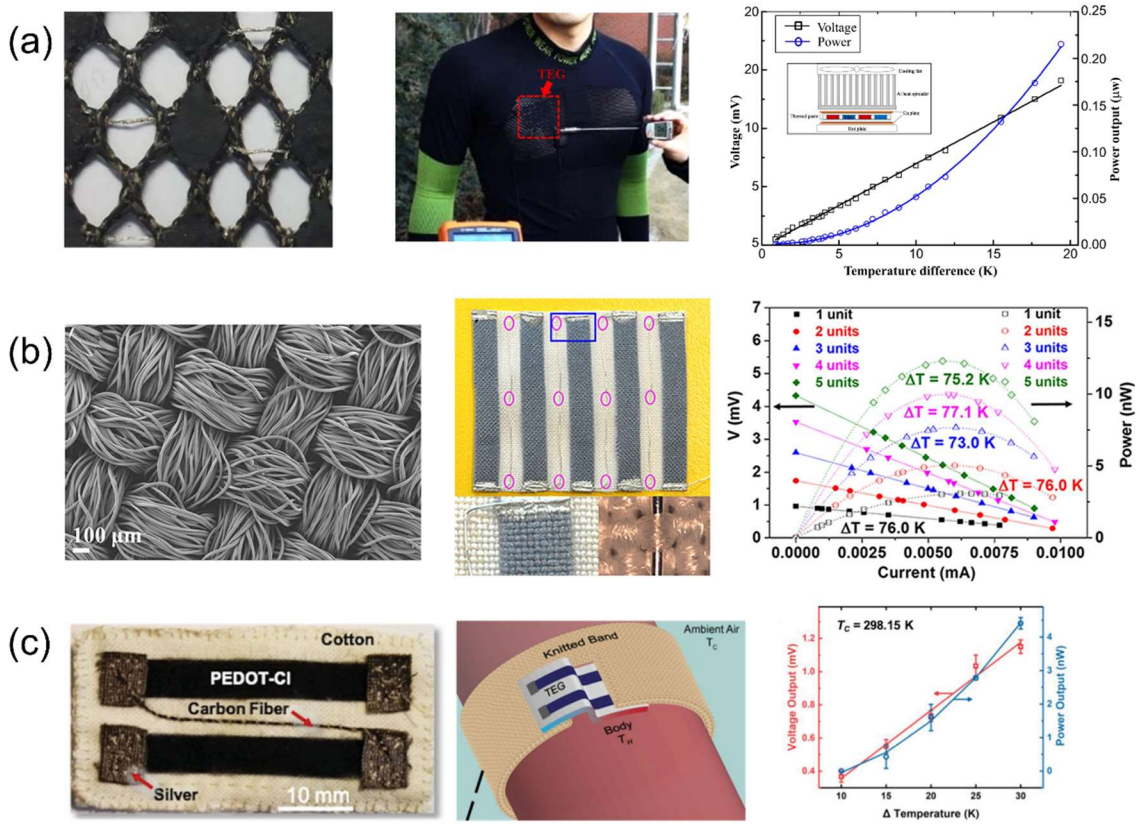

Figure 4.4 (a) Device performance and implementation of T-wTEG based on $Bi_{0.5}Sb_{1.5}Te_3$ and $Bi_2Se_{0.3}Te_{2.7}$. Reprinted with permission.[38] Copyright 2014, IOP Publishing Ltd. (b) SEM image, T-wTEG, and its performance. Reprinted with permission.[40] Copyright 2015, Springer Nature. (c) T-wTEG based on PEDOT:Cl and its performance. Reprinted with permission.[41] Copyright 2019, Wiley-VCH Verlag GmbH & Co. KGaA, Weinheim.

However, T-wTEGs based on rigid inorganic semiconductors are not suitable for dynamic applications. For this reason, the researchers promoted the development of T-wTEGs by using alternative materials such as conductive polymers, which are

biocompatible, flexible, and lightweight. In addition, due to the low thermal conductivity of conductive polymers, they are ideal candidates to quickly and economically obtain efficient T-wTEG. Du et al.[40] designed a textile-based thermoelectric generator by immersing a commercial fabric in a PEDOT:PSS solution, obtaining an output voltage of 4.3 mV with a temperature difference of 75 K, **Figure 4.4(b)**. Jia et al.[42] developed a T-wTEG by coating a textile with PEDOT by in situ polymerization, obtaining an output voltage of 5 mV at ΔT = 25 K. Allison et al.[41] coated commercial cotton fabric with PEDOT:Cl by steam printing, **Figure 4.4(c)**. The fabric was cut into two strips, which were used to obtain a band-shaped T-wTEG, generating a power output of 4.5 nW at ΔT = 30 K.

4.1.3 Textile-based wearable thermoelectric generators

As we have previously commented, the use of textiles in the field of wearable thermoelectric generators is due to the flexibility, breathability, usability, and comfortable sensation of fabrics.[4,43,44] In addition, the coating of textiles with conductive polymers to obtain T-wTEG is favored over its counterparts for its advantageous mechanical properties and ease of processing. The elasticity and plasticity of conductive polymers are similar to those of ordinary yarns, which should prevent delamination and fragmentation when bending or twisting coated textiles.[44] However, not all textile coating methods with conductive polymers offer the same coating stability against use. Next, we will see the different methods for depositing conductive polymers on textiles and analyze their advantages and disadvantages.

4.1.3.1 Dip coating

Dip coating of textiles is the most widely used method of deposition of conductive polymers on textiles due to its simplicity and low cost. The conductive polymer has to be soluble in a solvent that will not damage the fibers in which the conductive polymer is soaked. After the drying step, the coated fabric is obtained. By repeating the process, a greater coating thickness can be obtained, or different layers of different conductive polymers can be added as if it were the Layer-by-Layer (LbL) technique.[43] For example, Moraes et al.[45] coated polyamide 6,6 fibers with PEDOT:PSS and glycerol-doped PEDOT:PSS. In this work, they observed that the addition of glycerol not only doped the polymeric chain of PEDOT but also acted as a plasticizing additive. However, they were unable to control the uniformity of the coating. In fact, this is one of the main weak points

of coating textiles with conductive polymers by dip coating. The uniformity of the coating can generate areas where the conductive polymer is agglomerated in greater quantity. These areas can be a long-term point of debonding and delamination during textile processing or daily thermoelectric textile use.[23,43]

4.1.3.2 Vapor coating

Vapor-phase polymerization of conductive polymers is a technique that simultaneously combines the synthesis and deposition of conductive polymers in a single step.[46,47] This method allows for a uniform and thin coating on textile fibers. Thus, the mechanical properties of the coated fabric will be predominantly those of the pristine textile.[48,49] Two components are required for vapor phase polymerization: a monomer and an oxidant. The textile is generally impregnated with a solution containing the oxidizing salt, and then the fabric is exposed to the monomer vapors. Another way to coat the textile is through oxidative chemical vapor deposition (oCVD). The monomer and the oxidant are simultaneously introduced into the vapor phase and directed to the fabric's surface through this technique. In both methods, the exposed oxidant on the fiber surface reacts with the monomer producing reactive radical cations that become anchored to the fiber surface. These radical cations continue to react with the rest of the monomers, producing the polymer chain. Finally, the fabrics must be washed to remove excess oxidant.

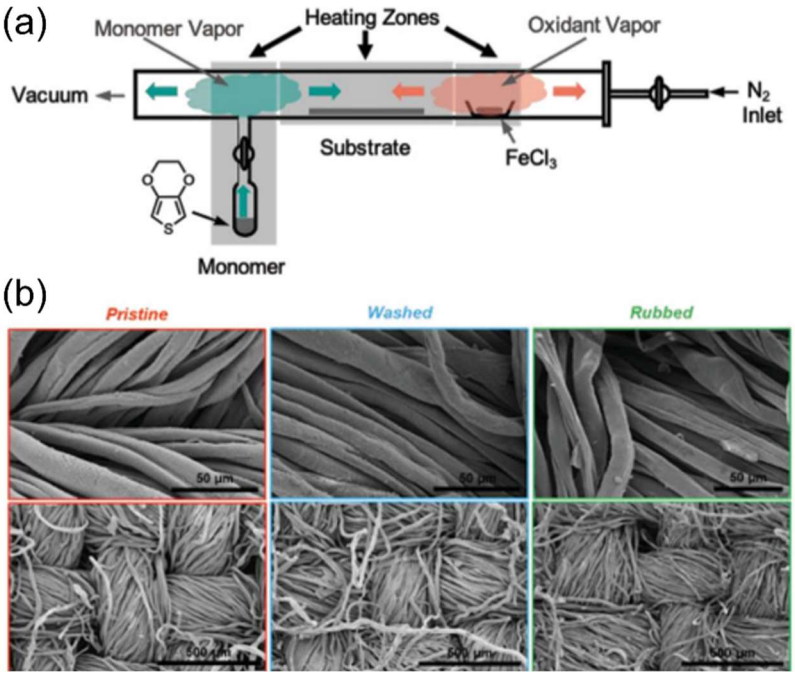

Figure 4.5 (a) Schematic process of oCVD. (b) SEM images after laundering and rubbering tests. Reprinted with permission.[41] Copyright 2019, Wiley-VCH Verlag GmbH & Co. KGaA, Weinheim.

In the work of Allison et al.,[41] cotton textiles were coated with PEDOT:Cl using the oCVD technique, **Figure 4.5(a)**. They conducted coating durability tests by rubbing or laundering the clothes in warm water, observing that the coating does not break or peel, **Figure 4.5(b)**. This is precisely one of the main advantages of the technique. Using vapor coating, uniformly coated textiles with high resistance to washing and wear are obtained.[43] Also, vapor-coated fabrics' electrical conductivity is typically higher than dip-coated fabrics.[50–52] The only drawback of this textile coating method is the high cost of scaling production to an industrial level.

4.1.3.3 *In-situ* solution polymerization

In-situ solution polymerization represents an alternative for those polymers, such as polypyrrole (PPy) and polyaniline (PANI), that cannot be stably formulated into conductive inks. In this case, the textile substrate is introduced into a solution containing the desired monomer and adding a solution of an oxidizing agent to initiate polymerization. In this way, once the polymerization reaction has started, part of the polymer generated in the reaction medium will adhere passively to the surface of the fibers. Zhang et al.[53] developed a near room-temperature *in-situ* interfacial polymerization method to obtain thermoelectric textiles with a core-shell structure. As a result, the fabrics showed a conductivity of 2.19 S cm^{-1} and a Seebeck coefficient of 14 μV K^{-1}.

Although the method is simple, a priori, it is difficult to control the mass transport during the polymerization reaction; therefore, control over the growth of the conductive coating is lost. This indicates that this method achieves a low degree of coating uniformity. The loss of uniformity has consequences regarding the stability of the coating on the textile fibers and the electronic properties of the final textile.[43]

4.1.3.4 Electrochemical coating

Electrochemical polymerization is another method in which synthesis and deposition take place simultaneously. In this method, the monomer is dissolved in an appropriate solvent with an electrolytic salt. An anodic current capable of oxidizing the monomer is applied to the working electrode.[54] Typically, the three-electrode configuration (working electrode, counter electrode, and reference electrode) is used. The fabrics acting as the working electrode must be conducive to the electrodeposition of conductive polymers on textiles. In general, textile substrates are insulating, and in order to carry out this method, different

approaches have been used to provide textiles with a certain conductivity. For example, Babu et al.[55] wrapped a graphite electrode with cotton fibers to electrodeposit polypyrrole. The electrochemical polymerization reaction begins on the graphite electrode, and as the polymer chain grows, it passively adheres to the textile fibers.

Most of the work published generates a thin prime layer on the textile fibers by immersion, polymerization in the vapor phase, or polymerization in solution to provide the fabric with a certain electrical conductivity. They then use this fabric with the prime layer as a working electrode where the growth of the coating from the coated fibers continues. In general, the uniformity of the electrodeposited conductive polymer coating will depend on the morphology of the underlying layer. For example, Maziz et al.[56] covered Lyocell cellulose yarns with a PEDOT primer layer via vapor phase polymerization and electrochemical deposition of polypyrrole on this fabric. SEM images revealed the high homogeneity of the coating.

In this chapter, we have developed a method for coating textiles with conductive polymers by electrodeposition. The adhesion of conductive polymers to flexible substrates is generally low,[42] and therefore, we first coated the fibers with carbon nanotubes (CNTs) using the Layer-by-Layer (LbL) technique. Compatibilizing agents used to disperse carbon nanotubes help make CNTs firmly adhere to textile fibers.[57] Once the fabric is coated with carbon nanotubes, it is possible to use it as a working electrode and carry out electrodeposition of conductive polymers.

4.2 Electrochemical synthesis of conductive polymers over fabrics

4.2.1 Materials

Aniline 99.5 %, pyrrole 98 %, poly (diallyl dimethylammonium chloride) (PDADMAC, $M_w = 10^5$ g mol^{-1}, 20 wt. % in water), and sodium deoxycholate (DOC, ≥ 97 % by titration) were purchased from Sigma-Aldrich. 3,4-Ethylenedioxytiophene (EDOT) 97 % lithium perchlorate ($LiClO_4$), and acetonitrile (ACN) were purchased from Alfa Aesar. Multiwalled carbon nanotubes (MWCNTs, 12−15 nm outer and 4 nm inner wall diameter, > 1 μm length, C ≥ 95 wt %) were obtained from Bayer MaterialScience (Leverkusen,

Germany). Sulphuric acid 96 % was obtained from VWR Chemicals. Felt fabric (made by polyester fibers) with a grammage 140 g m^{-2} and 0.8 mm of thickness was purchased from MW Materials World (Barcelona, Spain). All chemicals except felt fabric were used as received. The fabric was washed with ethanol in an ultrasound bath for 15 minutes.

4.2.2 Layer-by-Layer coating of felt fabrics with MWCNT

The felt fabric was coated with multiwalled carbon nanotubes (MWCNTs) by Layer-by-Layer deposition (LbL) to obtain a conductive material. Since the LbL technique is based on the electrostatic interaction between a positive and a negative charge, it is necessary to functionalize the surface of the carbon nanotubes to optimize the coating process. The functionalization of CNT can be of two types: covalent (chemical functionalization), which is based on the covalent bonding of the carbon nanotube with functional groups in the end caps or defects in their sidewalls;[58–60] and non-covalent (physical functionalization), which is capable of modifying the interfacial properties of carbon nanotubes through π–π or hydrophobic interactions.[58,61,62] Generally, chemical functionalization degrades the conjugated structure of the nanotubes since they tend to modify the hybridization of sp^2 to sp^3 and, therefore, decrease the electronic performance of the nanotubes.[58] For this reason, for the functionalization of nanotubes with positive and negative charges, a non-covalent method has been chosen using cationic and anionic tensioactive agents, respectively. Furthermore, for a better tensioactive – nanotube interaction, a mechanochemical method has been used to disperse the carbon nanotubes in water.[63]

Two MWCNT dispersions (0.05 wt%) were prepared in an aqueous medium using PDADMAC (0.25 wt%) as a cationic stabilizer and DOC (0.25 wt%) as an anionic stabilizer, respectively. First, the weighed quantity of carbon nanotubes and surfactant, together with 1 mL of low conductivity water, were introduced into the ball mill mortar, and a pre-dispersion was carried out by ball milling for 30 minutes, obtaining a mixture with a paste texture. Next, it was introduced into a beaker containing the rest of the water and homogenized in an ultrasound bath for 15 minutes. Then, the dispersions were ultrasonicated (10 min, ½ " tip, 90% amplitude, 1.0/0.1 s pulse/pause sequence) to obtain a homogeneous dispersion of the nanotubes in the aqueous medium. Once the cationic and anionic dispersions of the MWCNTs have been obtained, the ζ-potential is measured, obtaining values of (+32.6 ± 0.8) mV and (-45.2 ± 1.1) mV for the dispersions of MWCNT/PDADMAC and MWCNT/DOC, respectively. The ζ-potential values obtained

indicate that the carbon nanotubes with PDADMAC have a positive surface charge due to the cationic polyelectrolyte, and the MWCNTs with DOC have a negative surface charge due to the coating with the anionic surfactant. This difference in surface charge allows the Layer-by-Layer (LbL) method to coat textiles with MWCNT due to the electrostatic interaction between MWCNT/PDADMAC and MWCNT/DOC.

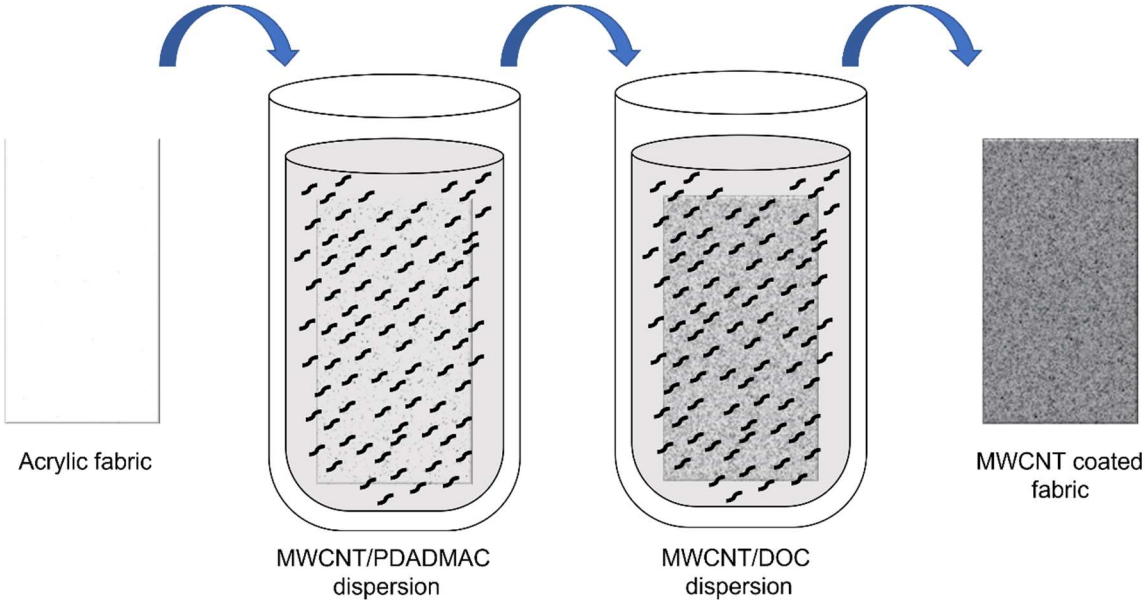

Figure 4.6 Schematic process of LbL coating of felt fabrics with MWCNT.

Once the nanotube dispersions had been prepared, the fabrics were coated as explained. Before coating with MWCNT, the fabrics were washed with ethanol in an ultrasonic bath for 15 min and allowed to dry at 50 °C overnight. Then, the fabrics were dipped in a solution of MWCNT/PDADMAC for 2 min, and finally, the fabric was washed with water and drained. Next, the fabric was immersed in a solution of MWCNT/DOC, and the non-attached elements were removed by several washing steps and drained. These two sequential depositions of MWCNTs, schematically depicted in **Figure 4.6**, correspond to one cycle called bilayer (BL).

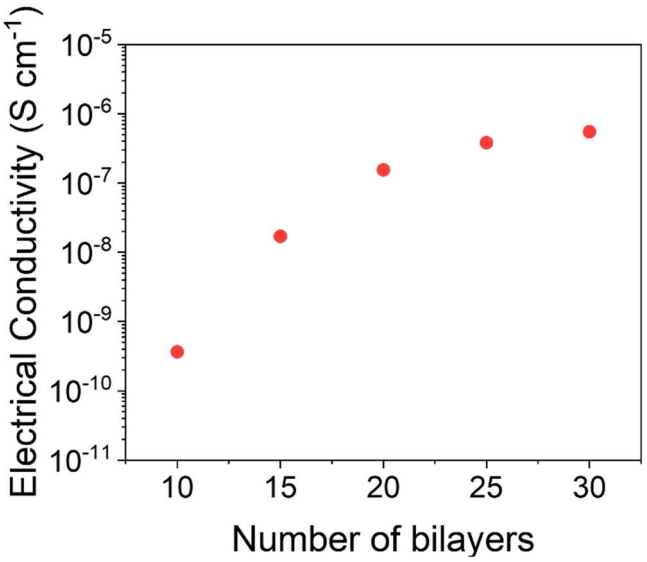

Figure 4.7 Electrical conductivity as a function of the number of bilayers of MWCNTs onto felt fabric.

The assembly of MWCNT bilayers (BLs) is controlled by the electrostatic interaction between PDADMAC and DOC. The electrical conductivity was evaluated as a function of the number of bilayers (from 10 to 30) deposited on the fabrics. **Figure 4.7** plot the electrical conductivity as a function of the number of MWCNT on the felt fabric. The electrical conductivity increases until 20 BLs and reaches a plateau at a value around 1.5 10^{-7} S cm^{-1}, presumably due to saturation. Since no significant improvement in the conductivity is observed after 20 BLs, we used this value in the subsequent electrodeposition experiments of conductive polymers on the fabrics.

4.2.3 Electrodeposition of conductive polymers

During electropolymerization, an electric current of known potential or intensity is passed through a solution containing the monomer, the dopant, and the solvent, inside an electrolytic cell. The coating of the conductive polymer is generated simultaneously by applying an anodic current that polymerizes the monomer over the working electrode. By controlling the synthetic parameters (potential, intensity, concentration), it is possible to control the quantity of polymer produced and obtain a high reproducibility of the properties.[64]

The general mechanism of electrochemical polymerization of conductive polymers consists of two stages. In the first one, cation radicals of the monomer are electrogenerated on the surface of the working electrode due to the current flow. The second stage is

nucleation, in which polymerization begins by polycondensation of cation radicals or by reactions of the cation radical with the monomer.[65–67]

The synthesis of poly (3,4-ethylenedioxythiophene) (PEDOT) and polypyrrole (PPy) on MWCNT–fabrics was carried out by electrochemical polymerization applying a constant current intensity of 6 mA during a different time. However, the electrosynthesis of polyaniline (PANI) was carried out using a constant voltage of 2 V. Therefore, the composition of the solutions for the electrosynthesis of the different conductive polymers is different. For the electrodeposition of PEDOT, a 0.01 M solution of EDOT and 0.1 M of $LiClO_4$ in acetonitrile were used. For the electrodeposition of PPy, the concentration of the monomer, pyrrole, was 0.1 M, and the dopant, $LiClO_4$, 0.1 M, in acetonitrile as solvent. The electrodeposition of PANI was carried out in an aqueous medium with a concentration of 0.5 M of aniline and 1.0 M of H_2SO_4.

Three electrodes formed the electrochemical cell: a counter electrode (platinum grid), a reference electrode (Ag/AgCl), and the MWCNT–fabric as the working electrode. Two clamps have been designed to hold the carbon nanotube coated textile to avoid contact between the electrochemical solution and the copper electrodes. For the electrodeposition of PEDOT and PPy, the MWCNT–fabric was placed between two pieces of polyethylene terephthalate–indium tin oxide (PET–ITO), one of them connected to a copper tape. Then, PET–ITO sheets with the fabric are held with a clamp, as shown in **Figure 4.8(a)**. In the case of PANI electrodeposition, it is impossible to use this clamp since the presence of sulfuric acid damages the ITO layer.[68] For this reason, for the electrosynthesis of PANI, the MWCNT-fabric was placed between two stainless steel sheets (**Figure 4.8(b)**), which on their external part have an insulating coating that inhibits polymerization and, therefore, electrochemical polymerization only occurs in the part of the steel that is in contact with the fabric. After polymerization, the MWCNT–fabric coated with conductive polymer was rinsed several times with acetonitrile and ethanol to remove the monomers that had not reacted.

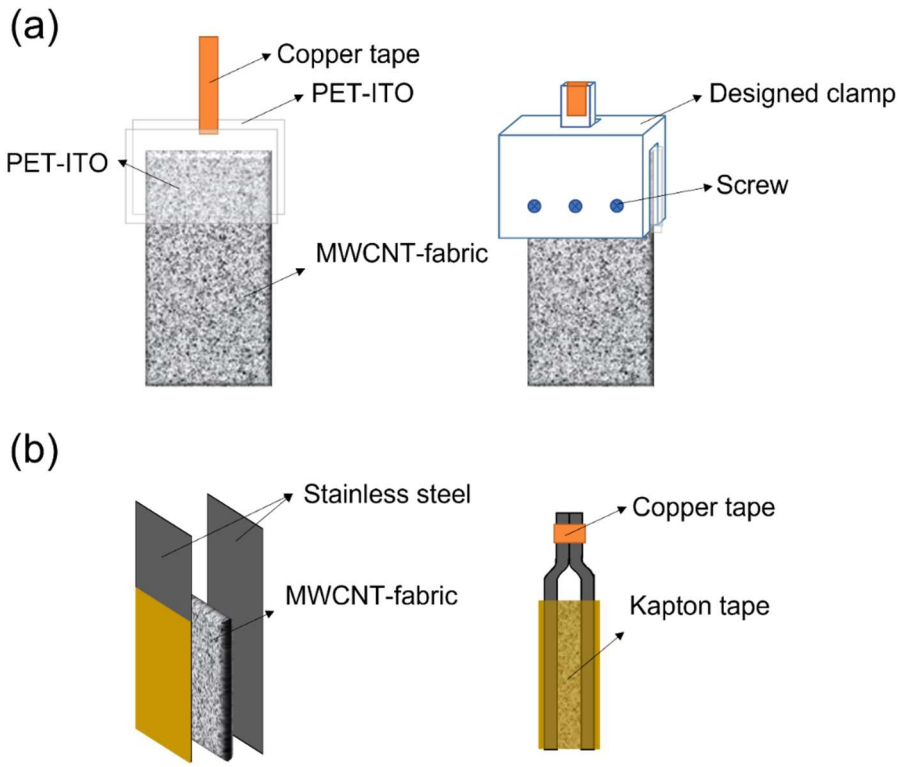

Figure 4.8 Clamps designed for (a) electrodeposition of PEDOT and PPy, and (b) electrodeposition of PANI on MWCNT coated fabrics.

4.2.4 Thermoelectric properties of fabrics

The prepared fabric-MWCNTs were coated with different conductive polymers by electropolymerization. For the synthesis of conductive polymers, static electrochemical techniques were used in which a constant intensity of current (chronopotentiometry) or voltage (chronoamperometry) is applied over time. In the case of the PEDOT and PPy deposition, chronopotentiometry was used, and chronoamperometry was used to synthesize PANI. The homogeneity of the coating of the fabrics with conductive polymers and their thermoelectric properties will depend on the polymerization time; therefore, it is necessary to determine the optimal value. For this, the electrical conductivity, the Seebeck coefficient, and the polymer mass deposited as a function of the polymerization time were followed, as shown in **Figure 4.9**.

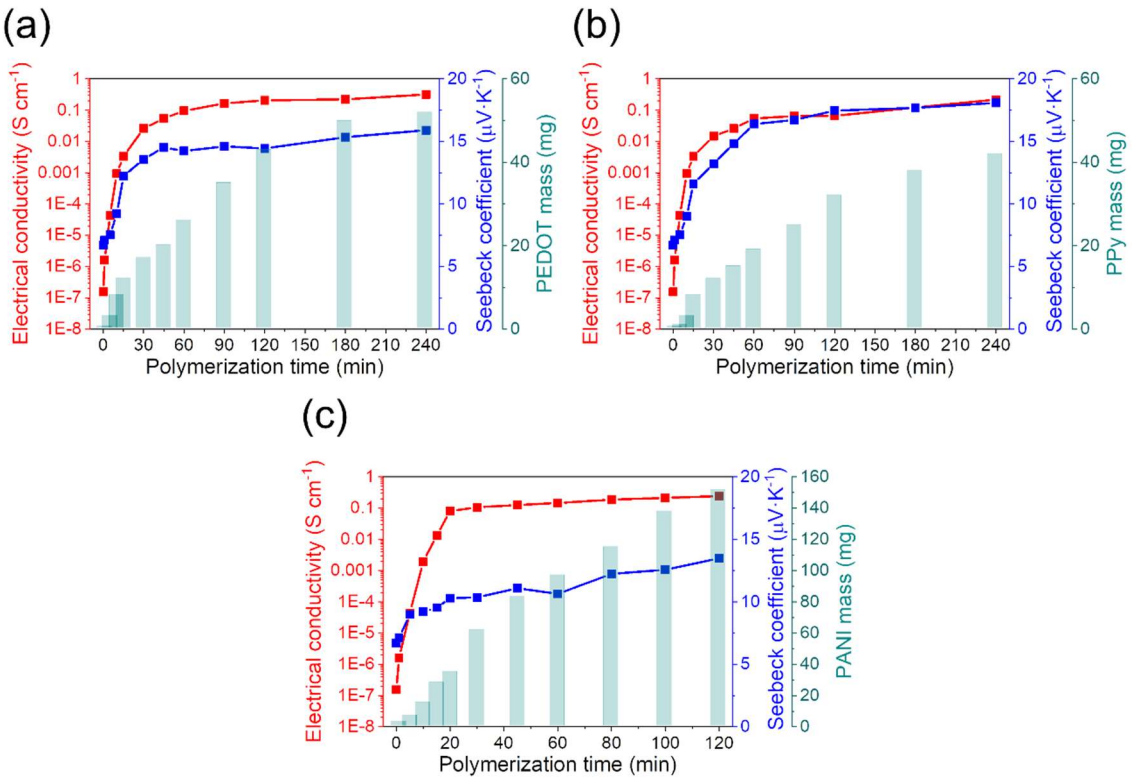

Figure 4.9 Electrical conductivity, Seebeck coefficient, and polymer mass deposition as a function of the polymerization time for (a) PEDOT:ClO_4, (b) PPy:ClO_4, and (c) PANI:H_2SO_4.

The general trend observed is that the deposited mass of conductive polymer on the MWCNT-fabric increases rapidly in the first moments of polymerization and finally stabilizes. This stabilization may be because new fragments of the generated polymeric chain do not remain adhered to the fabric and return to the heart of the solution. Regarding electrical conductivity, a similar trend can be observed, with a rapid increase in the first moments of polymerization and an electrical conductivity stabilization, although the mass of polymer deposited increases. The Seebeck coefficient also changes with the polymerization time with an initial value of 7 μV K^{-1}, which corresponds to the Seebeck coefficient of the fabric coated with MWCNTs. However, at higher polymerization times, the Seebeck coefficient achieves a stable value of around 15 μV K^{-1}, corresponding to a highly doped conductive polymer.[69]

The optimal polymerization time will be when the electrical conductivity and Seebeck coefficient are maximum with the minimum mass of conductive polymer deposited. This is important since a high amount of conductive polymer coating the felt fibers can impair the mechanical properties of the final fabric.[70] In the case of the PEDOT:ClO_4 and PPy:ClO_4 coatings, the values of electrical conductivity and Seebeck coefficient stabilize

after 60 minutes of electrochemical polymerization. Although the amount of mass deposited on the fabric increases at longer polymerization times, the thermoelectric properties do not. In this way, an optimal value is reached after 60 minutes of deposition with an electrical conductivity of 0.1 S cm^{-1} and a Seebeck coefficient of 14.5 μV K^{-1} for the PEDOT:ClO_4 coating and electrical conductivity of 0.05 S cm^{-1} and Seebeck coefficient of 16.4 μV K^{-1} for the PPy:ClO_4 coating. A similar trend is found in the case of the electrochemical deposition of polyaniline. In this case, after 20 minutes of polymerization, a plateau is reached in the thermoelectric properties despite the deposited mass of PANI increases. The electrical conductivity was 0.08 S cm^{-1}, and the Seebeck coefficient was 12.3 μV K^{-1}. Therefore, the highest thermoelectric efficiency is for PEDOT:ClO_4 with a Power Factor of 2.1 10^{-3} μW m^{-1} K^{-2}.

4.2.5 Morphology of thermoelectric fabrics

Once the felt fabrics are covered with the carbon nanotubes and the different conductive polymers, the morphology is observed by scanning electron microscopy (SEM), **Figure 4.10**. The pristine fabric has a practically smooth surface. After the deposition of multiwalled carbon nanotubes by LbL, the surface of the fibers becomes rougher. Even at higher magnifications, tiny threads can be observed, which correspond to the MWCNTs and amorphous agglomerates due to the interaction between the PDADMAC and DOC. Once the fabric fibers are coated with MWCNTs, the fabric acquires a certain electrical conductivity, as shown in **Figure 4.7,** and, therefore, it is possible to electrodeposit conductive polymers on the fibers. After the electrodeposition of PEDOT:ClO_4, it is observed that the polymer is distributed around the felt fibers coated with MWCNTs with a globular morphology, typical of conductive polymers obtained by electrochemical deposition.[71,72] The electrodeposition of PPy:ClO_4 also takes place around the fibers of Felt-MWCNTs, but a lower degree of coating can be seen since a greater number of uncoated areas are observed. Similar to PEDOT:ClO_4, polypyrrole also depicts a globular morphology. After the electrochemical deposition of PANI:H_2SO_4, it is observed that the coating of the fibers is not homogeneous, and even at high magnifications, the exfoliation of the layer of MWCNTs deposited on the felt yarn can be seen. This may be due to the presence of sulfuric acid during the electrochemical polymerization process, which degrades the felt fabric in acid conditions.[43,73]

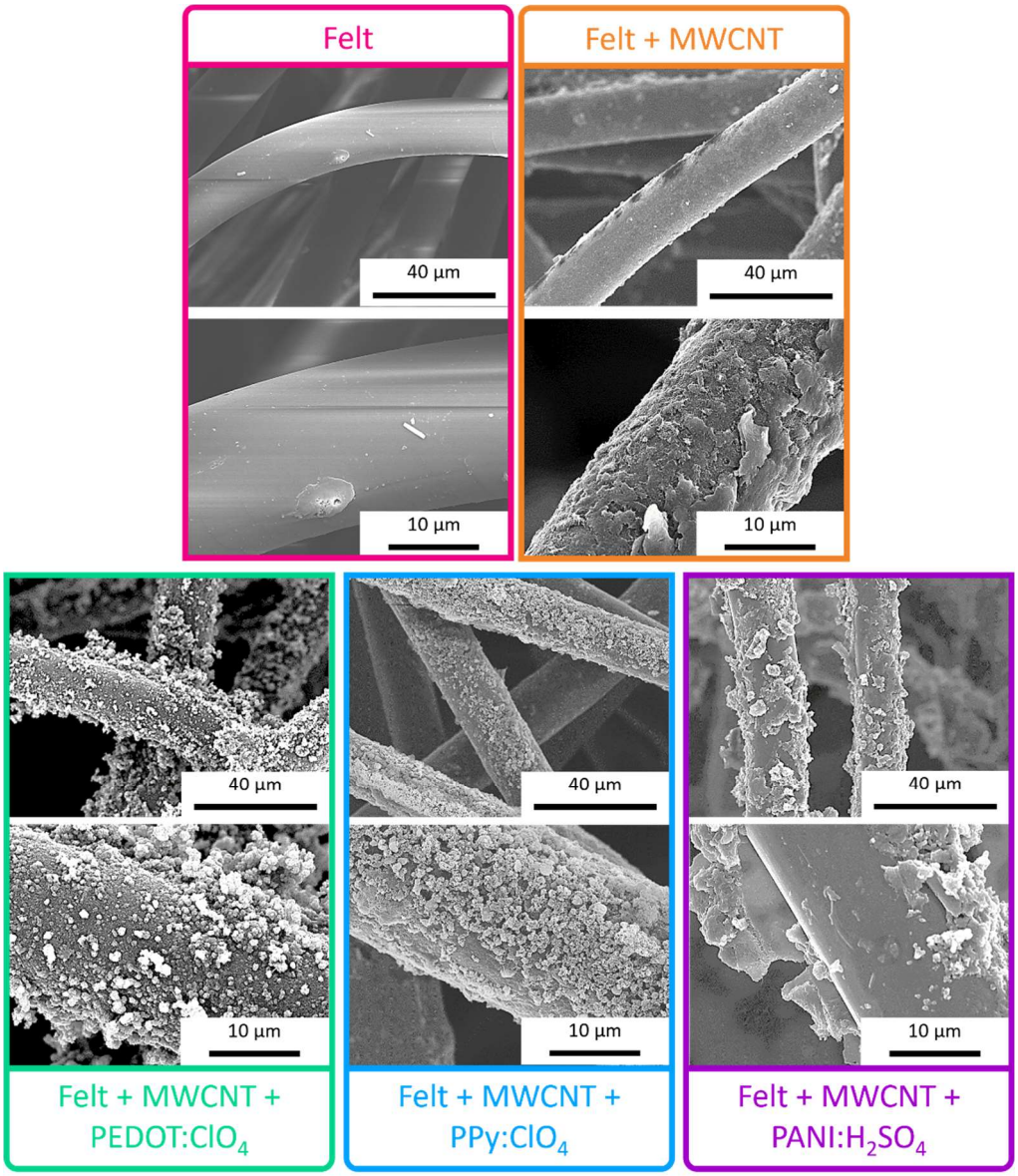

Figure 4.10 SEM images of uncoated felt fabric, felt-MWCNTs fabric, and felt-MWCNTs-PEDOT:ClO_4, felt-MWCNTs-PPy:ClO_4, felt-MWCNTs-PANI:H_2SO_4 fabrics.

4.2.6 Raman spectroscopy measurements

Raman spectroscopy gives information about the composition of the coating of felt fibers. **Figure 4.11** shows the Raman spectra of the pristine fabric and the fabric with the different coatings. The main peaks of each sample have been marked with points. The assignation of peaks is detailed in **Table 4.1**.

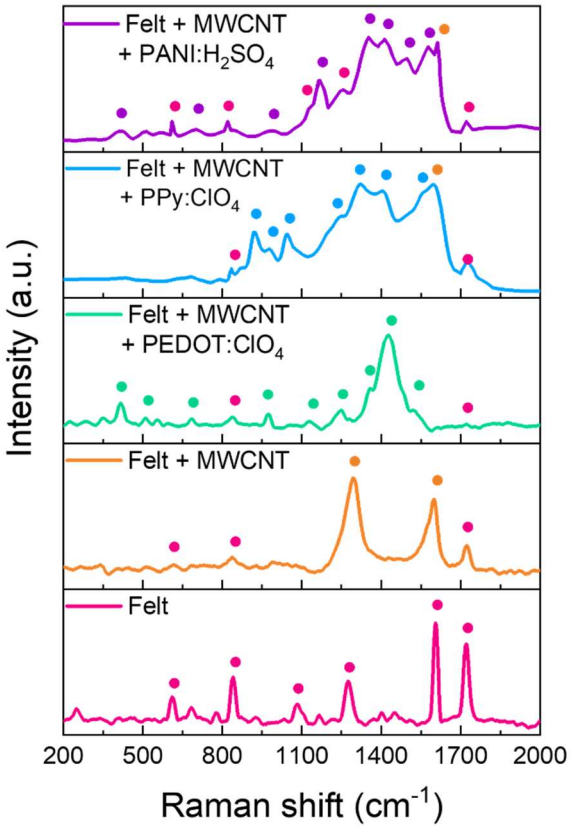

Figure 4.11 Raman spectra of felt fabric coated with MWCNTs and after polymer electrodeposition.

Raman spectra of the felt fabric present the typical peaks of polyester, including an aromatic ring in its monomeric unit since two intense peaks appear at 1604 and 1720 cm^{-1}, corresponding with the stretching of the aromatic ring and the carbonyl group, respectively. When the fibers are coated with MWCNTs by LbL, the Raman spectra show the D and G bands. The first is related to the disorder in sp^2-hybridized carbon systems, and the second is related to sp^2 vibrations of the graphite crystal and associated with an ordered graphitic structure.[74] However, small peaks related to some felt fibers are also observed. This indicates that the coating of the fibers with MWCNTs is not completely homogeneous. After the electrodeposition of PEDOT:ClO_4, the residual peaks of the felt fabric decrease in intensity, and practically only the peaks related to the PEDOT polymer chain are observed, see **Table 4.1**. On the other hand, after the electrodeposition of PPy:ClO_4, the peaks corresponding to the polypyrrole polymer chain are observed, together with some residual peaks of felt and MWCNTs. Coating the felt fibers-MWCNTs with PANI:H_2SO_4 shows a Raman spectrum in which the peaks corresponding to the PANI polymeric chain are present and numerous peaks corresponding to the felt fibers.

Table 4.1 Assignation of Raman modes for each material.

	Raman Shift (cm^{-1})	Assignation
Felt	610	C–C aliphatic chain stretching
	840	Symmetric C–O–C deformation
	1082	Asymmetric C–O–C deformation
	1274	C–C aliphatic chain stretching
	1604	Aromatic ring stretching
	1720	C=O stretching of the ester group
MWCNT	1297	D-band
	1597	G-band
PEDOT:ClO_4	420	oxyethylene ring stretching
	560	oxyethylene ring stretching
	690	symmetric C–S–C deformation
	980	oxyethylene ring stretching
	1120	symmetric C–O–C deformation
	1247	C_α–C_α (inter-ring) stretching
	1356	C_β–C_β stretching
	1431	Symmetric stretching of C_α= C_β(–O)
	1486	Asymmetric stretching of C=C
	1524	Asymmetric stretching of C=C
PPy:ClO_4	918	Ring deformation of bipolarons
	985	Ring deformation of polarons
	1040	C–H in-plane deformation
	1240	C=C stretching
	1323	Ring-stretching mode
	1405	C–N stretching
	1557	Symmetric stretching of aromatic C=C ring
PANI:H_2SO_4	410	In-plane bending of benzenoid ring
	700	In-plane bending of quinoid ring
	984	C–H in-plane bending of benzenoid ring
	1168	C–H bending deformation of benzenoid ring
	1352	C-N^+ stretching
	1412	C–N stretching amine
	1497	C=N stretching imine
	1577	C=C stretching of quinoid structure

These results suggest that the electrochemical coating of the fibers with PEDOT is the most homogeneous since the presence of peaks derived from the felt fabric is residual. On the other hand, the electrodeposition of PANI on the fibers is the one that gives the worst

result since the presence of felt peaks is detected. Furthermore, these results agree with the SEM images in **Figure 4.10**. Therefore, we can affirm that the strategy used is suitable for the electrochemical coating of felt fibers with PEDOT and PPy, but not for PANI since there is an exfoliation of the coating on the fibers that can be a severe drawback for its use in wearable thermoelectric devices.

4.2.7 Thermal stability

Another important parameter is the thermal stability of the fabrics obtained. This parameter was studied through thermogravimetric analysis (TGA) of the felt, and the felt after the different coatings. **Figure 4.12** shows the thermogram of the different samples analyzed.

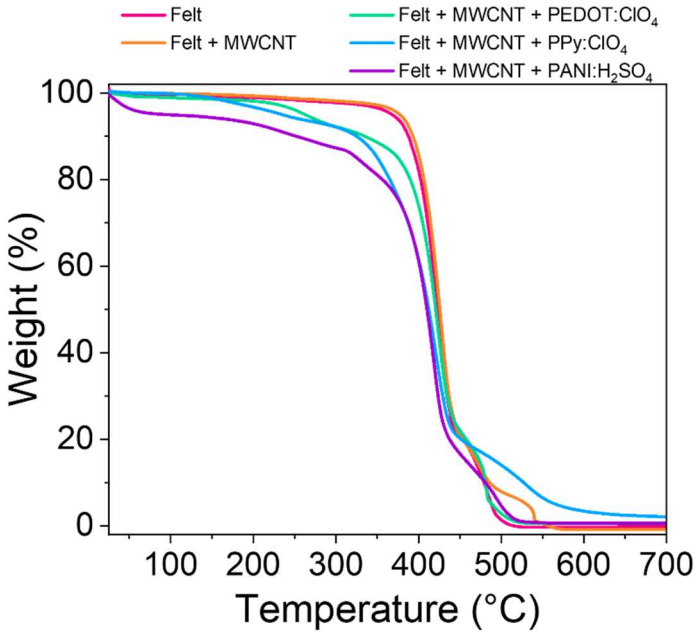

Figure 4.12 TGA curves of pristine felt fabric and the felt fabric coated with MWCNT, PEDOT:ClO_4, PPy:ClO_4, PANI:H_2SO_4.

The pristine felt shows an abrupt drop at 450 ºC due to the decomposition of the polymeric chains.[75] After coating the fibers with multiwall carbon nanotubes, the thermal stability of the textile increases slightly since the decomposition start temperature at 5% loss weight ($T_{5\%}$) increases practically 10 ºC (**Table 4.2**).[76] However, the electrochemical coating of felt-MWCNTs fibers with conductive polymers decreases the thermal stability of the fabric. Coating the fibers with PEDOT:ClO_4 and PPy:ClO_4 reduces the decomposition initiation temperature by approximately 100 and 130 ºC, respectively, compared to the pristine fabric. These results suggest that electrosynthesis reduces its

thermal stability by coating felt fabrics with PEDOT:ClO_4 and PPy:ClO_4. However, the decomposition starting temperature of the fabrics coated with these conductive polymers is above the range of use of the fabrics as thermoelectric materials without being a serious drawback.

Table 4.2 Weight loss temperature at different percentages and residue percentages at 700 ºC of pristine felt fabric and the felt fabric coated with MWCNT, PEDOT:ClO_4, PPy:ClO_4, PANI:H_2SO_4.

	Felt	**Felt + MWCNT**	**Felt + MWCNT + PEDOT:ClO_4**	**Felt + MWCNT + PPy:ClO_4**	**Felt + MWCNT + PANI:H_2SO_4**
$T_{5\%}$ (ºC)	367.65	376.85	262.22	234.39	91.87
$T_{10\%}$ (ºC)	387.51	393.02	334.41	324.54	251.39
$T_{20\%}$ (ºC)	402.33	406.45	389.81	365.05	355.95
$T_{30\%}$ (ºC)	411.02	414.41	404.90	387.32	387.70
$T_{40\%}$ (ºC)	417.45	420.40	413.88	401.99	401.25
$T_{50\%}$ (ºC)	422.87	425.65	420.59	412.31	410.09
$T_{60\%}$ (ºC)	427.91	430.68	426.71	420.69	417.00
$T_{70\%}$ (ºC)	433.93	436.84	434.19	429.13	423.59
$T_{80\%}$ (ºC)	452.84	453.28	457.64	451.20	437.39
$T_{90\%}$ (ºC)	479.08	486.04	480.68	527.04	480.87
$T_{95\%}$ (ºC)	487.97	530.56	488.68	498.77	482.07
Residue % (700 ºC)	0	0	0.56	2.068	0.669

On the other hand, coating with PANI:H_2SO_4 drastically reduces the decomposition initiation temperature to 92 ºC. This result and the exfoliation observed in the SEM images (**Figure 4.10**) indicate that the felt fabric is partially degraded during the PANI:H_2SO_4 electrochemical deposition process. Therefore, the decomposition initiation temperature is just at the limit of the range of applicability of these fabrics as thermoelectric materials.

4.3 Electrochemical Synthesis of an Organic Thermoelectric Power Generator

In the previous section, the electrodeposition process of conductive polymers on a felt textile has been optimized, with the PEDOT:ClO_4 coating the one that provides the best

thermoelectric properties and thermal stability. Therefore, in this section, a thermoelectric generator will be made using two textiles (felt and cotton) with a PEDOT:ClO_4 coating.

4.3.1 Materials

Poly (diallyl dimethylammonium chloride) (PDADMAC, $M_w = 10^5$ g mol^{-1}, 20 wt. % in water), and sodium deoxycholate (DOC, ≥ 97 % by titration) were purchased from Sigma-Aldrich. 3,4-Ethylenedioxytiophene (EDOT) 97 % lithium perchlorate ($LiClO_4$), and acetonitrile (ACN) were purchased from Alfa Aesar. Multiwalled carbon nanotubes (MWCNTs, 12−15 nm outer and 4 nm inner wall diameter, > 1 μm length, C ≥ 95 wt %) were obtained from Bayer MaterialScience (Leverkusen, Germany). Cotton fabric 400 with a grammage of 100 g m^{-2} was purchased from Testfabrics Inc. (West Pittston PA, USA). Felt fabric (made by polyester fibers) with a grammage 140 g m^{-2} and 0.8 mm of thickness was purchased from MW Materials World (Barcelona, Spain). All chemicals except fabrics were used as received. The fabrics were washed with ethanol in an ultrasound bath for 15 minutes.

4.3.2 Layer-by-Layer Assembly of MWCNT over fabrics

Cotton and felt fabric materials were coated with MWCNTs by Layer-by-Layer deposition to obtain a conductive material. The coating of the fabric surface followed the procedure schematically depicted in **Figure 4.13**. MWCNT suspensions were stabilized either with poly(diallyldimethylammonium chloride) (PDADMAC, cationic polyelectrolyte) or with sodium deoxycholate (DOC, anionic surfactant).[77] The assembly of MWCNT bilayers (BLs) is controlled by the electrostatic interaction between these two oppositely charged substances. The cotton and felt fabrics were coated with 10, 15, 20, 25, and 30 BLs to optimize the MWCNTs coating process.

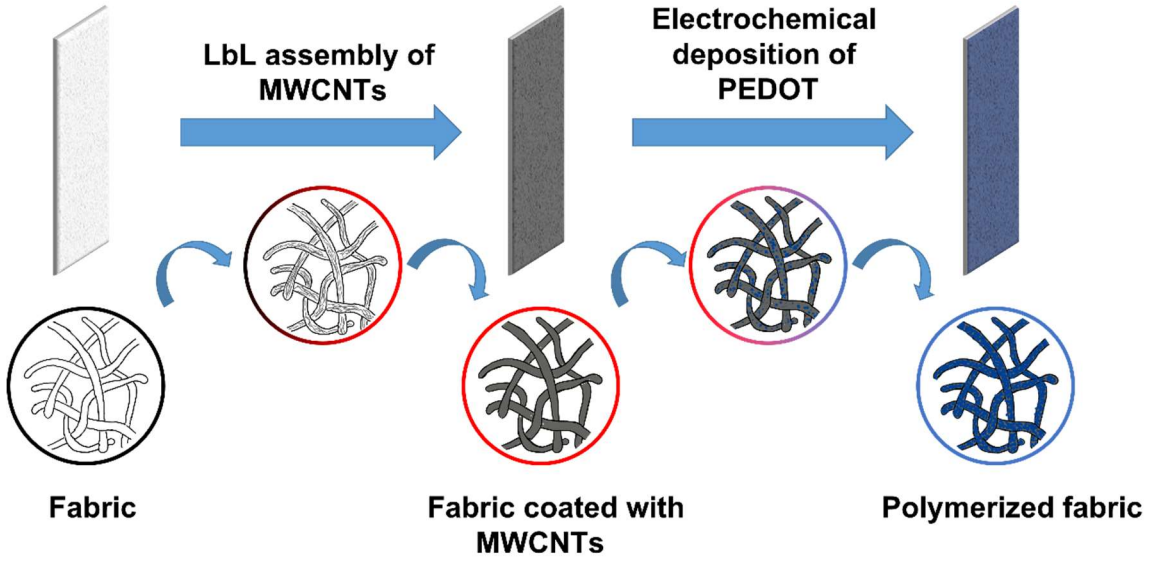

Figure 4.13 Schematic representation of the preparation of PEDOT by electrochemical deposition on fabric substrates coated with carbon nanotubes through Layer-by-Layer (LbL).

The results in **Figure 4.14** indicate that the conductivity increases until 20 BLs and reaches a plateau afterward, presumably due to saturation. The cotton fabric achieved a plateau after 20 BLs with a conductivity of 2.03 10^{-6} S cm^{-1}, while the felt fabric reached the plateau at the same number of BLs but with an electrical conductivity of 1.5 10^{-7} S cm^{-1}. Since no improvement in the conductivity is observed after 20 BLs, we used this number of layers in the subsequent experiments of polymerization of EDOT on the fabrics.

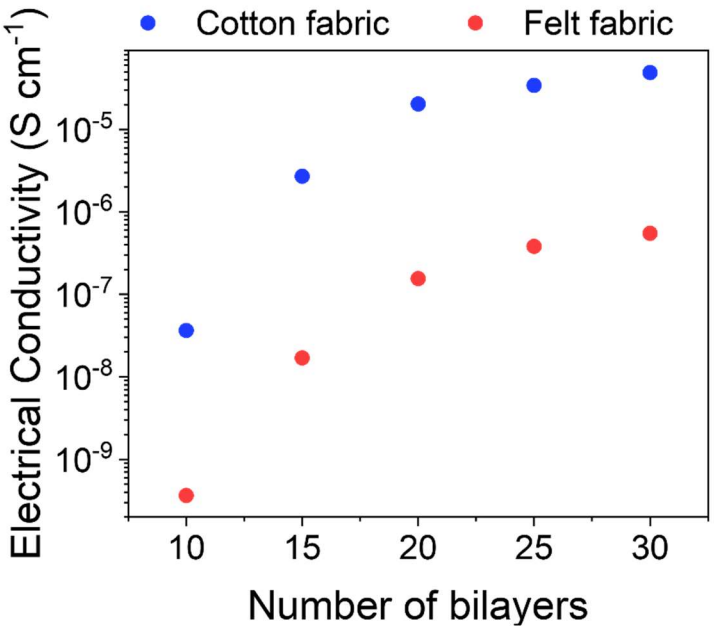

Figure 4.14 Electrical conductivity as a function of the number of bilayers of MWCNTs onto cotton and felt fabrics.

4.3.3 Electrosynthesis of PEDOT:ClO_4 on MWCNT-fabrics

The synthesis of PEDOT on MWCNT–fabrics was carried out by electrochemical polymerization applying a current intensity of 6 mA for 1 h using a solution containing EDOT (0.01 M) and LiClO4 (0.1 M) in acetonitrile. Three electrodes formed the electrochemical cell: a counter electrode (platinum grid), a reference electrode (Ag/AgCl), and the MWCNT–fabric, the latter used as the working electrode. The working electrode was assembled as follows to avoid contact between the electrochemical solution and the copper electrodes: the MWCNT–the fabric was placed between two pieces of polyethylene terephthalate–indium tin oxide (PET–ITO), one of them connected to a copper tape. Then, PET–ITO sheets with the fabric in between, held with a clamp. After polymerization, the MWCNT–PEDOT fabric was rinsed several times with acetonitrile and ethanol.

The electropolymerization of EDOT was achieved using the MWCNT-coated fabric as a working electrode and applying a current intensity to the working electrode (MWCNT–fabric).[77] The polymerization mechanism proceeds as follows. Two monomer radicals are initially generated through electrochemical oxidation. Subsequently, the radicals react with each other, forming a dimer and releasing two protons. New electrochemical oxidation forms oligomeric radicals, which results in the polymer reacting successively with other oligomeric or monomeric radicals. The electrochemical polymerization of EDOT on the fabrics is also shown in the representation of **Figure 4.13**. LbL assembly of MWCNTs by electrostatic interactions was used to coat the fabrics, followed by the electrochemical synthesis of PEDOT:ClO_4. At the beginning of the electrochemical deposition, small polymer nuclei form and serve as centers from which the conductive coat grows.

4.3.4 Raman and FTIR spectroscopy analysis

The infrared spectra (FTIR) of cotton, **Figure 4.15(a)**, show the typical vibrational modes of the cellulose structure, ν O–H at 3310 cm^{-1} and ν C–O–C at 1315 cm^{-1}. The successive coating with MWCNTs and PEDOT decreases the intensity of the cotton peaks. In the infrared spectra of the felt fabric (**Figure 4.15(b)**), based on polyester, a sharp peak is observed at 1715 cm^{-1}, ascribed to the presence of the carbonyl group. Two peaks at 1250 and 1100 cm^{-1} can be attributed to the symmetric and asymmetric stretching of the ester group.

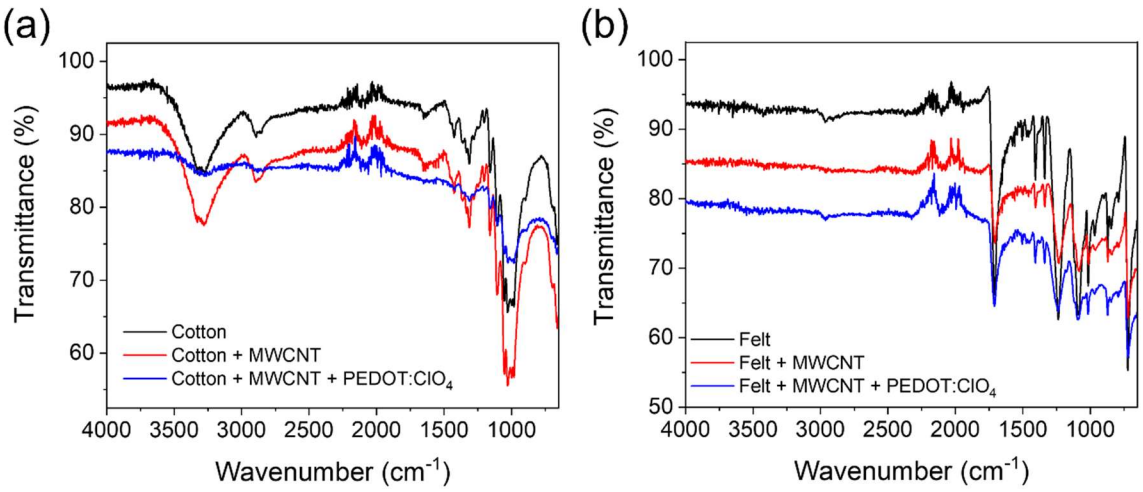

Figure 4.15 FTIR spectra of pristine fabrics, coated with MWCNTs and after EDOT polymerization for (a) cotton and (b) felt fabrics.

The effect of the different coatings was analyzed by Raman spectroscopy (**Figure 4.16**). Spectra corresponding to cotton fabric substrates shows two regions of signals: 1750–800 cm^{-1} and 610–200 cm^{-1}. The bands in the first region are related to skeletal, symmetric, and asymmetric glycosidic ring breathing (at 1040 and 1128 cm^{-1}), methylene (CH_2) bending, rocking, and wagging (at 1508, 1460, 1356, and 969 cm^{-1}).[78,79] The second region is given by CCC and COC ring deformation (at 478, 394, 355, and 310 cm^{-1}).[80] Spectra of felt substrates present different vibrational modes at 610 and 1274 cm^{-1} related to the C–C aliphatic chain vibration. The peaks at 840 cm^{-1} and 1082 cm^{-1} correspond to the symmetric C–O–C deformation and asymmetric C–O–C deformation, respectively; the peak at 1604 cm^{-1} is related to the aromatic ring vibration; and, finally, the peak at 1720 cm^{-1} corresponds to the carbonyl vibration of the ester group. After the coating process of the fabrics with the carbon nanotubes, the intensity of the Raman peaks related to the fabrics decreased, and appeared the peaks corresponding to the MWCNTs. The D-band at around 1300 cm^{-1} is ascribed to the presence of disorder in sp^2-hybridized carbon systems. The peak around 1600 cm^{-1} is related to the G-band, which corresponds to sp^2 vibrations of the graphite crystal and is associated with an ordered graphitic structure.[74] Finally, after the electrodeposition of PEDOT, the Raman intensity of the peaks related to the fabrics and the MWCNTs decreased. Therefore, the Raman peaks observed are mainly attributed to the vibrational modes of PEDOT. Peaks at around 420, 560, and 980 cm^{-1} are related to the vibrational modes of the oxyethylene ring. The symmetric C–S–C and C–O–C deformation appears at 690 and 1120 cm^{-1}, respectively. The C_α–C_α (inter-ring) and C_β–C_β stretching modes are located at 1252 and 1363 cm^{-1}, each one. The peak at 1430 cm^{-1}

corresponds to the symmetric stretching mode $C_\alpha = C_\beta(-O)$ and the asymmetric stretching of C=C appears into two Raman peaks at 1490 cm^{-1} (overlapped with the previous peak) and 1530 cm^{-1}.[81] These spectra indicate that all fabrics were well-coated with MWCNTs and PEDOT.

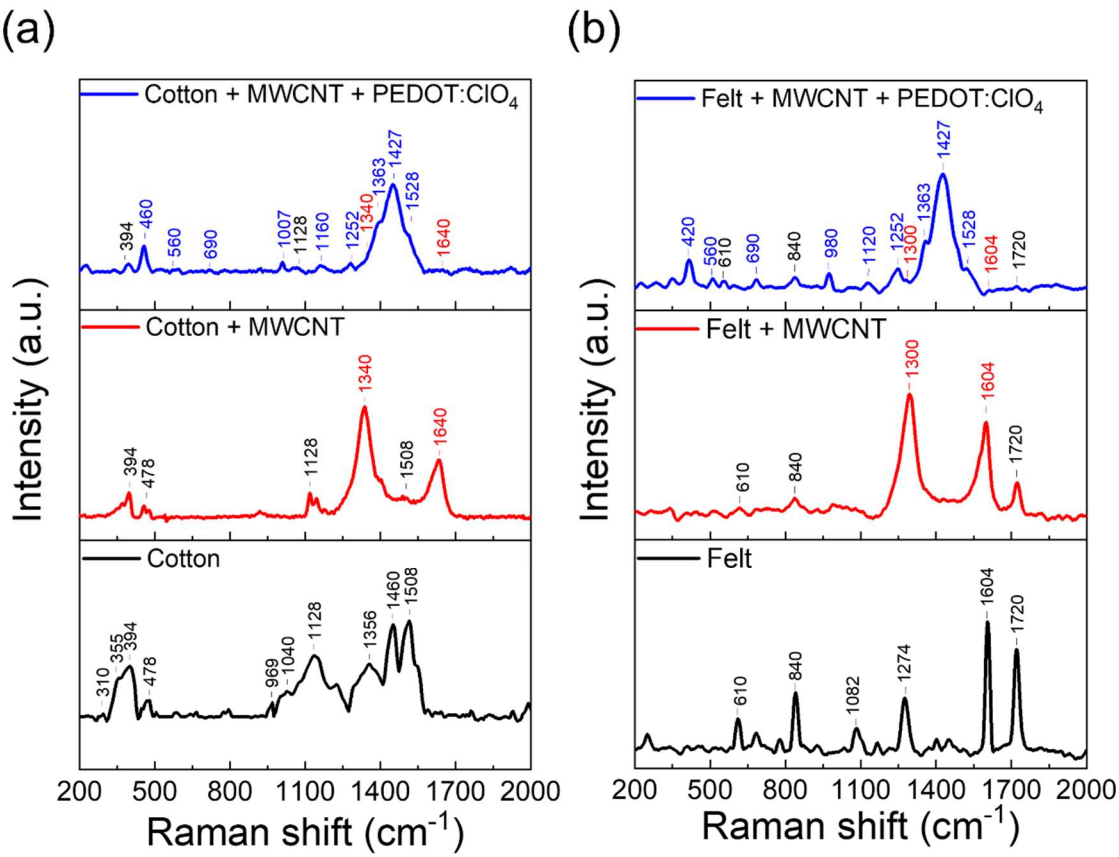

Figure 4.16 Raman spectra of fabric substrates coated with MWCNT and after PEDOT deposition based on (a) cotton and (b) felt fabrics.

4.3.5 Morphology of PEDOT coating

The morphology of the PEDOT deposited on the fabrics was studied by scanning electron microscopy (SEM). Micrographs of both fabrics (**Figure 4.17**) show that, after deposition, MWCNTs were homogeneously distributed around the fibers, as judged by the lack of agglomerates. Some bridges observed between fabrics correspond to MWCNTs that electrically connect the fibers. After electrodeposition of PEDOT on the fabrics covered with MWCNT, the polymer is homogeneously distributed around the fabric. SEM images indicate that PEDOT is not only deposited on the superficial layer but also on most of the internal fibers. PEDOT depicts globular, typical of the electrochemical deposition of conductive polymers using the chronopotentiometry method.[71,72,81]

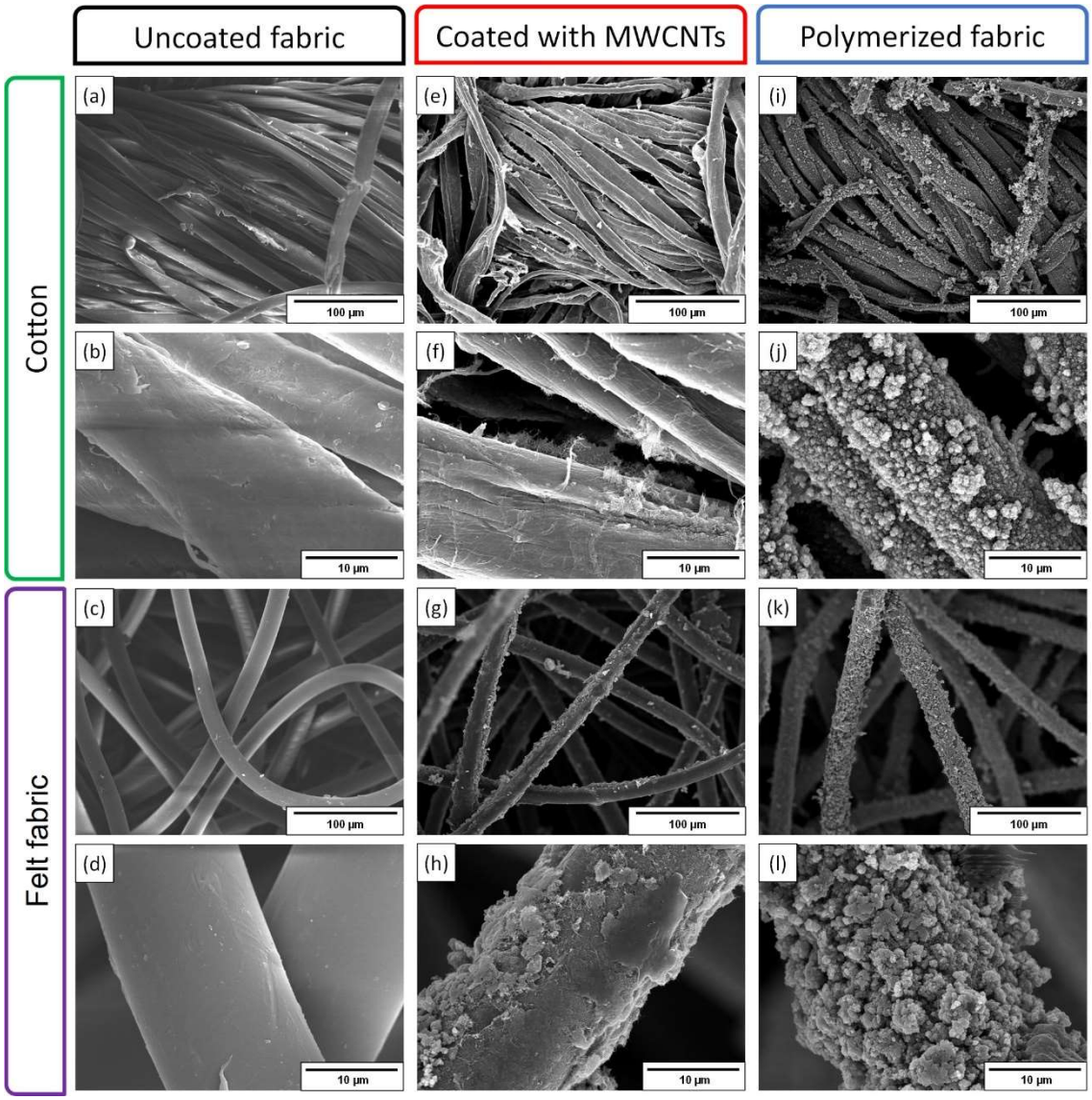

Figure 4.17 SEM images of uncoated fabrics (a–d), coated with MWCNTs (e–h), and after EDOT polymerization (i–l).

4.3.6 Thermoelectric properties of PEDOT-coated fabrics

The electrical conductivity and the Seebeck coefficient of the fabrics were determined through the plane because the designed thermoelectric generator required it. Dielectric relaxation spectroscopy measured the electrical conductivity through the plane, in which the sample was introduced between two gold electrodes. The real component of the complex conductivity $\sigma' = \sigma_{ac}$ (S cm^{-1}) of the fabrics covered with MWCNTs and PEDOT was determined as a function of frequency at room temperature, as shown in **Figure 4.18** for cotton and felt fabrics. The electrical conductivity of fabric samples without coating increases as a function of the frequency from 10^{-11} to 10^{-7} S cm^{-1} in the case of cotton and from 10^{-15} to 10^{-9} S cm^{-1} for felt samples, reflecting the dipole polarization contribution

to macroscopic conductivity. After the deposition of 20 BLs of MWCNTs onto the fabric samples, the electric conductivity increases, reaching a constant value independent of the frequency, reflecting that polarization due to charge migration is dominant. The electrical conductivity of cotton and felt fabrics coated with MWCNT was $2.03 \cdot 10^{-5}$ S cm^{-1}, and $1.55 \cdot 10^{-7}$ S cm^{-1}, respectively. Then, PEDOT was deposited by electrosynthesis onto fabrics covered by 20 BLs of MWCNTs, increasing the conductivity by 5 and 6 orders of magnitude for cotton and felt fabrics, respectively, compared to fabrics covered with only MWCNTs. The electrical conductivity of cotton and felt fabrics after PEDOT electrodeposition was 4.18 S cm^{-1}, and 0.318 S cm^{-1}, respectively. The big increase in the electrical conductivity results from the presence of PEDOT, which acts as an electrical connector between the fibers covered with MWCNTs, making a highly electrically conductive fabric network. Nevertheless, the higher thickness of the felt fabric compared to the cotton fabrics can be responsible for the differences observed in the conductivity values of both samples. The higher number of interfaces and boundaries in felt fabric affect electric transport through the sample, being lower than the cotton fabric.

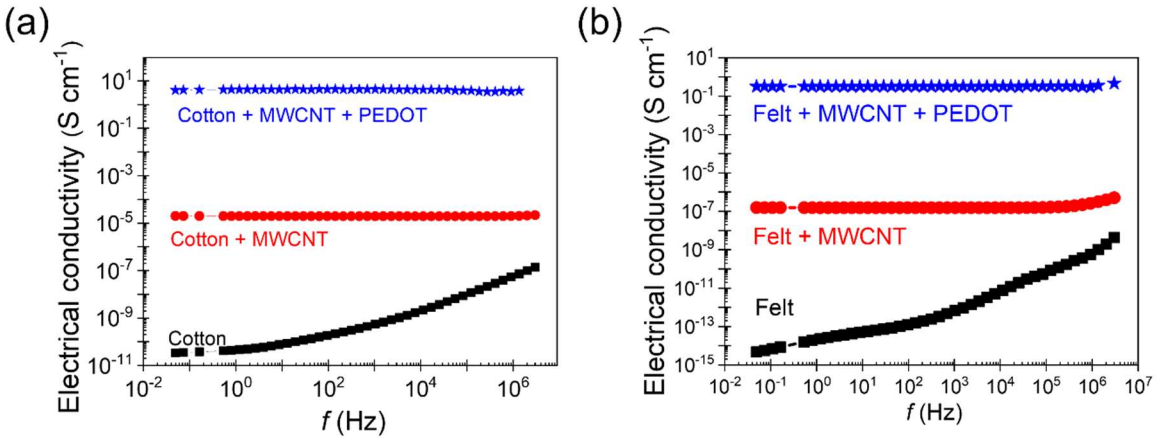

Figure 4.18 Electrical conductivity at room temperature as a function of the frequency for (a) cotton, and (b) felt fabrics, coated with MWCNTs, and after EDOT polymerization.

The Seebeck voltage, **Figure 4.19**, was measured as a function of the temperature gradient through the plane for the fabrics coated with MWCNTs and MWCNTs/PEDOT. It should be noted that the Seebeck coefficient of the uncoated fabrics could not be measured due to their insulating nature. For the case of the fabrics coated with MWCNTs, the Seebeck coefficient was 9.7 μV K^{-1} and 6.7 μV K^{-1} for cotton and felt fabrics, respectively. After PEDOT deposition by electrochemical polymerization, the Seebeck coefficient of the fabrics increases until values around 15 μV K^{-1}. These values are very similar to typical ones of PEDOT films and other fabrics coated with PEDOT,[82–87]

evidencing that the whole fabric is coated by PEDOT, which is consistent with the SEM observations (**Figure 4.17**).

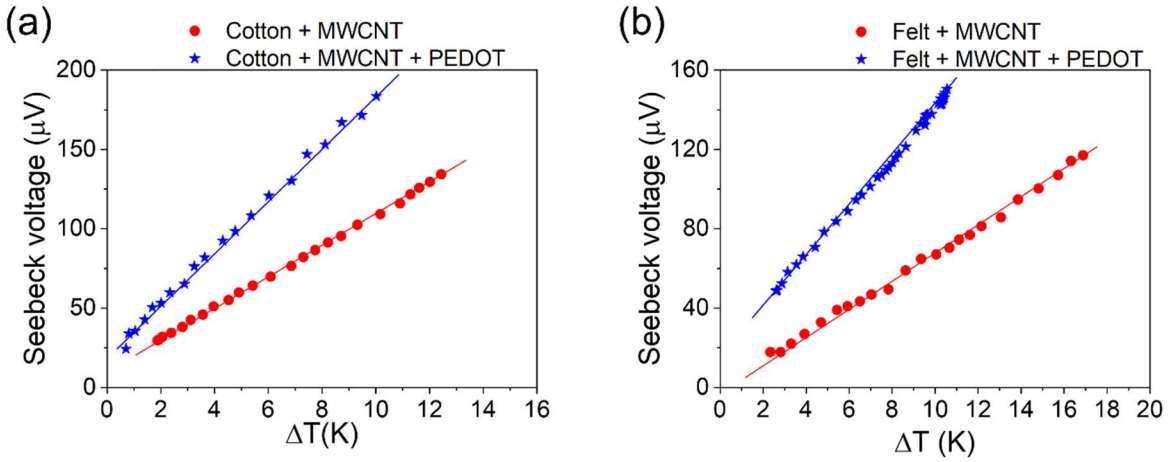

Figure 4.19 Seebeck coefficient (a) cotton, and (b) felt coated with MWCNTs, and after EDOT polymerization.

4.3.7 Torsion and bending test

In developing fabric-based wearable thermoelectric devices, it is essential to assess their flexibility to guarantee their stability during daily use. Therefore, the normalized electrical conductivity of the fabrics coated with MWCNTs and PEDOT were evaluated as a function of torsion and bending tests. For this purpose, five twisting cycles were carried out. The corresponding data, shown in **Figure 4.20**, indicates that the electrical conductivity increases as the torsion angle increases due to the interconnection improvement between the fibers of the fabrics. This increase is more remarkable in the case of felt fabric, which can be correlated with a decrease in the number of boundaries while twisting. The electrical conductivity only decreases as the torsion cycles vary due to the wear that this causes on the fabric. Bending tests, also performed on both fabrics, show that after 3000 bending cycles, the electrical conductivity drops by 5% for the case of cotton fabrics and 3% for the felts, thus showing high flexibility and stability of the fabrics.

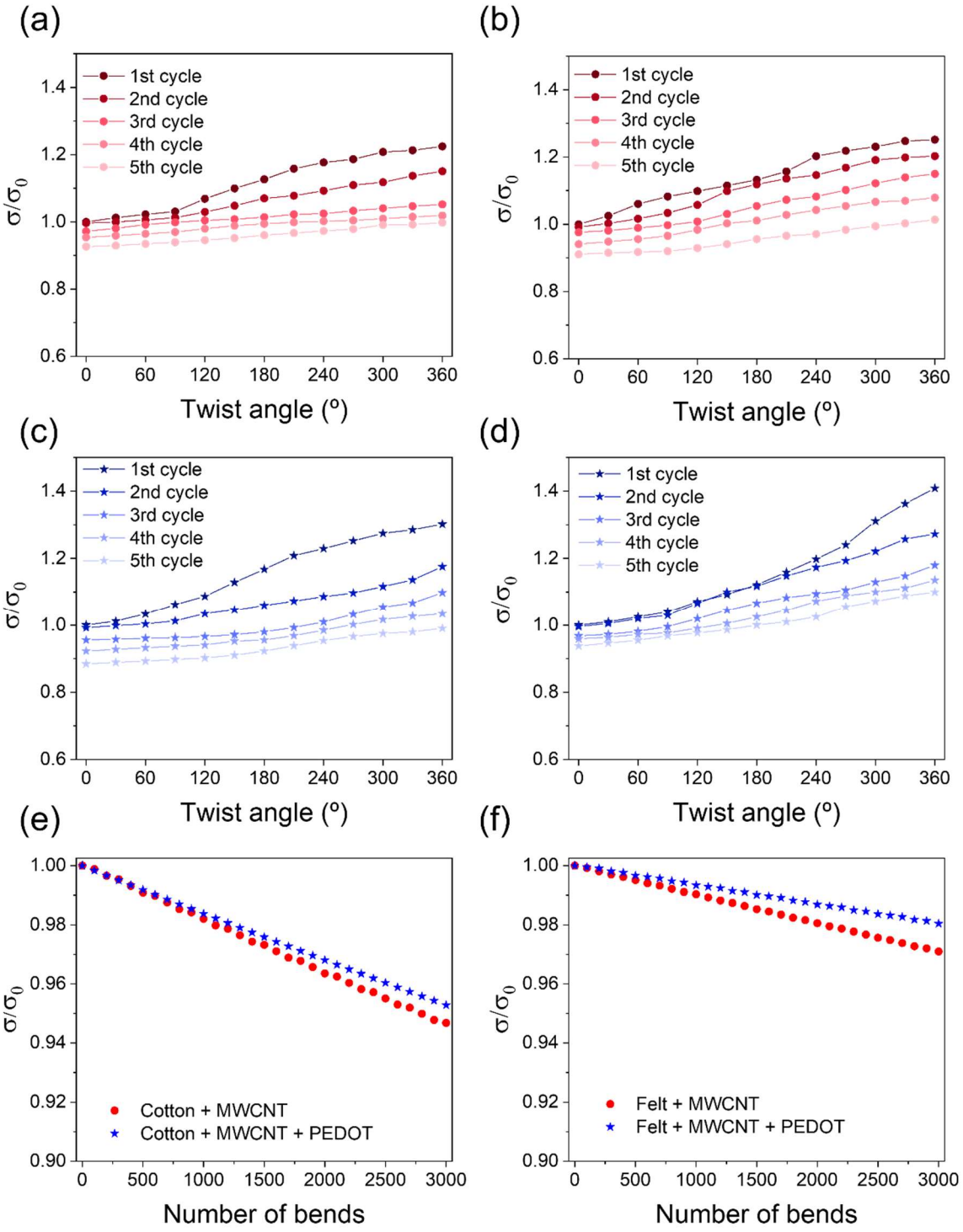

Figure 4.20 Variation of the normalized electrical conductivity (σ_0 is the initial electrical conductivity) as a function of twist angle for: (a) cotton + MWCNT, (b) felt + MWCNT, (c) cotton + MWCNT + PEDOT:ClO_4, and (d) felt + MWCNT + PEDOT:ClO_4 fabrics for 5 cycles. Variation of the normalized electrical conductivity as a function of the number of bendings for: (e) cotton and (f) felt fabrics coated with MWCNT and PEDOT:ClO_4.

4.3.8 Thermoelectric generator based on fabrics

The MWCNT-coated cotton and felt fabrics, after electrodeposition of PEDOT:ClO_4 on them, were cut into small squares of 0.5 cm^2 and assembled as shown in **Figure 4.21(a)**. Each piece represents an element of the thermoelectric generator (TEG). The bottom and top parts of each element were covered with silver paste and then with copper tape (0.5 cm^2). Each element was electrically connected with aluminum wires thermally bounded with tin. The TEGs were composed of 20 and 30 elements connected in series and distributed on a 7 x 8 cm support fabric, as shown in **Figure 4.21(b)**.

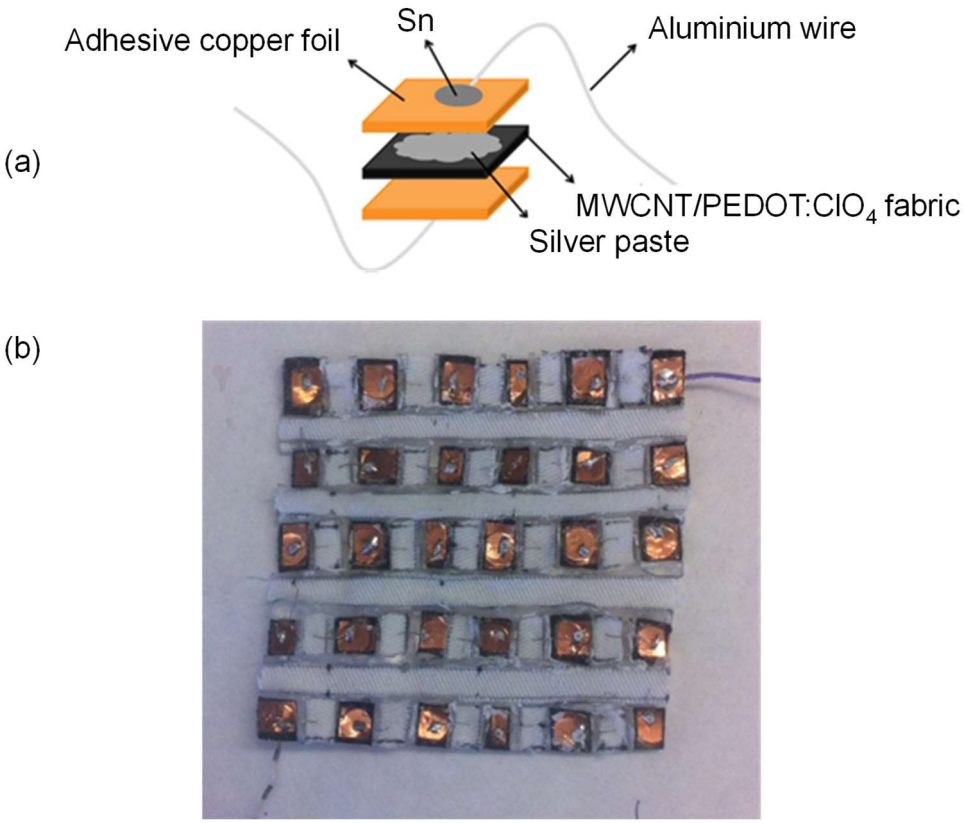

Figure 4.21 (a) Schematic representation of each element of the thermoelectric module, and (b) photograph of the thermoelectric module.

Three thermoelectric modules were built to test the thermoelectric performance of the fabrics. First, a TEG was made based on 20 elements series-connected of cotton fabric coated with MWCNT and PEDOT:ClO_4. The maximum power of the generator based on cotton fabrics was 47 nW with a temperature difference of 9 K, **Figure 4.22(a)**. A 20-element TEG based on the felt fabric coated with MWCNT and PEDOT:ClO_4 was also produced. This generator based on felt fabrics allowed a higher temperature gradient, around 25 K. Thus, the power output increased six times (0.3 μW) compared with the

cotton TEG one, **Figure 4.22(b)**. The use of felt fabrics allows higher thermal gradients, increasing the power output obtained by a TEG with the same number of elements. For this reason, a third thermoelectric generator was made, increasing the number of elements to 30, and they were distributed in the same area as the previous TEG. In this case, the output power was 0.9 μW with a temperature difference of 31 K, **Figure 4.22(c)**. In addition, it is worth highlighting the lower internal resistance of the thermoelectric generators (lower than 40 Ω), which indicates that the architecture of the device is adequate for electron propagation across the thermoelectric elements.

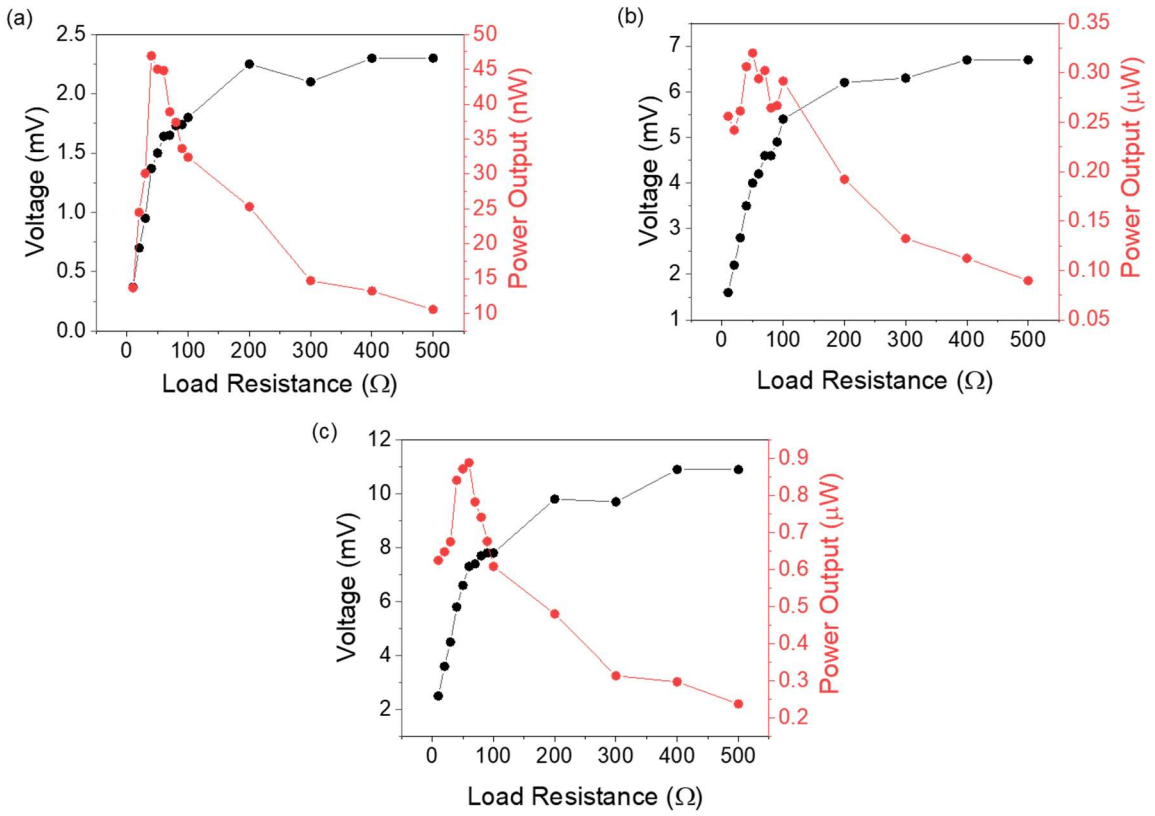

Figure 4.22 Voltage and power output as a function of the load resistance for the thermoelectric modules composed by (a) 20 elements of cotton/MWCNTs/PEDOT at ΔT = 9 K, (b) 20 elements of felt/MWCNTS/PEDOT ΔT = 25 K and (c) 30 elements felt/MWCNTS/PEDOT ΔT= 31 K.

These results look very promising when compared to other thermoelectric devices based on fabrics coated with PEDOT:PSS using polyester fabric or using a cleanroom wiper fabric, where they show a TGE with a power output of 12.29 nW at ΔT = 75.2 K and 2 nW at ΔT = 0.6 K, respectively.[86,88] Other works based on vapor phase polymerization of PEDOT:Cl onto cotton textiles or the deposition of PEDOT:Tos with ionic liquid in different textiles; reached a power output of 4.5 nW at ΔT = 25 K and 62 nW at ΔT = 100 K, respectively.[87,89] On the other hand, the results obtained are more similar to those

obtained by bulk synthesis of PEDOT:Cl (power output 0.375 μW at ΔT = 16.5 K);[90] by alternative doping of carbon nanotube fibers with PEDOT:PSS and oleamine wrapped with felt fibers (power output 4.64 μW at ΔT = 44.4 K);[91] or by dipping cotton cellulose fibers with a solution of PEDOT:PSS and ethylene glycol (power output density 2.6 $\mu W \cdot cm^{-2}$ at ΔT = 48.5 K);[92] thus indicating that MWCNTs coated felt fabrics and subsequently the electrochemical deposition of PEDOT:ClO_4 are a good alternative for the manufacture of textile-based TEGs.

4.4 Effect of counterions on the thermoelectric and mechanical properties of PEDOT coated fabrics

In the previous section, the felt fabric-based thermoelectric generator obtained a better power output because it could establish a more significant thermal gradient than the cotton fabric-based thermoelectric generator. Therefore, this section will try to increase the thermoelectric efficiency of PEDOT-coated felt fabrics by using different counterions. At the same time, the effect of these counterions on the thermal and mechanical properties will be studied. Finally, a new thermoelectric generator with a different architecture will be developed.

4.4.1 Materials

Poly(diallyldimethylammonium chloride) (PDADMAC) with a molecular weight of 10^5 g mol^{-1}, sodium deoxycholate (DOC), 1-Butyl-3-methylimidazolium hexafluorophosphate (PF_6), and 1-Ethyl-3-methylimidazolium bis(trifluoromethylsulfonyl)imide (BTFMSI) were purchased from Sigma-Aldrich. 3,4-Ethylenedioxythiophene (EDOT), lithium perchlorate, and acetonitrile were purchased from Alfa Aesar. Multiple-wall carbon nanotubes (MWCNTs) were obtained from Bayer Material Science (Leverkusen, Germany, 12–15 nm outer and 4 nm inner wall diameter, length > 1mm, purity 95 wt %). Felt fabric (made by polyester fibers) with a grammage 140 g m^{-2} and 0.8 mm of thickness was purchased from MW Materials World (Barcelona, Spain). All chemicals were used as received.

4.4.2 Electrochemical deposition of PEDOT

The synthesis of PEDOT with different counterions on MWCNT–fabrics was carried out following the optimized conditions above. That was, by applying a current intensity of 6 mA for 1 h using as a working electrode a felt fabric coated with 20 BL of MWCNT. In this section, the PEDOT polymeric chain was doping with three counterions: ClO_4, PF_6, and BTFMSI. The first comes from $LiClO_4$ and the others from two ionic liquids, 1-Butyl-3-methylimidazolium hexafluorophosphate and 1-Ethyl-3-methylimidazolium bis(trifluoromethylsulfonyl)imide, respectively. Different solutions were prepared. To obtain PEDOT:ClO_4, a 0.01 M EDOT and 0.1 M $LiClO_4$ solution was prepared in acetonitrile. For the deposition of PEDOT:PF_6 and PEDOT:BTFMSI, 0.01 M solutions of EDOT and 0.01 M of the ionic liquids were prepared using acetonitrile as solvent. Three electrodes formed the electrochemical cell: a counter electrode (platinum grid), a reference electrode (Ag/AgCl), and the MWCNT–fabric as the working electrode. As previously mentioned, the working electrode was assembled between two sheets of PET–ITO connected to the copper tape. Then, PET–ITO sheets with the fabric are clamped. The polymerization of EDOT is achieved using the MWCNT-coated fabric as a working electrode and applying a current intensity to the working electrode (MWCNT–fabric).[77] The electrochemical polymerization of EDOT on the fabrics is also shown in the representation of **Figure 4.13**.

4.4.3 Morphology of felt fiber coatings

Once the felt fabrics coated with MWCNTs and PEDOT with different counterions were obtained, the homogeneity of the coating was determined by scanning electron microscopy (SEM). **Figure 4.23** shows SEM micrographs at two magnifications. The low magnification images give us an idea of the uniformity of the coating of the felt fibers, showing a consistent coating both with MWCNTs and PEDOT. Then, at higher magnifications, the coating of the fibers can be observed in more detail.

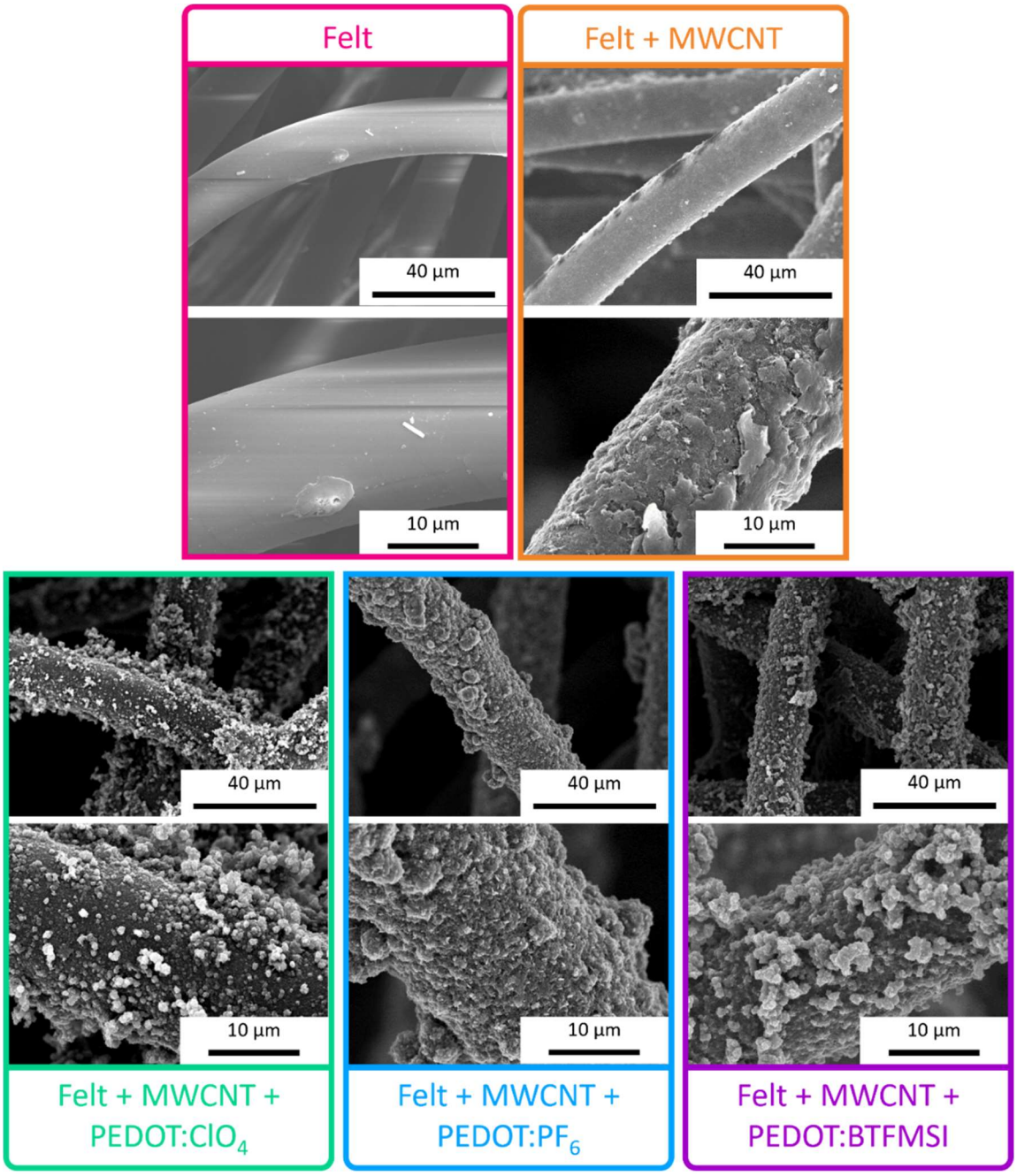

Figure 4.23 SEM images of felt and felt coated fabrics with carbon nanotubes and PEDOT with different counterions.

On the one hand, as we have seen in the previous sections, after coating the felt fabric with multi-walled carbon nanotubes, fibers are perfectly coated with MWCNTs and some PDADMAC-DOC agglomerates. Once the felt fabrics have been coated with MWCNTs, PEDOT is electrodeposited in the presence of different counterions. At first glance, a clear trend is observed, indicating that PEDOT electrodeposition using ionic liquids as counterions leads to a higher degree of fiber coating compared to the fibers coated with lithium perchlorate as a counterion. Moreover, several differences in terms of the

morphology of the coating have been observed between the different samples produced. For the PEDOT:ClO_4, the coating depicted a globular morphology, while the coating based on PEDOT:PF_6 and PEDOT:BTFMSI presented a cauliflower-like morphology indicating a more compacted deposition which is preferable for the electric transport. Both morphologies are typical of the electrochemical deposition of conductive polymers by chronoamperometry.[71,72]

4.4.4 Raman spectroscopy analysis

The effect of the coating can also be analyzed by Raman spectroscopy, **Figure 4.24**. As in the previous section, the spectrum of the felt fabric presents the vibrational modes corresponding to the vibration of the aliphatic chain (610 and 1274 cm^{-1}), the symmetric and asymmetric C–O–C deformation (840 and 1082 cm^{-1}), the vibration of the aromatic ring (1604 cm^{-1}) and the vibration of the carbonyl corresponding to the ester group (1720 cm^{-1}).[93] After coating the felt fibers with MWCNTs, the PET signals are masked due to the typical carbon nanotube D and G bands (located at 1300 and 1600 cm^{-1}, respectively). Also, bands located at 610, 840, and 1720 cm^{-1} are present in a much lower intensity, relative to that of the D and G bands, which evidences the homogeneity of the MWCNTs on top of the felt fabrics. The spectra drastically enhance after the electrochemical deposition of PEDOT due to the presence of its typical bands. For the case of PEDOT:ClO_4, it is still possible to find some bands attributed to the felt. In contrast, the PEDOT:PF_6 and PEDOT:BTFMSI coatings do not show these residual peaks, revealing an improved adhesion onto the textile fibers when these ionic liquids are used as counterions.

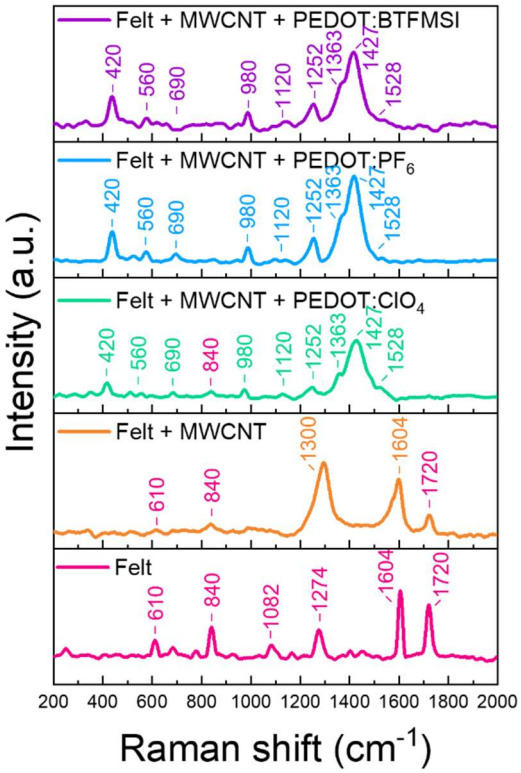

Figure 4.24 Raman spectra of felt fabric substrate (pink) coated with MWCNT (orange) and after PEDOT deposition with different counterions: PEDOT:ClO_4 (green), PEDOT:PF_6 (blue), and PEDOT:BTFMSI (purple).

4.4.5 Thermo-mechanical analysis

After the chemical characterization of the coatings on the felt fibers, one of the main objectives of this section is to evaluate the effect of the deposition of the different coatings on the thermo-mechanical properties of the felt fibers. The textile properties can be affected when they are heated due to their thermosensitivity. Therefore, this analysis is required to evaluate its use in wearable devices. The thermogravimetry curves (TGA) in **Figure 4.25** shows that the degradation of the felt control sample takes place in two steps, the first with a thermogravimetric derived temperature peak of 425 ºC and the second of 480 ºC.[75] When the felt fibers are covered with carbon nanotubes, a slight increase in thermal stability is observed since the decomposition initiation temperature ($T_{5\%}$) increases by 10 ºC, see **Table 4.3**. However, when the fibers are electrochemically coated with PEDOT, a decrease in mass is observed at temperatures below 367 °C. This weight loss in the range between 300 and 400 ºC could be attributed to the decomposition of the thiophene chain.[94]

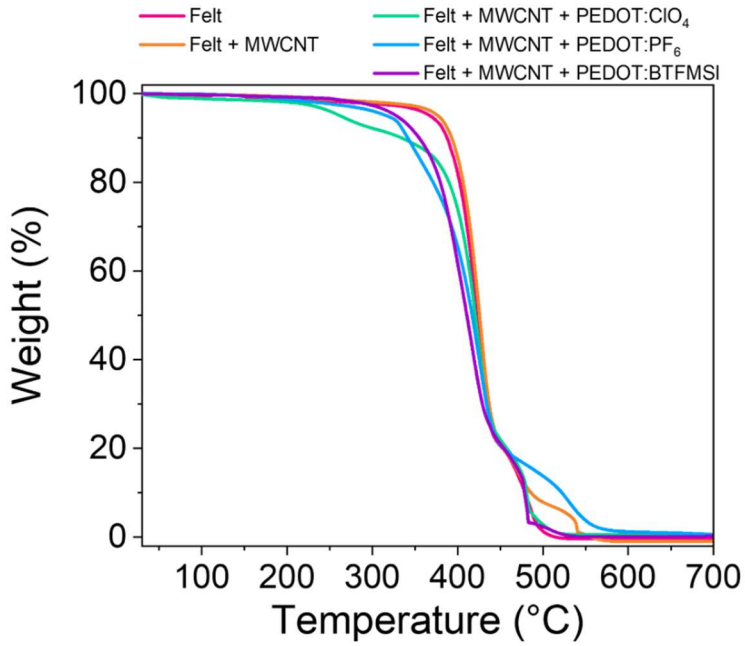

Figure 4.25 TGA measurements of felt fabric and coated felt fabrics.

In addition, the decomposition initiation temperature decreases by approximately 100 ºC for PEDOT:ClO_4, 50 ºC for PEDOT:PF_6, and 40 ºC for PEDOT:BTFMSI, see **Table 4.3**. These results show that PEDOT coatings with ionic liquids as counter ions provide greater thermal stability than the PEDOT:ClO_4 coating. Therefore, these fabrics are more stable against higher thermal gradients.

Table 4.3 Weight loss temperature at different percentages and residue percentages at 700 ºC of pristine felt fabric and the felt fabric coated with MWCNT, PEDOT:ClO_4, PEDOT:PF_6 and PEDOT:BTFMSI.

	Felt	**Felt + MWCNT**	**Felt + MWCNT + PEDOT:ClO_4**	**Felt + MWCNT + PEDOT:PF_6**	**Felt + MWCNT + PEDOT:BTFMSI**
$T_{5\%}$ (ºC)	367.65	376.85	262.22	316.87	328.10
$T_{10\%}$ (ºC)	387.51	393.02	334.41	341.50	354.88
$T_{20\%}$ (ºC)	402.33	406.45	389.81	371.16	379.62
$T_{30\%}$ (ºC)	411.02	414.41	404.90	393.11	391.97
$T_{40\%}$ (ºC)	417.45	420.40	413.88	406.97	401.68
$T_{50\%}$ (ºC)	422.87	425.65	420.59	416.94	410.81
$T_{60\%}$ (ºC)	427.91	430.68	426.71	425.74	417.80
$T_{70\%}$ (ºC)	433.93	436.84	434.19	433.91	429.01
$T_{80\%}$ (ºC)	452.84	453.28	457.64	454.26	454.06
$T_{90\%}$ (ºC)	479.08	486.04	480.68	522.32	478.32
$T_{95\%}$ (ºC)	487.97	530.56	488.68	543.47	482.07
Residue % (700 ºC)	0	0	0.56	0.615	0.199

The DSC allows rapid detection and measurement of the physical and chemical transformations of the material as a function of temperature. The thermal program used consisted of a first heating cycle up to 300°C to erase the thermal history of the sample. The sample was kept at 300 °C for 10 min to ensure that all the sample is molten. After this first heating cycle, a cooling cycle was carried out to 0°C at 50 ºC/min, and finally, a second heating cycle was carried out to 300°C. The thermogram obtained from the second heating cycle, **Figure 4.26**, was used for the analysis. It shows a step in the baseline of the measurement curve around 80 ºC associated with the glass transition of the felt. At higher temperatures, an endothermic process is observed between 240°C -255°C associated with the melting of the crystalline phase present in the samples. The thermogram corresponding to the second heating cycle of the pristine felt fabric shows a glass transition temperature (T_g) at 83 ºC and a melting point of 253 ºC. The DSC thermogram of pure polyethylene terephthalate (PET) shows a T_g at 85.4 ºC and a T_m of 254.9 ºC.[95,96] These results indicate that the felt fabric used is made of PET. In addition, the FTIR and Raman spectra (**Figure 4.15(b)** and **Figure 4.24**, respectively**)** confirm the presence of ester groups and aromatic rings, which supports that the felt fabric is made of PET.

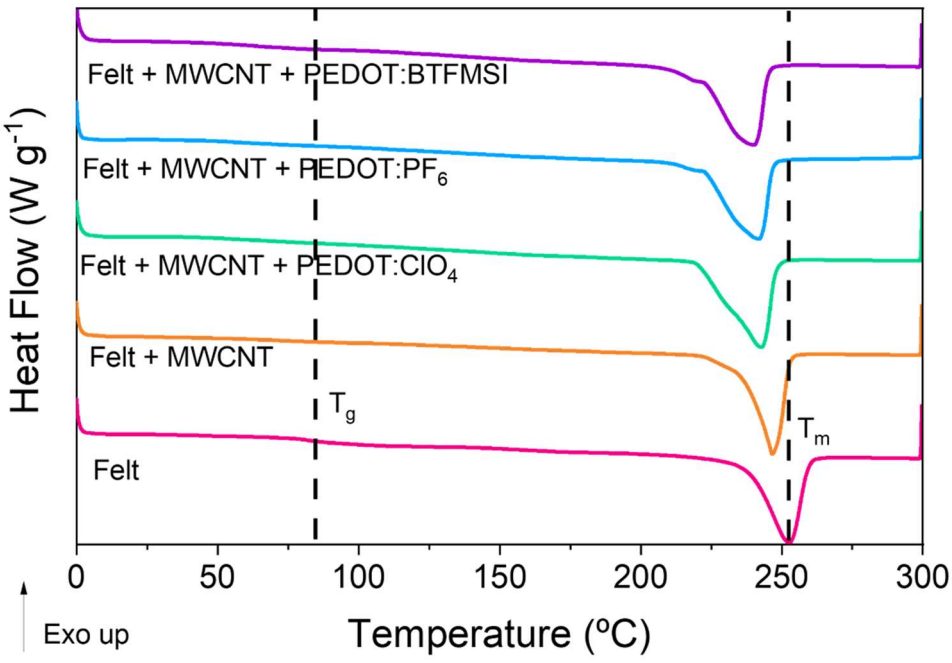

Figure 4.26 DSC measurements of felt, felt coated with MWCNT, and after PEDOT deposition with different counterions: PEDOT:ClO_4, PEDOT:PF_6, and PEDOT:BTFMSI. The thermograms have been moved vertically to observe better the evolution of the glass transition temperature and the melting temperature.

Focusing on the evolution of the T_g after the different coatings, we can observe that it decreases when the felt fibers are coated with the MWCNTs, and it decreases even more after the electrodeposition of PEDOT with the different counterions. Especially noticeable is the case of the use of ionic liquids as counterions of the PEDOT chains since the glass transition temperature decreases 20 ºC compared to the pure felt fabric. This suggests that the ionic liquid can easily diffuse on the surface of the fibers resulting in an improved plasticization of the felt fibers.[45] It can also be clearly seen in the DSC thermogram that adding the different coatings decreases the melting temperature while keeping the melting enthalpy constant (**Table 4.4**). This melting point decrease indicates that the coating of felt fibers slightly reduce the backbone rigidity. From the values of the enthalpy of fusion, ΔH_m (J g^{-1}), obtained by measuring the area under the melting curve in each of the thermograms, we can estimate the crystalline fraction (χ_c) of each of the samples with the **Equation (4.1)**. For this, we compare the values obtained with the crystalline melting enthalpy for a 100% crystalline polyester felt material. For the calculation, a value of $\Delta H_{m,lit}$ (J g^{-1}) = 140.1 J g^{-1} has been used, in accordance with the literature.[96]

$$\chi_c(\%) = \frac{\Delta H_m}{\Delta H_{m,lit}} \cdot 100 \qquad \textbf{(4.1)}$$

Table 4.4 Glass transition temperature (T_g), melting temperature (T_m), enthalpy of fusion (ΔH_m) and crystallinity percentage (χ_c) of felt fabric and coated felt obtained by DSC.

	T_g (ºC)	T_m (ºC)	ΔH_m (J g^{-1})	χ_c (%)
Felt	83.06	252.96	45.493	32.5
Felt + MWCNT	78.30	246.58	43.581	31.1
Felt + MWCNT + PEDOT:ClO_4	76.43	242.90	51.004	36.4
Felt + MWCNT + PEDOT:PF_6	63.90	242.09	46.695	33.3
Felt + MWCNT + PEDOT:BTFMSI	64.58	240.28	45.990	32.8

According to Rodríguez et al.[97] polyester fibers are obtained by spinning the polymer above its glass transition temperature. This process produces an outer layer in the fibers whose orientation is significantly greater than that of the inner or core layer. So that the felt fibers are composed of microfibrils with crystalline blocks (crystallites) linked by an isotropic amorphous phase oriented in the fiber axis direction. These microfibrils are linked to each other in the transverse direction by an amorphous phase also oriented along the fiber axis. **Figure 4.27** shows the pattern of the felt fiber microstructure.

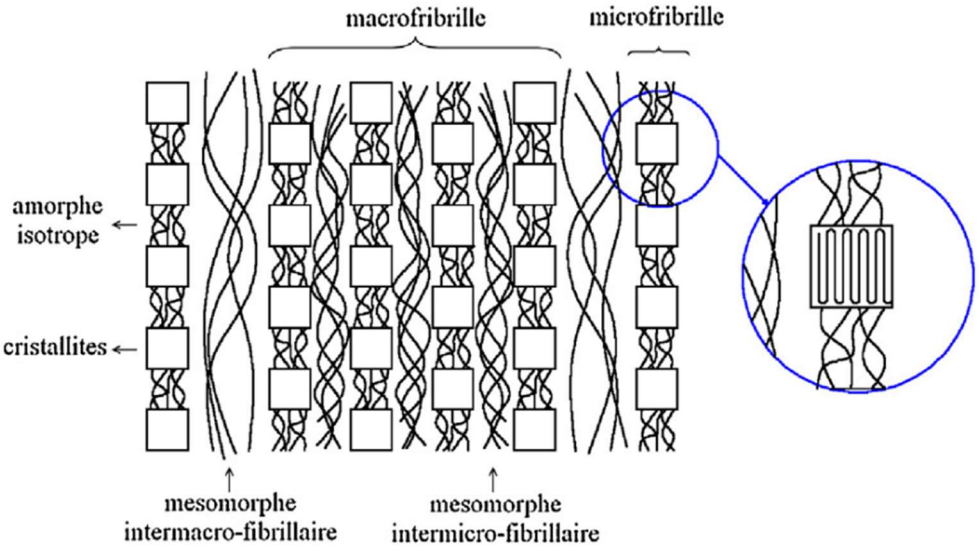

Figure 4.27 Model of felt fiber microstructure. Reproduced with permission.[97] Copyright 2018, Sociedade Portuguesa de Materiais (SPM).

The dynamic mechanical analysis provides valuable information about the polymer stiffness, molecular motion, and relaxation processes of composite systems.[98] **Figure 4.28** shows the evolution of the storage modulus (E'), loss modulus (E"), and tan δ as a function of temperature for the felt, felt + MWCNT, and felt + MWCNT coated with PEDOT:ClO_4 fabrics, PEDOT:PF_6 and PEDOT:BTFMSI by electrodeposition. From the DSC and DMA results, it is clear how the complex microstructure of the polyester fibers affects molecular mobility, both in terms of the amorphous phase portions and the crystalline phase portions present. The plot of tan δ and loss modulus (E") as a function of temperature shows the presence of two relaxation processes that are attributed to two glass transition temperatures. This indicates the presence of two amorphous phases of a different nature, with very different mobility of the chain segments. The first, around 80 ºC, corresponds to the free amorphous phase with greater mobility. The second, around 125 ºC, corresponds to the amorphous phase constrained between the crystalline phase of the microfibrils that make up the felt polyester fibers, with restricted mobility. This second glass transition is very poorly visible on DSC.

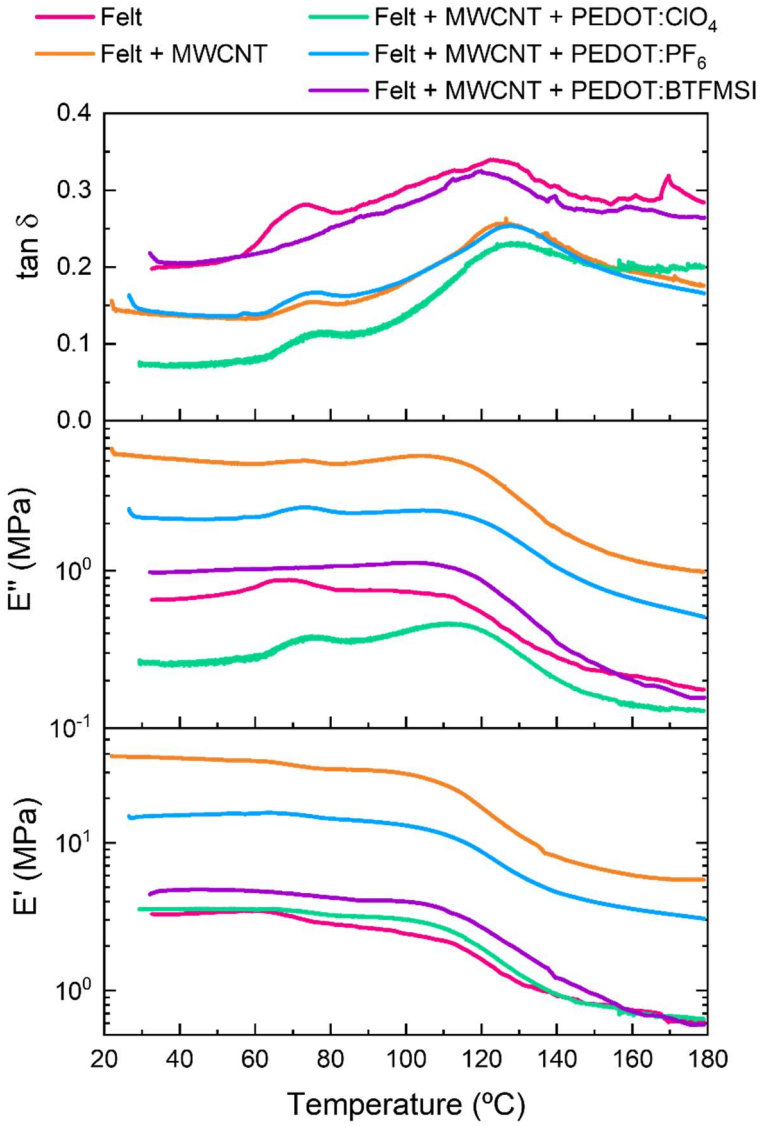

Figure 4.28 Storage modulus (E'), loss modulus (E''), and tan δ as a function of the temperature for the felt, felt coated with MWCNT, and after PEDOT deposition with different counterions: PEDOT:ClO_4, PEDOT:PF_6, and PEDOT:BTFMSI.

In addition, **Figure 4.28** shows that the pristine felt fabric has a storage modulus value at 35 ºC of 3.2 MPa. After deposition of 20 BL of MWCNT by LbL on the felt fabric, the storage modulus at 35°C increased to 38 MPa, indicating that MWCNT act as a reinforcement.[99] However, the electrochemical polymerization of PEDOT with the different counterions reduces the storage modulus at 35 ºC until 15 MPa, 4.7 MPa, and 3.5 MPa for the PEDOT:PF_6, PEDOT:BTFMSI, and PEDOT:ClO_4 coatings, respectively.

The nature of the felt fabric is non-woven, and therefore the felt fibers are randomly distributed and spaced. The behavior of the storage modulus can be attributed to the fact that during the coating of the felt fibers with MWCNT, the fibers compact, decreasing the free volume between them. However, upon electrodeposition of PEDOT with the different

counterions, the PEDOT polymer chains begin to grow on the surface of the MWCNT-coated fibers so that the free volume between the fibers increases. These results show that coating the felt fibers with carbon nanotubes increases the viscoelastic stiffness. However, the electrodeposition of PEDOT with different counterions decreases, being the PEDOT:ClO_4 and PEDOT:BTFMSI coatings those with similar viscoelastic stiffness to that of pristine felt. The tan δ shows an α relaxation process that corresponds to the T_g. The decrease in the tan δ values at 35 ºC upon adding the different coatings to the felt fibers suggests a good interfacial adhesion between the fibers and the coating.[45,100]

4.4.6 Torsion and bending test

Thermoelectric fabric bending and torsion tests are essential to evaluate their potential use in wearable thermoelectric generators since reliability during daily use must be guaranteed. Three types of tests were carried out. Therefore, the evolution in the electrical conductivity was evaluated as a function of the twist angle, bending cycles on a 15 mm diameter cylinder, and bending radius. In the first study, the fabric was clamped with two clamps, one fixed and one freely rotating. Electrical conductivity was evaluated every 30º of rotation. **Figure 4.29(a)** to **(d)** show the normalized electrical conductivity evolution as a function of the twist angle for the fabrics coated with MWCNT and PEDOT:counterions. The general trend depicted that as the twist angle increases, the electrical conductivity increases due to a higher degree of compaction between the felt fibers, which causes greater electrical contact between the coated fibers. This improves the mobility of electrons through the fabric, reaching higher electrical conductivity. This trend is more evident in the fabrics coated with PEDOT, in which the electrical conductivity at high twist angles is higher than in the fabric coated with MWCNTs. This indicates that the PEDOT is coating the fibers and polymerizing beyond them, occupying interstitial voids. On the other hand, the electrical conductivity slightly decreases after each torsion cycle. This is probably because after performing the previous cycle, the stress caused on the fibers during the torsion generates distension when they return to the original state (0º twist angle), increasing the free space between the fibers. However, despite this decrease in electrical conductivity after five complete torsion cycles, the electrical conductivity only decreased by 10% over the initial one, indicating a high torque capacity.

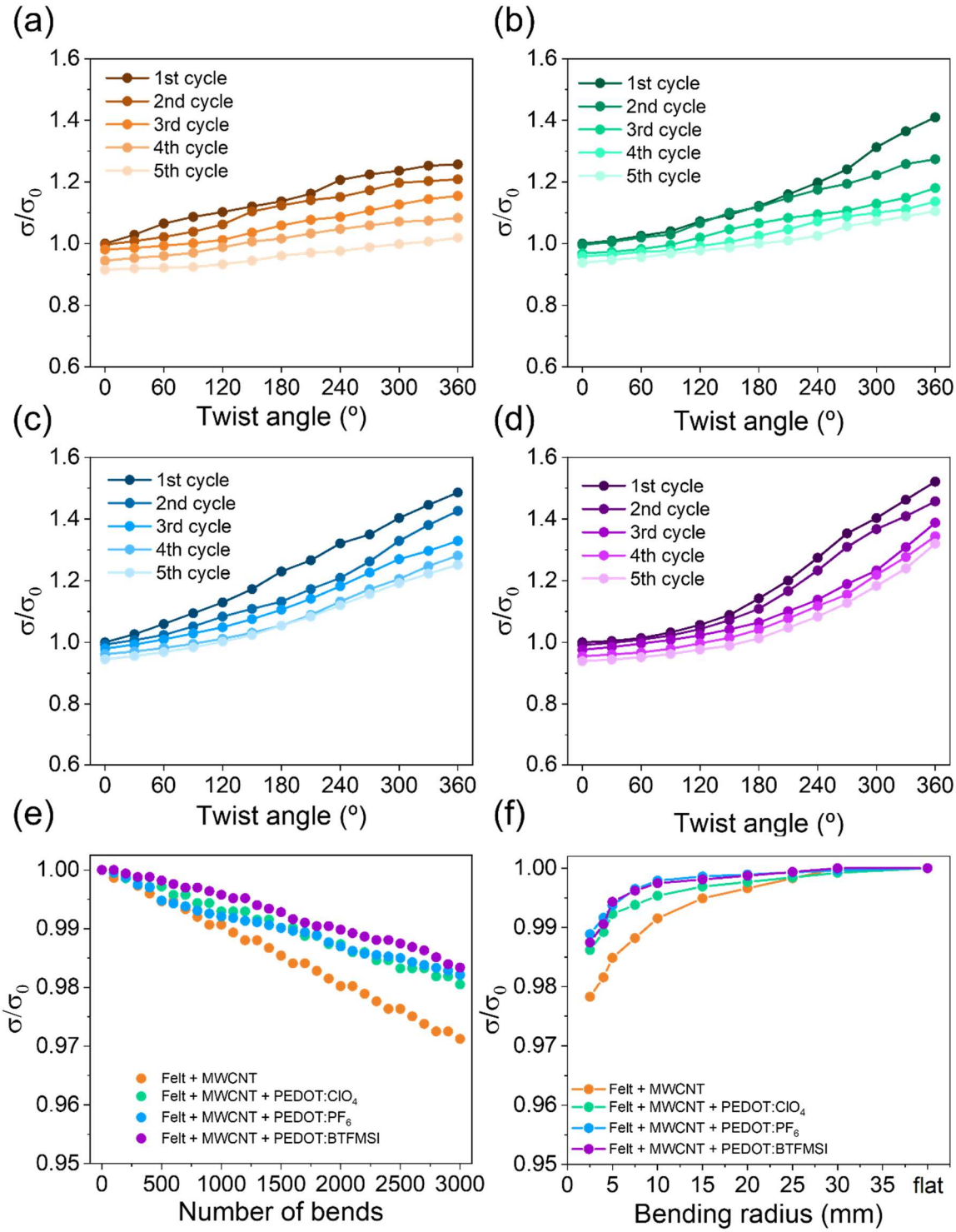

Figure 4.29 Variation of the normalize electrical conductivity (σ_0 is the initial electrical conductivity) as a function of twist angle of (a) felt + MWCNT, (b) felt + MWCNT + PEDOT:ClO4, (c) felt + MWCNT + PEDOT:PF6, and (d) felt + MWCNT + PEDOT:BTFMSI fabrics for 5 cycles. (e) Variation of the normalize electrical conductivity as a function of the number of bendings, and (f) variation of the normalize electrical conductivity as a function of the bending radius for the different coated felt fabrics.

For the second study, **Figure 4.29(e)**, the electrical conductivity was studied as a function of the number of bendings made on the same fabric with a constant bending radius of 15 mm. The graph shows that the electrical conductivity slightly decreases with the number of bendings cycles, reaching a 3% loss of the electrical conductivity after 3000 bending cycles in the MWCNTs-coated felt fabric. However, the electrical conductivity after completing the bending cycles of electrochemically coated PEDOT felt fibers shows a loss of only 1.5%, which indicates an excellent adhesion of the coating to the fibers. Finally, in the last study, **Figure 4.29(f)**, the electrical conductivity is studied as a function of the bending radius. In this case, it is also observed that the MWCNTs-coated felt fabric exhibits a greater electrical conductivity variation than the PEDOT-coated felt fabrics.

Overall, the results indicated that the electrochemical coating of PEDOT on textile fibers coated with MWCNTS is an excellent alternative for coating textiles for wearable thermoelectric applications since the electrical conductivity remains practically constant after the different torsion and flexibility tests.

4.4.7 Thermoelectric properties

The electrical conductivity and Seebeck coefficient were measured at 25 ºC in the plane. **Figure 4.30(a)** shows the evolution of electrical conductivity measured by Van der Pauw method, the Seebeck coefficient, and Power Factor as a function of the coating on the felt fibers. The electrical conductivity and the Seebeck coefficient increase simultaneously with the different coatings deposited on the felt fabric following the order BTFMSI > PF_6 > ClO_4. The electrical conductivity of the fabric coated with MWCNTs is of the order of 10^{-4} S cm^{-1}, and after the electrochemical deposition of PEDOT, the electrical conductivity increases four orders of magnitude. The Seebeck coefficient also increases progressively after PEDOT electrodeposition, reaching a maximum value of 52.3 μV K^{-1} for the PEDOT:BTFMSI coating. It is unusual that the electrical conductivity and the Seebeck coefficient increase simultaneously because both are inversely dependent on the carrier concentration. For this reason, we measured carrier concentration and mobility with the Van der Pauw geometry at room temperature using an Ecopia HMS-3000 Hall Measurement system. An external magnetic field of 1T and a current of ~150 μA were applied with ohm contact established using Au electrodes. Ten separate measurements were taken on each sample at 100, 150, and 200 μA, and the measurements were averaged to represent the reported values, **Figure 4.30(b)**.

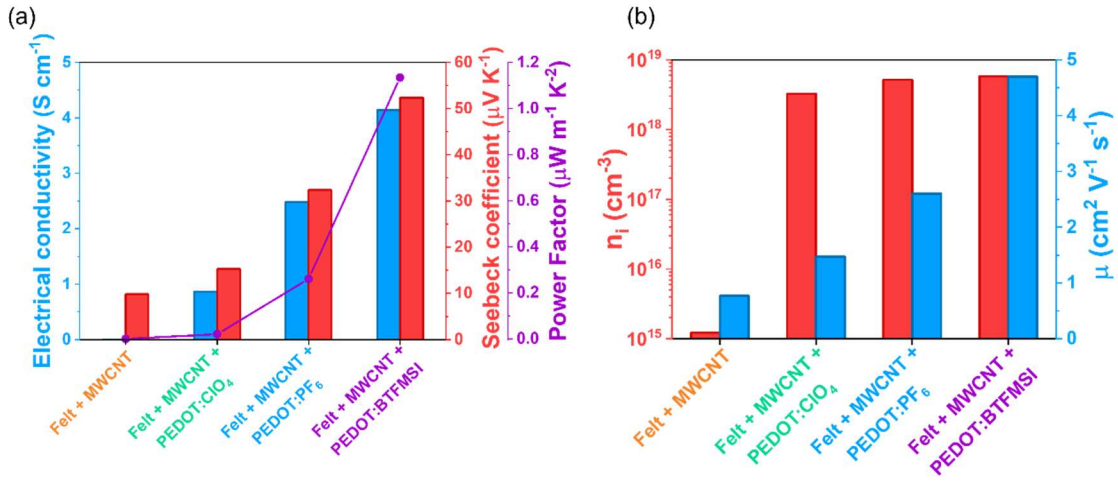

Figure 4.30 (a) Electrical conductivity, Seebeck coefficient and Power Factor for the different coatings of the felt fabrics. (b) Carrier concentration (n) and carrier mobility (μ) for the different coatings of the felt fabrics.

The fabrics coated with PEDOT:counterions show that the concentration of charge carriers remained practically unvaried. This trend agrees with the expected oxidation level of PEDOT generated by electrochemical polymerization. This process typically controls the charge carrier concentration in the synthesized materials. In the present study, the same experimental conditions were used for the electrodeposition of PEDOT with the three counterions. Therefore, the concentration of charge carriers should be the same. Thus, electron mobility is responsible for the simultaneous increase in electrical conductivity and the Seebeck coefficient. This trend agrees with several studies that have reported that the order improvement of the polymeric chains induces an increase in the mobility of the charge carrier, which causes the simultaneous increase in the Seebeck coefficient and the electrical conductivity in the π–π stacking direction.[101–104] Therefore, the counterion used plays a fundamental role not only in the doping of the polymeric chains but also in the polymer chain conformation. **Figure 4.31** shows a schematic of ordering the PEDOT polymeric chains depending on the counterion used during the electrochemical synthesis. The PEDOT chains are randomly ordered with the perchlorate ion, which is the smallest in size. However, increasing a counterion size, such as PF_6 or BTFMSI, can instigate the polymer chains to take on a linear-like conformation that is more favorable for the PEDOT chains to be orderly stacked.[81]

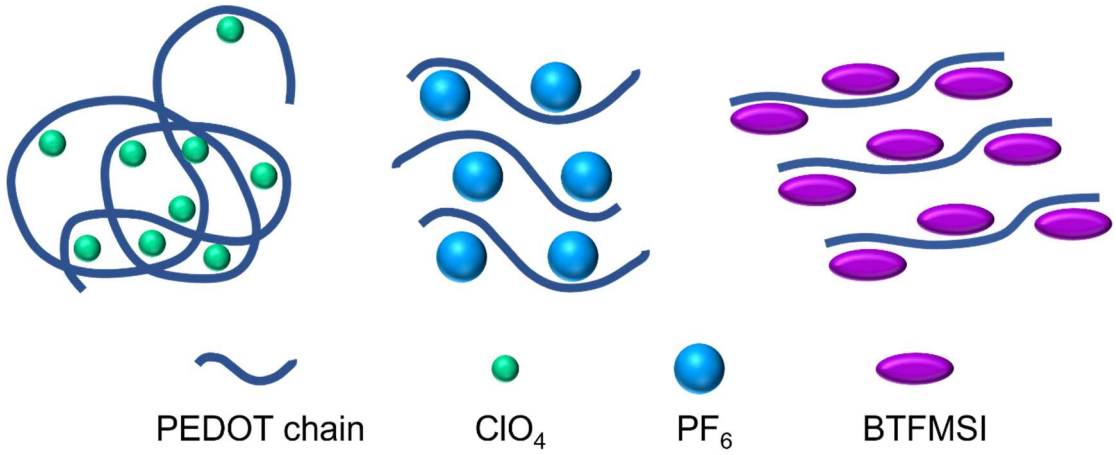

Figure 4.31 Schematic representation of counterion effect on the PEDOT chain conformation.

In addition, another factor to consider in the enhancement of the Seebeck coefficient is the delocalization of the polarons since it improves charge transport.[105,106] If we consider the Seebeck coefficient as an entropy flux per unit charge,[107,108] the presence of polarons in the polymeric chain can modify the vibrational frequencies associated with the atomic positions, producing a change in vibrational entropy. As the polaron delocalizes and spreads over more positions (larger counterion), the vibrational modes smooth out, and the total vibrational entropy change for the polaron associated with these atomic positions increases, improving the Seebeck coefficient.[104] Therefore, the use of BTFMSI as a counterion in the PEDOT chain allows higher Power Factor values to be achieved since, being the largest counterion used, it allows a greater delocalization of the polarons as well as an improvement in the ordering of the polymeric chains.

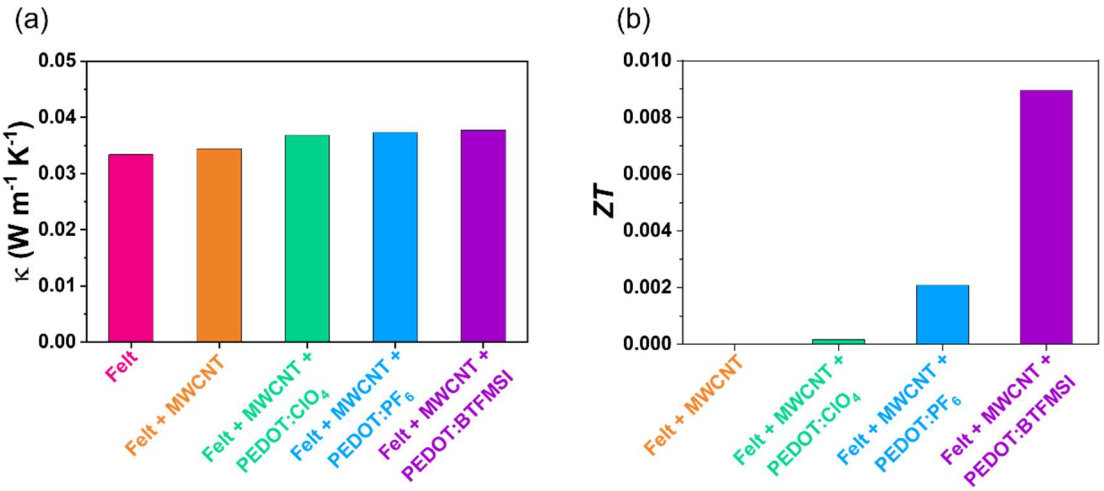

Figure 4.32 (a) Thermal conductivity of different felt fabric, felt + MWCNT and felt + MWCNT coated with PEDOT:ClO_4, PEDOT:PF_6, and PEDOT:BTFMSI. (b)

Figure of Merit for felt + MWCNT and felt + MWCNT coated with PEDOT:ClO_4, PEDOT:PF_6, and PEDOT:BTFMSI.

Thermal conductivity is an important parameter in determining the thermoelectric efficiency of TE materials. For this purpose, the research group has built up a setup to determine the thermal conductivity of textiles based on the axial heat flow method, which is indicated for the measurements of thermal conductivity of textiles.[109] **Figure 4.32(a)** shows that the thermal conductivity remains practically constant after the different coatings with MWCNT and PEDOT. The value for felt fabric is 0.033 W m^{-1} K^{-1}, very similar to the obtained by Yang et al.[110] in the study of thermal properties of a polyester nonwoven textile. After the LbL coating of MWCNTs on the felt fibers, the thermal conductivity increases by only 3%. However, after electrochemical deposition of PEDOT:BTFMSI, the increase up to 0.037 W m^{-1} K^{-1}. Despite this increase, the thermal conductivity of the final material is an order of magnitude lower than that of the conductive polymer due to the fiber architecture of the final material.[81] Therefore, these results demonstrate that coating textile fibers with conductive polymers are an effective method to obtain thermoelectric materials with a low thermal conductivity since the interstitial spaces in the fiber effectively contribute to the reduction of heat transfer. Finally, the Figure of Merit, ZT (**Figure 4.32(b)**) was determined with the results of the Power Factor and the thermal conductivity. The thermoelectric efficiency of the felt fabric coated with MWCNT has a value of ZT = $1.5 \cdot 10^{-8}$, which is two orders of magnitude lower than the ZT estimated by Paleo et al.[111], where they coated cotton fabric with carbon nanotubes. After the electrochemical polymerization, the ZT value increases reaching the best thermoelectric efficiency (ZT = 0.009) with the fabric based on PEDOT:BTFMSI. This value is very similar to other ZT values from the literature on thermoelectric textiles based on conductive polymers and carbon nanotubes.[112–114]

4.4.8 Textile-based wearable thermoelectric generator

The felt fabric coated with MWCNT and PEDOT:BTFMSI has the best thermoelectric performance, and we chose this coating to manufacture a wearable thermoelectric generator (wTEG) with a bracelet shape. The prototype consisted of 14 thermoelectric units connected in series, in which the final open-circuit voltage and resistance are equal to the sum of the voltage and resistance of each unit, respectively. The basic thermoelectric unit was made with ten pieces of felt coated with MWCNT and PEDOT:BTFMSI (10 x 5 mm)

connected in parallel to reduce the final resistance (**Figure 4.33(a)**). The initial resistance of each piece was around 8 Ω, and the final resistance of one basic unit was 1.2 Ω. After connecting the 14 units, the designed thermoelectric generator gave a total resistance of 16.5 Ω. The textile-based wearable thermoelectric generator (T-wTEG) was thermally contacted with thermal paste, and different thermal gradients were applied to evaluate the power output **Figure 4.33(b)**.

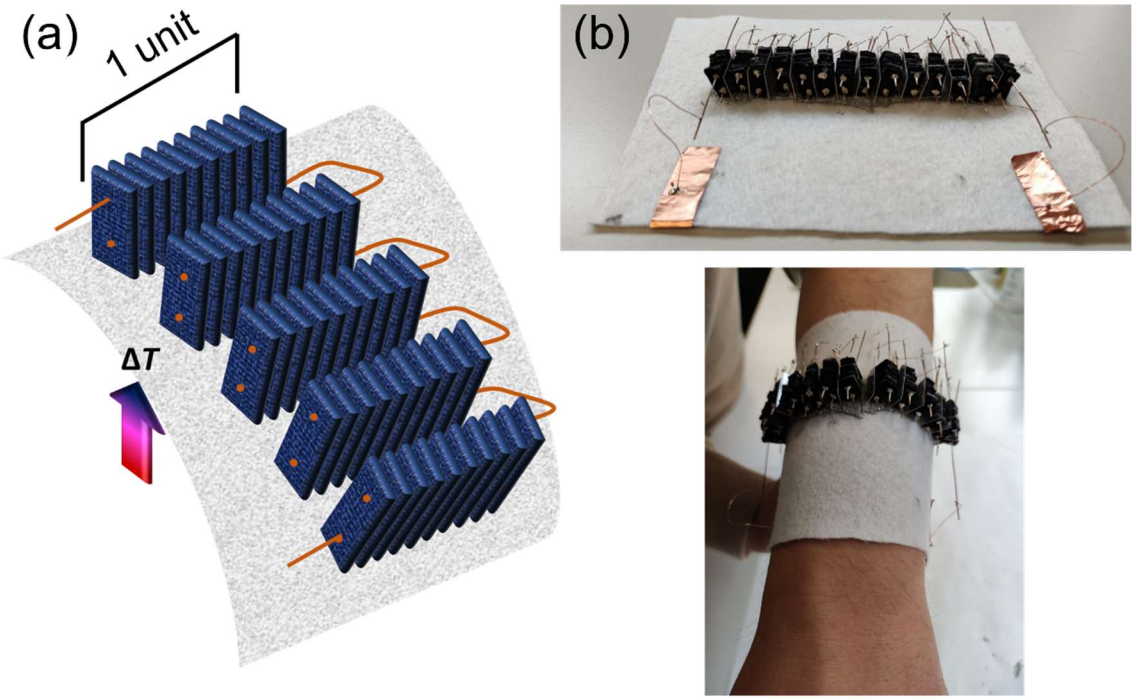

Figure 4.33 (a) Schematic representation of T-wTEG bracelet designed. (b) Real images of the T-wTEG bracelet.

The power generated by the thermoelectric generator was determined as a function of the output current intensity (**Figure 4.34(a)**) and the input resistance (**Figure 4.34(b)**). **Figure 4.34(a)** shows a linear trend of output voltage with output current, following Ohm's Law. The output voltage (**Figure 4.34(b))** increases progressively until reaching a plateau corresponding to the open-circuit voltage. Both figures show that the output power increases with the thermal gradient reaching a maximum power output of 6.5 µW with a thermal gradient of 57 K. In the case of **Figure 4.34(b),** the maximum output power obtained by the generator is reached when the input resistance is equal to the internal resistance of the TEG.

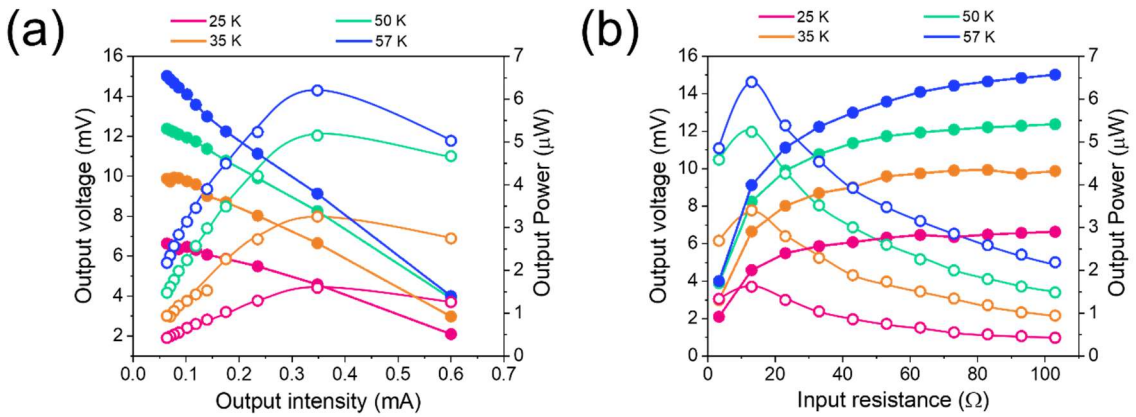

Figure 4.34 (a) Output voltage and output power as a function of output intensity for different thermal gradients. (b) Output voltage and output power as a function of input resistance for different thermal gradients. Open dots for Output Power and full dots for Output voltage.

The results show that the electrochemical coating of PEDOT:BTFMSI on the felt fibers-MWCNTs and the new architecture of the wearable thermoelectric generator improves four times the Power Output obtained in the previous section (0.9 μW, ΔT=31 K) with the approximately the same thermal gradient (3.6 μW, ΔT=35 K). In addition, if we compare the results with other works published until the date based on textile-based thermoelectric generators, we can consider that the results obtained in this work are promising. **Table 4.5** shows the main textile-based wearable thermoelectric generators during the last seven years. Textile-based wTEGs have been developed with inorganic semiconductors,[115–118] with carbonaceous materials,[113,119,120] with conductive polymers,[40,41,114,121–124] and with hybrid materials combining inorganic semiconductors or carbonaceous materials with conductive polymers.[42,125–133] The power output obtained by the wearable thermoelectric generator developed in this work, 6.5 μW at ΔT =57 K, is superior to many of the textile-based TEGs reported. This value is similar to those obtained in the literature. Komatsu et al.[120] synthesized a knittable carbon nanotube fiber with excellent thermoelectric properties. This resulted in a thermoelectric generator with a power output of 5 μW for a thermal gradient of 60 K. Sun et al.[131] coated carbon nanotube fibers with PEDOT:PSS (p-type) and with oleamine (n-type). The obtained generator produced an output power of 4.64 μW with a thermal gradient of 44 K. Therefore, the method presented in this work based on the electrochemical coating of textile fibers/MWCNTs with PEDOT:BTFMSI has enormous potential for further development

on T-wTEGs due to fact that the resulting internal resistance is very low maximizing the final power output.

Table 4.5 Comparison of textile-based wTEG performance.

Textile TEG	p-n pairs/ legs *	ΔT (K)	Maximum Voltage Output	Maximum Power Output	Year	Reference
p-type: PEDOT:PSS n-type: Ag_2Te	2 pairs	20	3.5 mV	5 nW	2015	[125]
PEDOT:PSS	5 legs	75.2	4.4 mV	12.29 nW	2015	40
p-type: Sb_2Te_3 n-type: Bi_2Te_3	-	200	45.2 mV	14.1 µW	2016	[115]
p-type: $Bi_{0.5}Sb_{1.5}Te_3$ n-type: $Bi_2Se_{0.3}Te_{2.7}$	2 pairs	12	10 mV	18 nW	2016	[116]
p-type: CNT/$FeCl_3$ n-type: CNT/PEI	60 pairs	5	47 mV	4.2 µW	2017	[113]
PEDOT:PSS	26 legs	66	21 mV	12 nW	2017	[121]
p-type: $Bi_{0.5}Sb_{1.5}Te_3$ n-type: Bi_2Se_3	7 pairs	60	97 mV	1.65 µW	2017	[117]
p-type: PEDOT:PSS n-type: constantan	5 pairs	74.3	18.7 mV	212.6 nW	2017	[126]
p-type: CNT/PEG n-type: CNT/[BMIM]PF_6/PEG	-	25	10 mV	8 nW	2017	[119]
p-type: WPU/PEDOT:PSS/CNT n-type: WPU/n-doped CNT	10 pairs	66	0.8 mV	2.6 nW	2017	[127]
p-type: PEDOT:PSS/CNT n-type: PEDOT:PSS/CNT/PEI	12 pairs	10	8 mV	0.43 µW	2018	[128]
p-type: PEDOT:PSS/CNT n-type: PEDOT:PSS/CNT/PEI	12 pairs	10	16 mV	0.61 µW	2018	[129]
p-type: PEDOT:PSS n-type: CNT/PEI	5 pairs	60	21 mV	0.43 µW	2018	[130]
p-type:P3HT n-type: Ag paste	13 pairs	50	12 mV	1.15 µW	2018	[122]
PEDOT:Cl	2 legs	25	1.2 mV	4.5 nW	2019	41
Ag_2Se	4 legs	30	18 mV	0.46 µW	2019	[118]
p-type: PEDOT:Tos n-type: n-doped CNT	5 pairs	100	22 mV	62 nW	2019	42
PEDOT:PSS	48 legs	0.6	0.98 mV	2 nW	2019	[123]
PEDOT:Cl	-	16.5	14 mV	0.375 µW	2019	[114]
PEDOT:PSS	5 legs	70	7 mV	1.4 µW	2020	[124]
p-type: CNT/PEDOT:PSS n-type: CNT/oleamine	-	44	26 mV	4.64 µW	2020	[131]
CNT/PEDOT:ClO_4	30 legs	31	11 mV	0.9 µW	2020	Our work
p-type: rGO/PEDOT:PSS n-type: rGO	10 pairs	16.5	20 mV	0.45 µW	2021	[132]
CNT fibers doped with ICl	4 legs	60	80 mV	5 µW	2021	[120]
p-type: CNT/PEDOT:PSS n-type: CNT/PEI	8 pairs	51	35.2 mV	0.62 µW	2022	[133]
CNT/PEDOT:BTFMSI	14 legs	57	15 mV	6.5 µW	2022	Our work

* The term pair is used for TEGs made with p-n junctions. The term leg is used for TEGs made with p-p junctions or n-n junctions.

4.5 Conclusions

This chapter has developed a different methodology to obtain textiles electrochemically coated by conductive polymers. This new methodology involves coating textile fibers with carbon nanotubes using the LbL technique to use the MWCNT-coated textile as a working electrode and electrodeposit different conductive polymers. In the first section of this chapter, three of the most widely used conductive polymers were used: PEDOT, PPy, and PANI. First, a study was carried out by varying the electrodeposition time to determine the optimal time for the electrical conductivity and the Seebeck coefficient to be high but for the polymer mass deposited to be low. Then, the quality of the different coatings was evaluated using SEM images and Raman spectroscopy. As a result, the coating of the textile fibers with MWCNTs, PEDOT, and PPy were very homogeneous, unlike that of PANI. In addition, the thermal stability study carried out by TGA showed that the felt fabric coated with PANI:H_2SO_4 is the least stable, probably due to a deterioration of the fibers in the acid medium necessary for the synthesis of PANI.

Since the coating of the textile with PEDOT:ClO_4 is the one that offers the best thermoelectric properties and the one that best covers the fibers, it was decided to continue the development of thermoelectric fabrics with said coating. In the second section of this chapter, two textiles were used: one made of felt, which is not woven, and the other made of cotton, which is woven. As in the previous section, these fabrics were coated with carbon nanotubes and then with PEDOT:ClO_4 by electrodeposition. Through Raman spectroscopy and analysis of SEM images, it was shown that the coating of both MWCNTs and PEDOT:ClO_4 was very homogeneous in both fabrics. The flexible properties of both fabrics were evaluated by monitoring the evolution of electrical conductivity as a function of the torsion angle and the number of bends performed on each fabric. The results showed that the cotton and felt fabrics maintained 90% of the initial electrical conductivity after the flexibility tests were performed. Finally, a thermoelectric module of 20 elements was made with cotton fabric and another with felt fabric. The results showed an eight times higher power output favorable to the felt cloth. This difference in power output was attributed to the felt fabric's ability to generate a higher thermal gradient and thus generate higher power. Finally, a third thermoelectric generator based on the felt cloth coated with PEDOT:ClO_4 and with 30 legs was elaborated, with which an output power of 0.9 μW was obtained with a thermal gradient of 31 K.

The last section of this chapter sought to improve the thermoelectric efficiency of PEDOT-coated felt fabrics with different counterions. SEM images and Raman spectroscopy showed that the coating of the PEDOT felt fibers with the different counterions is excellent. The thermogravimetric analysis showed that all the coatings are stable up to 250 ºC. Differential scanning calorimetry together with DMA determined the glass transition temperature of the felt fabrics. Furthermore, the storage modulus showed that the viscoelastic stiffness increases after coating the pristine felt fabric with MWCNT. Then, the electrodeposition of PEDOT with different counterions decreases the storage modulus of the Felt/MWCNT fabric. The flexible capacity of thermoelectric fabrics was also evaluated by monitoring the change in electrical conductivity as a function of twist angle, a number of bends, and bending radius. After testing, the fabrics with the PEDOT coatings showed less variation in electrical conductivity. The thermoelectric properties of felt fabrics (electrical conductivity, Seebeck coefficient, and thermal conductivity) were evaluated for the different coatings, showing that the PEDOT:BTFMSI coating offers the highest thermoelectric efficiency. For this reason, a wearable thermoelectric generator was finally elaborated with the felt fabrics coated with MWCNTs and PEDOT:BTFMSI, through which an output power of 6.5 μW was obtained with a temperature difference of 57 K.

References

(1) Pan, S.; Yang, Z.; Chen, P.; Deng, J.; Li, H.; Peng, H. Wearable Solar Cells by Stacking Textile Electrodes. *Angew. Chemie* **2014**, *126* (24), 6224–6228. https://doi.org/10.1002/ange.201402561.

(2) Gao, W.; Emaminejad, S.; Nyein, H. Y. Y.; Challa, S.; Chen, K.; Peck, A.; Fahad, H. M.; Ota, H.; Shiraki, H.; Kiriya, D.; Lien, D.-H.; Brooks, G. A.; Davis, R. W.; Javey, A. Fully Integrated Wearable Sensor Arrays for Multiplexed in Situ Perspiration Analysis. *Nature* **2016**, *529* (7587), 509–514. https://doi.org/10.1038/nature16521.

(3) Dargusch, M.; Liu, W.; Chen, Z. Thermoelectric Generators: Alternative Power Supply for Wearable Electrocardiographic Systems. *Adv. Sci.* **2020**, *7* (18), 2001362. https://doi.org/10.1002/advs.202001362.

(4) Lage-Rivera, S.; Ares-Pernas, A.; Abad, M. Last Developments in Polymers for Wearable Energy Storage Devices. *Int. J. Energy Res.* **2022**, *46* (8), 10475–10498. https://doi.org/10.1002/er.7934.

(5) Starner, T. Human-Powered Wearable Computing. *IBM Syst. J.* **1996**, *35* (3.4), 618–629. https://doi.org/10.1147/sj.353.0618.

(6) Wang, Z. L. On Maxwell's Displacement Current for Energy and Sensors: The Origin of Nanogenerators. *Mater. Today* **2017**, *20* (2), 74–82. https://doi.org/10.1016/j.mattod.2016.12.001.

(7) Dong, K.; Peng, X.; An, J.; Wang, A. C.; Luo, J.; Sun, B.; Wang, J.; Wang, Z. L. Shape Adaptable and Highly Resilient 3D Braided Triboelectric Nanogenerators as E-Textiles for Power and Sensing. *Nat. Commun.* **2020**, *11* (1), 2868. https://doi.org/10.1038/s41467-020-16642-6.

(8) Wang, Z. L.; Song, J. Piezoelectric Nanogenerators Based on Zinc Oxide Nanowire Arrays. *Science (80-.).* **2006**, *312* (5771), 242–246. https://doi.org/10.1126/science.1124005.

(9) Shi, X.; He, J. Thermopower and Harvesting Heat. *Science (80-.).* **2021**, *371* (6527), 343–344. https://doi.org/10.1126/science.abf3342.

(10) Wang, Z. L.; Wu, W. Nanotechnology-Enabled Energy Harvesting for Self-Powered Micro-/Nanosystems. *Angew. Chemie Int. Ed.* **2012**, *51* (47), 11700–11721. https://doi.org/10.1002/anie.201201656.

(11) Strolwijk, J. A. J.; Hardy, J. D. *Handbook of Physiology*; American Physiological Society, 1977.

(12) Riemer, R.; Shapiro, A. Biomechanical Energy Harvesting from Human Motion: Theory, State of the Art, Design Guidelines, and Future Directions. *J. Neuroeng. Rehabil.* **2011**, *8* (1), 22. https://doi.org/10.1186/1743-0003-8-22.

(13) Suarez, F.; Nozariasbmarz, A.; Vashaee, D.; Öztürk, M. C. Designing Thermoelectric Generators for Self-Powered Wearable Electronics. *Energy Environ. Sci.* **2016**, *9* (6), 2099–2113. https://doi.org/10.1039/C6EE00456C.

(14) Webb, P. Temperatures of Skin, Subcutaneous Tissue, Muscle and Core in Resting Men in Cold, Comfortable and Hot Conditions. *Eur. J. Appl. Physiol. Occup. Physiol.* **1992**, *64* (5), 471–476. https://doi.org/10.1007/BF00625070.

(15) Gayner, C.; Kar, K. K. Recent Advances in Thermoelectric Materials. *Prog. Mater. Sci.* **2016**, *83*, 330–382. https://doi.org/10.1016/j.pmatsci.2016.07.002.

(16) Ma, Z.; Wei, J.; Song, P.; Zhang, M.; Yang, L.; Ma, J.; Liu, W.; Yang, F.; Wang, X. Review of Experimental Approaches for Improving ZT of Thermoelectric Materials. *Mater. Sci. Semicond. Process.* **2021**, *121*, 105303. https://doi.org/10.1016/j.mssp.2020.105303.

(17) Fan, Z.; Du, D.; Guan, X.; Ouyang, J. Polymer Films with Ultrahigh Thermoelectric Properties Arising from Significant Seebeck Coefficient Enhancement by Ion Accumulation on Surface. *Nano Energy* **2018**, *51*, 481–488. https://doi.org/10.1016/j.nanoen.2018.07.002.

(18) Tian, R.; Wan, C.; Wang, Y.; Wei, Q.; Ishida, T.; Yamamoto, A.; Tsuruta, A.; Shin, W.; Li, S.; Koumoto, K. A Solution-Processed TiS 2 /Organic Hybrid Superlattice Film towards Flexible Thermoelectric Devices. *J. Mater. Chem. A* **2017**, *5* (2), 564–570. https://doi.org/10.1039/C6TA08838D.

(19) Liu, P.; Ding, W.; Liu, J.; Shen, L.; Jiang, F.; Liu, P.; Zhu, Z.; Zhang, G.; Liu, C.; Xu, J. Surface Termination Modification on High-Conductivity MXene Film for Energy Conversion. *J. Alloys Compd.* **2020**, *829*, 154634. https://doi.org/10.1016/j.jallcom.2020.154634.

(20) Stevens, D. L.; Parra, A.; Grunlan, J. C. Thermoelectric Performance Improvement of Polymer Nanocomposites by Selective Thermal Degradation. *ACS Appl. Energy Mater.* **2019**, *2* (8), 5975–5982. https://doi.org/10.1021/acsaem.9b01079.

(21) Kim, W. S.; Anoop, G.; Jeong, I.-S.; Lee, H. J.; Kim, H. Bin; Kim, S. H.; Goo, G. W.; Lee, H.; Lee, H. J.; Kim, C.; Lee, J.-H.; Mun, B. S.; Park, J.-W.; Lee, E.; Jo, J. Y. Feasible Tuning of Barrier Energy in PEDOT:PSS/Bi2Te3 Nanowires-Based Thermoelectric Nanocomposite Thin Films through Polar Solvent Vapor Annealing. *Nano Energy* **2020**, *67*, 104207. https://doi.org/10.1016/j.nanoen.2019.104207.

(22) Panigrahy, S.; Kandasubramanian, B. Polymeric Thermoelectric PEDOT: PSS & Composites: Synthesis, Progress, and Applications. *Eur. Polym. J.* **2020**, *132*, 109726. https://doi.org/10.1016/j.eurpolymj.2020.109726.

(23) Jia, Y.; Jiang, Q.; Sun, H.; Liu, P.; Hu, D.; Pei, Y.; Liu, W.; Crispin, X.; Fabiano, S.; Ma, Y.; Cao, Y. Wearable Thermoelectric Materials and Devices for Self-Powered Electronic Systems. *Adv. Mater.* **2021**, *33* (42), 2102990. https://doi.org/10.1002/adma.202102990.

(24) Kishi, M.; Nemoto, H.; Hamao, T.; Yamamoto, M.; Sudou, S.; Mandai, M.; Yamamoto, S. Micro Thermoelectric Modules and Their Application to Wristwatches as an Energy Source. In *18th International Conference on Thermoelectrics. Proceedings, ICT'99 (Cat. No.99TH8407)*; IEEE: Baltimore, MD, 1999; pp 301–307. https://doi.org/10.1109/ICT.1999.843389.

(25) Leonov, V.; Vullers, R. J. M. Wearable Electronics Self-Powered by Using Human Body Heat: The State of the Art and the Perspective. *J. Renew. Sustain. Energy* **2009**, *1* (6), 062701. https://doi.org/10.1063/1.3255465.

(26) Lay-Ekuakille, A.; Vendramin, G.; Trotta, A.; Mazzotta, G. Thermoelectric Generator Design Based on Power from Body Heat for Biomedical Autonomous Devices. In *2009 IEEE International Workshop on Medical Measurements and Applications*; IEEE: Cetraro, 2009; pp 1–4. https://doi.org/10.1109/MEMEA.2009.5167942.

(27) Chanditha Janaka Udalagama. Electrical Energy Generation from Body Heat. In *2010 IEEE International Conference on Sustainable Energy Technologies (ICSET)*; IEEE: Kandy, 2010; pp 1–5. https://doi.org/10.1109/ICSET.2010.5684932.

(28) Wahbah, M.; Alhawari, M.; Mohammad, B.; Saleh, H.; Ismail, M. Characterization of Human Body-Based Thermal and Vibration Energy Harvesting for Wearable Devices. *IEEE J. Emerg. Sel. Top. Circuits Syst.* **2014**, *4* (3), 354–363.

https://doi.org/10.1109/JETCAS.2014.2337195.

(29) Song, H.; Cai, K. Preparation and Properties of PEDOT:PSS/Te Nanorod Composite Films for Flexible Thermoelectric Power Generator. *Energy* **2017**, *125*, 519–525. https://doi.org/10.1016/j.energy.2017.01.037.

(30) Massetti, M.; Bonfadini, S.; Nava, D.; Butti, M.; Criante, L.; Lanzani, G.; Qiu, L.; Hummelen, J. C.; Liu, J.; Koster, L. J. A.; Caironi, M. Fully Direct Written Organic Micro-Thermoelectric Generators Embedded in a Plastic Foil. *Nano Energy* **2020**, *75*, 104983. https://doi.org/10.1016/j.nanoen.2020.104983.

(31) Francioso, L.; De Pascali, C.; Sglavo, V.; Grazioli, A.; Masieri, M.; Siciliano, P. Modelling, Fabrication and Experimental Testing of an Heat Sink Free Wearable Thermoelectric Generator. *Energy Convers. Manag.* **2017**, *145*, 204–213. https://doi.org/10.1016/j.enconman.2017.04.096.

(32) We, J. H.; Kim, S. J.; Cho, B. J. Hybrid Composite of Screen-Printed Inorganic Thermoelectric Film and Organic Conducting Polymer for Flexible Thermoelectric Power Generator. *Energy* **2014**, *73*, 506–512. https://doi.org/10.1016/j.energy.2014.06.047.

(33) Zeng, W.; Tao, X.-M.; Lin, S.; Lee, C.; Shi, D.; Lam, K.; Huang, B.; Wang, Q.; Zhao, Y. Defect-Engineered Reduced Graphene Oxide Sheets with High Electric Conductivity and Controlled Thermal Conductivity for Soft and Flexible Wearable Thermoelectric Generators. *Nano Energy* **2018**, *54*, 163–174. https://doi.org/10.1016/j.nanoen.2018.10.015.

(34) Rojas, J. P.; Singh, D.; Conchouso, D.; Arevalo, A.; Foulds, I. G.; Hussain, M. M. Stretchable Helical Architecture Inorganic-Organic Hetero Thermoelectric Generator. *Nano Energy* **2016**, *30*, 691–699. https://doi.org/10.1016/j.nanoen.2016.10.054.

(35) Xu, X.; Zuo, Y.; Cai, S.; Tao, X.; Zhang, Z.; Zhou, X.; He, S.; Fang, X.; Peng, H. Three-Dimensional Helical Inorganic Thermoelectric Generators and Photodetectors for Stretchable and Wearable Electronic Devices. *J. Mater. Chem. C* **2018**, *6* (18), 4866–4872. https://doi.org/10.1039/C8TC01183D.

(36) Yang, Y.; Hu, H.; Chen, Z.; Wang, Z.; Jiang, L.; Lu, G.; Li, X.; Chen, R.; Jin, J.; Kang, H.; Chen, H.; Lin, S.; Xiao, S.; Zhao, H.; Xiong, R.; Shi, J.; Zhou, Q.; Xu, S.; Chen, Y. Stretchable Nanolayered Thermoelectric Energy Harvester on Complex and Dynamic Surfaces. *Nano Lett.* **2020**, *20* (6), 4445–4453. https://doi.org/10.1021/acs.nanolett.0c01225.

(37) Kim, N.; Lienemann, S.; Petsagkourakis, I.; Alemu Mengistie, D.; Kee, S.; Ederth, T.; Gueskine, V.; Leclère, P.; Lazzaroni, R.; Crispin, X.; Tybrandt, K. Elastic Conducting Polymer Composites in Thermoelectric Modules. *Nat. Commun.* **2020**, *11* (1), 1424. https://doi.org/10.1038/s41467-020-15135-w.

(38) Kim, M.-K.; Kim, M.-S.; Lee, S.; Kim, C.; Kim, Y.-J. Wearable Thermoelectric Generator for Harvesting Human Body Heat Energy. *Smart Mater. Struct.* **2014**, *23* (10), 105002. https://doi.org/10.1088/0964-1726/23/10/105002.

(39) Lu, Z.; Zhang, H.; Mao, C.; Li, C. M. Silk Fabric-Based Wearable Thermoelectric Generator for Energy Harvesting from the Human Body. *Appl. Energy* **2016**, *164*, 57–63. https://doi.org/10.1016/j.apenergy.2015.11.038.

(40) Du, Y.; Cai, K.; Chen, S.; Wang, H.; Shen, S. Z.; Donelson, R.; Lin, T. Thermoelectric Fabrics: Toward Power Generating Clothing. *Sci. Rep.* **2015**, *5* (1), 6411. https://doi.org/10.1038/srep06411.

(41) Allison, L. K.; Andrew, T. L. A Wearable All-Fabric Thermoelectric Generator. *Adv. Mater. Technol.* **2019**, *4* (5), 1800615. https://doi.org/10.1002/admt.201800615.

(42) Jia, Y.; Shen, L.; Liu, J.; Zhou, W.; Du, Y.; Xu, J.; Liu, C.; Zhang, G.; Zhang, Z.; Jiang, F. An Efficient PEDOT-Coated Textile for Wearable Thermoelectric Generators and Strain Sensors. *J. Mater. Chem. C* **2019**, *7* (12), 3496–3502. https://doi.org/10.1039/C8TC05906C.

(43) Allison, L.; Hoxie, S.; Andrew, T. L. Towards Seamlessly-Integrated Textile Electronics: Methods to Coat Fabrics and Fibers with Conducting Polymers for Electronic Applications. *Chem. Commun.* **2017**, *53* (53), 7182–7193. https://doi.org/10.1039/C7CC02592K.

(44) *Handbook of Smart Textiles*; Tao, X., Ed.; Springer Singapore: Singapore, 2015. https://doi.org/10.1007/978-981-4451-45-1.

(45) Moraes, M. R.; Alves, A. C.; Toptan, F.; Martins, M. S.; Vieira, E. M. F.; Paleo, A. J.; Souto, A. P.; Santos, W. L. F.; Esteves, M. F.; Zille, A. Glycerol/PEDOT:PSS Coated Woven Fabric as a Flexible Heating Element on Textiles. *J. Mater. Chem. C* **2017**, *5* (15), 3807–3822. https://doi.org/10.1039/C7TC00486A.

(46) Alf, M. E.; Asatekin, A.; Barr, M. C.; Baxamusa, S. H.; Chelawat, H.; Ozaydin-Ince, G.; Petruczok, C. D.; Sreenivasan, R.; Tenhaeff, W. E.; Trujillo, N. J.; Vaddiraju, S.; Xu, J.; Gleason, K. K. Chemical Vapor Deposition of Conformal, Functional, and Responsive Polymer Films. *Adv. Mater.* **2009**, *22* (18), 1993–2027.

https://doi.org/10.1002/adma.200902765.

(47) Bhattacharyya, D.; Howden, R. M.; Borrelli, D. C.; Gleason, K. K. Vapor Phase Oxidative Synthesis of Conjugated Polymers and Applications. *J. Polym. Sci. Part B Polym. Phys.* **2012**, *50* (19), 1329–1351. https://doi.org/10.1002/polb.23138.

(48) Vaeth, K. M.; Jensen, K. F. Selective Growth of Poly(p-Phenylene Vinylene) Prepared by Chemical Vapor Deposition. *Adv. Mater.* **1999**, *11* (10), 814–820. https://doi.org/10.1002/(SICI)1521-4095(199907)11:10<814::AID-ADMA814>3.0.CO;2-Z.

(49) Lau, K. K. S.; Gleason, K. K. Initiated Chemical Vapor Deposition (ICVD) of Poly(Alkyl Acrylates): An Experimental Study. *Macromolecules* **2006**, *39* (10), 3688–3694. https://doi.org/10.1021/ma0601619.

(50) Gleason, K. K. *CVD Polymers: Fabrication of Organic Surfaces and Devices*; Gleason, K. K., Ed.; John Wiley & Sons: Weinheim, 2015.

(51) Heydari Gharahcheshmeh, M.; Gleason, K. K. Device Fabrication Based on Oxidative Chemical Vapor Deposition (OCVD) Synthesis of Conducting Polymers and Related Conjugated Organic Materials. *Adv. Mater. Interfaces* **2019**, *6* (1), 1801564. https://doi.org/10.1002/admi.201801564.

(52) Heydari Gharahcheshmeh, M.; Tavakoli, M. M.; Gleason, E. F.; Robinson, M. T.; Kong, J.; Gleason, K. K. Tuning, Optimization, and Perovskite Solar Cell Device Integration of Ultrathin Poly(3,4-Ethylene Dioxythiophene) Films via a Single-Step All-Dry Process. *Sci. Adv.* **2019**, *5* (11). https://doi.org/10.1126/sciadv.aay0414.

(53) Zhang, X.; Li, T.-T.; Ren, H.-T.; Peng, H.-K.; Jiang, Q.; Wu, L.; Shiu, B.-C.; Wang, Y.; Lou, C.-W.; Lin, J.-H. Near Room-Temperature in Situ Interfacial Polymerization for PEDOT-Based Thermoelectric Textile. *Mater. Today Commun.* **2022**, 103856. https://doi.org/10.1016/j.mtcomm.2022.103856.

(54) Culebras, M.; Uriol, B.; Gómez, C. M.; Cantarero, A. Controlling the Thermoelectric Properties of Polymers: Application to PEDOT and Polypyrrole. *Phys. Chem. Chem. Phys.* **2015**, *17* (23), 15140–15145. https://doi.org/10.1039/C5CP01940K.

(55) Babu, K. F.; Senthilkumar, R.; Noel, M.; Kulandainathan, M. A. Polypyrrole Microstructure Deposited by Chemical and Electrochemical Methods on Cotton Fabrics. *Synth. Met.* **2009**, *159* (13), 1353–1358. https://doi.org/https://doi.org/10.1016/j.synthmet.2009.03.005.

(56) Maziz, A.; Concas, A.; Khaldi, A.; Stålhand, J.; Persson, N.-K.; Jager, E. W. H.

Knitting and Weaving Artificial Muscles. *Science Advances*. 2017, p e1600327. https://doi.org/10.1126/sciadv.1600327.

(57) Sadi, M. S.; Pan, J.; Xu, A.; Cheng, D.; Cai, G.; Wang, X. Direct Dip-Coating of Carbon Nanotubes onto Polydopamine-Templated Cotton Fabrics for Wearable Applications. *Cellulose* **2019**, *26* (12), 7569–7579. https://doi.org/10.1007/s10570-019-02628-1.

(58) Jeon, I.-Y.; Chang, D. W.; Kumar, N. A.; Baek, J.-B. Functionalization of Carbon Nanotubes. In *Carbon Nanotubes*; Yellampalli, S., Ed.; IntechOpen: Rijeka, 2011. https://doi.org/10.5772/18396.

(59) Prato, M.; Kostarelos, K.; Bianco, A. Functionalized Carbon Nanotubes in Drug Design and Discovery. *Acc. Chem. Res.* **2008**, *41* (1), 60–68. https://doi.org/10.1021/ar700089b.

(60) Engtrakul, C.; Davis, M. F.; Gennett, T.; Dillon, A. C.; Jones, K. M.; Heben, M. J. Protonation of Carbon Single-Walled Nanotubes Studied Using 13C and 1H−13C Cross Polarization Nuclear Magnetic Resonance and Raman Spectroscopies. *J. Am. Chem. Soc.* **2005**, *127* (49), 17548–17555. https://doi.org/10.1021/ja0557886.

(61) Yi, W.; Malkovskiy, A.; Chu, Q.; Sokolov, A. P.; Colon, M. L.; Meador, M.; Pang, Y. Wrapping of Single-Walled Carbon Nanotubes by a π-Conjugated Polymer: The Role of Polymer Conformation-Controlled Size Selectivity. *J. Phys. Chem. B* **2008**, *112* (39), 12263–12269. https://doi.org/10.1021/jp804083n.

(62) Yu, J.; Grossiord, N.; Koning, C. E.; Loos, J. Controlling the Dispersion of Multi-Wall Carbon Nanotubes in Aqueous Surfactant Solution. *Carbon N. Y.* **2007**, *45* (3), 618–623. https://doi.org/https://doi.org/10.1016/j.carbon.2006.10.010.

(63) Munkhbayar, B.; Nine, M. J.; Jeoun, J.; Bat-Erdene, M.; Chung, H.; Jeong, H. Influence of Dry and Wet Ball Milling on Dispersion Characteristics of the Multi-Walled Carbon Nanotubes in Aqueous Solution with and without Surfactant. *Powder Technol.* **2013**, *234*, 132–140. https://doi.org/https://doi.org/10.1016/j.powtec.2012.09.045.

(64) Ferraris, J. P.; Hanlon, T. R. Optical, Electrical and Electrochemical Properties of Heteroaromatic Copolymers. *Polymer (Guildf).* **1989**, *30* (7), 1319–1327. https://doi.org/https://doi.org/10.1016/0032-3861(89)90054-2.

(65) Sadki, S.; Schottland, P.; Brodie, N.; Sabouraud, G. The Mechanisms of Pyrrole Electropolymerization. *Chem. Soc. Rev.* **2000**, *29* (5), 283–293. https://doi.org/10.1039/A807124A.

(66) Tanaka, K.; Shichiri, T.; Wang, S.; Yamabe, T. A Study of the Electropolymerization of Thiophene. *Synth. Met.* **1988**, *24* (3), 203–215. https://doi.org/https://doi.org/10.1016/0379-6779(88)90258-5.

(67) Zotti, G.; Cattarin, S.; Comisso, N. Cyclic Potential Sweep Electropolymerization of Aniline: The Role of Anions in the Polymerization Mechanism. *J. Electroanal. Chem. Interfacial Electrochem.* **1988**, *239* (1), 387–396. https://doi.org/https://doi.org/10.1016/0022-0728(88)80293-6.

(68) Tsai, T.-H.; Wu, Y.-F. Wet Etching Mechanisms of ITO Films in Oxalic Acid. *Microelectron. Eng.* **2006**, *83* (3), 536–541. https://doi.org/https://doi.org/10.1016/j.mee.2005.12.003.

(69) Horta-Romarís, L.; González-Rodríguez, M. V.; Lasagabáster, A.; Rivadulla, F.; Abad, M.-J. Thermoelectric Properties and Intrinsic Conduction Processes in DBSA and NaSIPA Doped Polyanilines. *Synth. Met.* **2018**, *243*, 44–50. https://doi.org/10.1016/j.synthmet.2018.06.002.

(70) Wang, L.; Lin, T.; Wang, X.; Kaynak, A. Frictional and Tensile Properties of Conducting Polymer Coated Wool and Alpaca Fibers. *Fibers Polym.* **2005**, *6* (3), 259–262. https://doi.org/10.1007/BF02875651.

(71) Castagnola, V.; Bayon, C.; Descamps, E.; Bergaud, C. Morphology and Conductivity of PEDOT Layers Produced by Different Electrochemical Routes. *Synth. Met.* **2014**, *189*, 7–16. https://doi.org/https://doi.org/10.1016/j.synthmet.2013.12.013.

(72) Vlamidis, Y.; Lanzi, M.; Salatelli, E.; Gualandi, I.; Fraboni, B.; Setti, L.; Tonelli, D. Electrodeposition of PEDOT Perchlorate as an Alternative Route to PEDOT:PSS for the Development of Bulk Heterojunction Solar Cells. *J. Solid State Electrochem.* **2015**, *19* (6), 1685–1693. https://doi.org/10.1007/s10008-015-2802-2.

(73) Hong, K. H.; Oh, K. W.; Kang, T. J. Preparation and Properties of Electrically Conducting Textiles Byin Situ Polymerization of Poly(3,4-Ethylenedioxythiophene). *J. Appl. Polym. Sci.* **2005**, *97* (3), 1326–1332. https://doi.org/10.1002/app.21835.

(74) Montes-Morán, M. A.; Young, R. J. Raman Spectroscopy Study of HM Carbon Fibres: Effect of Plasma Treatment on the Interfacial Properties of Single Fibre/Epoxy Composites. *Carbon N. Y.* **2002**, *40* (6), 845–855. https://doi.org/https://doi.org/10.1016/S0008-6223(01)00212-3.

(75) Das, P.; Tiwari, P. Thermal Degradation Study of Waste Polyethylene Terephthalate

(PET) under Inert and Oxidative Environments. *Thermochim. Acta* **2019**, *679*, 178340. https://doi.org/10.1016/j.tca.2019.178340.

(76) Zhou, T. Y.; Tsui, G. C. P.; Liang, J. Z.; Zou, S. Y.; Tang, C. Y.; Mišković-Stanković, V. Thermal Properties and Thermal Stability of PP/MWCNT Composites. *Compos. Part B Eng.* **2016**, *90*, 107–114. https://doi.org/10.1016/j.compositesb.2015.12.013.

(77) Culebras, M.; Cho, C.; Krecker, M.; Smith, R.; Song, Y.; Gómez, C. M.; Cantarero, A.; Grunlan, J. C. High Thermoelectric Power Factor Organic Thin Films through Combination of Nanotube Multilayer Assembly and Electrochemical Polymerization. *ACS Appl. Mater. Interfaces* **2017**, *9* (7), 6306–6313. https://doi.org/10.1021/acsami.6b15327.

(78) Edwards, H. G. M.; Farwell, D. W.; Webster, D. FT Raman Microscopy of Untreated Natural Plant Fibres. *Spectrochim. Acta Part A Mol. Biomol. Spectrosc.* **1997**, *53* (13), 2383–2392. https://doi.org/https://doi.org/10.1016/S1386-1425(97)00178-9.

(79) Kavkler, K.; Demšar, A. Examination of Cellulose Textile Fibres in Historical Objects by Micro-Raman Spectroscopy. *Spectrochim. Acta Part A Mol. Biomol. Spectrosc.* **2011**, *78* (2), 740–746. https://doi.org/https://doi.org/10.1016/j.saa.2010.12.006.

(80) Was-Gubala, J.; Machnowski, W. Application of Raman Spectroscopy for Differentiation Among Cotton and Viscose Fibers Dyed with Several Dye Classes. *Spectrosc. Lett.* **2014**, *47* (7), 527–535. https://doi.org/10.1080/00387010.2013.820760.

(81) Culebras, M.; Gómez, C. M.; Cantarero, A. Enhanced Thermoelectric Performance of PEDOT with Different Counter-Ions Optimized by Chemical Reduction. *J. Mater. Chem. A* **2014**, *2* (26), 10109–10115. https://doi.org/10.1039/C4TA01012D.

(82) Culebras, M.; Serrano-Claumarchirant, J. F.; Sanchis, M. J.; Landfester, K.; Cantarero, A.; Gómez, C. M.; Muñoz-Espí, R. Conducting PEDOT Nanoparticles: Controlling Colloidal Stability and Electrical Properties. *J. Phys. Chem. C* **2018**, *122* (33), 19197–19203. https://doi.org/10.1021/acs.jpcc.8b04981.

(83) Seki, Y.; Takahashi, M.; Takashiri, M. Enhanced Thermoelectric Properties of Electropolymerized Poly (3,4-Ethylenedioxythiophene) Thin Films by Optimizing Electrolyte Temperature and Thermal Annealing Temperature. *Org. Electron.* **2018**, *55*, 112–116. https://doi.org/https://doi.org/10.1016/j.orgel.2018.01.028.

(84) Massonnet, N.; Carella, A.; Jaudouin, O.; Rannou, P.; Laval, G.; Celle, C.; Simonato, J.-P. Improvement of the Seebeck Coefficient of PEDOT:PSS by Chemical Reduction Combined with a Novel Method for Its Transfer Using Free-Standing Thin Films. *J. Mater. Chem. C* **2014**, *2* (7), 1278–1283. https://doi.org/10.1039/C3TC31674B.

(85) Du, Y.; Tian, T.; Meng, Q.; Dou, Y.; Xu, J.; Shen, S. Z. Thermoelectric Properties of Flexible Composite Fabrics Prepared by a Gas Polymerization Combining Solution Coating Process. *Synth. Met.* **2020**, *260*, 116254. https://doi.org/10.1016/j.synthmet.2019.116254.

(86) Chen; Lwo. Large-Area Laying of Soft Textile Power Generators for the Realization of Body Heat Harvesting Clothing. *Coatings* **2019**, *9* (12), 831. https://doi.org/10.3390/coatings9120831.

(87) Allison, L. K.; Andrew, T. L. A Wearable All-Fabric Thermoelectric Generator. *Adv. Mater. Technol.* **2019**, *4* (5), 1800615. https://doi.org/10.1002/admt.201800615.

(88) Du, Y.; Cai, K.; Chen, S.; Wang, H.; Shen, S. Z.; Donelson, R.; Lin, T. Thermoelectric Fabrics: Toward Power Generating Clothing. *Sci. Rep.* **2015**, *5* (1), 6411. https://doi.org/10.1038/srep06411.

(89) Jia, Y.; Shen, L.; Liu, J.; Zhou, W.; Du, Y.; Xu, J.; Liu, C.; Zhang, G.; Zhang, Z.; Jiang, F. An Efficient PEDOT-Coated Textile for Wearable Thermoelectric Generators and Strain Sensors. *J. Mater. Chem. C* **2019**, *7* (12), 3496–3502. https://doi.org/10.1039/C8TC05906C.

(90) Khoso, N. A.; Ahmed, A.; Deb, H.; Tian, S.; Jiao, X.; Gong, X. Y.; Wang, J. Controlled Template-Free in-Situ Polymerization of PEDOT for Enhanced Thermoelectric Performance on Textile Substrate. *Org. Electron.* **2019**, *75*, 105368. https://doi.org/10.1016/j.orgel.2019.07.026.

(91) Sun, T.; Zhou, B.; Zheng, Q.; Wang, L.; Jiang, W.; Snyder, G. J. Stretchable Fabric Generates Electric Power from Woven Thermoelectric Fibers. *Nat Commun* **2020**, *11* (1), 572. https://doi.org/10.1038/s41467-020-14399-6.

(92) Kirihara, K.; Wei, Q.; Mukaida, M.; Ishida, T. Thermoelectric Power Generation Using Nonwoven Fabric Module Impregnated with Conducting Polymer PEDOT:PSS. *Synth. Met.* **2017**, *225*, 41–48. https://doi.org/10.1016/j.synthmet.2017.01.001.

(93) Bower, D. I.; Ward, I. M. Quantitative Characterization of Orientation in PET Fibres

by Raman Spectroscopy. *Polymer (Guildf).* **1982**, *23* (5), 645–649. https://doi.org/10.1016/0032-3861(82)90044-1.

(94) Lee, C. J.; Tsai, I. S. Effect of Different Dielectric Constant Solvents Addition on PEDOT-PSS Conductive Polymer and Its Application. *Mater. Sci. Forum* **2011**, *687*, 625–633. https://doi.org/10.4028/www.scientific.net/MSF.687.625.

(95) Panowicz, R.; Konarzewski, M.; Durejko, T.; Szala, M.; Łazińska, M.; Czerwińska, M.; Prasuła, P. Properties of Polyethylene Terephthalate (PET) after Thermo-Oxidative Aging. *Materials (Basel).* **2021**, *14* (14), 3833. https://doi.org/10.3390/ma14143833.

(96) Bernhard Wunderlich. *Thermal Analysis of Polymeric Materials*; Springer-Verlag: Berlin/Heidelberg, 2005. https://doi.org/10.1007/b137476.

(97) Rodrigues, A.; Figueiredo, L.; Diogo, H.; Bordado, J. Mechanical Behavior of PET Fibers and Textiles for Stent-Grafts Using Video Extensometry and Image Analysis. *Sci. Technol. Mater.* **2018**, *30*, 23–33. https://doi.org/10.1016/j.stmat.2018.11.001.

(98) Rahimi, M. H.; Parvinzadeh, M.; Navid, M. Y.; Ahmadi, S. Thermal Characterization and Flammability of Polyester Fiber Coated with Nonionic and Cationic Softeners. *J. Surfactants Deterg.* **2011**, *14* (4), 595–603. https://doi.org/10.1007/s11743-011-1255-6.

(99) Gudayu, A. D.; Steuernagel, L.; Meiners, D.; Gideon, R. Characterization of the Dynamic Mechanical Properties of Sisal Fiber Reinforced PET Composites; Effect of Fiber Loading and Fiber Surface Modification. *Polym. Polym. Compos.* **2021**, *29* (9_suppl), S719–S728. https://doi.org/10.1177/09673911211023032.

(100) Corradini, E.; Imam, S. H.; Agnelli, J. A. M.; Mattoso, L. H. C. Effect of Coconut, Sisal and Jute Fibers on the Properties of Starch/Gluten/Glycerol Matrix. *J. Polym. Environ.* **2009**, *17* (1), 1–9. https://doi.org/10.1007/s10924-009-0115-1.

(101) Yao, Q.; Wang, Q.; Wang, L.; Wang, Y.; Sun, J.; Zeng, H.; Jin, Z.; Huang, X.; Chen, L. The Synergic Regulation of Conductivity and Seebeck Coefficient in Pure Polyaniline by Chemically Changing the Ordered Degree of Molecular Chains. *J. Mater. Chem. A* **2014**, *2* (8), 2634–2640. https://doi.org/10.1039/C3TA14008C.

(102) Ding, J.; Liu, Z.; Zhao, W.; Jin, W.; Xiang, L.; Wang, Z.; Zeng, Y.; Zou, Y.; Zhang, F.; Yi, Y.; Diao, Y.; McNeill, C. R.; Di, C.; Zhang, D.; Zhu, D. Selenium-Substituted Diketopyrrolopyrrole Polymer for High-Performance P-Type Organic Thermoelectric Materials. *Angew. Chemie* **2019**, *131* (52), 19170–19175. https://doi.org/10.1002/ange.201911058.

(103) Untilova, V.; Hynynen, J.; Hofmann, A. I.; Scheunemann, D.; Zhang, Y.; Barlow, S.; Kemerink, M.; Marder, S. R.; Biniek, L.; Müller, C.; Brinkmann, M. High Thermoelectric Power Factor of Poly(3-Hexylthiophene) through In-Plane Alignment and Doping with a Molybdenum Dithiolene Complex. *Macromolecules* **2020**, *53* (15), 6314–6321. https://doi.org/10.1021/acs.macromol.0c01223.

(104) Dexter Tam, T. L.; Moudgil, A.; Teh, W. J.; Wong, Z. M.; Handoko, A. D.; Chien, S. W.; Yang, S.-W.; Yeo, B. S.; Leong, W. L.; Xu, J. Polaron Delocalization Dependence of the Conductivity and the Seebeck Coefficient in Doped Conjugated Polymers. *J. Phys. Chem. B* **2022**, *126* (9), 2073–2085. https://doi.org/10.1021/acs.jpcb.2c00303.

(105) Steyrleuthner, R.; Zhang, Y.; Zhang, L.; Kraffert, F.; Cherniawski, B. P.; Bittl, R.; Briseno, A. L.; Bredas, J.-L.; Behrends, J. Impact of Morphology on Polaron Delocalization in a Semicrystalline Conjugated Polymer. *Phys. Chem. Chem. Phys.* **2017**, *19* (5), 3627–3639. https://doi.org/10.1039/C6CP07485E.

(106) Moser, M.; Savva, A.; Thorley, K.; Paulsen, B. D.; Hidalgo, T. C.; Ohayon, D.; Chen, H.; Giovannitti, A.; Marks, A.; Gasparini, N.; Wadsworth, A.; Rivnay, J.; Inal, S.; McCulloch, I. Polaron Delocalization in Donor–Acceptor Polymers and Its Impact on Organic Electrochemical Transistor Performance. *Angew. Chemie Int. Ed.* **2021**, *60* (14), 7777–7785. https://doi.org/10.1002/anie.202014078.

(107) Bulusu, A.; Walker, D. G. Review of Electronic Transport Models for Thermoelectric Materials. *Superlattices Microstruct.* **2008**, *44* (1), 1–36. https://doi.org/10.1016/j.spmi.2008.02.008.

(108) Goupil, C.; Seifert, W.; Zabrocki, K.; Müller, E.; Snyder, G. J. Thermodynamics of Thermoelectric Phenomena and Applications. *Entropy* **2011**, *13* (8), 1481–1517. https://doi.org/10.3390/e13081481.

(109) Shen, H.; Xie, K.; Shi, H.; Yan, X.; Tu, L.; Xu, Y.; Wang, J. Analysis of Heat Transfer Characteristics in Textiles and Factors Affecting Thermal Properties by Modeling. *Text. Res. J.* **2019**, *89* (21–22), 4681–4690. https://doi.org/10.1177/0040517519842790.

(110) Yang, T.; Xiong, X.; Petrů, M.; Tan, X.; Kaneko, H.; Militký, J.; Sakuma, A. Theoretical and Experimental Studies on Thermal Properties of Polyester Nonwoven Fibrous Material. *Materials (Basel).* **2020**, *13* (12). https://doi.org/10.3390/ma13122882.

(111) Paleo, A. J.; Vieira, E. M. F.; Wan, K.; Bondarchuk, O.; Cerqueira, M. F.; Bilotti,

E.; Melle-Franco, M.; Rocha, A. M. Vapor Grown Carbon Nanofiber Based Cotton Fabrics with Negative Thermoelectric Power. *Cellulose* **2020**, *27* (15), 9091–9104. https://doi.org/10.1007/s10570-020-03391-4.

(112) Kim, Y.; Lund, A.; Noh, H.; Hofmann, A. I.; Craighero, M.; Darabi, S.; Zokaei, S.; Park, J. Il; Yoon, M.-H.; Müller, C. Robust PEDOT:PSS Wet-Spun Fibers for Thermoelectric Textiles. *Macromol. Mater. Eng.* **2020**, *305* (3), 1900749. https://doi.org/https://doi.org/10.1002/mame.201900749.

(113) Choi, J.; Jung, Y.; Yang, S. J.; Oh, J. Y.; Oh, J.; Jo, K.; Son, J. G.; Moon, S. E.; Park, C. R.; Kim, H. Flexible and Robust Thermoelectric Generators Based on All-Carbon Nanotube Yarn without Metal Electrodes. *ACS Nano* **2017**, *11* (8), 7608–7614. https://doi.org/10.1021/acsnano.7b01771.

(114) Khoso, N. A.; Ahmed, A.; Deb, H.; Tian, S.; Jiao, X.; Gong, X. Y.; Wang, J. Controlled Template-Free in-Situ Polymerization of PEDOT for Enhanced Thermoelectric Performance on Textile Substrate. *Org. Electron.* **2019**, *75*, 105368. https://doi.org/10.1016/j.orgel.2019.07.026.

(115) Lee, J. A.; Aliev, A. E.; Bykova, J. S.; de Andrade, M. J.; Kim, D.; Sim, H. J.; Lepró, X.; Zakhidov, A. A.; Lee, J.; Spinks, G. M.; Roth, S.; Kim, S. J.; Baughman, R. H. Woven-Yarn Thermoelectric Textiles. *Adv. Mater.* **2016**, *28* (25), 5038–5044. https://doi.org/10.1002/adma.201600709.

(116) Ren, F.; Menchhofer, P.; Kiggans, J.; Wang, H. Development of Thermoelectric Fibers for Miniature Thermoelectric Devices. *J. Electron. Mater.* **2016**, *45* (3), 1412–1418. https://doi.org/10.1007/s11664-015-4050-8.

(117) Zhang, T.; Li, K.; Zhang, J.; Chen, M.; Wang, Z.; Ma, S.; Zhang, N.; Wei, L. High-Performance, Flexible, and Ultralong Crystalline Thermoelectric Fibers. *Nano Energy* **2017**, *41*, 35–42. https://doi.org/10.1016/j.nanoen.2017.09.019.

(118) Ding, Y.; Qiu, Y.; Cai, K.; Yao, Q.; Chen, S.; Chen, L.; He, J. High Performance N-Type Ag2Se Film on Nylon Membrane for Flexible Thermoelectric Power Generator. *Nat. Commun.* **2019**, *10* (1), 841. https://doi.org/10.1038/s41467-019-08835-5.

(119) Ito, M.; Koizumi, T.; Kojima, H.; Saito, T.; Nakamura, M. From Materials to Device Design of a Thermoelectric Fabric for Wearable Energy Harvesters. *J. Mater. Chem. A* **2017**, *5* (24), 12068–12072. https://doi.org/10.1039/C7TA00304H.

(120) Komatsu, N.; Ichinose, Y.; Dewey, O. S.; Taylor, L. W.; Trafford, M. A.; Yomogida, Y.; Wehmeyer, G.; Pasquali, M.; Yanagi, K.; Kono, J. Macroscopic Weavable

Fibers of Carbon Nanotubes with Giant Thermoelectric Power Factor. *Nat. Commun.* **2021**, *12* (1), 4931. https://doi.org/10.1038/s41467-021-25208-z.

(121) Ryan, J. D.; Mengistie, D. A.; Gabrielsson, R.; Lund, A.; Müller, C. Machine-Washable PEDOT:PSS Dyed Silk Yarns for Electronic Textiles. *ACS Appl. Mater. Interfaces* **2017**, *9* (10), 9045–9050. https://doi.org/10.1021/acsami.7b00530.

(122) Qu, S.; Chen, Y.; Shi, W.; Wang, M.; Yao, Q.; Chen, L. Cotton-Based Wearable Poly(3-Hexylthiophene) Electronic Device for Thermoelectric Application with Cross-Plane Temperature Gradient. *Thin Solid Films* **2018**, *667*, 59–63. https://doi.org/10.1016/j.tsf.2018.09.046.

(123) Chen; Lwo. Large-Area Laying of Soft Textile Power Generators for the Realization of Body Heat Harvesting Clothing. *Coatings* **2019**, *9* (12), 831. https://doi.org/10.3390/coatings9120831.

(124) Lund, A.; Tian, Y.; Darabi, S.; Müller, C. A Polymer-Based Textile Thermoelectric Generator for Wearable Energy Harvesting. *J. Power Sources* **2020**, *480*, 228836. https://doi.org/10.1016/j.jpowsour.2020.228836.

(125) Finefrock, S. W.; Zhu, X.; Sun, Y.; Wu, Y. Flexible Prototype Thermoelectric Devices Based on Ag 2 Te and PEDOT:PSS Coated Nylon Fibre. *Nanoscale* **2015**, *7* (13), 5598–5602. https://doi.org/10.1039/C5NR00058K.

(126) Du, Y.; Cai, K. F.; Shen, S. Z.; Donelsonand, R.; Xu, J. Y.; Wang, H. X.; Lin, T. Multifold Enhancement of the Output Power of Flexible Thermoelectric Generators Made from Cotton Fabrics Coated with Conducting Polymer. *RSC Adv.* **2017**, *7* (69), 43737–43742. https://doi.org/10.1039/C7RA08663F.

(127) Wu, Q.; Hu, J. A Novel Design for a Wearable Thermoelectric Generator Based on 3D Fabric Structure. *Smart Mater. Struct.* **2017**, *26* (4), 045037. https://doi.org/10.1088/1361-665X/aa5694.

(128) Kim, J.-Y.; Lee, W.; Kang, Y. H.; Cho, S. Y.; Jang, K.-S. Wet-Spinning and Post-Treatment of CNT/PEDOT:PSS Composites for Use in Organic Fiber-Based Thermoelectric Generators. *Carbon N. Y.* **2018**, *133*, 293–299. https://doi.org/10.1016/j.carbon.2018.03.041.

(129) Kim, J.-Y.; Mo, J.-H.; Kang, Y. H.; Cho, S. Y.; Jang, K.-S. Thermoelectric Fibers from Well-Dispersed Carbon Nanotube/Poly(Vinyliedene Fluoride) Pastes for Fiber-Based Thermoelectric Generators. *Nanoscale* **2018**, *10* (42), 19766–19773. https://doi.org/10.1039/C8NR06415F.

(130) Liu, J.; Jia, Y.; Jiang, Q.; Jiang, F.; Li, C.; Wang, X.; Liu, P.; Liu, P.; Hu, F.; Du,

Y.; Xu, J. Highly Conductive Hydrogel Polymer Fibers toward Promising Wearable Thermoelectric Energy Harvesting. *ACS Appl. Mater. Interfaces* **2018**, *10* (50), 44033–44040. https://doi.org/10.1021/acsami.8b15332.

(131) Sun, T.; Zhou, B.; Zheng, Q.; Wang, L.; Jiang, W.; Snyder, G. J. Stretchable Fabric Generates Electric Power from Woven Thermoelectric Fibers. *Nat. Commun.* **2020**, *11* (1), 572. https://doi.org/10.1038/s41467-020-14399-6.

(132) Khoso, N. A.; Jiao, X.; GuangYu, X.; Tian, S.; Wang, J. Enhanced Thermoelectric Performance of Graphene Based Nanocomposite Coated Self-Powered Wearable e-Textiles for Energy Harvesting from Human Body Heat. *RSC Adv.* **2021**, *11* (27), 16675–16687. https://doi.org/10.1039/D0RA10783B.

(133) Wang, K.; Hou, C.; Zhang, Q.; Li, Y.; Wang, H. Highly Integrated Fiber-Shaped Thermoelectric Generators with Radially Heterogeneous Interlayers. *Nano Energy* **2022**, *95*, 107055. https://doi.org/10.1016/j.nanoen.2022.107055.

Chapter 5

In-situ polymerization of polythiophene in polymer matrices

Content

This chapter shows the *in-situ* polymerization of terthiophene within a polymer matrix and their thermoelectric properties to develop flexible thermoelectric thin films. Furthermore, a hybrid plasmonic/TEG system has been designed with a synergy of plasmonic and thermoelectric materials properties to generate thermal gradients by the sunlight absorption. This chapter is divided into several sections. First, an introduction explains the different routes to obtaining blends with conductive polymers and the fundamentals of plasmonic heating. Then, three studies such as the optimization of polymerization conditions to obtain polythiophene (PTh) films embedded in polymethyl methacrylate (PMMA) and polyurethane (PU) matrices using silver (I) and copper (II) perchlorate as an oxidizing agent, the optimization conditions of the plasmonic material, and the development of the hybrid plasmon/TEG are presented.

5.1 Introduction

The use of wearable and stretchable electronic devices is becoming more and more common in our daily lives. Therefore, there is a need to improve mechanical stretchability without compromising electrical performance. Conductive materials with versatile properties such as flexibility, stretchability, light weight, and thermal stability are required to face these improvements. As shown in previous chapters, conductive polymers are one of the most promising candidates due to their mechanical properties, high electrical conductivity, and low density. However, one of the main challenges of conductive polymers is their processability since, due to the rigidity of the aromatic backbone and the stacking force between molecules, the solubility of conductive polymers is compromised.[1] The most significant advance in improving the processability of conductive polymers is the addition of polystyrene sulfonate (PSS), which stabilizes poly(3,4-ethylenedioxythiophene) (PEDOT) polymer chains in water and some polar organic solvents.[2] Currently, aqueous PEDOT:PSS is a commercial product with modifiable electrical properties during the processing, secondary doping, and post-treatment methods. These processes remove the dopant excess (PSS, for example), leading to phase separation or a morphological rearrangement.[3–7] However, despite the high electrical conductivity (up

to 2240 S cm^{-1}) obtained by these processes, PEDOT:PSS films have a tensile strain of around 2%. Therefore, the next generation of wearable devices requires materials with good electrical conductivity and deformability beyond flexibility, that is, a degree of stretchability greater than 10%.[8–10] For this reason, in recent years, different blending routes have been established to obtain conductive materials with improved mechanical properties.

5.1.1 Blending routes for conductive polymers

The term blending in the area of polymers is known as the mixture of polymers to modify their properties. The development of blending methods to process conductive polymers is based on understanding the difficulties in the processability of conductive polymers due to their aromatic structure and charge delocalization.[11]

5.1.1.1 Molecularly Miscible Polymer Blends

This blending route uses small molecular plasticizers, such as surfactants (Zonyl, Xylitol, Triton X-100),[12–14] ionic liquids, and polymeric matrices to process conductive polymers. For example, when PEDOT:PSS films are mixed with increasing concentrations of Zonyl, an increase in the size of the PEDOT domains is observed, as seen in the AFM images of **Figure 5.1(a)**. In addition, the 10% Zonyl weight concentration sample exhibits a high aspect ratio, indicating greater ductility. The mixture of conductive polymers with a plasticizer causes a partial swelling of the PEDOT:PSS films, weakening the hydrogen bonds between the PSS chains. Then, the free volume of the PEDOT and PSS chains increases, allowing a greater relaxation of the chains against tensile stress.[15] In addition, small molecular additives can promote the mobility of charge carriers, obtaining higher electrical conductivity. However, the main disadvantage of using molecular plasticizers is that they can seep out during the application of the material and, therefore, lose mechanical properties. Apart from using molecular plasticizers, it is possible to obtain highly stretchable PEDOT:PSS films by incorporating ionic liquids.[16–18] The work developed by Bao et al.[19] reported a highly stretchable conductive polymer doped with ionic liquids, with an electrical conductivity greater than 3100 S cm^{-1} below 0% tension and 4100 S cm^{-1} below 100% tension. The author proposed that ionic liquids with sulfonate or sulfonimide functional groups reduce the electrostatic interaction between PEDOT and PSS chains by

triggering an aggregation of PEDOT chains within a PSS matrix schematized in **Figure 5.1(b)**.

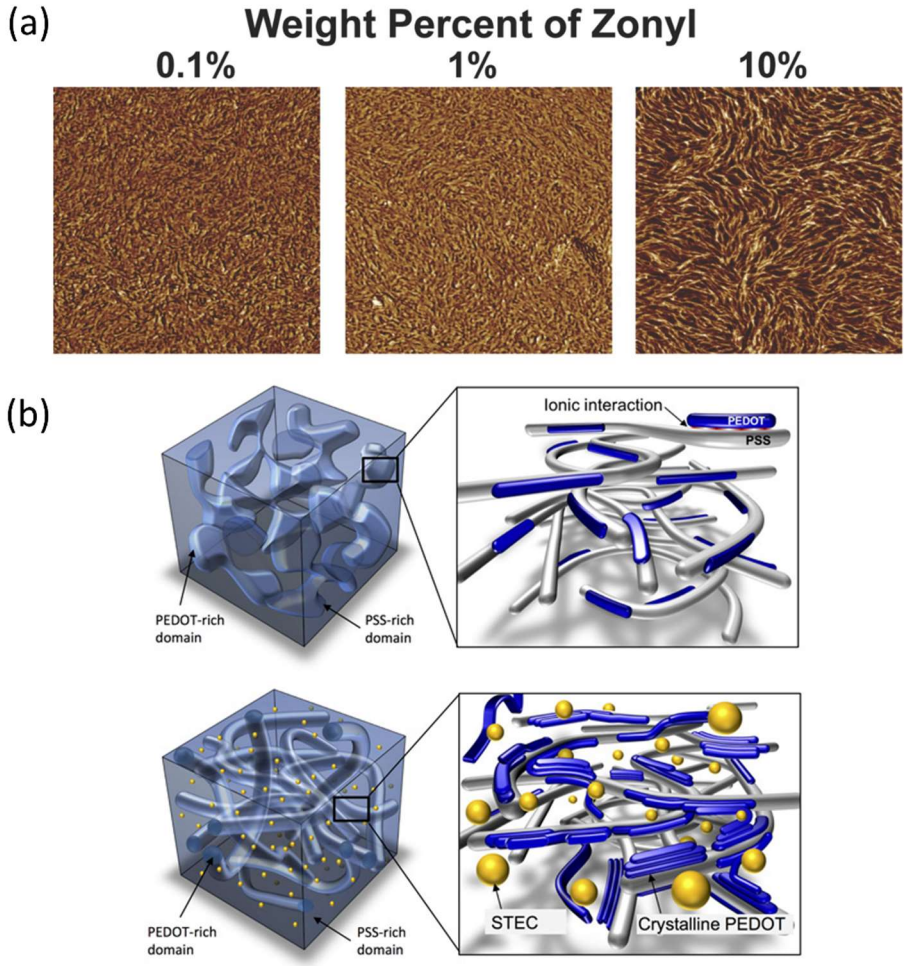

Figure 5.1 (a) AFM images of PEDOT:PSS films with different weight percentages of Zonyl. Reprinted with permission.[15] Copyright 2014, WILEY-VCH Verlag GmbH & Co. KGaA, Weinheim. (b) Representation of the PEDOT:PSS film morphology before and after adding ionic liquids. Reprinted with permission.[19] Copyright 2017, The Authors; American Association for the Advancement of Science.

Another way to obtain stretchable PEDOT:PSS films is by blending PEDOT:PSS with a high loading of soft polymers such as PVA, PEO, and PEG. According to Reynolds et al.[20] electrical conductivity and stretchability depend on the morphology and crystallinity of the polymer used. Their work showed that PEDOT:PSS blends with crystalline polymers showed a faster increase in conductivity than blends with amorphous polymers, but, on the contrary, the elongation at break was lower. In addition to these polymers, it is also possible to obtain blends of PEDOT:PSS with triblock copolymers and water-based polyurethane (WPU) to prepare stretchable conductive materials.[21,22]

The main drawback of this blending route is the need for the conductive polymer and the host polymeric matrix to be miscible. As we know, conductive polymers have very low solubility in organic solvents and water. Only PEDOT:PSS is soluble in water and polar organic solvents, so this blending route privates the use of the rest of the conductive polymers and requires that the additives also be soluble in the same solvent.

5.1.1.2 Phase-separated polymer blends

This route involves obtaining a continuous conductive pathway on an elastomeric matrix by mixing immiscible polymers. The incompatibility of the blended polymers can be solved by the addition of amphiphilic agents such as PDMS-b-PEO block copolymer or Triton X-100.[23,24] Jin-Seo Noh showed that the addition of the PDMS-b-PEO block copolymer improved the miscibility between PEDOT:PSS and PDMS and also greatly influenced the morphology of the mixtures (**Figure 5.2(a)**). Without the block copolymer, the PEDOT:PSS and the PDMS are separated into two phases. After the progressive addition of the PDMS-b-PEO they begin to mix until the isolated PDMS granules significantly decrease, forming a continuous network of PEDOT:PSS supported in the PDMS matrix.

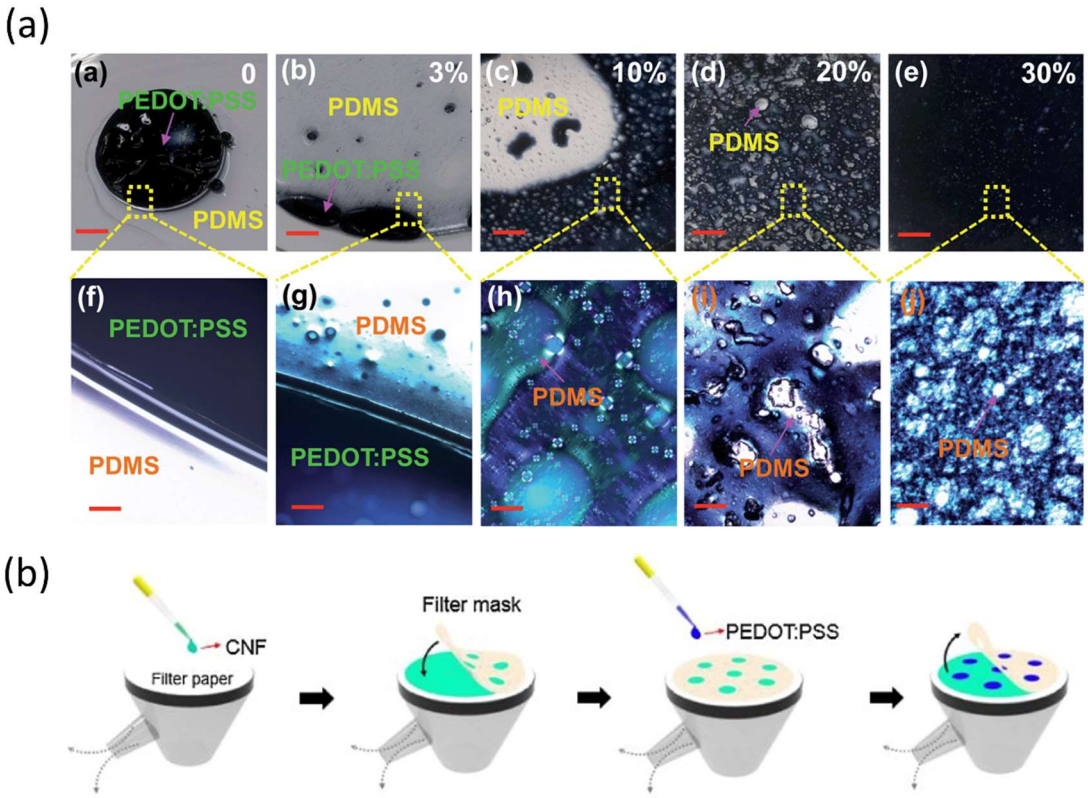

Figure 5.2 (a) Optical images of PEDOT:PSS/PDMS blends with different amounts of PDMS-b-PEO block copolymer. Reprinted with permission.[23] Copyright 2014, The Royal

Society of Chemistry. (b) Scheme of PEDOT preparation:PSS/cellulose blends by vacuum filtration. Reprinted with permission.[25] Copyright 2017, Elsevier Ltd.

On the other hand, Luo et al.[24] showed an improvement in the miscibility of PEDOT:PSS in the PDMS matrix by adding a non-ionic surfactant such as Triton X-100. The hydrophilic groups of the Triton X-100 come into contact with the aqueous PEDOT:PSS solution and the hydrophobic groups of the surfactant with the PDMS solution.

Another way to mix immiscible polymers without needing a compatibilizing agent is by vacuum-assisted sequential filtration of both components. For example, Ko et al.[25] demonstrated that the production of PEDOT:PSS composites with cellulose nanofibers (CNF) by vacuum-assisted filtration (**Figure 5.2(b)**) could achieve a competitive electrical conductivity compared to other previous works. In addition, flexibility tests demonstrated that the electrical conductivity of the final composite was not altered after bending cycles at different angles. This route also requires a soluble conductive polymer. Since only PEDOT:PSS is soluble, this route can only be used to obtain mixtures with PEDOT:PSS.

5.1.1.3 *In-situ* polymerization in polymer matrices

As an alternative to the two previous routes, *in-situ* polymerization allows obtaining composites based on conductive polymers and insulating polymeric matrices by mixing the host polymeric matrix with monomers or oligomers and their initiator. Therefore, this route enables using other non-soluble conductive polymers. In addition, an interpenetrating polymeric network (IPN) is obtained after polymerization, which improves the mechanical properties of conductive polymers and prevents phase segregation.

Teng et al.[26] proposed using PEDOT:PSS as a host matrix to which they incorporated PDMS oligomers and curing agents (**Figure 5.3(a)**). As a result, they obtained an interpenetrating polymeric network composed of a PEDOT:PSS aerogel network and a flexible PDMS network (**Figure 5.3(b)**). The composite remained elastic under deformation stress (43%) and compression stress (60%) and, in addition, maintained its electrical conductivity under deformation.

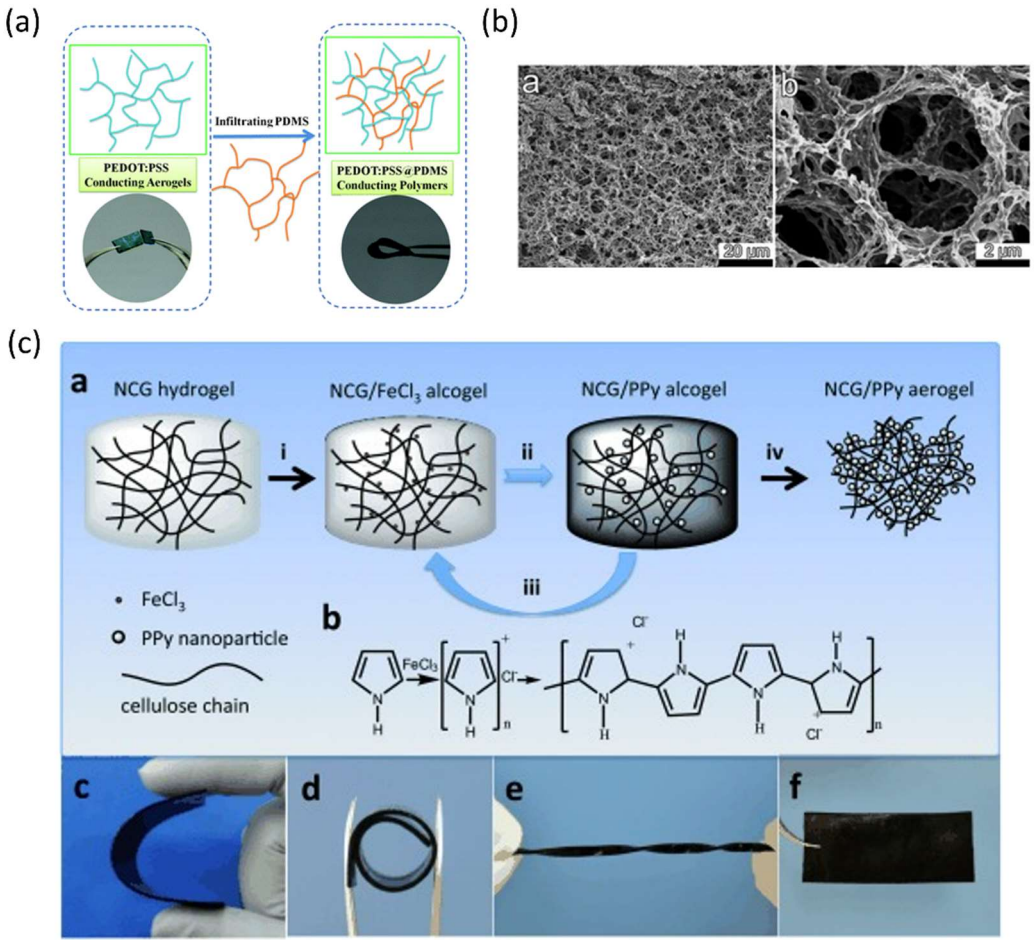

Figure 5.3 (a) Schematic procedure of PDMS infiltration in a PEDOT:PSS aerogel matrix. (b) SEM images of the PEDOT:PSS/PDMS aerogel. Reprinted with permission.[26] Copyright 2013, The Royal Society of Chemistry. (c) Schematic procedure and optical images of nanocellulose/polypyrrole aerogel. Reprinted with permission.[27] Copyright 2014, WILEY-VCH Verlag GmbH & Co. KGaA, Weinheim.

For the formation of blends with other conductive polymers, it is necessary to introduce the monomer and the oxidizing agent into the insulating host polymer matrix. After the *in-situ* polymerization, the conductive polymer becomes interpenetrated within the host polymeric matrix. For example, Lin et al.[28] synthesized a PANI/PEEK composite using a one-step *in-situ* polymerization in which PANI grows in the free volume of the PEEK chains. On the other hand, Shi et al.[27] and Li et al.[29] used cellulose as a templating agent for the *in-situ* polymerization of polypyrrole, forming an interpenetrating polymeric network. First, they synthesized a hydrogel based on nanocellulose and immersed it in an iron (III) chloride solution (oxidant). Once the hydrogel was impregnated with the oxidant, the *in-situ* polymerization of the pyrrole was carried out differently. In the first work, Shi et al. used the vapor phase polymerization method to avoid polymerization outside the hydrogel (**Figure 5.3(c)**). Li et al. simply immersed the oxidant-doped hydrogel in a

monomer solution. In both cases, the polymerization of the pyrrole generated an interpenetrating polymeric network in which the nanocellulose matrix supports the polypyrrole. Barani et al.[30] used a similar technique to coat cotton fabrics with polyaniline and polypyrrole. In this case, they first impregnated the cotton with a solution containing the monomer and then introduced the oxidant, producing oxidative polymerization on the fibers of the cotton fabric.

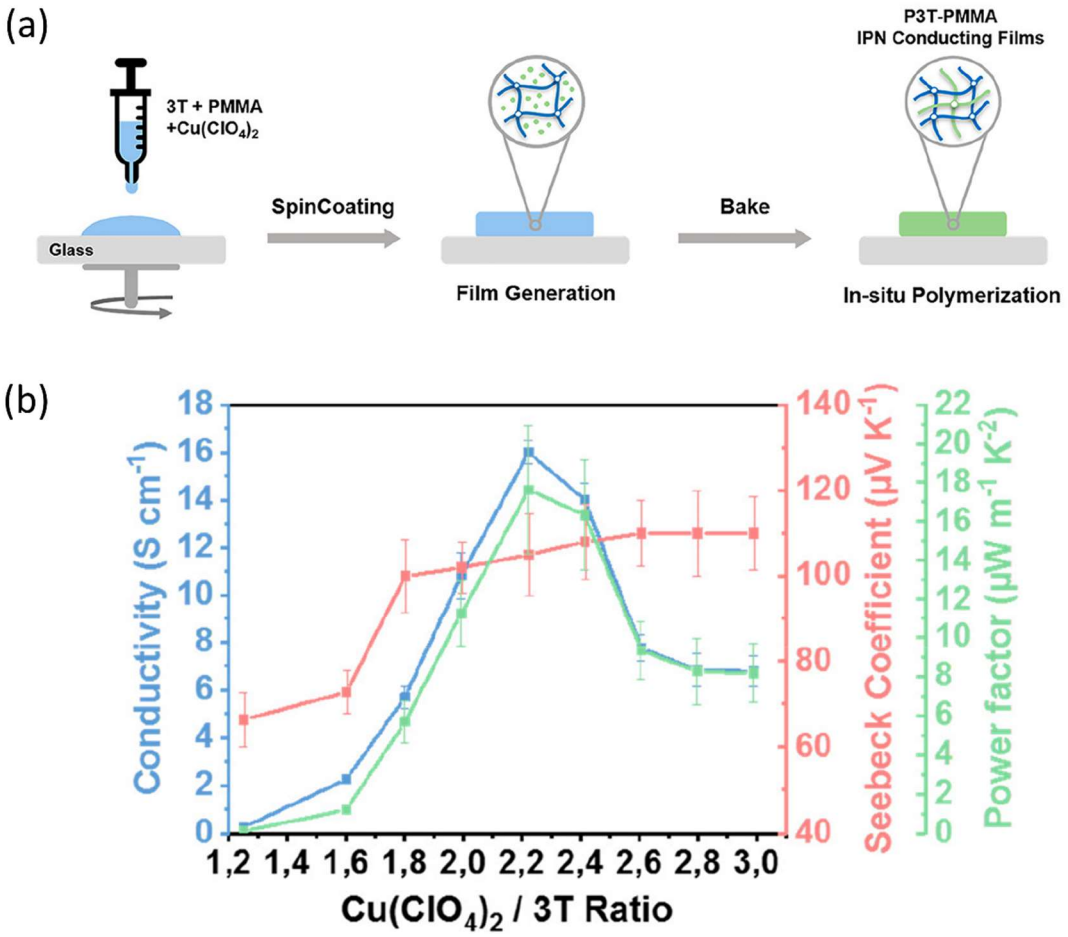

Figure 5.4 (a) Scheme of the *in-situ* polymerization process. (b) Evaluation of thermoelectrical properties as a function of the molar ratio oxidant:monomer. Reprinted with permission.[31] Copyright 2020, American Chemical Society.

These *in-situ* polymerization methods are good strategies for obtaining hydrogels, membranes, and textiles coated with conductive polymers. However, it may not be the best choice if thin films are the goal. Our research group developed an *in-situ* synthesis of polythiophene thin films embedded in a PMMA polymeric matrix (**Figure 5.4(a)**).[31] In this method, the thiophene polymerization, and doping reaction occur simultaneously in the solid state within a host matrix of PMMA using copper (II) perchlorate as an oxidizing agent. As a result, the polymerization reaction is very fast, and it is possible to obtain a thin

film, 80 nm, with good conductive properties in a matter of minutes. Furthermore, it is easy to modify the thermoelectric properties of the film since the concentration of charge carriers can be adjusted by controlling the oxidant:monomer molar ratio (**Figure 5.4(b)**). This innovative *in-situ* polymerization method is compatible with large-area industrial printing methods and therefore represents a new approach to obtaining thermoelectric materials based on conductive polymers.

5.1.2 Solar thermoelectric generators

The development of wearable thermoelectric materials aims to replace the batteries and supercapacitors needed to supply electrical energy to portable electronic devices. The main advantage of thermoelectric materials is that they do not need to be constantly charged to provide electrical energy since they harness thermal gradients to generate it. However, the power they can supply depends significantly on the thermal gradient they are exposed to. If we consider, for example, a thermoelectric generator for body heat harvesting, the temperature difference between the epidermis and the ambient temperature is barely a couple of degrees.[32] Therefore, the power supplied by the thermoelectric generator for body heat harvesting will be much lower than the power generated with higher temperature gradients. However, incorporating plasmonic nanoparticles into thermoelectric material can increase the thermal gradient through the absorption of solar radiation. This phenomenon is known as plasmonic heating.[33,34] Thus, the output power of a thermoelectric generator for body heat harvesting incorporating plasmonic nanoparticles should increase due to the higher thermal gradient.

5.1.2.1 Plasmonic heating

The plasmonic heating phenomenon is a physical phenomenon within a subfield of plasmonics called thermo-plasmonics, which uses metallic nanoparticles as light-controlled nanoheat sources. This phenomenon is particularly interesting in bio-applications since it can be used in hyperthermic cancer therapies through the adhesion of metallic nanoparticles to cancerous organs. Only the cancerous organs are damaged when the nanoparticles are irradiated at a specific wavelength.[35] Another biomedical application of thermo-plasmonics is the release of drugs for therapeutic purposes. In this case, the therapeutic agents adhere to the metallic nanoparticles, and when they are in the desired position, the drug is released by heating the nanoparticles with laser illumination.[36]

Plasmonic heating is due to a localized surface plasmon resonance (LSPR), defined as a collective oscillation of electrons in a metal.[37,38] Metals are not good conductors at optical frequencies; therefore, upon illumination, electrons oscillating at the electric field frequency of the incident light dampen the incident radiation by a Joule mechanism resulting in heat generation (**Figure 5.5(a)**).[39] The loss of kinetic energy of the electrons produces the Joule effect. This effect occurs as a consequence of the collision between the atoms of the metallic nanoparticles during electronic transitions when excited by the incident radiation.

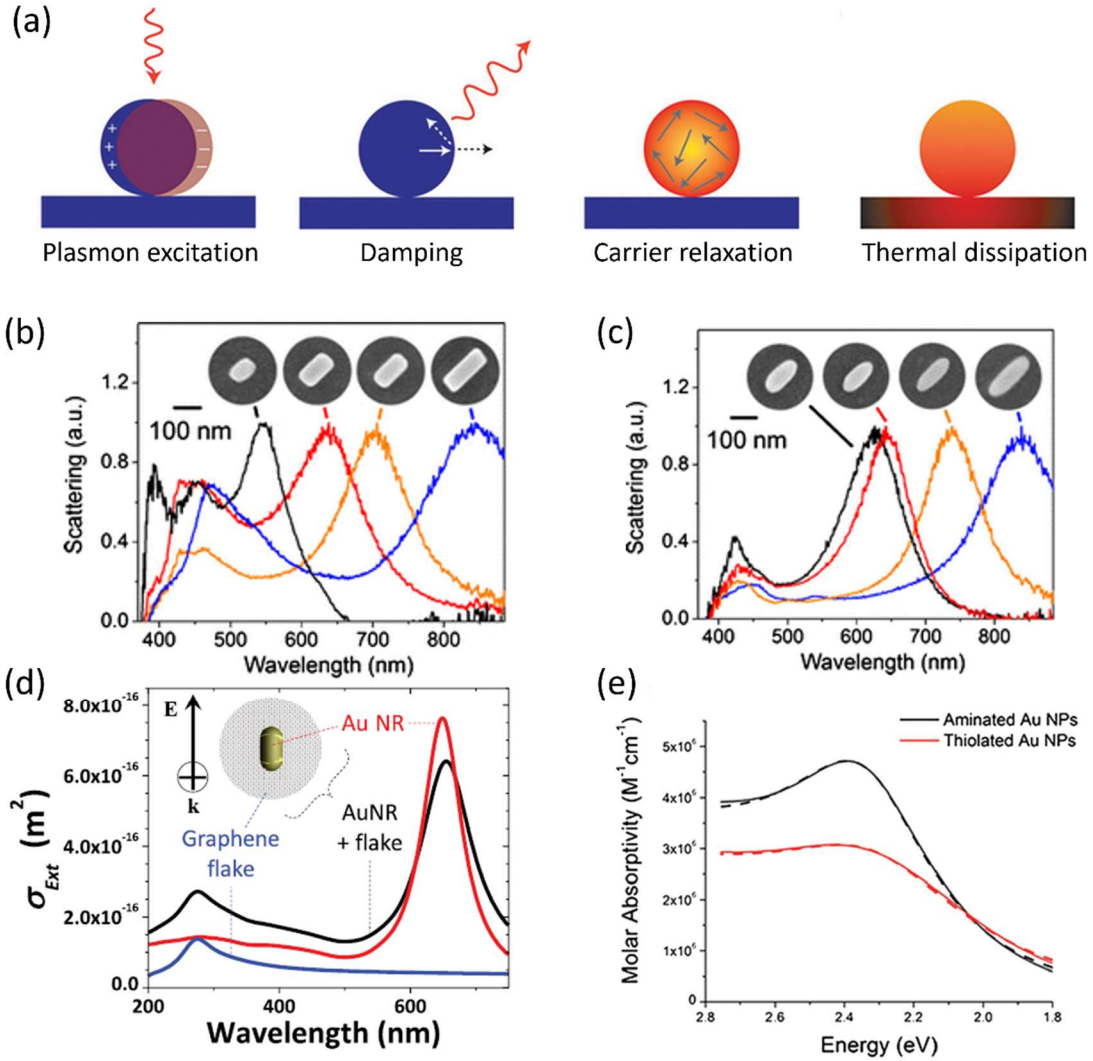

Figure 5.5 (a) Schematic process of plasmonic heating. Reprinted with permission.[39] Copyright 2017, IOP Publishing Ltd. Ag-Plasmonic band resonance as a function of particle size for (b) nanobars and (c) nanorice. Reprinted with permission.[40] Copyright 2006, American Chemical Society. Au-Plasmonic band resonance as a function of (d) graphene coating and (e) amines and thiols ligands. Reprinted with permission.[41] Copyright 2007, American Chemical Society.

The surface plasmon resonance of nanostructured plasmonic materials can be modified mainly by morphology (shape and size) and environment. The shape of the plasmonic metal nanoparticles determines the position of the plasmonic resonance bands. For example, Wiley et al.[40] synthesized different morphologies of silver nanoparticles. Each sample had a plasmon resonance band visible in UV-Vis but centered at different wavelengths (**Figure 5.5(b)**). In other work, Wiley et al.[41] modified the dimensions of two different morphologies of silver nanoparticles, and it was observed that, for a given morphology, an increase in size leads to a bathochromic shift in the plasmonic resonance band (**Figure 5.5(c)**). Another factor that influences plasmonic resonance and, therefore, the efficiency of plasmonic heating is the environment. The nanometric size of plasmonic nanoparticles makes a large part of the atoms located on the surface. Thus, these atoms are highly exposed to the environment and will be sensitive to environmental dielectric properties such as changes in the density of liquids or gases, the formation of organic layers of the ligands that stabilize the nanoparticles, and, in general, to any surface adsorption of the different chemical agents (**Figure 5.5(d) and (e)**).[42,43]

5.1.2.2 Thermoelectric solar harvesting

A solar thermoelectric generator (STEG) is a system that harvests solar power by converting solar heat into electricity. In general, a STEG consists of five main elements (see **Figure 5.6(a)**): an optical collector, which collects the photons coming from the sun; an opto-thermal converter, which converts the captured photons into heat; a thermal collector, which conducts the heat obtained towards the thermoelectric material; a thermoelectric converter, which converts heat into electricity using the Seebeck effect; and, a heat sink, which dissipates heat from the thermoelectric generator at the cold end.[44] The efficiency of a solar thermoelectric generator depends on the individual efficiency of each element that makes up the STEG. However, the efficiency of the opto-thermal converter is the most critical because, in this type of thermoelectric generator, the final efficiency will largely depend on the conversion of the captured photons into heat. In general, an opto-thermal converter should have an absorbance equal to one and an emissivity equal to zero over the full range of the solar spectrum. Thus, solar power absorption would be maximized while minimizing thermal loss. These characteristics are found in materials with high absorbance in the UV-Vis range and high reflectance at longer wavelengths (**Figure 5.6(b)**).

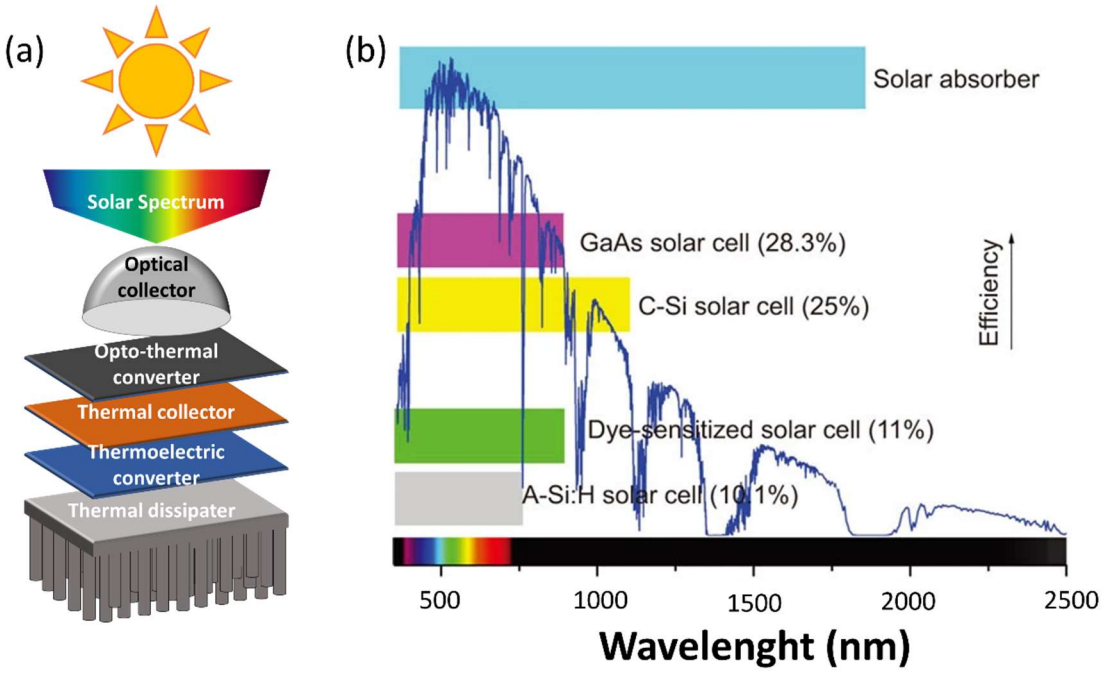

Figure 5.6 (a) Basic scheme of a solar thermoelectric generator. (b) Solar spectra and different opto-thermal converters. Reprinted with permission.[45] Copyright 2014, CIOMP.

One of the materials used as an opto-thermal converter is the solar cells, giving rise to the Hybrid Thermoelectric Photovoltaic Generator.[46] Solar cells can produce electrical power by themselves and convert solar energy into thermal power. In fact, a large part of the solar power not converted to electrical power is converted to heat in the solar cell.[47] Therefore, the efficiency of a hybrid thermoelectric/photovoltaic system will be given by the efficiency of the thermoelectric generator and the photovoltaic contribution of the solar cell. However, the main drawback of using solar cells as opto-thermal converters is the need for high thicknesses to increase light absorption. On numerous occasions, this leads to low conversion efficiencies.[48] The integration of plasmonic structures in solar cells allows a significant decrease in the thickness of the photovoltaic cell while maintaining good absorbance.[49,50] Therefore, another potential candidate for solar absorbing is plasmonic nanoparticles since they absorb light at the wavelength corresponding to plasmonic resonance and convert it into heat. In addition, the addition of ligands to crosslink the metallic nanoparticles helps to achieve a more significant aggregation of the nanoparticles and increases the light absorption in the entire visible spectrum instead of a particular wavelength corresponding to the plasmonic resonance.[51,52]

5.2 *In-situ* synthesis of polythiophene in a PMMA matrix

This first part of the chapter aims to optimize the synthesis of polythiophene films by *in-situ* polymerization of terthiophene within polymethylmethacrylate (PMMA) matrix using as oxidant a silver perchlorate salt, based on the previous work in the research group.

5.2.1 Materials

Terthiophene (3T) 99% purity, silver perchlorate, (1-methoxy-2-propyl) acetate (MPA) stabilized with 2,6-di-tert-butyl-4-methylphenol for synthesis and poly(methyl methacrylate) (PMMA) with weight-average molar mass of 996.000 by GPC and glass transition temperature (T_g) is 112 ºC were purchased from Aldrich.

5.2.2 Synthesis of polythiophene films

The *in-situ* polymerization of terthiophene (3T) within a PMMA polymeric matrix takes place through an oxidative polymerization mechanism with silver perchlorate ($AgClO_4$) as an oxidizing agent. PMMA was used as a host polymer matrix because PMMA can be quickly processed into thin films utilizing different solvents by several deposition techniques. First, different amounts of 3T were dissolved in a solution of 4 wt % of PMMA in MPA. Then, a specific quantity of oxidant salt solution in MPA was added to obtain several Ag(I)/3T molar ratios. During the formation of the film, the precursor solution, which contains the PMMA, 3T, and $AgClO_4$, was deposited by spin-coating (1800 rpm, 30 s) on a glass substrate and then heat treatment was performed. Initially colorless, the film acquires a yellowish tone at the initial heat treatment state. Later on, the film begins to develop a bluish tone. As a result, a thermoelectric material based on a conductive polymer interpenetrated in a polymer network of PMMA has been synthesized in a single step by oxidative polymerization, as shown in **Figure 5.7**.

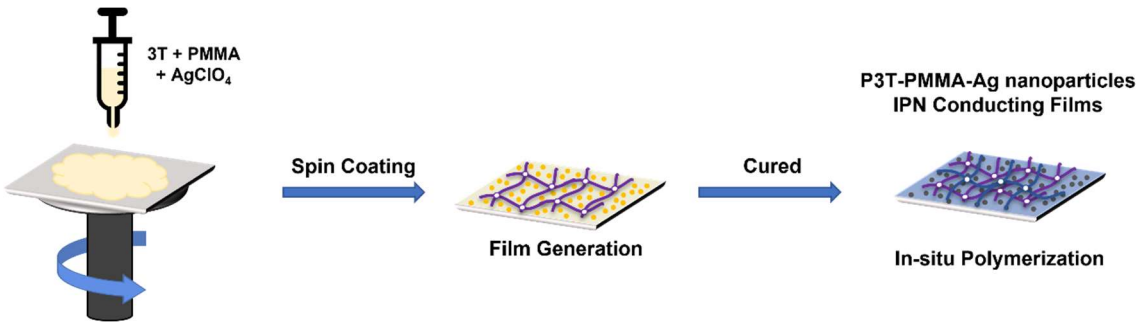

Figure 5.7 Scheme of the *in-situ* polymerization of 3T in PMMA matrix.

This section studies different experimental conditions such as reaction time, reaction temperature, and oxidant:oligomer molar ratio to optimize the synthesis of polythiophene thermoelectric films embedded in a PMMA matrix. The reaction was studied at a fixed temperature and oxidant:oligomer molar ratio, being possible to obtain information on the reaction mechanism. After the previous step, the reaction temperature was varied at the previously optimized time and a fixed $AgClO_4$:3T molar ratio. Finally, the molar ratio was varied, keeping the previously optimized reaction time and temperature constant. This procedure allowed us to study the doping level of thermoelectric films and, therefore, to obtain a film with the highest possible efficiency.

5.2.3 Optimization of reaction time

The first parameter optimized was the reaction time since it is necessary to determine the time needed to complete the polymerization reaction for a fast film processing. The reaction time was optimized with an oxidant:oligomer molar ratio of 2.8:1 (based on previous works) exposed to heat treatment at 160 ºC for different reaction times.[31] **Figure 5.8(a)** shows the electrical conductivity dependence with polymerization time. During the first 15 seconds, the electrical conductivity reaches values around 80 S cm^{-1} and continues increasing until it reaches a maximum of 117 S cm^{-1} when the curing time is 60 seconds. From this point on, the electrical conductivity decreases due to the conductive polymer's degradation, which disturbs the π-conjugate system.[53] These results indicate that the optimum reaction time is 60 s. This oxidative chemical polymerization kinetics was followed using UV−Vis−NIR spectroscopy, shown in **Figure 5.8(b)**. Initially, the colorless film turned yellow in a few seconds and then blue due to the doping of perchlorate anions in the polythiophene polymer chain.[54–56]. The PTh−$AgClO_4$−PMMA films first exhibited a maximum absorption peak around 367 nm, corresponding to the π−π* band transition of

the 3T because the PMMA is transparent in that region of the spectra. With increasing reaction time, this peak shifts towards values around 560 nm due to the transitions of the conjugated π–π* bands. At the same time, the polaronic (800 nm) and bipolaronic states (1400 nm) bands also appear due to the increase in the doping level of the conductive polymer by perchlorate.[57,58] These three bands increase progressively until reaching a maximum at a reaction time of 60 s when the maximum electrical conductivity is observed. At higher reaction times, the bands corresponding to the polaronic and bipolaronic states decrease in intensity due to possible decomposition of the polythiophene.

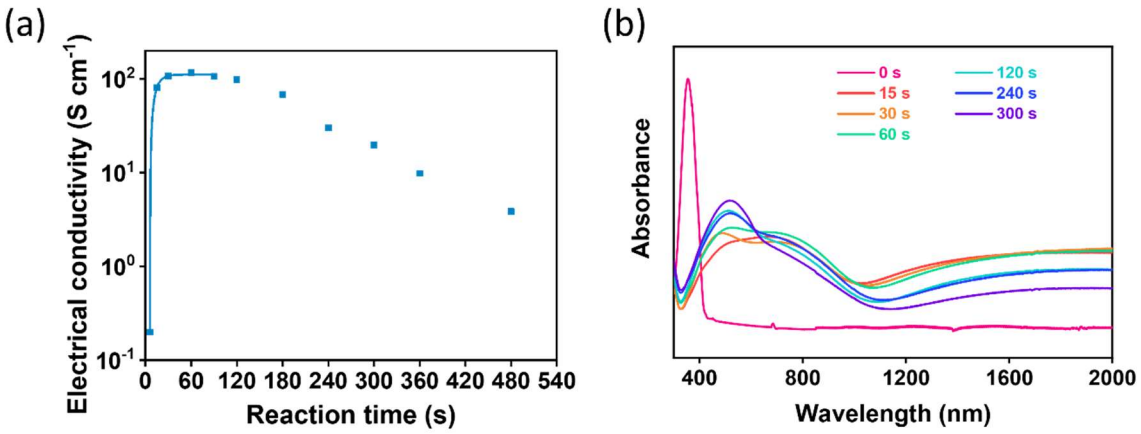

Figure 5.8 (a) Electrical conductivity and (b) UV-Vis-NIR spectra of a PTh-PMMA IPN film as a function of reaction time.

The fact that the peak located at 560 nm does not decrease in intensity evidenced the presence of the plasmonic band of silver nanoparticles.[59,60] The presence of silver nanoparticles and, therefore, of its plasmonic resonance band is confirmed through X-ray fluorescence spectroscopy, as seen in **Figure 5.9**. This figure shows the characteristic peaks of Ag $3d_{5/2}$ and Ag $3d_{3/2}$ whose binding energies are 368.4 and 374.4 eV, respectively, with a binding energy difference of 6 eV, indicating the formation of silver nanoparticles.[61–63] In addition, the different XPS spectra show the polymerization time effect. At 30 seconds of reaction, two additional bands also appear at 367 and 373 eV due to the presence of Ag^+ ions. After 60 seconds of reaction, the bands related to the Ag^+ ions are still present but in a much smaller proportion than the Ag^0 bands. Finally, after 120 seconds of reaction, the only bands that appear are those due to the silver nanoparticles. These results suggest that the reaction needs only 60 seconds to be completed since, at lower times, the presence of Ag^+ ions indicates that not all the 3T has been oxidized to PTh. This kinetic study of the reaction demonstrates that $AgClO_4$ is a fast-polymerizing agent and acts as an oxidizing

agent as well as a doping one. Moreover, this methodology makes it possible to obtain films with higher conductivity values due to the presence of silver nanoparticles.

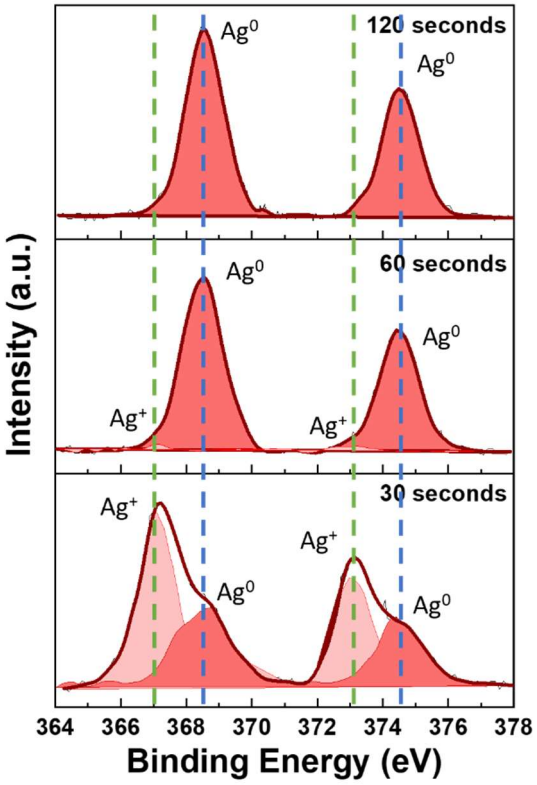

Figure 5.9 Ag 3d XPS spectra of a PTh-PMMA IPN film as a function of reaction time.

The results obtained from the electrical conductivity as a function of the reaction time, **Figure 5.8(a)**, fit an exponential equation at low reaction times, indicating that the kinetics is pseudo-first-order with a reaction constant of 0.14 s^{-1}. Therefore, the reaction mechanism would be the one that appears in **Figure 5.10**. The Ag^+ ions are responsible for initiating the oxidative polymerization of 3T within the PMMA matrix. As a result, Ag^+ ions are reduced to Ag^0, forming silver nanoparticles dispersed within the PMMA and polythiophene (PTh) matrix. Furthermore, perchlorate anions from the oxidizing salt act as doping agents along the polymeric chain of PTh, allowing the generation of bipolaronic states.[56] The presence of bipolaronic states implies an oxidation degree of the polythiophene with higher electronic transport.[54] The presence of silver nanoparticles explains the yellowish color that the terthiophene film acquires in the first reaction moments.[64]

Figure 5.10 Oxidative polymerization of terthiophene by $AgClO_4$.

5.2.4 Optimization of reaction temperature

Once the optimal reaction time has been determined to complete the in-situ polymerization in the shortest possible time, we optimized the reaction temperature. This parameter is important for the processability of polythiophene films because low temperatures can lead to slower reaction rates, and high temperatures could degrade the conductive polymer and the host matrix. **Figure 5.11** shows the effect of the curing temperature on the electrical conductivity for films with an oxidant:oligomer molar ratio of 2.8:1 and subjected to heating for 60 seconds.

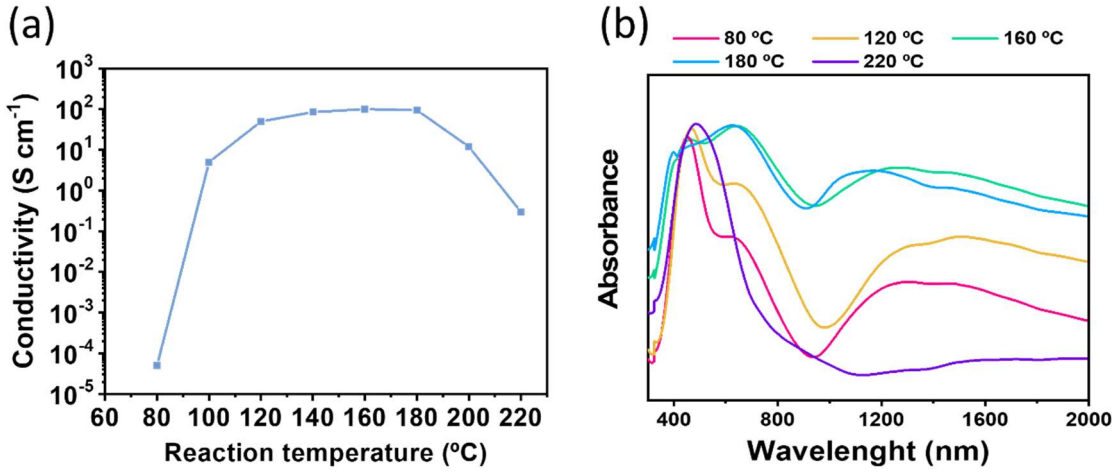

Figure 5.11 (a) Evolution of the electrical conductivity as a function of reaction temperature of PTh-PMMA for a curing time of 60 s;(b) UV-Vis-NIR spectra of a PTh-PMMA IPN film as a function of reaction temperature.

Usually, the polymerization reactions of conductive polymers occur at low temperatures,[65,66] however, **Figure 5.11(a)** shows that the film obtained at 80 ºC has an electrical conductivity of $5 \cdot 10^{-5}$ S cm^{-1}, suggesting that the extent of the reaction is not large enough to create a conductive path within the PMMA matrix. As the curing temperature increases, the electrical conductivity also increases, and at 120 ºC, the electrical conductivity is six orders of magnitude higher than the initial one. The highest electrical conductivity, 117 S cm^{-1}, is reached at curing temperatures of 160 ºC. Beyond 180 ºC, the electrical conductivity decreases gradually, confirming that an degradation of the conductive polymer occurs. **Figure 5.11(b)** confirms these observations with the UV-

Vis-NIR spectrum. At low reaction temperatures, the band corresponding to the π-π* electronic transitions of the conjugated polymeric chain has a greater intensity than the bands of the polaronic and bipolaronic states. This is indicative of very low electrical conductivity. However, as the curing temperature increases, the intensity of the polaronic and bipolaronic bands begins to increase until reaching maximum values between 160 and 180 ºC. This fact suggests that increasing the curing temperature increases the oxidation state (doping) of the polythiophene polymeric chain and, therefore, the electrical conductivity of the film will increase.[67,68] Finally, at a curing temperature of 220 ºC, the polaronic and bipolaronic bands of the PTh chain disappear entirely, indicating a decrease in the doping level.[69] With the results obtained, we can confirm that the films obtained are not stable at temperatures above 180 ºC. **Figure 5.12** shows the thermogravimetric analysis of the conductive IPN film *in-situ* synthesized and its precursors.

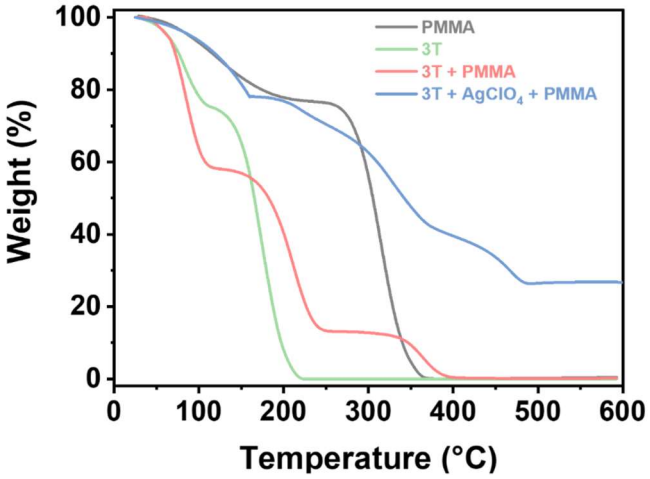

Figure 5.12 TGA curves of polymethylmethacrylate (PMMA), terthiophene (3T), 3T-PMMA, and 3T-$AgClO_4$-PMMA.

PMMA solution thermogram shows two stages of weight loss. The first of them, located between 120 and 160 ºC, is due to the evaporation of the solvent (MPA). The second stage, located between 300 and 360 ºC, corresponds to the decomposition of the PMMA. The thermogram of the oligomer (3T) also shows two steps. The first one also corresponds to solvent evaporation and the second one, with an intense weight loss at 140 ºC, almost corresponds to its flashpoint.

On the other hand, the thermogram of the mixture of 3T-PMMA shows an intense weight loss at 160 ºC, which corresponds to the solvent evaporation; at 230 ºC, corresponding to the decomposition of 3T; and at 350 ºC, corresponding to the decomposition of PMMA. These results indicate that the mixture of 3T with PMMA

improves the relative thermal stability. Finally, in the reaction mixture (Ag(I)-3T-PMMA), the thermal degradation between 120 and 300 ºC is significantly less than the degradation of the 3T-PMMA mixture, demonstrating the interpenetration of the polythiophene in the PMMA polymeric network since the thermal stability of the film is improved.[70] An important weight loss can be observed at 400 ºC, which corresponds to the decomposition of the aromatic rings of the polymeric chain since they are more stable against combustion.[71]

5.2.5 Optimization of oxidant:oligomer molar ratio

The last step in optimizing the synthesis of IPN films is to study the evolution of electrical conductivity as a function of the oxidant:oligomer molar ratio. This study is critical since the oxidant:oligomer ratio modifies the concentration of charge carriers and, therefore, the electrical conductivity values and the Seebeck coefficient.[72,73] To carry out this study, the previously optimized synthesis conditions (60 seconds and 160 ºC) have been used for the different $AgClO_4$:3T molar ratios. As expected, **Figure 5.13(a)** shows that the electrical conductivity of the obtained films increases with the $AgClO_4$:3T molar ratio, following a percolation-type curve.

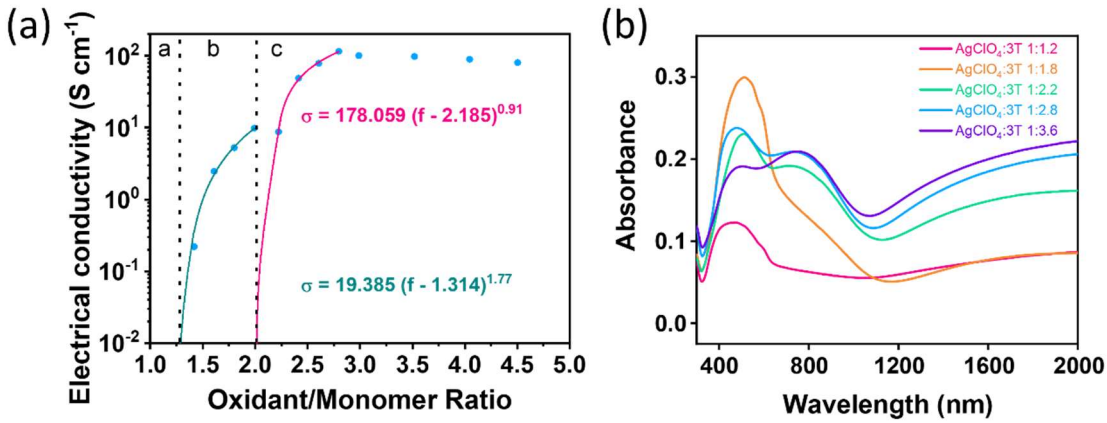

Figure 5.13 (a) Electrical conductivity of PTh-PMMA IPN films as a function of the $AgClO_4$:3T molar ratio. According to the percolation theory, fitting equations to the experimental results are included; (b) UV-Vis-IR spectra for the films obtained with different molar ratio $AgClO_4$:3T.

The electrical conductivity of an IPN is related to the conductive polymer content into the insulating host polymer and is based on the principles of the Percolation Theory given by:[74]

$$\sigma = \sigma_0(\mathrm{f} - \mathrm{f}_c)^t \qquad \textbf{(5.1)}$$

where σ is the IPN conductivity, f is the volume of the conductive polymer in the film, f_c is the percolation threshold, σ_0 is a scaling factor, and t is the critical exponent. Percolation theory is frequently used to describe insulating-to-conductive transitions of materials based on conductive fillers and an insulating matrix. Generally, a low percolation threshold indicates a homogeneous distribution of the conductive polymer in the polymeric matrix. Therefore, this value has a remarkable effect on the properties of the IPN film in terms of morphology, electrical, mechanical, and thermal properties of the host matrix.[75] On the other hand, the critical exponent in a percolation system is assumed to depend solely on the dimensionality of the lattice and is independent of the details of the lattice structure.[76] That is, for 3D systems, the critical exponent acquires values between 1.6 and 2.0, and for 2D systems, the critical exponent varies between 1.1 and 1.3.[74] However, in conductive systems, the critical exponent does not follow the universal trend. The inverted Swiss-cheese model can be applied in systems based on insulating matrices with embedded conductive fillers and where the conduction process is controlled by tunneling between fillings. This model predicts values of the critical exponent between 0.8 and 1 for 2D systems and between 1.6 and 1.8 for 3D systems.[74,77]

Figure 5.13(a) shows the electrical conductivity as a function of the molar ratio of silver perchlorate and terthiophene. Experimental data were fitted to **Equation (5.1)** to determine the percolation threshold, and three regions can be distinguished. At low oxidant:oligomer molar ratios (region a), the film's conductivity is very low and cannot be measured. The percolation threshold is achieved at a critical molar ratio (region b) around 1.25. At this point, enough polythiophene is synthesized, and the conductive polymer's chains begin to contact each other to form a continuous conductive network through the host polymer matrix. At values above the percolation threshold, there is an increase of 3 orders of magnitude in electrical conductivity, varying the molar ratio from 1.5 to 1.75. As the $AgClO_4$:3T molar ratio increases (region c), a second percolation curve can be observed in which the electrical conductivity increases by one order of magnitude. UV-Vis-NIR spectra, **Figure 5.13(b)**, supported these results. When the oxidant:oligomer molar ratio increases, the intensity of the conjugated π-π* band decreases, and the intensity of the polaronic and bipolaronic bands increases. This indicates a change in the oxidation state of the polythiophene polymeric chains. Furthermore, fitting the percolation curve also reveals the value of the critical exponent for electrical conductivity. From the fit of the first

percolation curve (green line), the value was t = 1.77. This value indicates a 3D distribution of the polythiophene throughout the host matrix.

The second percolation curve (pink line) shows t = 0.91. This second percolation curve appears at high values of the $AgClO_4$:3T molar ratio, meaning a high amount of silver content. Thus, this curve should be related to the percolation of silver nanoparticles in the PTh-PMMA polymeric matrix. The value of the critical exponent of the electrical conductivity of the IPN film suggests the possibility that the Ag nanoparticles are introduced into the host matrix forming 2D systems. This result can be explained by considering that the silver nanoparticles are placed between two polythiophene polymeric chains, as shown in **Figure 5.14**. So, in the end, the IPN film would be made up of a random distribution of the polythiophene polymeric chains in the three directions of space at the same time that the Ag-nanoparticles are always distributed between two polythiophene polymeric chains.

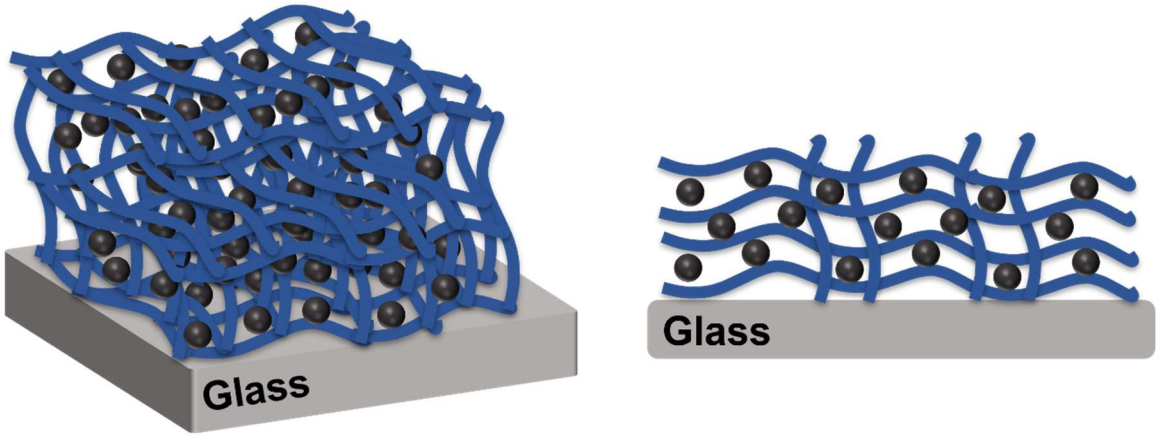

Figure 5.14 3D and cross-section schemes of the percolation distribution of Ag-nanoparticles in the PTh-PMMA matrix.

Figure 5.15(a) shows XPS spectra of PTh-Ag(I)-PMMA films measured in energy regions corresponding to the Ag 3d for three different Ag(I):3T ratios. According to the reaction proposed in **Figure 5.10**, after the oxidative polymerization of 3T, the main by-product may be Ag(0). Ag(0) shows the Ag $3d_{5/2}$ and $3d_{3/2}$ binding energy at 568.2 and 374.2 eV with a binding energy difference of 6 eV, indicating the formation of silver nanoparticles. That result agrees with the XRD spectra of PTh-Ag(I)-PMMA at different molar ratios oxidant:monomer (**Figure 5.15(b)**). The diffraction peak at a 2θ value of 38°, increases with the Ag(I):3T ratio. This diffraction peak is strongly associated with the plane (111) of silver nanoparticles.

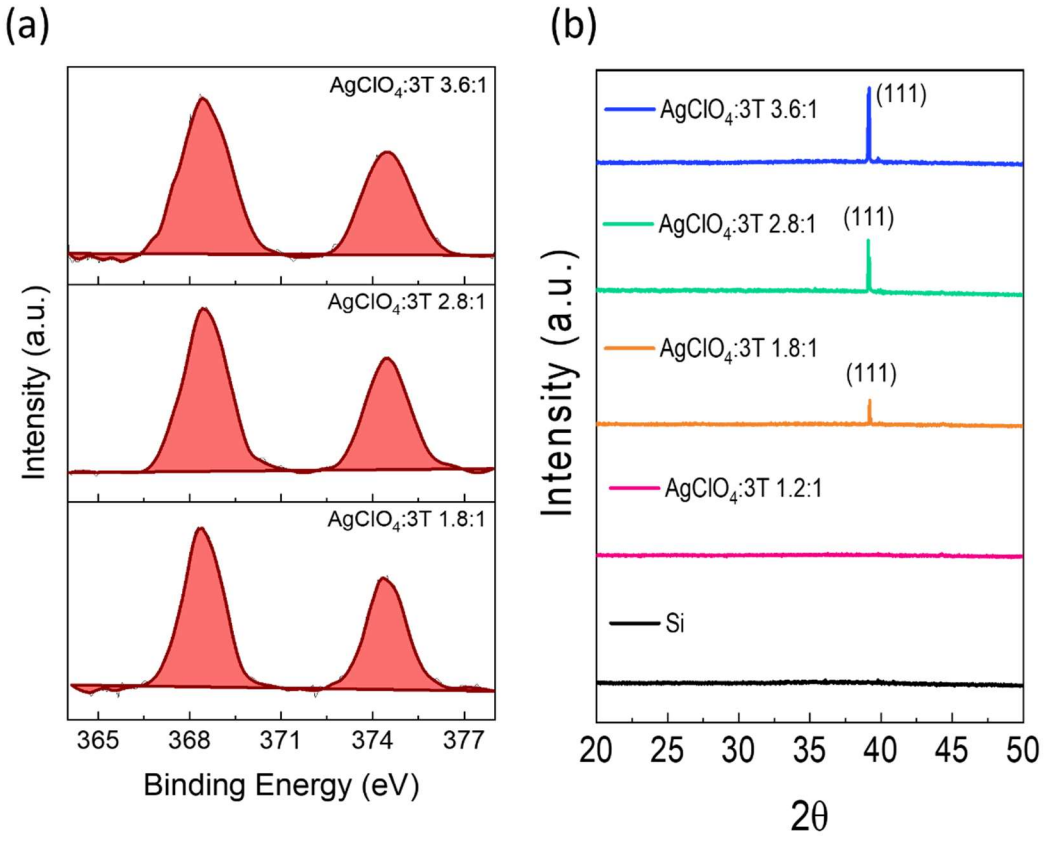

Figure 5.15 (a) Ag 3d XPS spectra and (b) XRD diffractogram of a PTh-PMMA IPN film as a function of $AgClO_4$:3T molar ratio.

As the Ag(I):3T ratio increases, a higher content of silver nanoparticles is *in-situ* formed inside the PMMA matrix. The formation of that nanoparticles is also observed in TEM images. **Figure 5.16** shows the TEM images of PTh-PMMA films synthesized at different Ag(I):3T molar ratios. We can observe that the *in-situ* polymerization of 3T inside PMMA generates homogeneous conductive IPNs, but as the Ag(I):3T ratio increases from 1.8 to 2.8 and 3.6, TEM images reveal the formation of Ag nanoparticles embedded in the IPN film. These results agree with the XPS spectra, the diffraction peak measured in XRD, and the percolation curve of **Figure 5.13(a)**.

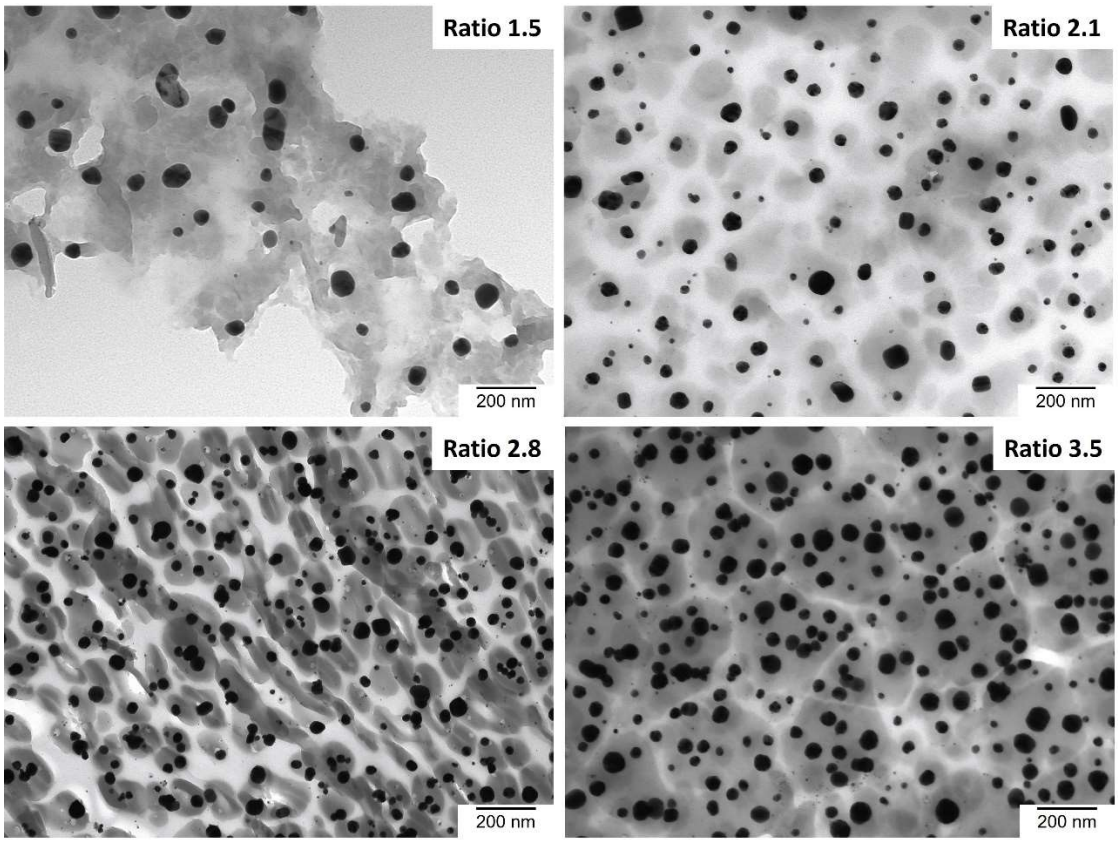

Figure 5.16 TEM images of PTh-PMMA IPN films with different $AgClO_4$:3T molar ratios.

Figure 5.17 shows the thermoelectric properties of the films as a function of the $AgClO_4$:3T molar ratio. As it was discussed earlier, the electrical conductivity increases as a function of the oxidant ratio with a maximum of 117 S cm^{-1} at a 2.8 $AgClO_4$:3T molar ratio. However, the values of the Seebeck coefficient follow a different trend. The Seebeck coefficient decreases from 66 to 52 μV K^{-1} until an $AgClO_4$:3T molar ratio of 2.0. This trend is typically observed in conductive polymers when the electrical conductivity increases, and the Seebeck coefficient decreases due to the presence of more charge carriers (holes in this case).

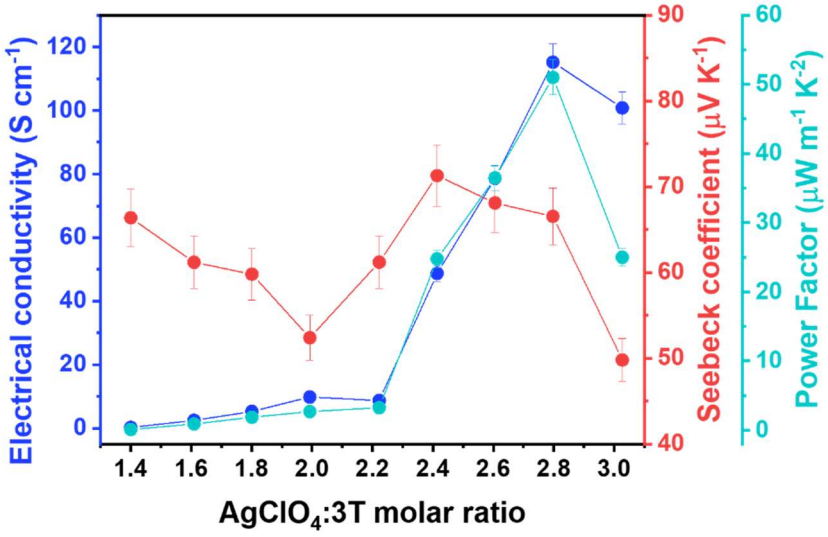

Figure 5.17 Electrical conductivity, Seebeck coefficient, and Power Factor as a function of $AgClO_4$:3T molar ratio.

In contrast, at larger $AgClO_4$:3T molar ratios, the Seebeck coefficient changes the trend and increases until values around 70 μV K^{-1} due to the presence of a higher amount of silver nanoparticles that have reached the percolation threshold. This fact is explained by the carrier filtering effect of the silver nanoparticles, allowing the Seebeck coefficient to increase without suppressing electrical conductivity, as shown in hybrid and nanocomposites based on conductive nanofillers.[78,79] At higher $AgClO_4$:3T molar ratios (3.0), this effect is inhibited by the overoxidation of the PTh, decreasing the Seebeck coefficient until 50 μV K^{-1}. A maximum power factor ($PF=S^2\,\sigma$) of 51 μW m^{-1} K^{-2} was obtained for an Ag(I):3T molar ratio of 2.8. These values are in the range of highly doped conductive polymers and nanocomposites.[69,80,81] However, thin films contain PMMA which helps to keep both the integrity and processability of the films.

5.3 *In-situ* synthesis of polythiophene in a polyurethane matrix

Once the polythiophene polymerization conditions were optimized in a PMMA matrix using $AgClO_4$ as an oxidant, we changed the PMMA polymeric matrix to a polyurethane one. This change is based on the difference in the mechanical properties of these two

matrices. PMMA, at room temperature, is a rigid polymer. In contrast, a thermoplastic elastomeric polyurethane is a flexible polymer at room temperature. This property is beneficial for obtaining flexible thermoelectric films suitable for developing wearable thermoelectric generators.

5.3.1 Materials

Terthiophene (3T), silver perchlorate, copper (II) perchlorate hexahydrate, analytical grade 1-Methoxy-2-propyl acetate (MPA), methoxy ethanol, and dimethylformamide (DMF) were purchased from Aldrich. The segmented thermoplastic elastomeric polyurethane was obtained from the reaction of methylene diphenyl diisocyanate (MDI) and polycarbonate diol UH100, using butanediol as chain extender. The mass average molecular weight is 250.000 and its glass transition temperature (T_g) is -6.4ºC. All chemicals were used as received.

5.3.2 Synthesis of polythiophene films

Thermoelectric thin films based on polythiophene (PTh) were obtained by *in-situ* oxidative polymerization of terthiophene in an oxidizing salt embedded in a polyurethane matrix. The previous work and the section before demonstrate that silver perchlorate and copper (II) perchlorate are two oxidizing salts that can be used in this process.[31] The reaction solution was prepared by mixing a terthiophene (3T) with a 4% polyurethane (PU) solution and the oxidizing agent. The solutions were then deposited on a PET substrate by spin coating at 1800 rpm (see **Figure 5.18(a)**). A thin polymeric film is formed after being subjected to a curing treatment at 160 °C for 1 minute. The solvent evaporates during the curing stage, and the polyurethane embeds the polythiophene. As a result, the oxidative polymerization reaction polymerizes the terthiophene to polythiophene, reducing the oxidizing salt metal. In the case of the silver salt, Ag^+, it will be reduced to Ag^0, and with the copper salt, Cu^{+2}, to Cu^+, as demonstrated in our previous works (see **Figure 5.18(b)**).[31]

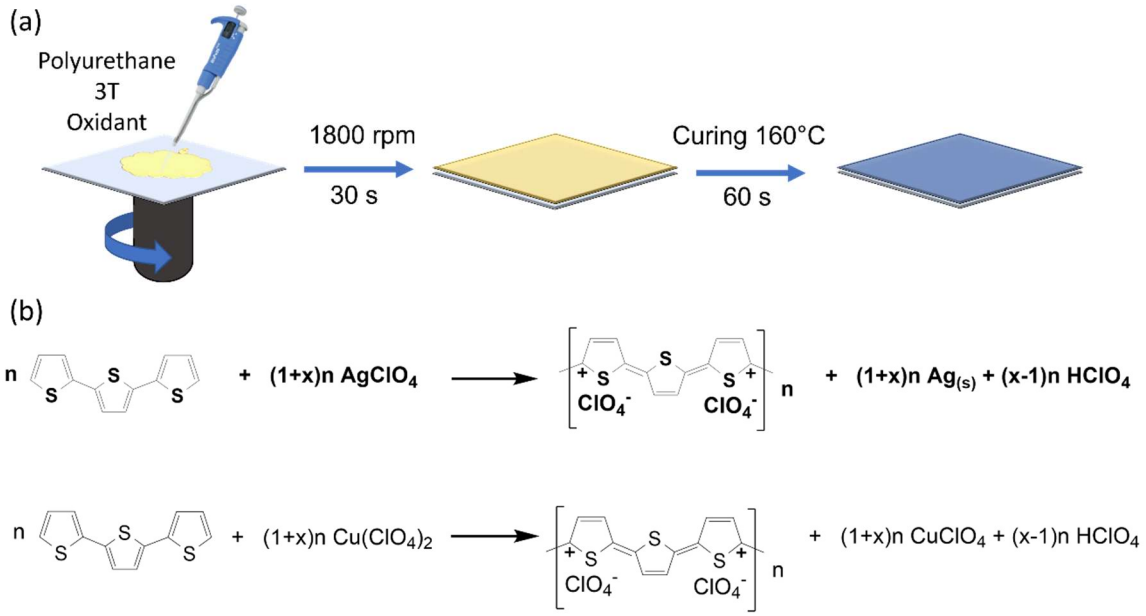

Figure 5.18 (a) Scheme of the synthesis procedure of polythiophene films in a polyurethane matrix. (b) Oxidative polymerization of terthiophene by $AgClO_4$ and $Cu(ClO_4)_2$.

5.3.3 Molar ratio oxidant:oligomer study

Thermoelectric properties depend on the concentration of charge carriers. The synthesis of polythiophene-based thermoelectric films can modulate the concentration of charge carriers through control of the oxidant:3T molar ratio. The charge carrier concentration is inversely proportional to the Seebeck coefficient (S) and directly proportional to the electrical conductivity (σ).[56,68] Therefore, the greater amount of oxidant, the higher concentration of charge carriers, and the greater the electrical conductivity of the film will be. However, it will have a lower Seebeck coefficient value. Therefore, the study seeks to find the optimal oxidant:3T molar ratio based on the maximum Power Factor (PF).

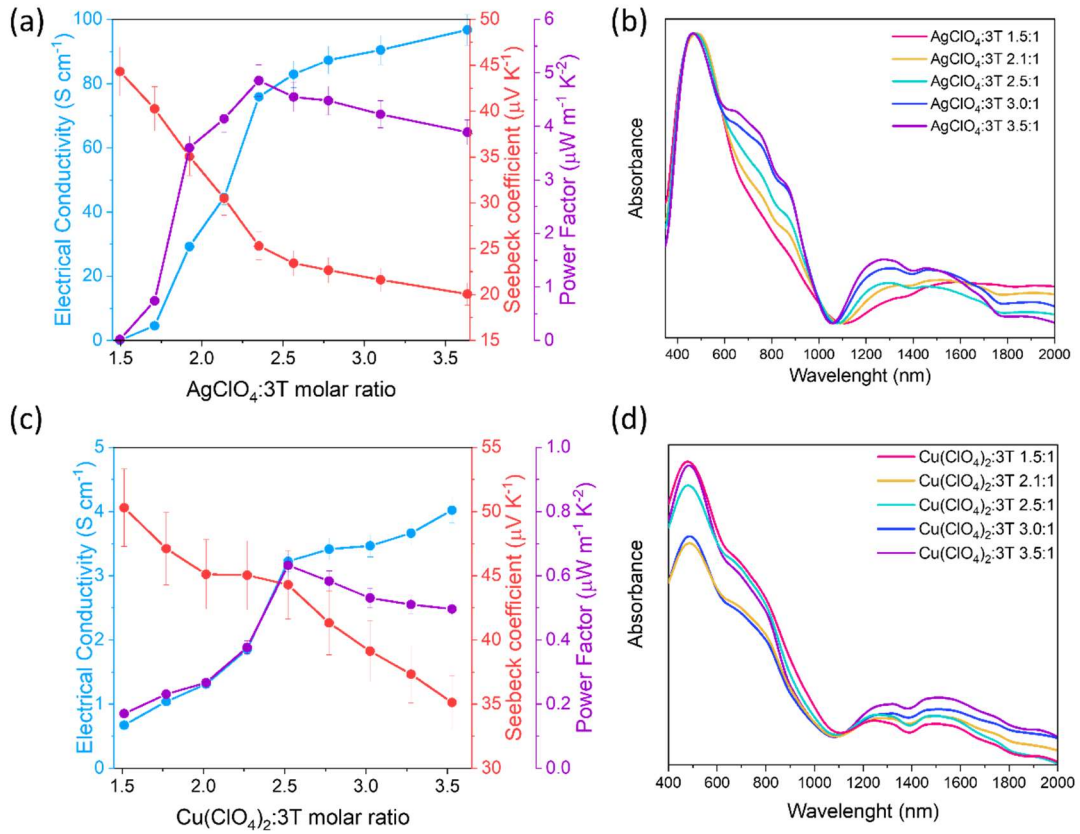

Figure 5.19 Electrical conductivity, Seebeck coefficient, Power Factor, and UV-Vis-NIR spectra of the polythiophene films as a function of the oxidant:3T molar ratio: (a) and (b) for $AgClO_4$, and (c) and (d) for $Cu(ClO_4)_2$.

Figure 5.19 shows the thermoelectric properties of the films as a function of the oxidant:3T molar ratio. As expected, the electrical conductivity increases as a function of the oxidant ratio, reaching 97 S cm^{-1} and 4 S cm^{-1} with $AgClO_4$ and $Cu(ClO4)_2$, respectively. This huge difference in the electrical conductivity can be explained by looking at the reduction potential of both metal species. The reduction reaction from Ag^+ to Ag^0 has a potential of 0.80 V, and the reduction reaction from Cu^{2+} to Cu^+ has a potential of 0.34 V. Therefore, the silver salt has a greater oxidizing behavior than the copper (II) salt, and that leads to a higher concentration of charge carriers along the polymer chain of polythiophene.[82,83] These results are supported by the UV-Vis-NIR spectra. In both spectra, regardless of the oxidant used, three bands appear. The first one is located between 400-550 nm and is related to aromatic fragments and π-π* transitions of the molecule; the second, over 775 nm, is associated with the polarons band, and the third band is centered at 1400 nm and is related with the presence of bipolarons. By increasing the proportion of oxidizing agents, the absorption intensity of the polaron and bipolar bands increases, indicating an increase in the charge carrier concentration.[56,84,85] Furthermore, the Seebeck

coefficient values follow a different trend decreasing with the oxidant:3T molar ratio. This trend is typically observed in conductive polymers due to the increased concentration of charge carriers. The Seebeck coefficient values are generally in the range of highly doped conductive polymers and nanocomposites.[58,80,81,86] Therefore, by increasing the oxidant molar ratio, the doping level of polythiophene is greater, increasing the electrical conductivity and decreasing the Seebeck coefficient. Finally, the maximum Power Factor was achieved for an oxidant:3T molar ratio of 2.5:1 for both oxidants.

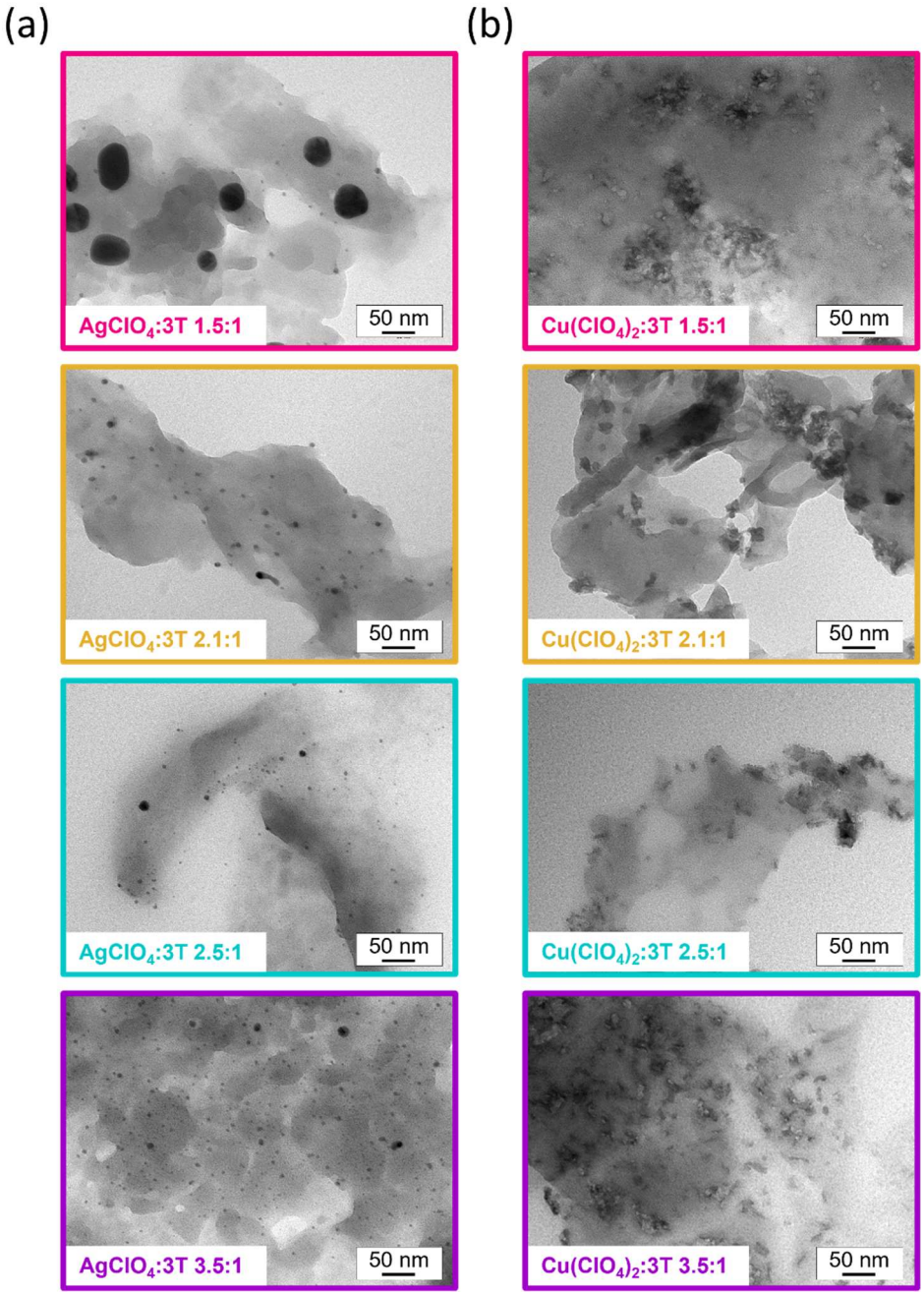

Figure 5.20 TEM images of thin films synthesized with different oxidant:3T molar ratios using (a) $AgClO_4$ and (b) $Cu(ClO_4)_2$.

Figure 5.20 shows TEM images of polythiophene films synthesized with silver and copper oxidant salts at different molar ratios. According to the reactions proposed in **Figure 5.18(b)**, after the oxidative polymerization of 3T with $AgClO_4$ the main by-product is Ag(0). However, after the polymerization of 3T with copper (II) perchlorate, a copper (I) salt is obtained as a by-product. **Figure 5.20(a)** shows that the polythiophene films obtained at different $AgClO_4$:3T molar ratios contain inorganic nanoparticles embedded within the film. After analyzing these films by XRD (**Figure 5.21(a)**), a defined diffraction peak is observed at a 2θ value of 38°, which increases with the $AgClO_4$:3T ratio. This diffraction peak is strongly associated with the plane (111) of silver nanoparticles. As the $AgClO_4$:3T ratio increases, higher content and smaller size of silver nanoparticles are *in-situ* formed inside the polyurethane matrix. The higher content and smaller silver nanoparticles are related to the explosive nucleation due to a higher concentration of $AgClO_4$. In this case, the nucleation process becomes dominant, making the growth of silver crystals relatively complicated.[87]

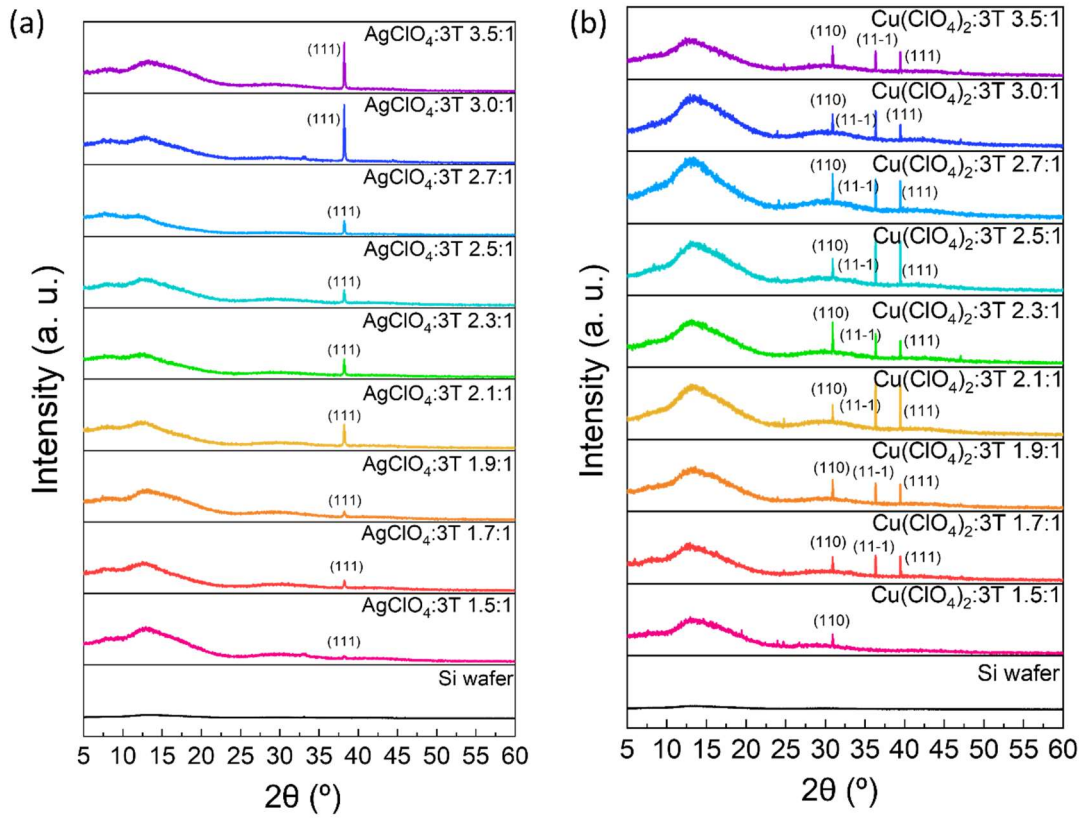

Figure 5.21 XRD diffractograms of the films as a function of the oxidant:3T molar ratio using (a) $AgClO_4$ and (b) $Cu(ClO_4)_2$.

TEM images of the film synthesized with $Cu(ClO_4)_2$ as oxidant (**Figure 5.20(b)**) show small crystalline solids embedded in the polyurethane matrix with a high Cu(II):3T molar

ratio. The XRD diffractogram (**Figure 5.21(b)**) reveals that the crystalline solids observed in the TEM images present an XRD pattern that corresponds to the planes (110), (11-1), and (111) of copper (II) oxide.[88] According to the reaction proposed in **Figure 5.18(b)**, the solid that should have been embedded in the polymeric matrix is copper (I) perchlorate, however, this was probably oxidized during the thermal treatment in the presence of oxygen and became formed copper(II) oxide.

5.3.4 Increasing the amount of 3T

One strategy to improve the thermoelectric properties of blends based on a conductive and an insulating material is by increasing the amount of conductive material on the insulating matrix. In this way, the electrical conductivity can increase without appreciably modifying the Seebeck coefficient, enhancing the final Power Factor.[89] In our case, we gradually increased the amount of oligomer (3T) on the polyurethane polymeric matrix, maintaining the previously optimized oxidant:3T molar ratio (2.5:1). **Figure 5.22** shows the thermoelectric properties and UV-Vis-NIR spectra as a function of the weight percentage of 3T regarding the polyurethane for both oxidants.

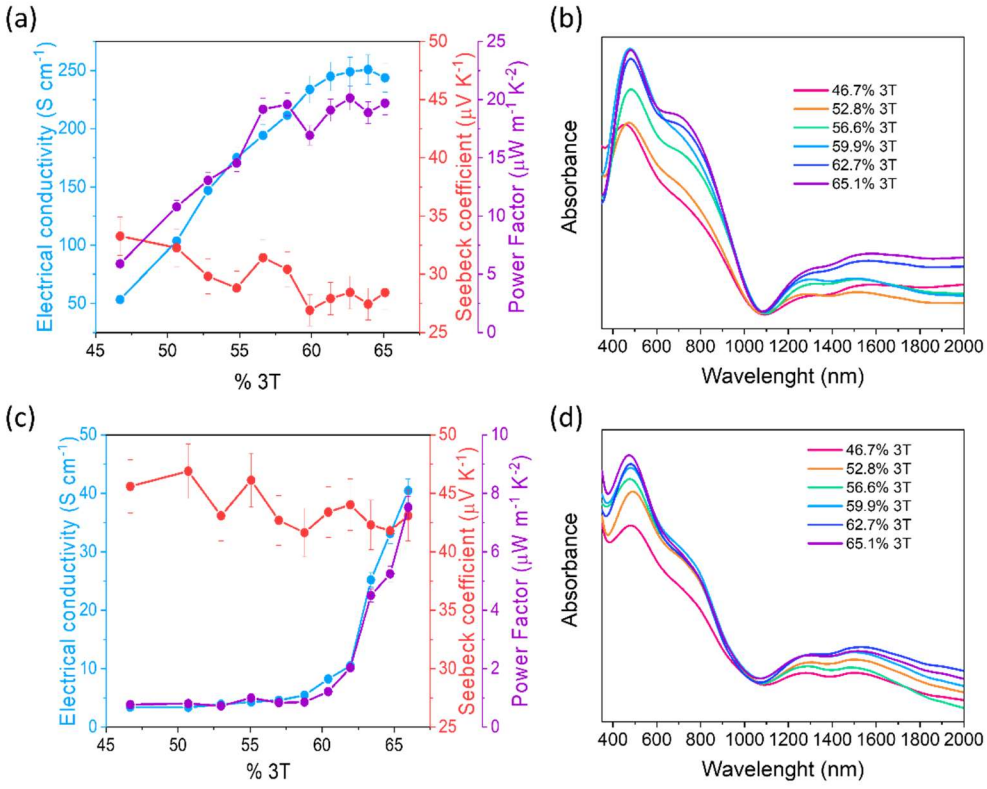

Figure 5.22 Electrical conductivity, Seebeck coefficient, Power Factor, and UV-Vis-NIR spectra as a function of the percentage of 3T with respect to the amount of polyurethane with an oxidant:3T molar ratio 2.5:1 for (a - b) $AgClO_4$ and (c - d) $Cu(ClO_4)_2$.

This study aims to know the maximum amount of 3T embedded in the polyurethane matrix to obtain maximum electrical conductivity, keeping the constant oxidant:3T molar ratio at 2.50:1. The Seebeck coefficient oscillates between (30 ± 4) μV K^{-1} and (42 ± 3) μV K^{-1} for the silver and copper oxidants, respectively. Since the oxidation states of the conductive polymer are not altered in this study, the concentration of charge carriers should be approximately the same, and it is expected that the Seebeck coefficient will remain constant around a given value. However, regarding electrical conductivity, a different trend is observed. In the presence of a silver oxidant, there is a progressive increase in electrical conductivity until reaching a plateau, which remains constant despite increasing the weight percentage of 3T. However, using the Cu (II) oxidant at low concentrations of 3T, the electrical conductivity increases slowly up to 60% of 3T, which grows exponentially. This difference in behavior is due to the greater oxidative character of Ag^{+}, which leads to a higher concentration of charge carriers along the polymer chain of polythiophene. Therefore, at lower 3T concentrations, we can reach the highest electrical conductivity. As a result, the maximum Power Factor (20 μW m^{-1} K^{-2}) is obtained with a 3T weight percentage of 62.7% in the case of silver salt. On the other hand, since with the copper (II) salt, the maximum of the percolation curve has not been reached, a stable Power Factor has not been obtained, and as seen in **Figure 5.22(c)**, it continues to increase with the percentage of 3T.

In addition, **Figure 5.22** shows the UV-Vis-NIR spectra of the samples as a function of the 3T weight percentage maintaining the oxidant:3T molar ratio at 2.50:1 for both oxidants. **Figure 5.22(b) and (d)** show that as the quantity of oligomer in the polyurethane matrix increases, the absorption intensity of the bands corresponding to the conjugated, polaron, and bipolar double bonds increases progressively. This indicates a higher concentration of charge carriers on the final film and, therefore, a higher electrical conductivity.

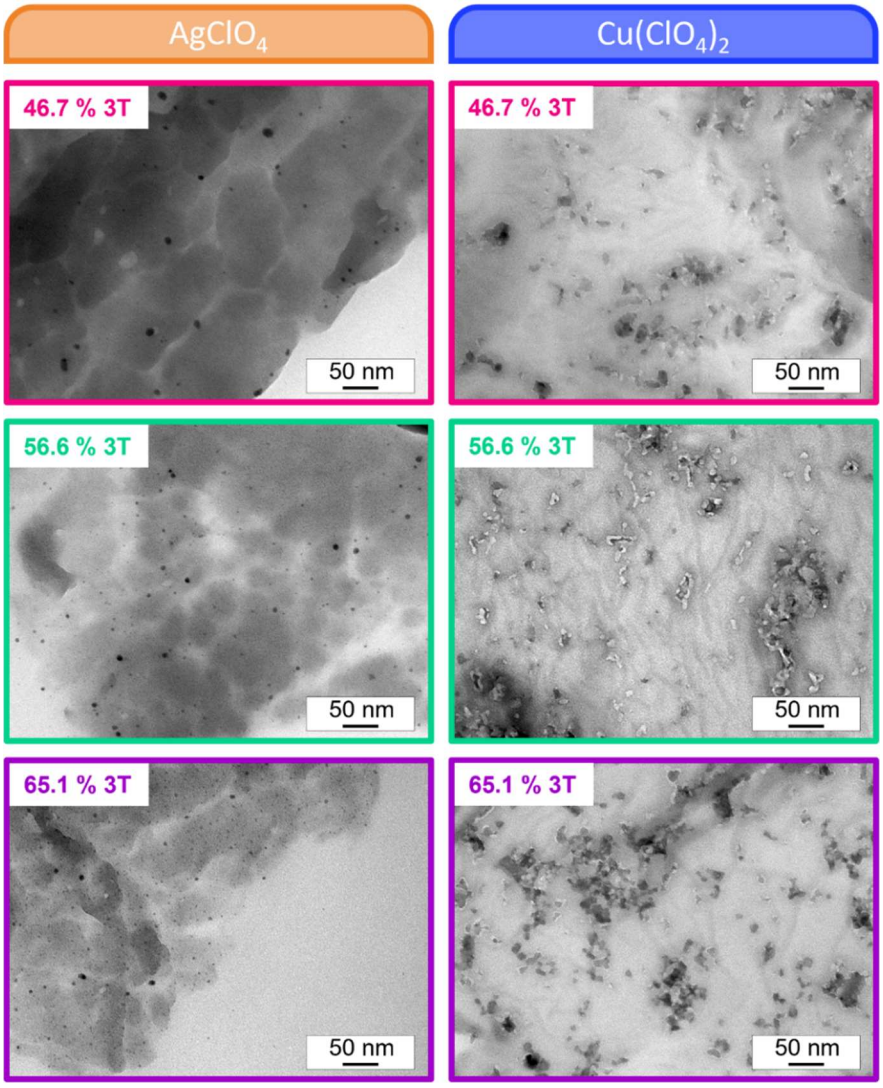

Figure 5.23 TEM images of polythiophene films obtained using silver and copper (II) oxidants with oxidant:3T molar ratio 2.5:1 at a different weight percentage of 3T.

Furthermore, the peak centered around 500 nm appears more defined in the case of silver oxidant. This can be related to the absorption of the plasmonic resonance of silver nanoparticles, indicating that their concentration has increased in the obtained film. TEM micrographs, **Figure 5.23**, confirm the formation of silver nanoparticles because of the reduction of Ag^{+} to Ag^{0}. In addition, nucleation is more visible since increasing the concentration of 3T in the synthesis increases the concentration of silver, and new crystallization nucleus are formed with smaller sizes. On the other hand, in the case of the copper (II) salt, small crystals are again observed due to copper (II) oxide, as suggested by the XRD pattern in **Figure 5.21**.

In addition, the thermal conductivity of the films optimized using the silver and copper oxidants was determined by the frequency-domain thermoreflectance method (**Table 5.1**).

Table 5.1 Thermal conductivity determined by frequency-domain thermoreflectance of thin films covered with gold. Composition: oxidant:oligomer molar ratio 2.5:1, 62.7% 3T.

	κ (W m^{-1} K^{-1})
PU	0.36
PTh-Ag-PU	0.40
PTh-Cu-PU	0.37

The results show that the thermal conductivity of PTh-Ag-PU and PTh-Cu-PU films is very similar to the thermal conductivity of a PU film, and they are of the order of other conductive polymers.[90–93] In addition, the presence of silver nanoparticles in the PTh-Ag-PU film causes a slight increase in thermal conductivity compared to the film PTh-Cu-PU because silver nanoparticles are excellent thermal conductors.[94,95]

5.3.5 Plasmonic effect

The plasmonic resonance band of the silver nanoparticles that appears in the UV-Vis-NIR spectrum invites us to study the effect of plasmonic heating of the films. As mentioned in the introduction, plasmonic heating is due to localized surface plasmon resonance (LSPR), in which electrons oscillate at the electric field frequency of the incident light and dampen the incident radiation by a Joule mechanism that generates heat.[37,38,96] Therefore, a different number of layers with an oxidant:3T molar ratio of 2.5:1 and a 3T weight percentage of 62.7% were deposited on the PET substrate to study this effect. The multilayer deposition aims to increase the concentration of silver nanoparticles generated in situ on the film and increase the plasmonic heating. In order to verify the effect of plasmonic heating of silver nanoparticles, a comparative study was conducted with both oxidants: silver perchlorate, which generates silver nanoparticles; and copper (II) perchlorate, which does not generate copper nanoparticles.

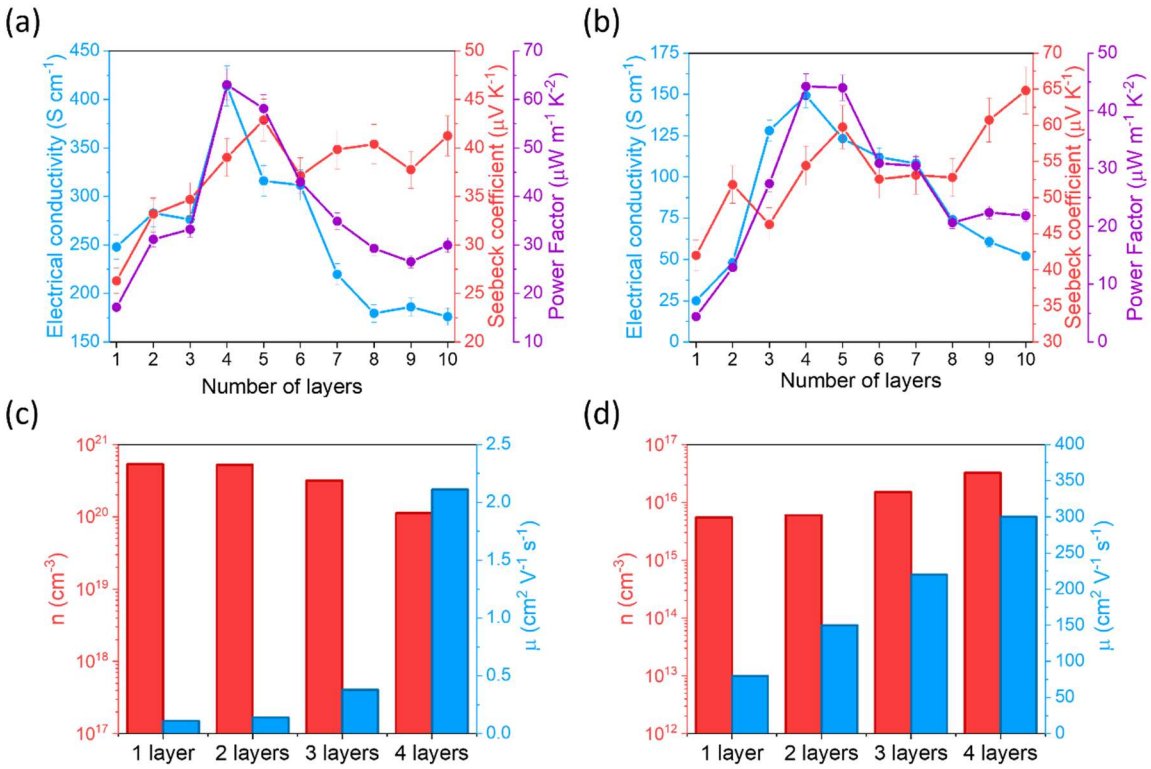

Figure 5.24 Electrical conductivity, Seebeck coefficient, and Power Factor of the films obtained in the presence of: (a) $AgClO_4$ and (b) $Cu(ClO_4)_2$ after the formation of successive layers. Carrier concentration (n) and carrier mobility (μ) as a function of the number of layers for (c) PTh-Ag-PU, and (d) PTh-Cu-PU films.

Chapter 3 demonstrates that multilayer systems are useful to improve thermoelectric properties.[97,98] Therefore, in the first place, the evolution of electrical conductivity, Seebeck coefficient, and Power Factor as a function of the number of layers deposited on the substrate was studied. **Figure 5.24(a) and (b)** show the evolution of these properties for the PTh-Ag-PU and PTh-Cu-PU films, respectively. In both cases, the Seebeck coefficient increases progressively with the number of layers. This enhance is due to a higher density of interconnections between the layers produced by the reaction of the residual oligomers on the surface of the film with the subsequent layer. **Figure 5.24(c)** and **(d)** show the Hall effect measurements on PTh-Ag-PU and PTh-Cu-PU films up to 4 layers. The concentration of charge carriers hardly varies with the increase in the number of layers while the carrier mobility is enhanced. These results indicate that the improved electrical conductivity and the Seebeck coefficient with the increasing number of layers are mainly due to the higher carrier mobility. In fact, the increase in carrier mobility supports the idea of a greater density of interconnections between layers. In addition, the results of the Hall effect explain the higher electrical conductivity and lower Seebeck coefficient of the PTh-

Ag-PU films compared to those of PTh-Cu-PU. The electrical conductivity increases as the number of layers increase until the fourth layer, then progressively decreases. This decrease in the electrical conductivity from the 4th layer is related to the rise of the thickness beyond the fourth layer. Finally, the maximum Power Factor was obtained with four layers, indicating that the optimal number of layers is four from the thermoelectric point of view.

The transmittance measurements of the films give us information about the relative absorption in the range of 350 to 2000 nm. **Figure 5.25** shows the evolution of transmittance as a function of the number of layers deposited on the PET substrate.

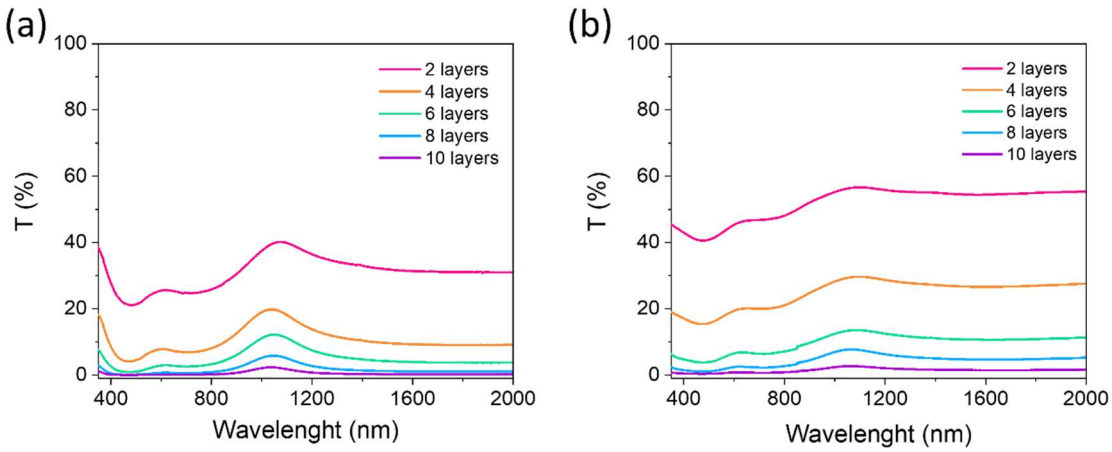

Figure 5.25 Transmittance spectra as a function of the number of layers deposited on the PET substrate using (a) $AgClO_4$ and (b) $Cu(ClO_4)_2$.

As expected, as the number of layers increases, the transmittance of the films progressively decreases, indicating a greater relative absorption in the range of wavelengths studied. If we compare the spectra of the films obtained with the different oxidizing salts, we observe that the films obtained with the same number of layers deposited with silver perchlorate have a higher relative absorption (**Table 5.2**). In addition, the peak centered at 500 nm appears more defined than in the films obtained with copper (II) perchlorate. This indicates the presence of silver nanoparticles embedded in the polymeric matrix. The deposition of 6 and 8 layers reaches practically 100% relative absorption for the films obtained with the silver and copper oxidant, respectively. Since the optimal Power Factor is found after the deposition of 4 layers and in the case of films obtained with $AgClO_4$ a relative absorption of 90% is reached, these films were used to study plasmonic heating.

Table 5.2 Relative absorption data as a function of the number of layers using the different oxidizing metal salts. The relative absorption is calculated as the percent area under the curve.

Absorption (%)		
No. Layers	**PTh-Ag-PU**	**PTh-Cu-PU**
1	47.69	28.39
2	69.10	48.15
3	79.53	62.92
4	89.51	75.32
5	93.02	84.17
6	95.14	90.36
7	97.47	92.50
8	98.35	95.64
9	99.19	98.04
10	99.53	98.60

The plasmonic heating tests were carried out by covering half of the film with plastic so that half of the film can be irradiated (see **Figure 5.26(a)**). Then, the coated film was introduced into a dark box with a hole to insert a solar simulator lamp ABET Technologies Light Sources of 1.5 suns.

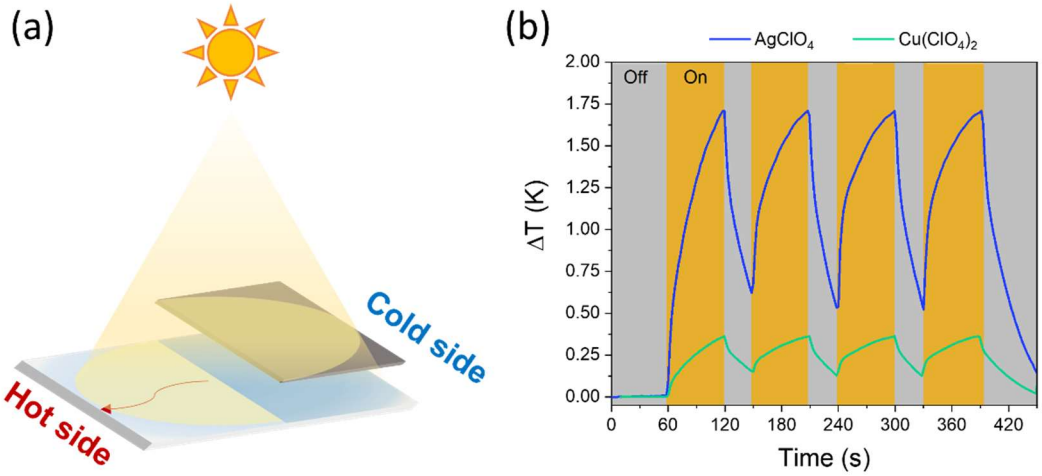

Figure 5.26 (a) Scheme of the plasmonic heating measure. (b) Temperature difference obtained by the plasmonic heating for PTh-Ag-PU and PTh-Cu-PU films with 4 layers.

As shown in **Figure 5.26(b)**, when irradiating with the lamp, a temperature difference of 1.7 ºC is reached when silver nanoparticles are embedded in the film. On the contrary, PTh-Cu-PU films show an increase of 0.4 ºC. This thermal gradient can be attributed to the absorption of the polymer. In the vast majority of applications of plasmonic materials,

plasmonic nanoparticles are excited by lasers or at the plasmonic resonance wavelength, which leads them to reach temperature increases of between 5 and 15 ºC.[99,100] In this work, we have reached a temperature difference of 1.7 ºC using a solar simulator of 1.5 suns. The thermal gradient is probably not that high because the metallic nanoparticles must resonate together for effective plasmonic heating and must be close. In these films, the silver nanoparticles are not distributed orderly throughout the polymeric matrix, as shown in TEM images in **Figure 5.23**. Therefore, the plasmonic resonance is slight, and the plasmonic heating is low. For this reason, an easy and low-cost method for obtaining a plasmonic layer has been developed in the third part of this work, which can generate a more significant thermal gradient.

5.4 Hybrid system thermoelectric-plasmonic

The thermal gradient obtained by the plasmonic heating of the silver nanoparticles generated *in-situ* during the polymerization of terthiophene in the polyurethane host matrix is not very high to create significant electrical power in a thermoelectric generator for the collection of bodies. For this reason, we decided to add a plasmonic layer to the developed thermoelectric material that acts as an optothermal converter and thus generates a higher thermal gradient.

5.4.1 Materials

Silver nitrate, titanium (IV) tetraisopropoxide (TTIP), triethanolamine (TEA), Pluronic P123, terthiophene (3T), silver perchlorate, copper (II) perchlorate hexahydrate, analytical grade 1-Methoxy-2-propyl acetate (MPA), methoxy ethanol, and dimethylformamide (DMF), polyvinyl alcohol (PVA) Mw = 30000, polymethylmethacrylate (PMMA) Mw = 360000, and poly(2-ethyl-2-oxazoline) (PEOX) Mw = 200000 were purchased from Aldrich. The segmented thermoplastic elastomeric polyurethane was obtained from the reaction of methylene diphenyl diisocyanate (MDI) and polycarbonate diol UH100, using butanediol as chain extender. All chemicals were used as received.

5.4.2 Synthesis of Ag-NP plasmonic layer

The plasmonic layer was obtained by photocatalyzed synthesis of silver nanoparticles embedded in different polymeric matrices using the spin-coating technique and subsequent exposure to UV light to reduce Ag^{+} to Ag^{0}. This reaction is photochemically catalyzed by a layer of titanium (IV) oxyhydroxide, $TiO_{2-0.5x}OH_x$ (Patent Application P202130501 of 06/02/2021) deposited on the PET substrate. In order to optimize the plasmonic performance of Ag nanoparticles embedded in a polyurethane matrix to obtain a maximum absorption in the visible range (380 - 750 nm), the influence of the $AgNO_3$ concentration and the exposure time under a UV light lamp for the formation of Ag nanoparticles have been investigated (**Figure 5.27(a)**).[101]

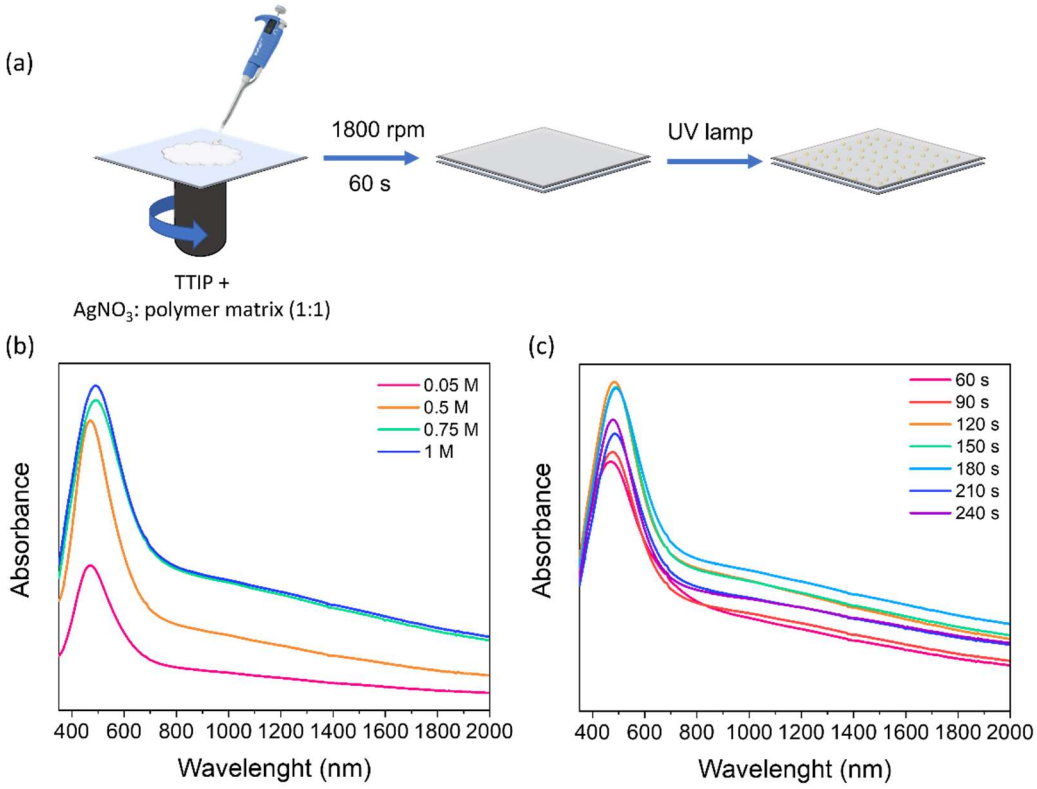

Figure 5.27 (a) Scheme of photocatalyzed synthesis of Ag nanoparticles. UV-Vis-NIR spectra of Ag nanoparticle films embedded in a polyurethane matrix as a function of (b) the $AgNO_3$ concentration and (c) the time it remains under the UV light lamp.

Figure 5.27(b) represents the UV-Vis-NIR spectra obtained at different $AgNO_3$ concentrations. The UV-Vis-NIR spectra show a peak centered between 450-500 nm, corresponding to the plasmonic resonance of Ag-NP obtained by the photoreduction reaction. The intensity of this peak increases with the concentration of silver nitrate until a maximum intensity when the concentration of $AgNO_3$ is 0.75 M. Once the optimal

concentration of the silver nitrate solution has been established, we study the time that the film should remain under UV light. As represented in **Figure 5.27(c)**, the intensity of the plasmonic resonance band of the silver nanoparticles progressively increases under the irradiation of the films with UV light. Beyond an irradiation time of 180 s, the intensity of the band decreases because the exposure of the polymeric matrix to UV light causes thermal degradation and exposes the nanoparticles to a different surrounding medium which can affect the plasmon resonance band.[101] Therefore, we have selected an $AgNO_3$ concentration of 0.75 M and a photoreduction time by $TiO_{2-0.5x}OH_x$ under a UV lamp of 120 seconds as optimal conditions for the photocatalyzed synthesis of Ag-NP plasmonic layer.

5.4.3 Stability of plasmonic layer

As mentioned before, the plasmonic resonance of metallic particles also depends on the surrounding medium. Therefore, finding a polymeric matrix capable of embedding silver nanoparticles and remaining stable under solar radiation is necessary. Four different ones have been selected. On the one hand, polyurethane (PU) has been chosen for its flexibility, which is important for developing flexible devices. On the other hand, polymethyl methacrylate (PMMA) has also been chosen because it is widely used in optoelectronic materials due to its transparency. Finally, polyvinyl alcohol (PVA) and poly(2-ethyl-2-oxazoline) (PEOX) matrices have been used because they are two of the most widely used polymeric matrices for the formation and stabilization of silver nanoparticles.[102,103] **Figure 5.28** shows the SEM images of the silver nanoparticle films embedded in different polymeric matrices. In the case of the PVA polymer matrix, silver aggregates are obtained. However, using PU and PMMA polymer matrices, it is possible to obtain silver nanoparticles of approximately 20 nm. On the other hand, silver nanoparticles with a cubic morphology of about 50 nm are obtained when the polymeric matrix is PEOX.

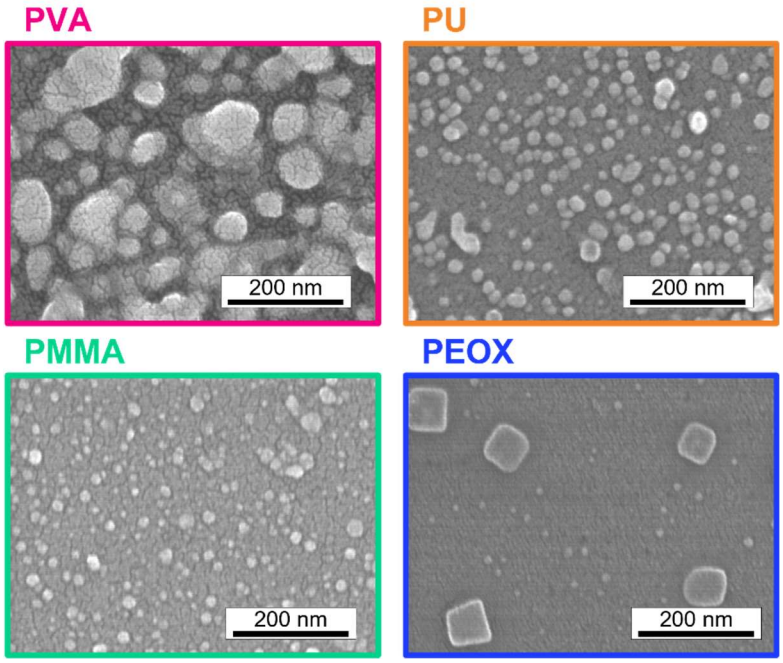

Figure 5.28 SEM micrographs of the films with silver nanoparticles embedded in different polymeric matrices.

Figure 5.29 shows the X-ray diffractogram (XRD) of the synthesized films. Ag-films with PVA, PU, and PMMA matrices show a diffraction plane (111) typical of silver nanoparticles. In the case of the film with PEOX, it presents two diffraction planes (111) and (200) characteristic of a silver fcc crystalline structure. The network constant calculated for this pattern was 4.087 Å, a value in agreement with that reported in the literature (a = 4.086 Å JCPDS 04-0783). In addition, the ratio between the (200) and (111) planes is slightly higher than the conventional value (0.57 vs. 0.4). This fact suggests that silver nanocubes have abundant {100} facets and are oriented parallel to the substrate.[104]

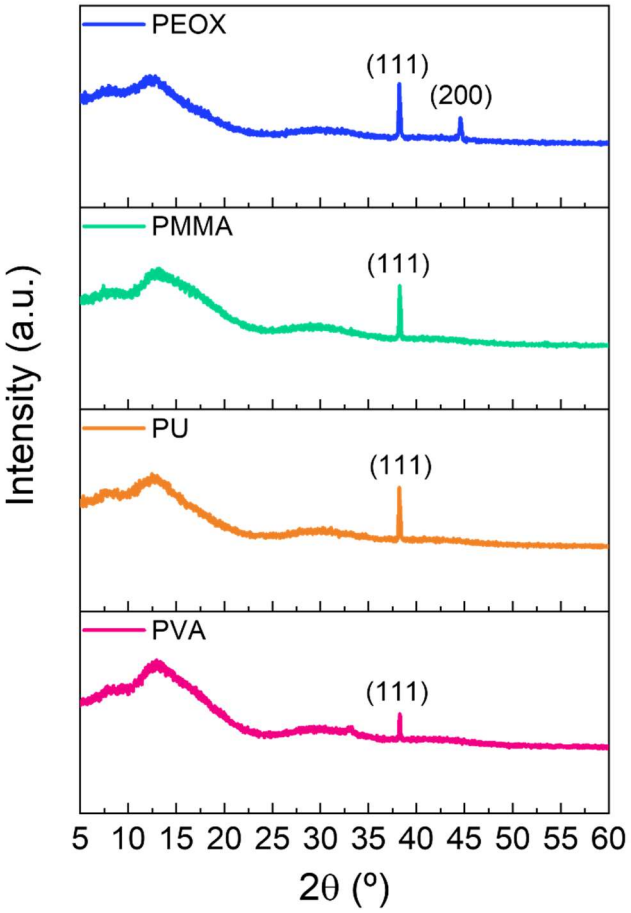

Figure 5.29 XRD diffractogram of the films with Ag-NP in different polymer matrices.

The main objective of introducing this plasmonic layer is to obtain the greatest temperature difference by irradiating it with sunlight. Since the localized surface plasmon resonance responsible for plasmonic heating depends on the environment in which the silver nanoparticles are placed, it is important to determine which polymeric matrix most effectively contributes to plasmonic heating. For this reason, we elaborated a measurement setup in which only half of the substrate was covered with Ag-films. Two K-type thermocouples were placed at the ends of the substrate, one in direct contact with the plasmonic layer and the other in contact only with the substrate. In this way, the plasmonic heating effect is due solely to light absorption since the solar simulator heats equally on both sides of the film. **Figure 5.30** shows the temperature difference between the end with the Ag-film and the end without it, generated by plasmonic heating. The PMMA and PU polymeric matrices reached the highest thermal gradients, 7.5 K and 7.3 K, respectively. However, the PVA and PEOX matrices obtained slightly smaller values (6.7 K and 6.2 K, respectively).

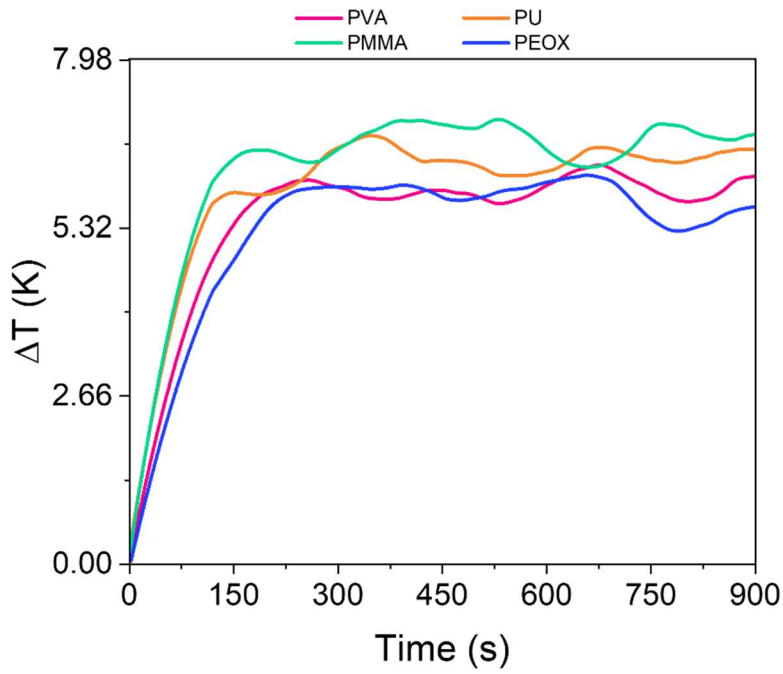

Figure 5.30 Temperature difference between the side with the Ag-film and without it, generated by plasmonic heating.

Looking at the SEM images, **Figure 5.28**, these temperature differences can be explained based on the different morphology of the silver nanoparticles obtained with the different polymeric matrices. With PU and PMMA matrices, the nanoparticles are smaller, allowing a greater number of nanoparticles to resonate when sunlight illuminates the film. On the contrary, with the PVA matrix, the silver aggregates interfere with the plasmonic resonance of the smaller silver nanoparticles, producing less plasmonic heating, as observed in **Figure 5.30**. Finally, with the PEOX matrix, the silver nanocubes are far away from each other, and thus the plasmon resonance effect of the nanocubes is diminished. If we look at the UV-Vis-NIR spectrum (**Figure 5.31**), the plasmonic resonance band of the film obtained in a PEOX matrix is very similar to that obtained in the rest of the matrices suggesting that the plasmon resonance that produces the heating is not due to the nanocubes but probably to small spherical silver nanoparticles. We can conclude that the PU and PMMA matrices contribute more significantly to the plasmonic heating since they favor the nucleation of silver nanoparticles, thus obtaining a significant number of smaller nanoparticles.[59,105]

Temporary stability in room conditions and stability against prolonged use are two important parameters in selecting the polymeric matrix that protects the plasmonic Ag-NPs and maintains their performance. In this work, two stability studies have been carried out

by monitoring the absorption changes of the plasmonic resonance of the Ag-NPs. On the one hand, the stability against a sun exposure of 15 min (**Figure 5.31(a)**) and, on the other hand, the stability under ambient conditions for two months (**Figure 5.31(b)**).

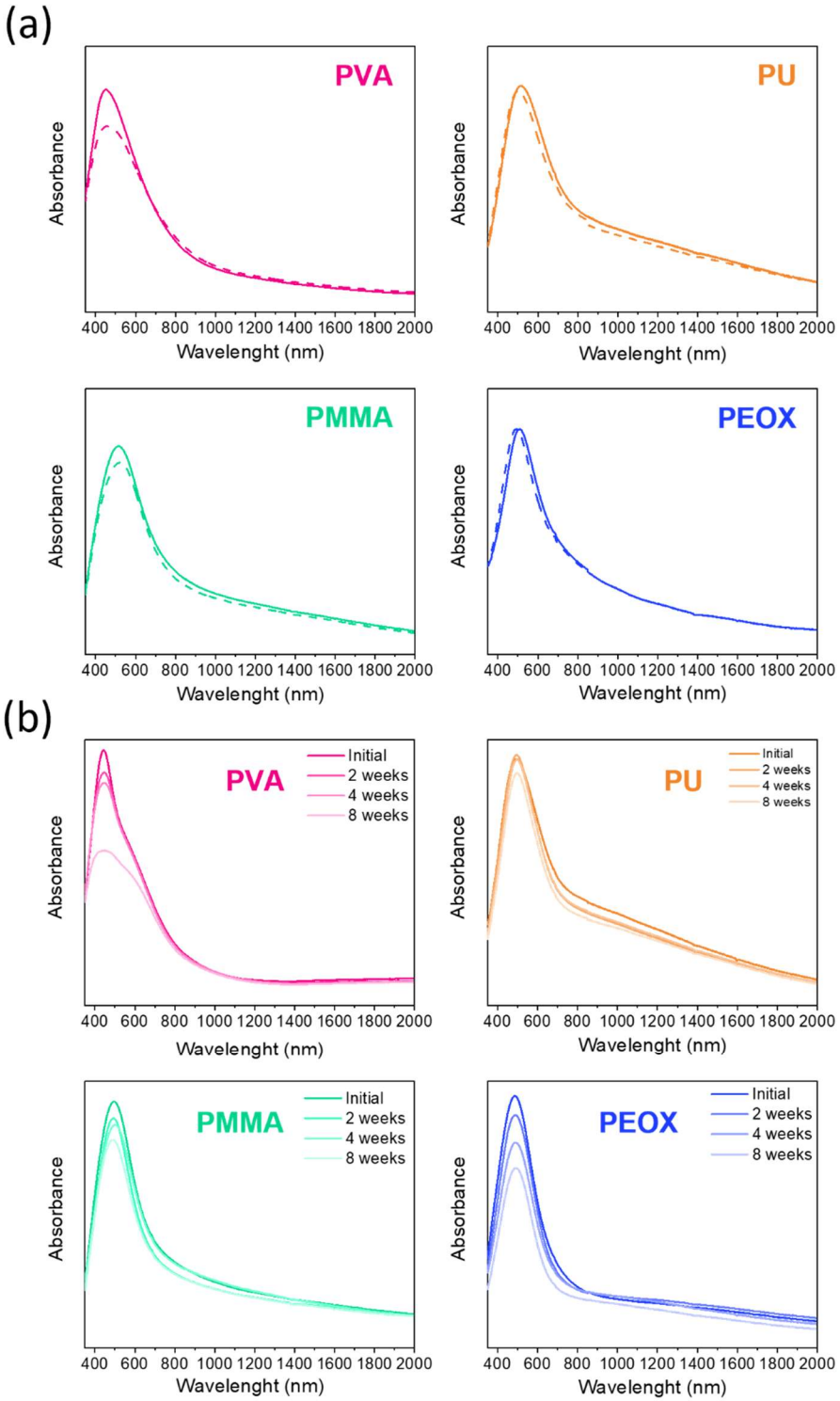

Figure 5.31 UV-Vis-NIR spectra of the films with Ag nanoparticles embedded in different polymeric matrices: (a) before (solid line) and after (dash line) solar simulator exposure for 15 min; (b) as a function of time under ambient conditions.

Figure 5.31(a) reveals that the plasmonic resonance band of the silver nanoparticles embedded in the PU and PEOX matrices was not altered after exposure to the solar simulator for 15 minutes. However, in the case of the PVA and PMMA matrices, a decrease in the plasmonic resonance band was observed. On the other hand, **Figure 5.31(b)** shows that the plasmonic resonance band of the plasmonic Ag-NPs in the PU and PMMA matrices hardly changed after two months in room conditions. On the contrary, absorption intensity decreased considerably after two months of obtaining the films with the PVA and PEOX matrices. These results can be explained considering that the PVA and PEOX matrices are soluble in water, and the environmental humidity can partially dissolve the polymeric matrix and expose the silver nanoparticles to the air. Therefore, the results of solar and temporal stability show that the polyurethane matrix is the most suitable.

5.4.4 Hybrid thermoelectric-plasmonic generator

The overall objective of this work is to take advantage of the plasmonic heating of silver nanoparticles to generate a temperature gradient with sunlight and transform it into electrical energy, maximizing the collection of residual energy and energy efficiency.[106] For this purpose, an assembly structure has been designed to generate a temperature increase in only one side of the film by plasmonic heating produced by the Ag-NPs absorption of sunlight, as shown in **Figure 5.32**. First, the Ag-NP plasmonic film was deposited using the PU matrix on a half substrate using the optimized conditions (0.75 M AgNO3 and 120 s UV lamp). Subsequently, on the complete substrate, the deposition and subsequent polymerization of the polythiophene were carried out with the conditions optimized in our previous work (2.5:1 oxidant:3T molar ratio, 62.7% 3T), using silver perchlorate as an oxidant.

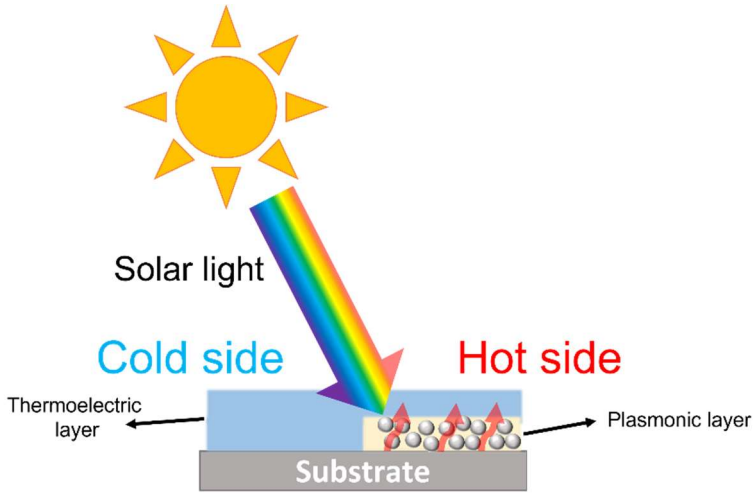

Figure 5.32 Scheme of the plasmonic heating mechanism to produce a thermal gradient in a thermoelectric layer deposited over the plasmonic layer.

According to the designed prototype, the thermoelectric layer needs to be transparent enough to allow sunlight to pass through it and reach the plasmonic layer. Therefore, optimizing the number of thermoelectric layers deposited over the plasmonic substrate is necessary. As seen in **Figure 5.24(a)**, the Power Factor of the thermoelectric film increases progressively up to the fourth layer. For this reason, the effect of plasmonic heating up to the fourth layer was studied. **Figure 5.33(a)** shows the transmittance spectra of the assembly of the plasmonic and thermoelectric films.

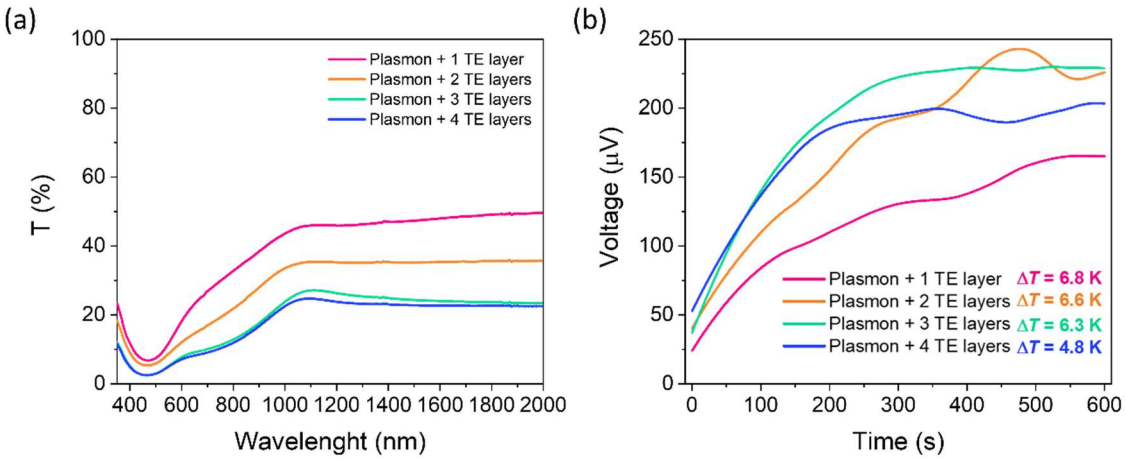

Figure 5.33 (a) Transmittance spectra and (b) open circuit voltage and thermal gradient as a function of the number of TE layers deposited over the plasmonic one.

As expected, as the number of thermoelectric layers deposited on the plasmonic substrate increases, the absorption of incident sunlight increases, indicating that the thermoelectric film is getting darker and does not allow solar radiation to reach the silver nanoparticles in the plasmonic layer. For this reason, the thermal gradients generated by

the plasmonic heating (see **Figure 5.33(b)**) decrease progressively with the number of layers. **Figure 5.33(b)** shows the electrical potentials generated by the hybrid system as a function of the number of layers exposed to sunlight. The highest voltage was 225 μV, achieved with the two and three thermoelectric layers deposited over the plasmonic film. Although the Seebeck coefficient of the three-layer system was higher than that of the two-layer system (**Figure 5.24(a)**), the temperature difference established between the ends of the film with two thermoelectric layers on the plasmonic layer was greater and, therefore, allowed reaching a final voltage similar with three layers one. The system formed by only a thermoelectric layer on top of the plasmonic layer reached the highest thermal gradient, but since its Seebeck coefficient was the lowest, the generated voltage was small. Finally, the system composed of four thermoelectric layers is the one that established the lowest thermal gradient between the ends of the film and, despite having the highest Seebeck coefficient, it did not reach the voltage obtained with the two- and three-layer system.

Incorporating the plasmonic heating effect in thermoelectric generators (TEG) allows for an increase in the thermal gradient of the TEG by the absorption of sunlight by the Ag-NP film and, therefore, increases the power output of the TEG. **Figure 5.34** shows the open circuit voltages generated by the hybrid plasmonic/TEG system, connecting 20 units in series, under illumination with a solar simulator. In both cases, the voltage with 20 units was practically 20 times the system voltage with a single unit. The hybrid plasmonic/TEG system fabricated with one plasmon layer and three thermoelectric layers reaches a higher open circuit voltage, around 4.8 mV.

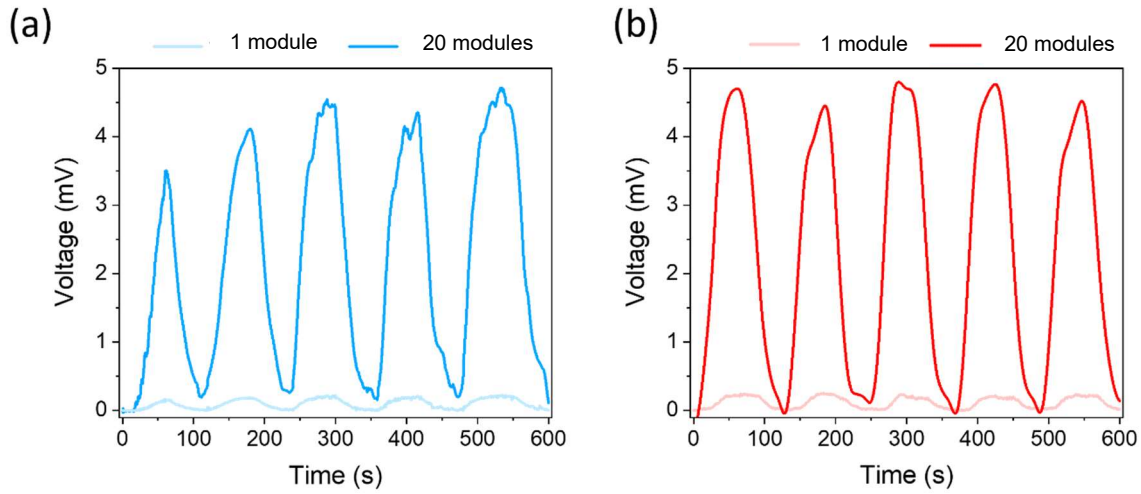

Figure 5.34 Open circuit voltage obtained under solar simulator of the hybrid plasmonic/thermoelectric generator with 1 and 20 units for: (a) plasmonic layer coated with two thermoelectric layers; and (b) plasmonic layer coated with three thermoelectric layers.

Another advantage offered by incorporating the plasmonic layer is the possibility of connecting the thermoelectric generator as if they were p-n systems by alternating the position of the plasmonic layer (**Figure 5.35(a)**).

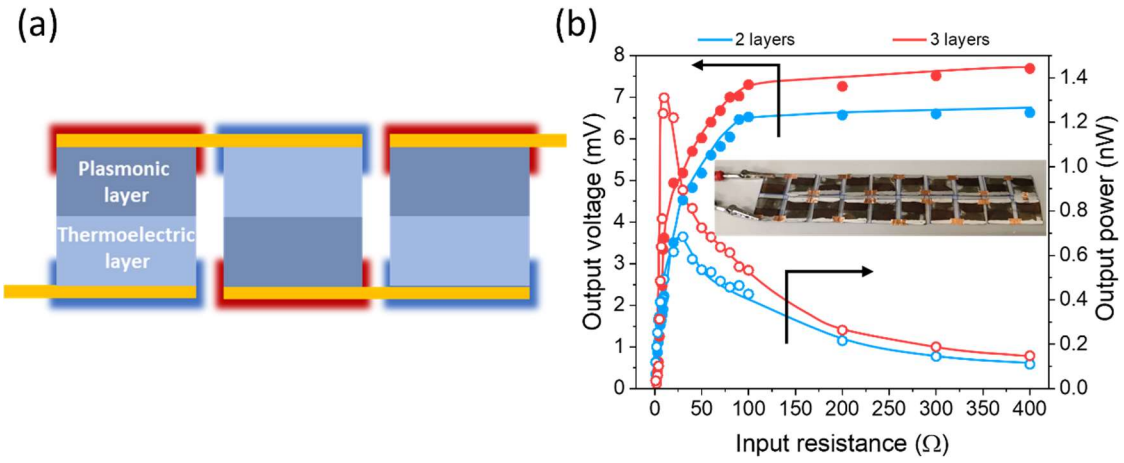

Figure 5.35 (a) Scheme of the hybrid plasmonic/thermoelectric generator. (b) Output voltage (full dots) and output power (open dots) as a function of the input resistance for the hybrid plasmonic/TEG films with two layers (ΔT = 6.6 K) and three layers (ΔT = 6.3 K). Inset of the real hybrid plasmonic/thermoelectric generator.

Using this configuration, two hybrid plasmon/TEG systems were elaborated by varying the number of thermoelectric layers (2 and 3), and the output power of the generator was measured under the illumination of a solar simulator (**Figure 5.35(b)**). The highest output power (1.3 nW) was achieved with the three thermoelectric layer system, while with the two-layer system, the output power reached 0.65 nW. The output power obtained with both generators is deficient, but we must consider that the resistance of each module is around 1 kΩ and, therefore, the final power generated is minimal. However, we must take this result as a proof of concept in which it is shown that a hybrid system made up of a plasmonic part and a thermoelectric part can generate an extra thermal gradient under solar stimulation, thanks to the effect of plasmonic heating, and improve the TEG performance for wearable devices.

5.5 Conclusions

This chapter showed a study of the optimal conditions based on the electrical conductivity of the *in-situ* polymerization of terthiophene within a PMMA matrix. Then these optimal conditions were transferred to a flexible polyurethane matrix. Optimized polymerization conditions were: reaction time, temperature, and oxidant:oligomer molar ratio. By varying the reaction time, it was observed that the electrical conductivity increased progressively until reaching a maximum of 60 s. Subsequently, the electrical conductivity decreased due to polythiophene decomposition processes. A similar trend was found in the variation of the polymerization temperature. The electrical conductivity increased progressively until reaching 160 ºC, and, beyond this temperature, the electrical conductivity decreased. Once these parameters were optimized, the influence of the oxidant:oligomer molar ratio was studied. In this case, a study was carried out applying the theory of percolation, and it was observed that at high values of the oxidant:oligomer ratio, the silver nanoparticles percolated between polythiophene polymer chains. The thermoelectric properties were also studied as a function of the oxidant:oligomer molar ratio, reaching a Power Factor of 50 $\mu W\ m^{-1}\ K^{-2}$ with a molar ratio of 2.8:1.

Next, the PMMA matrix was changed to a polyurethane one, and the previously optimized reaction conditions for the *in-situ* polymerization of terthiophene within the polyurethane matrix were applied, using $AgClO_4$ and $Cu(ClO_4)_2$ as oxidants. First, the optimal oxidant:oligomer molar ratio was determined again within this new matrix. Then, the amount of oligomer in the reaction mixture was increased while maintaining the optimal molar ratio constant. In this way, an improvement in electrical conductivity was produced without significantly changing the Seebeck coefficient, reaching a Power Factor of 20 $\mu W\ m^{-1}\ K^{-2}$ when the oxidizing silver salt was used and 8 $\mu W\ m^{-1}\ K^{-2}$ when the oxidizing salt of copper was used. TEM images showed silver nanoparticles embedded in the polythiophene/polyurethane matrix, while no copper nanoparticles were observed in the films with the copper oxidant. For this reason, it was decided to study the plasmonic heating effect of silver nanoparticles on the film. For this, the number of layers on the substrate was varied, finding that the highest Power Factor with both oxidants was found with 4 layers. Next, the effect of plasmonic heating was evaluated, showing that the films with silver nanoparticles reached a thermal gradient between the extremes of 1.72 ºC, and the films without silver nanoparticles (copper oxidant) only obtained a thermal gradient of

0.4 ºC. However, this temperature difference is not enough to generate significant electrical power. Therefore, a plasmonic layer was added to the PTh-Ag-PU film to generate a greater thermal gradient.

The reaction conditions (silver precursor concentration and reaction time) and the host polymeric matrix of the plasmonic layer were first optimized. The polymer host matrix is very important to ensure and maintain the plasmonic performance of the silver nanoparticles. With all this, it was concluded that the polyurethane matrix was the most suitable for this system. Finally, a hybrid system was developed in which the plasmonic layer was assembled with successive thermoelectric layers. The best values of the open-circuit voltage were obtained with 2 and 3 thermoelectric layers over the plasmonic one. Two plasmon/TEG with 2 and 3 thermoelectric layers were made, getting a value of 1.2 nW for the system with three thermoelectric layers. Although the output power obtained is very low, the combination of thermoelectric and plasmonic materials allows us to connect the modules as p-n junctions.

References

(1) Yang, Y.; Deng, H.; Fu, Q. Recent Progress on PEDOT:PSS Based Polymer Blends and Composites for Flexible Electronics and Thermoelectric Devices. *Mater. Chem. Front.* **2020**, *4* (11), 3130–3152. https://doi.org/10.1039/D0QM00308E.

(2) Spiteri, M. N.; Williams, C. E.; Boué, F. Pearl-Necklace-Like Chain Conformation of Hydrophobic Polyelectrolyte: A SANS Study of Partially Sulfonated Polystyrene in Water. *Macromolecules* **2007**, *40* (18), 6679–6691. https://doi.org/10.1021/ma060896d.

(3) Kim, Y. H.; Sachse, C.; Machala, M. L.; May, C.; Müller-Meskamp, L.; Leo, K. Highly Conductive PEDOT:PSS Electrode with Optimized Solvent and Thermal Post-Treatment for ITO-Free Organic Solar Cells. *Adv. Funct. Mater.* **2011**, *21* (6), 1076–1081. https://doi.org/10.1002/adfm.201002290.

(4) Wu, F.; Li, P.; Sun, K.; Zhou, Y.; Chen, W.; Fu, J.; Li, M.; Lu, S.; Wei, D.; Tang, X.; Zang, Z.; Sun, L.; Liu, X.; Ouyang, J. Conductivity Enhancement of PEDOT:PSS via Addition of Chloroplatinic Acid and Its Mechanism. *Adv. Electron. Mater.* **2017**, *3* (7), 1700047. https://doi.org/10.1002/aelm.201700047.

(5) Wang, C.; Sun, K.; Fu, J.; Chen, R.; Li, M.; Zang, Z.; Liu, X.; Li, B.; Gong, H.; Ouyang, J. Enhancement of Conductivity and Thermoelectric Property of PEDOT:PSS via Acid Doping and Single Post-Treatment for Flexible Power Generator. *Adv. Sustain. Syst.* **2018**, *2* (12), 1800085. https://doi.org/10.1002/adsu.201800085.

(6) Zhang, L.; Yang, K.; Chen, R.; Zhou, Y.; Chen, S.; Zheng, Y.; Li, M.; Xu, C.; Tang, X.; Zang, Z.; Sun, K. The Role of Mineral Acid Doping of PEDOT:PSS and Its Application in Organic Photovoltaics. *Adv. Electron. Mater.* **2020**, *6* (1), 1900648. https://doi.org/10.1002/aelm.201900648.

(7) Ouyang, J.; Xu, Q.; Chu, C.-W.; Yang, Y.; Li, G.; Shinar, J. On the Mechanism of Conductivity Enhancement in Poly(3,4-Ethylenedioxythiophene):Poly(Styrene

Sulfonate) Film through Solvent Treatment. *Polymer (Guildf).* **2004**, *45* (25), 8443–8450. https://doi.org/10.1016/j.polymer.2004.10.001.

(8) Lipomi, D. J. Stretchable Figures of Merit in Deformable Electronics. *Adv. Mater.* **2016**, *28* (22), 4180–4183. https://doi.org/10.1002/adma.201504196.

(9) Lipomi, D. J.; Bao, Z. Stretchable and Ultraflexible Organic Electronics. *MRS Bull.* **2017**, *42* (02), 93–97. https://doi.org/10.1557/mrs.2016.325.

(10) Root, S. E.; Savagatrup, S.; Printz, A. D.; Rodriquez, D.; Lipomi, D. J. Mechanical Properties of Organic Semiconductors for Stretchable, Highly Flexible, and Mechanically Robust Electronics. *Chem. Rev.* **2017**, *117* (9), 6467–6499. https://doi.org/10.1021/acs.chemrev.7b00003.

(11) Vikki, T.; Pietilä, L.-O.; Österholm, H.; Ahjopalo, L.; Takala, A.; Toivo, A.; Levon, K.; Passiniemi, P.; Ikkala, O. Molecular Recognition Solvents for Electrically Conductive Polyaniline. *Macromolecules* **1996**, *29* (8), 2945–2953. https://doi.org/10.1021/ma951555v.

(12) Li, Y.; Tanigawa, R.; Okuzaki, H. Soft and Flexible PEDOT/PSS Films for Applications to Soft Actuators. *Smart Mater. Struct.* **2014**, *23* (7), 074010. https://doi.org/10.1088/0964-1726/23/7/074010.

(13) Li, Y.; Masuda, Y.; Iriyama, Y.; Okuzaki, H. Stretchable and Highly Conductive Polymer Films. *Trans. Mater. Res. Soc. Japan* **2012**, *37* (2), 303–306. https://doi.org/10.14723/tmrsj.37.303.

(14) Yoon, S.-S.; Khang, D.-Y. Roles of Nonionic Surfactant Additives in PEDOT:PSS Thin Films. *J. Phys. Chem. C* **2016**, *120* (51), 29525–29532. https://doi.org/10.1021/acs.jpcc.6b12043.

(15) Savagatrup, S.; Chan, E.; Renteria-Garcia, S. M.; Printz, A. D.; Zaretski, A. V.; O'Connor, T. F.; Rodriquez, D.; Valle, E.; Lipomi, D. J. Plasticization of PEDOT:PSS by Common Additives for Mechanically Robust Organic Solar Cells and Wearable Sensors. *Adv. Funct. Mater.* **2015**, *25* (3), 427–436. https://doi.org/10.1002/adfm.201401758.

(16) Teo, M. Y.; Kim, N.; Kee, S.; Kim, B. S.; Kim, G.; Hong, S.; Jung, S.; Lee, K. Highly Stretchable and Highly Conductive PEDOT:PSS/Ionic Liquid Composite Transparent Electrodes for Solution-Processed Stretchable Electronics. *ACS Appl. Mater. Interfaces* **2017**, *9* (1), 819–826. https://doi.org/10.1021/acsami.6b11988.

(17) Kee, S.; Kim, H.; Paleti, S. H. K.; El Labban, A.; Neophytou, M.; Emwas, A.-H.; Alshareef, H. N.; Baran, D. Highly Stretchable and Air-Stable PEDOT:PSS/Ionic

Liquid Composites for Efficient Organic Thermoelectrics. *Chem. Mater.* **2019**, *31* (9), 3519–3526. https://doi.org/10.1021/acs.chemmater.9b00819.

(18) Döbbelin, M.; Marcilla, R.; Salsamendi, M.; Pozo-Gonzalo, C.; Carrasco, P. M.; Pomposo, J. A.; Mecerreyes, D. Influence of Ionic Liquids on the Electrical Conductivity and Morphology of PEDOT:PSS Films. *Chem. Mater.* **2007**, *19* (9), 2147–2149. https://doi.org/10.1021/cm070398z.

(19) Wang, Y.; Zhu, C.; Pfattner, R.; Yan, H.; Jin, L.; Chen, S.; Molina-Lopez, F.; Lissel, F.; Liu, J.; Rabiah, N. I.; Chen, Z.; Chung, J. W.; Linder, C.; Toney, M. F.; Murmann, B.; Bao, Z. A Highly Stretchable, Transparent, and Conductive Polymer. *Sci. Adv.* **2017**, *3* (3). https://doi.org/10.1126/sciadv.1602076.

(20) Hopkins, A. R.; Reynolds, J. R. Crystallization Driven Formation of Conducting Polymer Networks in Polymer Blends. *Macromolecules* **2000**, *33* (14), 5221–5226. https://doi.org/10.1021/ma991347t.

(21) Lee, J. H.; Jeong, Y. R.; Lee, G.; Jin, S. W.; Lee, Y. H.; Hong, S. Y.; Park, H.; Kim, J. W.; Lee, S.-S.; Ha, J. S. Highly Conductive, Stretchable, and Transparent PEDOT:PSS Electrodes Fabricated with Triblock Copolymer Additives and Acid Treatment. *ACS Appl. Mater. Interfaces* **2018**, *10* (33), 28027–28035. https://doi.org/10.1021/acsami.8b07287.

(22) Li, P.; Du, D.; Guo, L.; Guo, Y.; Ouyang, J. Stretchable and Conductive Polymer Films for High-Performance Electromagnetic Interference Shielding. *J. Mater. Chem. C* **2016**, *4* (27), 6525–6532. https://doi.org/10.1039/C6TC01619G.

(23) Noh, J.-S. Highly Conductive and Stretchable Poly(Dimethylsiloxane):Poly(3,4-Ethylenedioxythiophene):Poly(Styrene Sulfonic Acid) Blends for Organic Interconnects. *RSC Adv.* **2014**, *4* (4), 1857–1863. https://doi.org/10.1039/C3RA46087H.

(24) Luo, R.; Li, H.; Du, B.; Zhou, S.; Zhu, Y. A Simple Strategy for High Stretchable, Flexible and Conductive Polymer Films Based on PEDOT:PSS-PDMS Blends. *Org. Electron.* **2020**, *76*, 105451. https://doi.org/10.1016/j.orgel.2019.105451.

(25) Ko, Y.; Kim, D.; Kim, U.-J.; You, J. Vacuum-Assisted Bilayer PEDOT:PSS/Cellulose Nanofiber Composite Film for Self-Standing, Flexible, Conductive Electrodes. *Carbohydr. Polym.* **2017**, *173*, 383–391. https://doi.org/10.1016/j.carbpol.2017.05.096.

(26) Teng, C.; Lu, X.; Zhu, Y.; Wan, M.; Jiang, L. Polymer in Situ Embedding for Highly Flexible, Stretchable and Water Stable PEDOT:PSS Composite Conductors. *RSC*

Adv. **2013**, *3* (20), 7219. https://doi.org/10.1039/c3ra41124a.

(27) Shi, Z.; Gao, H.; Feng, J.; Ding, B.; Cao, X.; Kuga, S.; Wang, Y.; Zhang, L.; Cai, J. In Situ Synthesis of Robust Conductive Cellulose/Polypyrrole Composite Aerogels and Their Potential Application in Nerve Regeneration. *Angew. Chemie Int. Ed.* **2014**, *53* (21), 5380–5384. https://doi.org/10.1002/anie.201402751.

(28) Lin, Z.; Cao, N.; Sun, Z.; Li, W.; Sun, Y.; Zhang, H.; Pang, J.; Jiang, Z. Based On Confined Polymerization: In Situ Synthesis of PANI/PEEK Composite Film in One-Step. *Adv. Sci.* **2022**, *9* (1), 2103706. https://doi.org/10.1002/advs.202103706.

(29) Li, Y.; Zhang, H.; Ni, S.; Xiao, H. In Situ Synthesis of Conductive Nanocrystal Cellulose/Polypyrrole Composite Hydrogel Based on Semi-Interpenetrating Network. *Mater. Lett.* **2018**, *232*, 175–178. https://doi.org/10.1016/j.matlet.2018.08.115.

(30) Barani, H.; Miri, A.; Sheibani, H. Comparative Study of Electrically Conductive Cotton Fabric Prepared through the in Situ Synthesis of Different Conductive Materials. *Cellulose* **2021**, *28* (10), 6629–6649. https://doi.org/10.1007/s10570-021-03928-1.

(31) Seijas-Da Silva, A.; Noguera-Gomez, J.; Rodríguez-Canto, P. J.; Sanchez-Royo, J. F.; Cantarero, A.; Gómez, C. M.; Abargues, R. In Situ Synthesis of Conducting Polymers: A Novel Approach toward Polymer Thermoelectrics. *J. Phys. Chem. C* **2020**, *124* (42), 22884–22892. https://doi.org/10.1021/acs.jpcc.0c05333.

(32) Hyland, M.; Hunter, H.; Liu, J.; Veety, E.; Vashaee, D. Wearable Thermoelectric Generators for Human Body Heat Harvesting. *Appl. Energy* **2016**, *182*, 518–524. https://doi.org/10.1016/j.apenergy.2016.08.150.

(33) Jauffred, L.; Samadi, A.; Klingberg, H.; Bendix, P. M.; Oddershede, L. B. Plasmonic Heating of Nanostructures. *Chem. Rev.* **2019**, *119* (13), 8087–8130. https://doi.org/10.1021/acs.chemrev.8b00738.

(34) Herzog, J. B.; Knight, M. W.; Natelson, D. Thermoplasmonics: Quantifying Plasmonic Heating in Single Nanowires. *Nano Lett.* **2014**, *14* (2), 499–503. https://doi.org/10.1021/nl403510u.

(35) Vines, J. B.; Yoon, J.-H.; Ryu, N.-E.; Lim, D.-J.; Park, H. Gold Nanoparticles for Photothermal Cancer Therapy. *Front. Chem.* **2019**, *7*. https://doi.org/10.3389/fchem.2019.00167.

(36) Seynhaeve, A. L. B.; Amin, M.; Haemmerich, D.; van Rhoon, G. C.; ten Hagen, T. L. M. Hyperthermia and Smart Drug Delivery Systems for Solid Tumor Therapy.

Adv. Drug Deliv. Rev. **2020**, *163–164*, 125–144. https://doi.org/10.1016/j.addr.2020.02.004.

(37) Willets, K. A.; Van Duyne, R. P. Localized Surface Plasmon Resonance Spectroscopy and Sensing. *Annu. Rev. Phys. Chem.* **2007**, *58* (1), 267–297. https://doi.org/10.1146/annurev.physchem.58.032806.104607.

(38) Marty, R.; Baffou, G.; Arbouet, A.; Girard, C.; Quidant, R. Charge Distribution Induced inside Complex Plasmonic Nanoparticles. *Opt. Express* **2010**, *18* (3), 3035. https://doi.org/10.1364/OE.18.003035.

(39) Amendola, V.; Pilot, R.; Frasconi, M.; Maragò, O. M.; Iatì, M. A. Surface Plasmon Resonance in Gold Nanoparticles: A Review. *J. Phys. Condens. Matter* **2017**, *29* (20), 203002. https://doi.org/10.1088/1361-648X/aa60f3.

(40) Wiley, B. J.; Im, S. H.; Li, Z.-Y.; McLellan, J.; Siekkinen, A.; Xia, Y. Maneuvering the Surface Plasmon Resonance of Silver Nanostructures through Shape-Controlled Synthesis. *J. Phys. Chem. B* **2006**, *110* (32), 15666–15675. https://doi.org/10.1021/jp0608628.

(41) Wiley, B. J.; Chen, Y.; McLellan, J. M.; Xiong, Y.; Li, Z.-Y.; Ginger, D.; Xia, Y. Synthesis and Optical Properties of Silver Nanobars and Nanorice. *Nano Lett.* **2007**, *7* (4), 1032–1036. https://doi.org/10.1021/nl070214f.

(42) Mayer, K. M.; Hafner, J. H. Localized Surface Plasmon Resonance Sensors. *Chem. Rev.* **2011**, *111* (6), 3828–3857. https://doi.org/10.1021/cr100313v.

(43) Amendola, V.; Meneghetti, M. Size Evaluation of Gold Nanoparticles by UV−vis Spectroscopy. *J. Phys. Chem. C* **2009**, *113* (11), 4277–4285. https://doi.org/10.1021/jp8082425.

(44) Narducci, D.; Bermel, P.; Lorenzi, B.; Wang, N.; Yazawa, K. *Hybrid and Fully Thermoelectric Solar Harvesting*; 2018; Vol. 268.

(45) Fei Guo, C.; Sun, T.; Cao, F.; Liu, Q.; Ren, Z. Metallic Nanostructures for Light Trapping in Energy-Harvesting Devices. *Light Sci. Appl.* **2014**, *3*, 161. https://doi.org/10.1038/lsa.2014.42.

(46) Kraemer, D.; Hu, L.; Muto, A.; Chen, X.; Chen, G.; Chiesa, M. Photovoltaic-Thermoelectric Hybrid Systems: A General Optimization Methodology. *Appl. Phys. Lett.* **2008**, *92* (24), 243503. https://doi.org/10.1063/1.2947591.

(47) Dupré, O.; Vaillon, R.; Green, M. A. Physics of the Temperature Coefficients of Solar Cells. *Sol. Energy Mater. Sol. Cells* **2015**, *140*, 92–100. https://doi.org/10.1016/j.solmat.2015.03.025.

(48) Fei Guo, C.; Sun, T.; Cao, F.; Liu, Q.; Ren, Z. Metallic Nanostructures for Light Trapping in Energy-Harvesting Devices. *Light Sci. Appl.* **2014**, *3* (4), e161–e161. https://doi.org/10.1038/lsa.2014.42.

(49) Atwater, H. A.; Polman, A. Plasmonics for Improved Photovoltaic Devices. In *Materials for Sustainable Energy*; Co-Published with Macmillan Publishers Ltd, UK, 2010; pp 1–11. https://doi.org/10.1142/9789814317665_0001.

(50) Spinelli, P.; Ferry, V. E.; van de Groep, J.; van Lare, M.; Verschuuren, M. A.; Schropp, R. E. I.; Atwater, H. A.; Polman, A. Plasmonic Light Trapping in Thin-Film Si Solar Cells. *J. Opt.* **2012**, *14* (2), 024002. https://doi.org/10.1088/2040-8978/14/2/024002.

(51) Gradess, R.; Abderrafi, K.; Karoumi, A.; Bouchrif, B.; Habbou, A. A Simple Procedure to Assemble Silver and Gold Noble Metal Nanoparticles. *Chem. Sci. J.* **2018**, *09* (01). https://doi.org/10.4172/2150-3494.1000182.

(52) Jeong, M. H.; Kim, K.; Kim, J.-S.; Choi, K. J. Operation of Wearable Thermoelectric Generators Using Dual Sources of Heat and Light. *Adv. Sci.* **2022**, *9* (12), 2104915. https://doi.org/10.1002/advs.202104915.

(53) Refaey, S. A. M.; Schwitzgebel, G.; Schneider, O. Electrochemical Impedance Studies on Oxidative Degradation, Overoxidative Degradation, Deactivation and Reactivation of Conducting Polymers. *Synth. Met.* **1999**, *98* (3), 183–192. https://doi.org/10.1016/S0379-6779(98)00176-3.

(54) Culebras, M.; Gómez, C. M.; Cantarero, A. Review on Polymers for Thermoelectric Applications. *Materials (Basel).* **2014**, *7* (9), 6701–6732. https://doi.org/10.3390/ma7096701.

(55) Harbeke, G.; Baeriswyl, D.; Kiess, H.; Kobel, W. Polarons and Bipolarons in Doped Polythiophenes. *Phys. Scr.* **1986**, *T13*, 302–305. https://doi.org/10.1088/0031-8949/1986/t13/049.

(56) Zozoulenko, I.; Singh, A.; Singh, S. K.; Gueskine, V.; Crispin, X.; Berggren, M. Polarons, Bipolarons, And Absorption Spectroscopy of PEDOT. *ACS Appl. Polym. Mater.* **2019**, *1* (1), 83–94. https://doi.org/10.1021/acsapm.8b00061.

(57) Culebras, M.; Gómez, C. M.; Cantarero, A. Enhanced Thermoelectric Performance of PEDOT with Different Counter-Ions Optimized by Chemical Reduction. *J. Mater. Chem. A* **2014**, *2* (26), 10109–10115. https://doi.org/10.1039/C4TA01012D.

(58) Shen, L.; Liu, P.; Liu, C.; Jiang, Q.; Xu, J.; Duan, X.; Du, Y.; Jiang, F. Advances in Efficient Polymerization of Solid-State Trithiophenes for Organic Thermoelectric

Thin-Film. *Acs Appl. Polym. Mater.* **2020**, *2* (2), 376–384. https://doi.org/10.1021/acsapm.9b00842.

(59) Balan, L.; Malval, J.-P.; Lougnot, D.-J. In Situ Photochemically Assisted Synthesis of Silver Nanoparticles in Polymer Matrixes. In *Silver Nanoparticles*; Perez, D. P., Ed.; IntechOpen: Rijeka, 2010. https://doi.org/10.5772/8504.

(60) Aghlara, H.; Rostami, R.; Maghoul, A.; SalmanOgli, A. Noble Metal Nanoparticle Surface Plasmon Resonance in Absorbing Medium. *Optik (Stuttg).* **2015**, *126* (4), 417–420. https://doi.org/https://doi.org/10.1016/j.ijleo.2013.12.089.

(61) Behera, C.; Ghosh, S. P.; Kar, J. P.; Samal, S. L. Facile Synthesis and Enhanced Photocatalytic Activity of Ag-SnS Nanocomposites. *New J. Chem.* **2020**, *44* (27), 11684–11693. https://doi.org/10.1039/d0nj01225d.

(62) Gedi, S.; Minnam Reddy, V. R.; Reddy Kotte, T. R.; Kim, S. H.; Jeon, C. W. Chemically Synthesized Ag-Doped SnS Films for PV Applications. *Ceram. Int.* **2016**, *42* (16), 19027–19035. https://doi.org/10.1016/j.ceramint.2016.09.059.

(63) Jiang, Y.; Yang, Z.; Zhang, P.; Jin, H.; Ding, Y. Natural Assembly of a Ternary Ag-SnS-TiO2 Photocatalyst and Its Photocatalytic Performance under Simulated Sunlight. *RSC Adv.* **2018**, *8* (24), 13408–13416. https://doi.org/10.1039/c8ra01235k.

(64) Abargues, R.; Rodríguez-Cantó, P. J.; García-Calzada, R.; Martínez-Pastor, J. Patterning of Conducting Polymers Using UV Lithography: The in-Situ Polymerization Approach. *J. Phys. Chem. C* **2012**, *116* (33), 17547–17553. https://doi.org/10.1021/jp303425g.

(65) Culebras, M.; Serrano-Claumarchirant, J. F.; Sanchis, M. J.; Landfester, K.; Cantarero, A.; Gómez, C. M.; Muñoz-Espí, R. Conducting PEDOT Nanoparticles: Controlling Colloidal Stability and Electrical Properties. *J. Phys. Chem. C* **2018**, *122* (33), 19197–19203. https://doi.org/10.1021/acs.jpcc.8b04981.

(66) Serrano-Claumarchirant, J. F.; Culebras, M.; Muñoz-Espí, R.; Cantarero, A.; Gómez, C. M.; Collins, M. N. PEDOT Thin Films with N-Type Thermopower. *ACS Appl. Energy Mater.* **2020**, *3* (1), 861–867. https://doi.org/10.1021/acsaem.9b01985.

(67) Kim, D.; Zozoulenko, I. Why Is Pristine PEDOT Oxidized to 33%? A Density Functional Theory Study of Oxidative Polymerization Mechanism. *J. Phys. Chem. B* **2019**, *123* (24), 5160–5167. https://doi.org/10.1021/acs.jpcb.9b01745.

(68) Imae, I.; Akazawa, R.; Harima, Y. Seebeck Coefficients of Regioregular Poly(3-Hexylthiophene) Correlated with Doping Levels. *Phys. Chem. Chem. Phys.* **2018**,

20 (2), 738–741. https://doi.org/10.1039/C7CP07114K.

(69) Jacobs, I. E.; Moulé, A. J. Controlling Molecular Doping in Organic Semiconductors. *Adv. Mater.* **2017**, *29* (42), 1703063. https://doi.org/https://doi.org/10.1002/adma.201703063.

(70) Sperling, L. H. Interpenetrating Polymer Networks: An Overview; 1994; pp 3–38. https://doi.org/10.1021/ba-1994-0239.ch001.

(71) Tanudjaja, A.; Hifumi, R.; Inagi, S.; Tomita, I. π-Conjugated Organometallic Polymer Containing π-Extended Dithienotitanacyclopentadiene Units by Sonogashira-Hagihara Cross-Coupling Polycondensation. *Polymer (Guildf).* **2022**, *241*, 124511. https://doi.org/10.1016/j.polymer.2021.124511.

(72) Kim, D.; Zozoulenko, I. Why Is Pristine PEDOT Oxidized to 33%? A Density Functional Theory Study of Oxidative Polymerization Mechanism. *J. Phys. Chem. B* **2019**, *123* (24), 5160–5167. https://doi.org/10.1021/acs.jpcb.9b01745.

(73) Imae, I.; Akazawa, R.; Harima, Y. Seebeck Coefficients of Regioregular Poly(3-Hexylthiophene) Correlated with Doping Levels. *Phys. Chem. Chem. Phys.* **2018**, *20* (2), 738–741. https://doi.org/10.1039/C7CP07114K.

(74) Nan, C.-W. Physics of Inhomogeneous Inorganic Materials. *Prog. Mater. Sci.* **1993**, *37* (1), 1–116. https://doi.org/https://doi.org/10.1016/0079-6425(93)90004-5.

(75) Rodríguez-Cantó, P. J.; Martínez-Marco, M.; Sánchez-Royo, J. F.; Martínez-Pastor, J. P.; Abargues, R. In-Situ Synthesis of Thiophene-Based Multifunctional Polymeric Networks with Tunable Conductivity and High Photolithographic Performance. *Polymer (Guildf).* **2017**, *108*, 413–422. https://doi.org/10.1016/j.polymer.2016.12.003.

(76) Sahimi, M.; Hughes, B. D.; Scriven, L. E.; Davis, H. T. Critical Exponent of Percolation Conductivity by Finite-Size Scaling. *J. Phys. C Solid State Phys.* **1983**, *16* (16), L521--L527. https://doi.org/10.1088/0022-3719/16/16/004.

(77) Yoon, S.; Lee, S.-I. Possible Breakdown of the Universality of the Conductivity Critical Exponent in an Anisotropic Percolation System. *Phys. B Condens. Matter* **1990**, *167* (2), 133–137. https://doi.org/https://doi.org/10.1016/0921-4526(90)90005-F.

(78) Cho, C.; Culebras, M.; Wallace, K. L.; Song, Y.; Holder, K.; Hsu, J.-H.; Yu, C.; Grunlan, J. C. Stable N-Type Thermoelectric Multilayer Thin Films with High Power Factor from Carbonaceous Nanofillers. *Nano Energy* **2016**, *28*, 426–432. https://doi.org/https://doi.org/10.1016/j.nanoen.2016.08.063.

(79) Culebras, M.; Ren, G.; O'Connell, S.; Vilatela, J. J.; Collins, M. N. Lignin Doped Carbon Nanotube Yarns for Improved Thermoelectric Efficiency. *Adv. Sustain. Syst.* **2020**, *4* (11), 2000147. https://doi.org/https://doi.org/10.1002/adsu.202000147.

(80) Kiefer, D.; Kroon, R.; Hofmann, A. I.; Sun, H.; Liu, X.; Giovannitti, A.; Stegerer, D.; Cano, A.; Hynynen, J.; Yu, L.; Zhang, Y.; Nai, D.; Harrelson, T. F.; Sommer, M.; Moulé, A. J.; Kemerink, M.; Marder, S. R.; McCulloch, I.; Fahlman, M.; Fabiano, S.; Müller, C. Double Doping of Conjugated Polymers with Monomer Molecular Dopants. *Nat. Mater.* **2019**, *18* (2), 149–155. https://doi.org/10.1038/s41563-018-0263-6.

(81) Untilova, V.; Biskup, T.; Biniek, L.; Vijayakumar, V.; Brinkmann, M. Control of Chain Alignment and Crystallization Helps Enhance Charge Conductivities and Thermoelectric Power Factors in Sequentially Doped P3HT:F4TCNQ Films. *Macromolecules* **2020**, *53* (7), 2441–2453. https://doi.org/10.1021/acs.macromol.9b02389.

(82) Sönmez, G.; Schwendeman, I.; Schottland, P.; Zong, K.; Reynolds, J. R. N-Substituted Poly(3,4-Propylenedioxypyrrole)s: High Gap and Low Redox Potential Switching Electroactive and Electrochromic Polymers. *Macromolecules* **2003**, *36* (3), 639–647. https://doi.org/10.1021/ma021108x.

(83) Wheland, R. C. Correlation of Electrical Conductivity in Charge-Transfer Complexes with Redox Potentials, Steric Factors, and Heavy Atom Effects. *J. Am. Chem. Soc.* **1976**, *98* (13), 3926–3930. https://doi.org/10.1021/ja00429a031.

(84) Jacobs, I. E.; Moulé, A. J. Controlling Molecular Doping in Organic Semiconductors. *Adv. Mater.* **2017**, *29* (42), 1703063. https://doi.org/10.1002/adma.201703063.

(85) Lee, H. S.; Park, K.; Kim, J.-D.; Han, T.; Ryu, K. H.; Lim, H. S.; Lee, D. R.; Kwark, Y.-J.; Cho, J. H. Interpenetrating Polymer Network Dielectrics for High-Performance Organic Field-Effect Transistors. *J. Mater. Chem.* **2011**, *21* (19), 6968. https://doi.org/10.1039/c1jm10084j.

(86) Lindorf, M.; Mazzio, K. A.; Pflaum, J.; Nielsch, K.; Brütting, W.; Albrecht, M. Organic-Based Thermoelectrics. *J. Mater. Chem. A* **2020**, *8* (16), 7495–7507. https://doi.org/10.1039/C9TA11717B.

(87) Liu, W.; Zhao, X.; Dai, Y.; Qi, Y. Study on the Oriented Self-Assembly of Cuprous Oxide Micro-Nano Cubes and Its Application as a Non-Enzymatic Glucose Sensor. *Colloids Surfaces B Biointerfaces* **2022**, *211*, 112317.

https://doi.org/10.1016/j.colsurfb.2021.112317.

(88) Meghana, S.; Kabra, P.; Chakraborty, S.; Padmavathy, N. Understanding the Pathway of Antibacterial Activity of Copper Oxide Nanoparticles. *RSC Adv.* **2015**, *5* (16), 12293–12299. https://doi.org/10.1039/C4RA12163E.

(89) Serrano-Claumarchirant, J. F.; Hamawandi, B.; Ergül, A. B.; Cantarero, A.; Gómez, C. M.; Priyadarshi, P.; Neophytou, N.; Toprak, M. S. Thermoelectric Inks and Power Factor Tunability in Hybrid Films through All Solution Process. *ACS Appl. Mater. Interfaces* **2022**. https://doi.org/10.1021/acsami.1c24392.

(90) Liu, J.; Wang, X.; Li, D.; Coates, N. E.; Segalman, R. A.; Cahill, D. G. Thermal Conductivity and Elastic Constants of PEDOT:PSS with High Electrical Conductivity. *Macromolecules* **2015**, *48* (3), 585–591. https://doi.org/10.1021/ma502099t.

(91) Xu, Y.; Jia, Y.; Liu, P.; Jiang, Q.; Hu, D.; Ma, Y. Poly(3,4-Ethylenedioxythiophene) (PEDOT) as Promising Thermoelectric Materials and Devices. *Chem. Eng. J.* **2021**, *404*, 126552. https://doi.org/10.1016/j.cej.2020.126552.

(92) Hinckley, A. C.; Andrews, S. C.; Dunham, M. T.; Sood, A.; Barako, M. T.; Schneider, S.; Toney, M. F.; Goodson, K. E.; Bao, Z. Achieving High Thermoelectric Performance and Metallic Transport in Solvent-Sheared PEDOT:PSS. *Adv. Electron. Mater.* **2021**, *7* (3), 2001190. https://doi.org/10.1002/aelm.202001190.

(93) Chen, S.; Luan, T.; Di, C.; Lu, M.-H.; Yan, X.-J.; Song, C.; Deng, T. Thickness Dependent Thermal Performance of a Poly(3,4-Ethylenedioxythiophene) Thin Film Synthesized via an Electrochemical Approach. *RSC Adv.* **2022**, *12* (3), 1897–1903. https://doi.org/10.1039/D1RA07991C.

(94) Zhao, L.; Liao, C.; Liu, Y.; Huang, X.; Ning, W.; Wang, Z.; Jia, L.; Ren, J. A Combination of Aramid Nanofiber and Silver Nanoparticle Decorated Boron Nitride for the Preparation of a Composite Film with Superior Thermally Conductive Performance. *Compos. Interfaces* **2022**, *29* (4), 447–463. https://doi.org/10.1080/09276440.2021.1950378.

(95) Zhao, Z.-B.; Liu, J.-D.; Du, X.-Y.; Wang, Z.-Y.; Zhang, C.; Ming, S.-F. Fabrication of Silver Nanoparticles/Copper Nanoparticles Jointly Decorated Nitride Flakes to Improve the Thermal Conductivity of Polymer Composites. *Colloids Surfaces A Physicochem. Eng. Asp.* **2022**, *635*, 128104. https://doi.org/10.1016/j.colsurfa.2021.128104.

(96) Palpant, B. Photothermal Properties of Gold Nanoparticles. In *Gold Nanoparticles for Physics, Chemistry and Biology*; WORLD SCIENTIFIC (EUROPE), 2017; pp 87–130. https://doi.org/10.1142/9781786341259_0004.

(97) Cho, C.; Stevens, B.; Hsu, J.; Bureau, R.; Hagen, D. A.; Regev, O.; Yu, C.; Grunlan, J. C. Completely Organic Multilayer Thin Film with Thermoelectric Power Factor Rivaling Inorganic Tellurides. *Adv. Mater.* **2015**, *27* (19), 2996–3001. https://doi.org/10.1002/adma.201405738.

(98) Serrano-Claumarchirant, J. F.; Culebras, M.; Cantarero, A.; Gómez, C. M.; Muñoz-Espí, R. Poly(3,4-Ethylenedioxythiophene) Nanoparticles as Building Blocks for Hybrid Thermoelectric Flexible Films. *Coatings* **2019**, *10* (1), 22. https://doi.org/10.3390/coatings10010022.

(99) Politano, A.; Di Profio, G.; Fontananova, E.; Sanna, V.; Cupolillo, A.; Curcio, E. Overcoming Temperature Polarization in Membrane Distillation by Thermoplasmonic Effects Activated by Ag Nanofillers in Polymeric Membranes. *Desalination* **2019**, *451*, 192–199. https://doi.org/https://doi.org/10.1016/j.desal.2018.03.006.

(100) Moularas, C.; Georgiou, Y.; Adamska, K.; Deligiannakis, Y. Thermoplasmonic Heat Generation Efficiency by Nonmonodisperse Core–Shell Ag0@SiO2 Nanoparticle Ensemble. *J. Phys. Chem. C* **2019**, *123* (36), 22499–22510. https://doi.org/10.1021/acs.jpcc.9b06532.

(101) Kelly, K. L.; Coronado, E.; Zhao, L. L.; Schatz, G. C. The Optical Properties of Metal Nanoparticles: The Influence of Size, Shape, and Dielectric Environment. *J. Phys. Chem. B* **2003**, *107* (3), 668–677. https://doi.org/10.1021/jp026731y.

(102) Lezov, A.; Gubarev, A.; Mikhailova, M.; Lezova, A.; Mikusheva, N.; Kalganov, V.; Dudkina, M.; Ten'kovtsev, A.; Nekrasova, T.; Andreeva, L.; Saprykina, N.; Smyslov, R.; Gorshkova, Y.; Romanov, D.; Höppener, S.; Perevyazko, I.; Tsvetkov, N. Star-Shaped Poly(2-Ethyl-2-Oxazoline) and Poly(2-Isopropyl-2-Oxazoline) with Central Thiacalix[4]Arene Fragments: Reduction and Stabilization of Silver Nanoparticles. *Polymers (Basel).* **2019**, *11* (12), 2006. https://doi.org/10.3390/polym11122006.

(103) Kutsenko, A. S.; Granchak, V. M. Photochemical Synthesis of Silver Nanoparticles in Polyvinyl Alcohol Matrices. *Theor. Exp. Chem.* **2009**, *45* (5), 313–318. https://doi.org/10.1007/s11237-009-9099-0.

(104) Sun, Y.; Xia, Y. Shape-Controlled Synthesis of Gold and Silver Nanoparticles.

Science (80-.). **2002**, *298* (5601), 2176–2179. https://doi.org/10.1126/science.1077229.

(105) Nadal, E.; Barros, N.; Peres, L.; Goetz, V.; Respaud, M.; Soulantica, K.; Kachachi, H. In Situ Synthesis of Gold Nanoparticles in Polymer Films under Concentrated Sunlight: Control of Nanoparticle Size and Shape with Solar Flux. *React. Chem. Eng.* **2020**, *5*, 330. https://doi.org/10.1039/c9re00439d.

(106) Wu, B.; Guo, Y.; Hou, C.; Zhang, Q.; Li, Y.; Wang, H. High-Performance Flexible Thermoelectric Devices Based on All-Inorganic Hybrid Films for Harvesting Low-Grade Heat. *Adv. Funct. Mater.* **2019**, *29* (25), 1–11. https://doi.org/10.1002/adfm.201900304.

Chapter 6

General conclusions and future work

Content

This chapter summarizes the main general conclusions of this thesis. In addition, it presents future lines of work to consider for the development of the main outputs in this thesis.

6.1 General conclusions

In this thesis, thermoelectric hybrid materials have been developed in different ways. In chapter 3, layered hybrid thermoelectric materials were obtained based on two methods. The first one used the Layer-by-Layer technique to prepare multilayered structures by combining PEDOT:Tos nanoparticles and different types of CNTs (MWCNT, DWCNT, SWCNT). SWCNT with PEDOT:Tos nanoparticles at a 1:2 EDOT:FeTos molar ratio achieved the highest Power Factor, 72 μW m^{-1} K^{-2}, three orders of magnitude higher than the pristine PEDOT:Tos nanoparticles. The second method consisted of obtaining layered hybrid materials by electrodeposition PEDOT:ClO_4 and SnS:Ag. The morphology and thermoelectric properties vary depending on the amount of silver introduced.

In Chapter 4, thermoelectric fabrics were developed by electrodeposition of conductive polymers on MWCNT-coated fabrics. The electrical conductivity of the fabric increases progressively up to 20 BL of MWCNT. The electrodeposition of PANI:H_2SO_4 partially degrades the felt fibers. The PEDOT:ClO_4 coating showed a better Power Factor than the PPy:ClO_4 coating. The PEDOT:ClO_4 coating was applied to cotton and felt fabrics, both coated with 20 BL of MWCNT. The PEDOT:ClO_4 coated cotton fabric had a higher electrical conductivity. However, the felt fabric-based thermoelectric generator obtained a higher power output. Finally, an output power of 0.9 μW was reached at ΔT=31 K with 30 thermoelectric junctions. In the last part of this chapter, the influence of the electrochemical deposition of PEDOT with different counterions on the mechanical and electrical properties of the felt was studied. After coating the felt fabric with MWCNT, the storage modulus (E') increased. However, after electrochemical deposition of PEDOT, E' decreased, reaching values similar to those of the pristine fabric. The electrical conductivity and Seebeck coefficient of the PEDOT:BTFMSI coating was the highest. With this coating, a bracelet thermoelectric generator was elaborated, with an output power of 6.5 μW at ΔT=57 K with 14 thermoelectric units.

In chapter 5, thermoelectric blends based on PMMA and PU with polythiophene were developed through in-situ synthesis. The reaction time and temperature greatly influence the electrical conductivity. The optimal oxidizing:3T molar ratio was 2.5:1 for the oxidizing salts of silver perchlorate and copper (II) perchlorate. By keeping this molar ratio constant, it was possible to increase the amount of 3T in the polymeric matrix, reaching an electrical conductivity of 250 S cm^{-1}. The presence of silver nanoparticles generates a plasmonic heating effect, obtaining a thermal gradient of 1.72 K. A plasmonic layer of silver nanoparticles was then added in order to increase the thermal gradient. The polymeric matrix in which the Ag-NPs are embedded influences the plasmonic heating. Consequently, PU and PMMA matrices gave the highest thermal gradient. Finally, a hybrid thermoelectric-plasmonic generator was elaborated, obtaining an output power of 1.3 nW at ΔT=6.3 K with 20 thermoelectric units. In addition, this hybrid generator offers the possibility to connect p-type thermoelectric legs as if they were p-n junctions.

6.2 Future work

This thesis has been the starting point of many research lines that can be explored and developed further. For example, one of the main problems of wearable thermoelectric generators (wTEG) is the low thermal gradient established along the device. In chapter 5 we have seen that the inclusion of plasmonic materials can help to increase the thermal gradient due to the absorption of sunlight by the effect of plasmonic heating. Furthermore, the efficiency of the plasmonic material can be increased by modifying the aggregation state of the metallic nanoparticles. In recent months, we have worked on the colloidal synthesis of silver nanoparticles to cross-link the ligand with a spacer capable of aggregating the nanoparticles. In this way, the dispersion obtained acquires a black coloration and presents an absorption band in the entire visible range instead of only at the plasmonic resonance wavelength. Light absorption throughout the visible spectrum allows greater use of sunlight and, therefore, more significant plasmonic heating, generating a greater thermal gradient. With the colloidal dispersion, paints can be formulated to cover part of the units that make up the thermoelectric generator.

Another problem with wTEGs is that the thermal gradient they reach is not constant since the ambient temperature fluctuates depending on the time of day or the season. We are investigating a possible solution in our research group by including phase change

materials (PCM) in thermoelectric generators. In this way, when the ambient temperature is higher than the melting temperature of the PCM, this material melts, storing thermal energy. Conversely, when the ambient temperature drops below the melting temperature of the PCM, it crystallizes, releasing the previously-stored thermal energy. In the laboratory, we developed polystyrene nanocapsules with PCM inside and coated felt fabrics with these nanocapsules.

In general, I believe that for the development of wearable thermoelectric generators, we should not only focus on improving the thermoelectric properties or the architecture of the wTEG, but also on the search for new approaches that increase the thermal gradient along the wTEG and thus maximize its output power.

List of Figures

Chapter 1. General introduction

Chapter 2. Characterization techniques

Chapter 3. Hybrid layered thermoelectric materials

Chapter 4. Thermoelectric fabrics

Chapter 5. *In-situ* polymerization of polythiophene in polymer matrices

List of Tables

Abbreviations

3T	*Terthiophene*
ACN	*Acetonitrile*
AFM	*Atomic force microscope*
BL	*Bilayer*
BTFMSI	*Bis(trifluoromethylsulfonyl)imide*
ClO_4	*Perchlorate*
CNF	*Cellulose nanofibers*
CNT	*Carbon nanotube*
CB	*Conduction band*
DLS	*Dynamic light scattering*
DMA	*Dynamic mechanical analysis*
DMF	*Dimethylformamide*
DOC	*Sodium deoxycholate*
DRS	*Dielectric relaxation spectroscopy*
DSC	*Differential scanning calorimetry*
DWCNT	*Double-walled carbon nanotube*
E*	*Complex modulus*
E'	*Storage modulus*
E"	*Loss modulus*
EDOT	*3,4-ethylenedioxythiophene*
EDS	*Energy Dispersive Spectroscopy*
FeTos	*Iron(III) p-toluenesulfonate hexahydrate*
FTIR	*Fourier-transform infrared spectroscopy*
F-wTEG	*Flexible wearable thermoelectric generator*
GPC	*Gel permeation chromatography*
HOMO	*Highest occupied molecular orbital*
HRTEM	*High-resolution transmission electron microscopy*
IEA	*International Energy Agency*
IPN	*Interpenetrating polymeric network*
ITO	*Indium tin oxide*
LbL	*Layer-by-Layer*
LSPR	*Localized surface plasmon resonance*

LUMO	*Lowest unoccupied molecular orbital*
MDI	*Methylene diphenyl diisocyanate*
MPA	*(1-methoxy-2-propyl) acetate*
m-SWCNT	*Metallic single-walled carbon nanotube*
MWCNT	*Multi-walled carbon nanotube*
NIR	*Near infrared*
NP	*Nanoparticles*
oCVD	*Oxidative chemical vapor deposition*
PANI	*Polyaniline*
PDADMAC	*Poly(diallyldimethylammonium chloride)*
PDMS	*Polydimethylsiolxane*
PEDOT	*Poly(3,4-ethylenedioxythiophene)*
PEEK	*Polyetheretherketone*
PEG	*Polyethylene glycol*
PEO	*Polyethylene oxide*
PET	*Polyethylene terephthalate*
PF	*Power Factor*
PF_6	*Hexafluorophosphate*
PI	*Polyimide*
PMMA	*Polymethyl methacrylate*
PSS	*Polystyrenesulfonate*
PTh	*Polythiophene*
PU	*Polyurethane*
PVA	*Polyvinyl alcohol*
R-wTEG	*Rigid wearable thermoelectric generator*
S	*Seebeck coefficient*
SEM	*Scanning electron microscopy*
s-SWCNT	*Semiconductive single-walled carbon nanotube*
STEG	*Solar thermoelectric generator*
SWCNT	*Single-walled carbon nanotube*
S-wTEG	*Stretchable wearable thermoelectric generator*
TE	*Thermoelectric*
TEG	*Thermoelectric generator*
TEM	*Transmission electron microscopy*
*T*g	*Glass transition*
TGA	*Thermogravimetry analysis*
Tos	*p-toluenesulfonate*
T-wTEG	*Textile wearable thermoelectric generator*
UH100	*ETERNACOLL® Polycarbonate diol*
UN	*United Nations*
UV	*Ultraviolet*
VB	*Valence band*
Vis	*Visible*
WPU	*Water-based polyurethane*
wTEG	*Wearable thermoelectric generator*
XPS	*X-Ray phtoelectron spectroscopy*
XRD	*X-Ray diffraction*
*Z*T	*Figure of merit*
κ	*Thermal conductivity*
σ	*Electrical conductivity*

Scientific output

Journal publications

1. Culebras, M.; García-Barberá, A.; Serrano-Claumarchirant, J. F.; Gómez, C. M.; Cantarero, A. Hybrids Composites of NCCO/PEDOT for Thermoelectric Applications. *Synth. Met.* **2017**, *225*, 103–107. https://doi.org/10.1016/j.synthmet.2016.12.016.

2. Culebras, M.; Serrano-Claumarchirant, J. F.; Sanchis, M. J.; Landfester, K.; Cantarero, A.; Gómez, C. M.; Muñoz-Espí, R. Conducting PEDOT Nanoparticles: Controlling Colloidal Stability and Electrical Properties. *J. Phys. Chem. C* **2018**, *122* (33), 19197–19203. https://doi.org/10.1021/acs.jpcc.8b04981.

3. Serrano-Claumarchirant, J. F.; Culebras, M.; Cantarero, A.; Gómez, C. M.; Muñoz-Espí, R. Poly(3,4-Ethylenedioxythiophene) Nanoparticles as Building Blocks for Hybrid Thermoelectric Flexible Films. *Coatings* **2019**, *10* (1), 22. https://doi.org/10.3390/coatings10010022.

4. Serrano-Claumarchirant, J. F.; Culebras, M.; Muñoz-Espí, R.; Cantarero, A.; Gómez, C. M.; Collins, M. N. PEDOT Thin Films with N-Type Thermopower. *ACS Appl. Energy Mater.* **2020**, *3* (1), 861–867. https://doi.org/10.1021/acsaem.9b01985.

5. Serrano-Claumarchirant, J. F.; Brotons-Alcázar, I.; Culebras, M.; Sanchis, M. J.; Cantarero, A.; Muñoz-Espí, R.; Gómez, C. M. Electrochemical Synthesis of an Organic Thermoelectric Power Generator. *ACS Appl. Mater. Interfaces* **2020**, *12* (41), 46348–46356. https://doi.org/10.1021/acsami.0c12076.

6. Serrano-Claumarchirant, J. F.; Igual-Muñoz, A. M.; Culebras, M.; Collins, M. N.; Cantarero, A.; Gómez, C. M. Electrochemical Synthesis of Hybrid Layered Thermoelectric Materials Based on PEDOT/SnS Doped with Ag. *Adv. Mater. Interfaces* **2021**, *8* (23), 2100951. https://doi.org/10.1002/admi.202100951.

7. Serrano-Claumarchirant, J. F.; Hamawandi, B.; Ergül, A. B.; Cantarero, A.; Gómez, C. M.; Priyadarshi, P.; Neophytou, N.; Toprak, M. S. Thermoelectric Inks and Power Factor Tunability in Hybrid Films through All Solution Process. *ACS Appl. Mater. Interfaces* **2022**. https://doi.org/10.1021/acsami.1c24392.

8. Serrano-Claumarchirant, J. F.; Seijas-Da Silva, A.; Sanchez-Royo, J. F.; Culebras, M.; Cantarero, A.; Gómez, C. M.; Abargues, R. *In-situ* Synthesis of Polythiophene and Ag Nanoparticles within a PMMA Matrix: The Nanocomposite Approach to Thermoelectrics. *ACS Appl. Energy Mater.* Submitted.

9. Serrano-Claumarchirant, J. F.; Nasiri, M. A.; Cho, C.; Cantarero, A.; Gómez, C. M.; Culebras, M. Textile organic thermoelectric generators via electrochemical polymerization with a low internal resistance. *Adv. Compos. Hybrid Mater*. Submitted.

10. Serrano-Claumarchirant, J. F.; Cho, C.; Xu, K.; Reparaz, S.; Cantarero, A.; Culebras, M; Abargues, R.; Gómez, C. M. Hybrid plasmonic/thermoelectric generator based on polythiophene thin films. In preparation.

11. Carsí, M.; Serrano-Claumarchirant, J. F.; Culebras, M.; Gómez, C. M.; Sanchis, M. J. Exploring the effect of coating felt fibers with conductive polymers. In preparation.

Conference contributions

1. Culebras, M.; Cantarero, A.; Serrano-Claumarchirant, J. F.; Landfester, K.; Muñoz-Espí, R.; Gómez, C. M. *Enhancing thermoelectric performance with carbon nanotubes and PEDOT nanoparticles composites.* EMN Meeting on Polymer, Hong Kong, 2016. Oral Communication.

2. Culebras, M.; Serrano-Claumarchirant, J. F.; Gómez, C. M.; Muñoz-Espí, R.; Cantarero, A. *Thermoelectric properties of PEDOT nanoparticles prepared by miniemulsion polymerization.* International Conference on Nanotechnology Applications (NANOTEC 2016), Valencia, 2016. Poster Communication.

3. Serrano-Claumarchirant, J. F.; Culebras, M.; Gómez, C. M.; Muñoz-Espí, R.; Cantarero, A. *Synthesis of PEDOT nanoparticles via miniemulsion polymerization.* 10th European School on Molecular Nanoscience (ESMolNa 2017), El Escorial, 2017. Oral Communication.

4. Culebras, M.; Serrano-Claumarchirant, J. F.; Igual-Muñoz, A. M.; Cantarero, A; Gómez, C. M. *Hybrid inorganic-organic materials for a new generation of thermoelectric devices.* Spring Meeting, Strasbourg, 2017. Oral Communication.

5. Culebras, M.; Serrano-Claumarchirant, J. F.; Gómez, C. M.; Muñoz-Espí, R.; Cantarero, A. *Multifuncional PEDOT nanoparticles.* IX Congreso de Jóvenes Investigadores en Polímeros (JIP 2017), La Pineda, 2017. Oral Communication.

6. Gómez, C. M.; Culebras, M.; Serrano-Claumarchirant, J. F.; Brotons-Alcázar, I.; Cantarero, A; Grunlan, J. *Hybrid polymer-CNT films to obtain flexible modules for thermoelectric applications.* 10th International Symposium on Flexible Organic Electronics (ISFOE17), Thessaloniki, 2017. Oral Communication.

7. Culebras, M.; Serrano-Claumarchirant, J. F.; Ferrer-Crespo, J. F.; Sánchez-Soler A.; Sanchis, M. J.; Cantarero, A.; Gómez, C. M.; Muñoz-Espí, R. *Conducting Polymer Nanoparticles Prepared by Miniemulsion Polymerization: Pros and Cons for Thermoelectric Applications.* International Conference on Organic and Hybrid Thermoelectrics (ICOT 2018), Valencia, 2018. Oral Communication.

8. Culebras, M.; Serrano-Claumarchirant, J. F.; Seijas-Da Silva, A.; Gómez, C. M.; Carsí, M.; Sanchis, M. J.; Cantarero, A. *Different semiconducting behavior of PEDOT nanoparticles.* International Conference on Organic and Hybrid Thermoelectrics (ICOT 2018), Valencia, 2018. Poster Communication.

9. Serrano-Claumarchirant, J. F.; Culebras, M.; Muñoz-Espí, R.; Carsí, M.; Sanchis, M. J.; Gómez, C. M.; Cantarero, A. *Hybrid films based on PEDOT and CNTs for thermoelectric applications.* International Conference on Organic and Hybrid Thermoelectrics (ICOT 2018), Valencia, 2018. Poster Communication.

10. Seijas-Da Silva, A.; Culebras, M.; Serrano-Claumarchirant, J. F.; Cantarero, A.; Gómez, C. M. Films of carbonaceous nanofillers and polymers as stable n-type materials for thermoelectric devices. 37th International and 16th European Conference on Thermoelectrics (ICT/ECT2018), Caen, 2018. Oral Communication.

11. Serrano-Claumarchirant, J. F.; Brotons-Alcázar, I.; Culebras, M.; Cantarero, A.; Gómez, C. M. *Smart textiles functionalized with PEDOT and CNT as promising thermoelectric materials.* XV Reunión del Grupo Especializado de Polímeros (GEP2018), Punta Umbría, 2018. Oral Communication.

12. Serrano-Claumarchirant, J. F.; Culebras, M.; Muñoz-Espí, R.; Cantarero, A.; Gómez, C. M. *Flexible hybrid thermoelectric materials based on carbon nanotubes and poly(3,4-ethylenedioxythiophene)*. XV Reunión del Grupo Especializado de Polímeros (GEP2018), Punta Umbría, 2018. Oral Communication.

13. Serrano-Claumarchirant, J. F.; Muñoz-Espí, R.; Culebras, M.; Gómez, C. M.; Cantarero, A. *Completely organic thermoelectric nanocoatings for flexible films.* Young Researchers in Chemistry (YRChem2019), Valencia, 2019. Poster Communication.

14. Serrano-Claumarchirant, J. F.; Culebras, M.; Muñoz-Espí, R.; Cantarero, A.; Gómez, C. M. *PEDOT nanoparticles as a building-block for completely organic thermoelectric flexible films.* International conference on thermoelectric materials, San Sebastián, 2019. Oral Communication.

15. Serrano-Claumarchirant, J. F.; Sanchis, M. J.; Carsí, M.; Culebras, M.; Cantarero, A.; Gómez, C. M. *Textile thermoelectric modules based on pedot and carbon nanotubes.* 15th Brazilian Polymer Conference, Bento Gonçalves-RS, 2019. Oral Communication.

16. Serrano-Claumarchirant, J. F.; Culebras, M.; Muñoz-Espí, R.; Cantarero, A.; Gómez, C. M. *Construction of thermoelectric hybrid films using PEDOT nanoparticles as building-block.* 2nd Iberian Thermoelectric Workshop (ITW2019), Ciudad Real, 2019. Oral Communication.

17. Serrano-Claumarchirant, J. F.; Culebras, M.; Cantarero, A.; Muñoz-Espí, R.; Gómez, C. M. *Exploiting the potential of colloidal systems for thermoelectric coatings.* V Reunión de Jóvenes Investigadores en Coloides e Interfases (JICI2020), Zaragoza, 2020. Oral Communication.

18. Serrano-Claumarchirant, J. F.; Abargues, R.; Cantarero, A.; Gómez, C. M. *In-situ Polymerization of Polythiophene in a Polyurethane Matrix for Flexible Thermoelectric Devices.* Virtual Conference on Thermoelectrics (VCT20), Online, 2020. Oral Communication.

19. Serrano-Claumarchirant, J. F.; Culebras, M.; Abargues, R.; Cantarero, A.; Muñoz-Espí, R.; Gómez, C. M. *Flexible thermoelectric materials based on conducting polymers.* 25 Years of Materials Science, Paterna, 2020. Poster Communication.

20. Serrano-Claumarchirant, J. F.; Hamawandi, B.; Batili, H.; Culebras, M.; Muñoz-Espí, R.; Cantarero, A.; Abargues, R.; Toprak, M., Gómez, C. M. *Thermoelectric Composites for Wearable Applications.* IUPAC-MACRO 2020+ The 48th World Polymer Congress, Jeju-Online, 2021. Oral Communication.

21. Serrano-Claumarchirant, J. F.; Pinardo, M.; Cantarero, A.; Abargues, R.; Gómez, C. M. *Thermosolar conversion by plasmonic materials for a new generation of more efficient and environmentally friendly thermoelectric materials.* VI Jornadas Jóvenes ICMUV, Paterna, 2021. Poster Communication.

22. Serrano-Claumarchirant, J. F.; Adam-Cervera, I.; Rodríguez, S.; Culebras, M.; Cantarero, A.; Gómez, C. M.; Muñoz-Espí, R. *Hybrid PCM - thermoelectric systems for the conversion of stored thermal energy into electrical.* VI Jornadas Jóvenes ICMUV, Paterna, 2021. Poster Communication.

23. Serrano-Claumarchirant, J. F.; Culebras, M.; Muñoz-Espí, R.; Cantarero, A.; Gómez, C. M. *Electrochemical synthesis of thermoelectric fabrics.* Virtual Conference on Thermoelectrics (VCT21), Online, 2021. Oral Communication.

24. Serrano-Claumarchirant, J. F.; Abargues, R.; Cantarero, A.; Muñoz-Espí, R.; Gómez, C. M. *Harnessing the sun: how to convert waste solar heat into electrical energy.* RSEQ Symposium, Online, 2021. Oral Communication.

25. Adam-Cervera, I.; Rodríguez-Boscà, C.; Serrano-Claumarchirant, J. F.; Gómez, C. M.; Muñoz-Espí, R. *Coatings with Nanoencapsulated Phase Change Materials for Thermal Energy Storage.* RSEQ Symposium, Online, 2021. Poster Communication.

26. Gómez, C. M.; Serrano-Claumarchirant, J. F.; Culebras, M.; Cantarero, A.; Adam-Cervera, I.; Muñoz-Espí, R.; *Improving Thermoelectric Efficiency in Acrylic Fabrics without Compromising Mechanical Properties.* XVI Reunión del Grupo Especializado de Polímeros y XVII Simposio Latinoamericano de Polímeros (GEP-SLAP 2022), San Sebastián, 2022. Poster Communication.

27. Adam-Cervera, I.; Rodríguez-Boscà, C.; Serrano-Claumarchirant, J. F.; Culebras, M.; Gómez, C. M.; Muñoz-Espí, R. *Nanoencapsulation of Phase Change Materials and Integration in Polymer Coatings for Thermal Energy Storage.* XVI Reunión del Grupo Especializado de Polímeros y XVII Simposio Latinoamericano de Polímeros (GEP-SLAP 2022), San Sebastián, 2022. Oral Communication.

28. Culebras, M.; Serrano-Claumarchirant, J. F.; Collins, M.; Muñoz-Espí, R.; Cantarero, A.; Gómez, C. M. *Lignin, the sustainable biopolymer to develop the next generation of energy materials.* XVI Reunión del Grupo Especializado de Polímeros y XVII Simposio Latinoamericano de Polímeros (GEP-SLAP 2022), San Sebastián, 2022. Oral Communication.

29. Serrano-Claumarchirant, J. F.; Culebras, M.; Adam-Cervera, I.; Abargues, R.; Cantarero, A.; Muñoz-Espí, R.; Gómez, C. M. *How Plasmon Nanoparticles Can Improve the Power Performance in Wearable Thermoelectric Materials.* XVI Reunión del Grupo Especializado de Polímeros y XVII Simposio Latinoamericano de Polímeros (GEP-SLAP 2022), San Sebastián, 2022. Oral Communication.

Participation in projects

1. Semiconductor nanostructures and nanocomposites for energy recovery (MAT2015-63955-R). Ministry of Economy and Competitiveness, 2016 - 2018.

2. Thermoelectricity. New theories (MAT2016-82015-REDT). Ministry of Economy and Competitiveness, 2017 - 2019.

3. New frontiers in thermoelectric conversion and energy storage. Ministry of Science and Innovation, 2019 - 2022.

4. Applications of topological insulators to thermoelectricity and spintronics (PROMETEO/2020/016). 2020 - 2023.

Resumen en castellano

Motivación

Uno de los objetivos de la Organización de las Naciones Unidas (ONU) para el Desarrollo Sostenible 2030 es obtener energía asequible y no contaminante. Por este motivo, se recomiendan encarecidamente las mejoras en la eficiencia energética y las fuentes de energía verde como soluciones óptimas para reducir las emisiones de dióxido de carbono y, por tanto, reducir la huella de carbono de nuestra sociedad. Las emisiones de carbono se han cuadriplicado desde 1950 y actualmente contribuyen en torno al 80 % de las emisiones de gases de efecto invernadero. Como resultado de este cambio, el clima global sufre cambios en las tendencias globales de lluvia y una reducción en los casquetes polares. Con el impacto de los cambios climáticos globales cada vez más severos, los gobiernos están tratando de reducir los niveles de emisión de carbono y lograr un desarrollo sostenible en sus países mediante el uso de fuentes de energía renovables. Aprovechan recursos naturales como la luz solar, la lluvia, el calor geotérmico y las olas para producir energía limpia y sin emisiones de gases de efecto invernadero. Los resultados de generación eléctrica indican que la tendencia es cada vez más sostenible a medida que la apuesta por las energías renovables aumenta anualmente. Sin embargo, las fuentes de energía primaria más

consumidas a nivel mundial siguen siendo el petróleo y sus derivados (83,15%), y solo el 5,7% de la energía global consumida proviene de fuentes de energía renovables.

Además, el consumo de energía cayó en 2020 en torno a un 4,5% respecto al año anterior debido a la crisis provocada por el Covid-19. Sin embargo, se espera que el consumo de energía aumente en los próximos años según la Agencia Internacional de Energía (AIE). Es de vital importancia que este aumento de la demanda energética por parte de la sociedad vaya de la mano con la mejora de la eficiencia energética para cumplir con los objetivos sostenibles de la ONU. Solo así será posible alcanzar las Emisiones Netas Cero para el Escenario 2050 en el período 2020-2030.

Por otro lado, es de vital importancia mejorar la eficiencia energética ya que se estima que el 62% del combustible utilizado para generar energía se pierde en forma de calor. Además, la energía se pierde en forma de calor en las centrales eléctricas durante los procesos de conversión de energía, y solo el 5% de la energía se usa en los hogares. Por lo tanto, encontrar formas de recuperar toda esta energía desperdiciada es imperativo. Parte de esta energía perdida se puede recuperar recolectando energía y convirtiéndola en energía eléctrica. Los tres fenómenos principales que pueden recuperar energía son: piezoelectricidad, que puede convertir el estiramiento mecánico en corriente eléctrica, la triboelectricidad, que puede producir energía eléctrica a través del contacto friccional entre diferentes materiales, y la termoelectricidad, que puede recuperar energía eléctrica de pérdidas de calor. En los últimos años, este último fenómeno se ha convertido en la forma más prometedora de mejorar la eficiencia energética, ya que es una propiedad de los semiconductores que puede convertir un gradiente de temperatura en corriente eléctrica y viceversa. La eficiencia termoeléctrica de un material viene dada por la Figura de Mérito, ZT.

Los materiales termoeléctricos más utilizados para aplicaciones comerciales se han desarrollado gracias a los avances significativos en la síntesis de nuevos materiales y estructuras con un rendimiento termoeléctrico mejorado. Se ha buscado mejorar la Figura de Mérito mediante la reducción de la conductividad térmica de la red. Una forma de lograr este objetivo es a través de la llamada estrategia de cristal de electrones de vidrio de fonones, en la que el material debe conducir el calor como el vidrio, pero la electricidad como un cristal. El resultado de esta investigación son materiales como skutteruditas y clatratos.

Otra estrategia para mejorar la eficiencia termoeléctrica es mediante la reducción de la conductividad térmica de la red, basada en el uso de materiales con estructuras de baja

dimensionalidad. Hicks y Dresselhaus, en 1993, demostraron el uso potencial de los pozos cuánticos para mejorar la Figura de Mérito. Como resultado de este trabajo, materiales como Bi_2Te_3/Sb_2Te_3, PbSeTe o SiGe alcanzaron valores de ZT en torno a 2.

Sin embargo, estos materiales inorgánicos tienen varios inconvenientes, como el alto costo de producción, la toxicidad de algunos de los elementos utilizados y la escasez de materias primas. Todos estos inconvenientes hacen que los materiales termoeléctricos inorgánicos no sean adecuados desde el punto de vista del desarrollo energético sostenible. Por esta razón, muchos estudios se han centrado en la búsqueda de materiales termoeléctricos eficientes y amigables con el medio ambiente. Uno de los candidatos potenciales para aplicaciones a temperatura ambiente son los semiconductores orgánicos, particularmente los polímeros conductores, debido a su abundancia, bajo costo, flexibilidad, y fácil modificación. Además, los polímeros conductores brindan otros beneficios. Desde un punto de vista medioambiental, los polímeros conductores están compuestos principalmente por carbono, que es un elemento abundante, de bajo coste y no tóxico. Esas propiedades implican que la obtención de materiales termoeléctricos a partir de polímeros conductores es mucho más sostenible que los materiales inorgánicos tradicionales. Desde un punto de vista químico, los polímeros conductores se pueden modificar fácilmente para proporcionar funcionalidades adicionales y, además, las propiedades flexibles son útiles para imprimir áreas grandes. Otra ventaja es que los polímeros conductores suelen tener una conductividad térmica (0,1 – 1 $W\ m^{-1}\ K^{-1}$) por debajo de la conductividad térmica de metales y semiconductores inorgánicos. Todas esto hace que los polímeros conductores sean unos candidatos ideales para la próxima generación de materiales termoeléctricos porque es posible obtener dispositivos flexibles de bajo costo y gran área para la recolección de energía térmica de bajo grado. Sin embargo, a pesar del aumento significativo en la eficiencia termoeléctrica de los polímeros conductores en la última década, la Figura de Mérito sigue siendo mucho más baja que la ZT de los materiales inorgánicos. Por lo tanto, es necesario encontrar nuevas estrategias para mejorar la eficiencia de los polímeros conductores como: 1) optimización del nivel de dopaje, 2) mejora del ordenamiento de las cadenas poliméricas, 3) obtención de materiales híbridos orgánico-inorgánicos.

Objetivos

El principal objetivo de esta tesis ha sido elaborar materiales termoeléctricos híbridos basados en polímeros conductores para mejorar su eficiencia termoeléctrica. Este objetivo principal se divide en los siguientes subobjetivos:

1. Síntesis y preparación de materiales termoeléctricos híbridos basados en PEDOT con nanotubos de carbono y SnS:Ag.
2. Síntesis y desarrollo de tejidos termoeléctricos recubiertos con MWCNT/polímeros conductores para la obtención de materiales termoeléctricos vestibles.
3. Fabricación de un generador termoeléctrico a partir de los tejidos obtenidos.
4. Optimización de la polimerización in situ de mezclas de tertiofeno con diferentes matrices poliméricas y agentes oxidantes.
5. Elaboración de un sistema híbrido plasmónico/TEG para la captación de energía térmica a partir de la luz solar.

Metodología

Esta tesis doctoral se ha dividido en 6 capítulos. Cada capítulo, a excepción de la introducción general (Capítulo 1), las técnicas de caracterización (Capítulo 2) y las conclusiones generales (Capítulo 6), están organizados con el mismo esquema: una parte introductoria que repasa los conceptos fundamentales del capítulo, seguido de los resultados y discusión de los experimentos realizados y, finalmente, las principales conclusiones del capítulo.

El capítulo 3 se centra en la obtención de materiales laminares híbridos basados en PEDOT con nanotubos de carbono (CNT) o SnS:Ag. La primera serie de experimentos describe la formación y caracterización termoeléctrica de materiales híbridos PEDOT/CNT obtenidos por deposición capa por capa (LbL) de nanopartículas de PEDOT funcionalizadas con un polielectrolito catiónico (PDADMAC) y varios tipos de nanotubos de carbono (MWCNT, DWCNT, SWCNT) funcionalizados con un tensioactivo aniónico (DOC). El segundo trabajo se centra en la obtención y caracterización de películas híbridas estratificadas de PEDOT/SnS:Ag obtenidas por electrodeposición.

El Capítulo 4 se emplea la electrosíntesis para preparar tejidos termoeléctricos recubiertos con polímeros conductores (PEDOT, PPy, PANI). La primera parte de este capítulo describe la estrategia utilizada para cubrir textiles de fieltro con polímeros conductores por electrosíntesis. La segunda parte del capítulo se centra en el polímero conductor que ofrece las mejores propiedades termoeléctricas del apartado anterior (PEDOT) para depositarlo en diferentes textiles (algodón y fieltro) y construir un dispositivo termoeléctrico con ambos tejidos. Finalmente, en la última parte del capítulo, luego de seleccionar el textil recubierto de PEDOT que ofrece una mayor potencia de salida, se modifican los contraiones de las cadenas del polímero PEDOT y se realiza otro dispositivo termoeléctrico.

El capítulo 5 muestra la optimización de la polimerización in situ de tertiofeno (3T) en matrices poliméricas (PMMA y poliuretano) con diferentes agentes oxidantes ($AgClO_4$, $Cu(ClO_4)_2$). En la primera parte de este capítulo, se optimizan las condiciones de polimerización 3T dentro de la matriz de PMMA utilizando $AgClO_4$ como oxidante. Con estas condiciones, en la segunda parte del capítulo, se cambia la matriz polimérica de PMMA por la de poliuretano (PU), y se hace un estudio sistemático de las películas de politiofeno (PT) obtenidas con ambos oxidantes. Finalmente, en la última parte de este capítulo, debido a la presencia de nanopartículas de plata en la película de PT/PU/$AgClO_4$, se estudia el efecto de calentamiento plasmónico de estas nanopartículas metálicas tras irradiar la película con un simulador solar. La diferencia de temperatura alcanzada es mínima; por lo tanto, se añadió una capa plasmónica a la película termoeléctrica, consiguiendo un gradiente térmico más significativo. Con este sistema híbrido plasmón/termoeléctrico se diseñó un generador termoeléctrico que podría recuperar energía de la luz solar.

La caracterización de los materiales obtenidos se llevó a cabo mediante técnicas espectroscópicas, como Raman, FTIR, Uv-Vis, XRD y XPS; una caracterización morfológica, como microscopía electrónica de barrido y de transmisión; una caracterización eléctrica y térmica mediante medidas de efecto Seebeck, conductividad eléctrica y térmica, con equipos experimentales desarrollados durante la tesis; y una caracterización mecánica mediante análisis dinámico-mecánico y ensayos de flexibilidad y torsión. La conductividad eléctrica es uno de los factores que determinan la eficiencia termoeléctrica del material, ya que se encuentra en el numerador de la expresión de ZT. Por lo tanto, se diseñó un montaje experimental para llevar a cabo dichas medidas

siguiendo el método de Van Der Paw, el cual es adecuado para películas delgadas. Para ello se realizan 4 contactos metálicos equidistantes sobre la superficie de las muestras.

Para la medida del efecto Seebeck se diseñó un dispositivo experimental que fue desarrollado en el laboratorio para la realización de la presente tesis doctoral. El dispositivo para determinar el coeficiente de Seebeck consta de un multímetro para registrar la diferencia de potencial, un controlador de temperatura, dos peltiers (uno actúa como refrigerador y el otro como calentador), dos sensores de temperatura PT100 y dos cables que contactan los extremos de la muestra. Para la obtención del coeficiente Seebeck, la muestra es sometida a una diferencia de temperatura entre los extremos, de modo que se registra la tensión entre los contactos de los extremos de la muestra en función de la diferencia de temperatura.

Para la medida de la conductividad térmica se emplearon dos métodos distintos. Para películas delgadas se empleó el método de termoreflectancia en el dominio de la frecuencia y para los textiles termoeléctricos se empleó el método de flujo de calor axial. Este último se desarrolló en el laboratorio y consta de un peltier que suministra el calor, un sensor que detecta la variación del flujo de calor y dos termopares.

Conclusiones

En esta tesis se han desarrollado materiales híbridos termoeléctricos de diferentes maneras. En el Capítulo 3 se describe dos metodologías para obtener materiales termoeléctricos híbridos en capas. El primer método consiste en formar estructuras multicapa mediante la combinación de capas de nanopartículas de PEDOT:Tos funcionalizadas con un polielectrolito catiónico (PDADMAC) con capas de nanotubos de carbono (MWCNT, DWCNT, SWCNT) funcionalizados con un tensioactivo aniónico (DOC). El Factor de Potencia óptimo se alcanza a partir de 30-40 bicapas ya que, a mayor número de bicapas, un efecto de interdifusión crea aglomerados aislantes de PDADMAC y DOC. Además, se utilizaron diferentes nanotubos de carbono en el sistema multicapa con nanopartículas PEDOT:Tos. SWCNT con nanopartículas de PEDOT:Tos en una relación molar EDOT:FeTos de 1:2 logró el factor de potencia más alto, 72 $\mu W\ m^{-1}\ K^{-2}$, tres órdenes de magnitud más alto que el factor de potencia de las nanopartículas de PEDOT:Tos en el mismo molar relación.

El segundo método se basa en la electrodeposición de sulfuro de estaño dopado con plata sobre un electrodo de trabajo PEDOT:ClO_4. Para optimizar el dopaje electroquímico de SnS con plata, se añadieron a la mezcla de reacción diferentes cantidades en peso de nitrato de plata. La morfología de las películas está influenciada por la adición de Ag y la temperatura de síntesis. El análisis estructural (XPS) y las imágenes SEM indican la presencia de Ag_8SnS_6, que se muestra que influye negativamente en las propiedades termoeléctricas de las películas. La conductividad eléctrica aumenta en función del contenido de Ag mientras que el coeficiente de Seebeck alcanza el valor máximo a una concentración de Ag de 0.15% en la solución electroquímica. El factor de potencia máximo observado es de 58.6 $\mu W\ m^{-1}\ K^{-2}$, alcanzado con 0.15 % de Ag, cuatro veces mayor que la película PEDOT:ClO_4 prístina. Además, las películas de PEDOT/SnS:Ag tienen una buena flexibilidad que permite 1800 ciclos de doblado con un radio de 20 mm con poca influencia en la resistencia eléctrica. No hay duda de que los materiales termoeléctricos híbridos en capas representan una excelente estrategia para mejorar la eficiencia termoeléctrica de los polímeros conductores. Además, los resultados de este capítulo representan una clara mejora en la eficiencia termoeléctrica híbrida y orgánica sobre materias primas sostenibles en comparación con el estado del arte.

En el Capítulo 4 se ha desarrollado una metodología diferente para obtener textiles revestidos electroquímicamente por polímeros conductores. Esta nueva metodología consiste en recubrir fibras textiles con nanotubos de carbono utilizando la técnica LbL para utilizar el tejido recubierto con MWCNT como electrodo de trabajo y electrodepositar diferentes polímeros conductores. En la primera sección de este capítulo, se utilizaron tres de los polímeros conductores más utilizados: PEDOT, PPy y PANI. En primer lugar, se realizó un estudio variando el tiempo de electrodeposición para determinar el tiempo óptimo para que la conductividad eléctrica y el coeficiente de Seebeck sean altos pero la masa de polímero depositada sea baja. Luego, se evaluó la calidad de los diferentes recubrimientos mediante imágenes SEM y espectroscopia Raman. Como resultado, el recubrimiento de las fibras textiles con MWCNTs, PEDOT y PPy fue muy homogéneo, a diferencia del PANI. Además, el estudio de estabilidad térmica realizado por TGA mostró que el tejido de fieltro recubierto con PANI:H_2SO_4 es el menos estable, probablemente debido a un deterioro de las fibras en el medio ácido necesario para la síntesis de PANI.

Dado que el recubrimiento del textil con PEDOT:ClO_4 es el que mejores propiedades termoeléctricas ofrece y el que mejor cubre las fibras, se decidió continuar con el desarrollo

de tejidos termoeléctricos con dicho recubrimiento. En la segunda sección de este capítulo se utilizaron dos textiles: uno de fieltro, que no es tejido, y otro de algodón, que es tejido. Al igual que en el apartado anterior, estos tejidos se recubrieron con nanotubos de carbono y luego con PEDOT:ClO_4 por electrodeposición. Mediante espectroscopía Raman y análisis de imágenes SEM, se demostró que el recubrimiento tanto de MWCNT como de PEDOT:ClO_4 era muy homogéneo en ambos tejidos. Las propiedades flexibles de ambos tejidos se evaluaron mediante el seguimiento de la evolución de la conductividad eléctrica en función del ángulo de torsión y del número de pliegues realizados en cada tejido. Los resultados mostraron que las telas de algodón y fieltro mantuvieron el 90% de la conductividad eléctrica inicial después de realizar las pruebas de flexibilidad. Finalmente, se elaboró un módulo termoeléctrico de 20 elementos con tela de algodón y otro con tela de fieltro. Los resultados mostraron una salida de potencia ocho veces superior favorable a la tela de fieltro. Esta diferencia en la producción de energía se atribuyó a la capacidad del tejido de fieltro para generar un gradiente térmico más alto y, por lo tanto, generar más energía. Finalmente, se elaboró un tercer generador termoeléctrico en base de tela de fieltro recubierta con PEDOT:ClO_4 y de 30 unidades, con el cual se obtuvo una potencia de salida de 0.9 μW con un gradiente térmico de 31 K.

La última sección de este capítulo buscó mejorar la eficiencia termoeléctrica de las telas de fieltro recubiertas de PEDOT con diferentes contraiones. Las imágenes SEM y la espectroscopia Raman mostraron que el recubrimiento de las fibras de fieltro PEDOT con los diferentes contraiones es excelente. El análisis termogravimétrico mostró que todos los recubrimientos son estables hasta los 250 ºC. La calorimetría diferencial de barrido junto con DMA determinaron la temperatura de transición vítrea de las telas de fieltro. Además, el módulo de almacenamiento mostró que la rigidez viscoelástica aumenta después de recubrir el tejido de fieltro prístino con MWCNT. Luego, la electrodeposición de PEDOT con diferentes contraiones disminuye el módulo de almacenamiento del tejido Fieltro/MWCNT. La capacidad flexible de las telas termoeléctricas también se evaluó mediante el control del cambio en la conductividad eléctrica en función del ángulo de torsión, el número de flexión y el radio de curvatura. Después de las pruebas, las telas con recubrimientos de PEDOT mostraron menos variación en la conductividad eléctrica. Se evaluaron las propiedades termoeléctricas de los tejidos de fieltro (conductividad eléctrica, coeficiente de Seebeck y conductividad térmica) para los diferentes recubrimientos, demostrando que el recubrimiento PEDOT:BTFMSI ofrece la mayor eficiencia termoeléctrica. Por tal motivo, finalmente se elaboró un generador termoeléctrico portátil

con las telas de fieltro recubiertas con MWCNTs y PEDOT:BTFMSI, a través del cual se obtuvo una potencia de salida de 6.5 μW con una diferencia de temperatura de 57 K.

El Capítulo 5 mostró un estudio de las condiciones óptimas, basadas en la conductividad eléctrica, de la polimerización *in-situ* de tertiofeno dentro de una matriz de PMMA. Luego estas condiciones óptimas fueron transferidas a una matriz de poliuretano flexible. Las condiciones de polimerización optimizadas fueron: tiempo de reacción, temperatura y relación molar oxidante:oligómero. Variando el tiempo de reacción se observó que la conductividad eléctrica aumentaba progresivamente hasta alcanzar un máximo de 60 s. Posteriormente, la conductividad eléctrica disminuyó debido a los procesos de descomposición del politiofeno. Se encontró una tendencia similar en la variación de la temperatura de polimerización. La conductividad eléctrica aumentó progresivamente hasta alcanzar los 160 ºC y, más allá de esta temperatura, la conductividad eléctrica disminuyó. Una vez optimizados estos parámetros, se estudió la influencia de la relación molar oxidante:oligómero. En este caso, se realizó un estudio aplicando la teoría de la percolación, y se observó que a valores altos de la relación oxidante:oligómero, las nanopartículas de plata percolaban entre cadenas de polímero de politiofeno. También se estudiaron las propiedades termoeléctricas en función de la relación molar oxidante:oligómero, alcanzando un Factor de Potencia de 50 μW m^{-1} K^{-2} con una relación molar de 2.8:1.

A continuación, se cambió la matriz de PMMA a una de poliuretano y se aplicaron las condiciones de reacción previamente optimizadas para la polimerización *in-situ* del tertiofeno dentro de la matriz de poliuretano, utilizando como oxidantes $AgClO_4$ y $Cu(ClO_4)_2$. En primer lugar, se determinó de nuevo la relación molar óptima de oxidante:oligómero dentro de esta nueva matriz. Luego, se aumentó la cantidad de oligómero en la mezcla de reacción mientras se mantenía constante la proporción molar óptima. De esta forma, se produjo una mejora en la conductividad eléctrica sin cambiar significativamente el coeficiente de Seebeck, alcanzando un Factor de Potencia de 20 μW m^{-1} K^{-2} cuando se utilizó la sal de plata oxidante y de 8 μW m^{-1} K^{-2} cuando se utilizó como oxidante la sal de cobre. Las imágenes de TEM mostraron nanopartículas de plata incrustadas en la matriz de politiofeno/poliuretano, mientras que no se observaron nanopartículas de cobre en las películas con el oxidante de cobre. Por esta razón, se decidió estudiar el efecto de calentamiento plasmónico de las nanopartículas de plata sobre la película. Para ello se varió el número de capas sobre el sustrato, encontrando que el mayor

Factor de Potencia con ambos oxidantes se encontró con 4 capas. A continuación, se evaluó el efecto del calentamiento plasmónico, mostrando que las películas con nanopartículas de plata alcanzaron un gradiente térmico entre los extremos de 1.72 ºC, y las películas sin nanopartículas de plata (oxidante de cobre) solo obtuvieron un gradiente térmico de 0.4 ºC. Sin embargo, esta diferencia de temperatura no es suficiente para generar energía eléctrica significativa. Por lo tanto, se agregó una capa plasmónica a la película de PTh-Ag-PU para generar un mayor gradiente térmico.

Primero se optimizaron las condiciones de reacción (concentración de precursor de plata y tiempo de reacción) y la matriz polimérica huésped de la capa plasmónica. La matriz polimérica huésped es muy importante para asegurar y mantener el rendimiento plasmónico de las nanopartículas de plata. Con todo esto se concluyó que la matriz de poliuretano era la más adecuada para este sistema. Finalmente, se desarrolló un sistema híbrido en el que la capa plasmónica se ensamblaba con sucesivas capas termoeléctricas. Los mejores valores de voltaje en circuito abierto se obtuvieron con 2 y 3 capas termoeléctricas sobre la plasmónica. Se realizaron dos sistemas plasmón/TEG con 2 y 3 capas termoeléctricas, obteniendo un valor de 1.2 nW para el sistema con tres capas termoeléctricas. Aunque la potencia de salida obtenida es muy baja, la combinación de materiales termoeléctricos y plasmónicos nos permite conectar los módulos como uniones p-n.

Esta tesis ha sido el punto de partida de muchas líneas de investigación que pueden explorarse y desarrollarse más. Por ejemplo, uno de los principales problemas de los generadores termoeléctricos portátiles (wTEG) es el bajo gradiente térmico que se establece a lo largo del dispositivo ya que la diferencia de temperatura entre el ambiente y la epidermis es de apenas un par de grados centígrados. En el capítulo 5 hemos visto que la inclusión de materiales plasmónicos puede ayudar a aumentar el gradiente térmico debido a la absorción de la luz solar por efecto del calentamiento plasmónico. Además, se puede aumentar la eficiencia del material plasmónico modificando el estado de agregación de las nanopartículas metálicas, de manera que se mejora la resonancia plasmónica de las nanopartículas metálicas. En los últimos meses hemos trabajado en la síntesis coloidal de nanopartículas de plata para entrecruzar el ligando con un espaciador capaz de agregar las nanopartículas. De esta forma, la dispersión obtenida adquiere una coloración negra y presenta una banda de absorción en todo el rango visible en lugar de sólo en la longitud de onda de resonancia plasmónica. La absorción de luz en todo el espectro visible permite un

mayor aprovechamiento de la luz solar y, por tanto, un calentamiento plasmónico más importante, generando un mayor gradiente térmico. Con la dispersión coloidal se pueden formular pinturas para cubrir parte de las unidades que componen el generador termoeléctrico.

Otro problema de los wTEG es que el gradiente térmico que alcanzan no es constante ya que la temperatura ambiente fluctúa según la hora del día o la estación del año. Estamos investigando una posible solución en nuestro grupo de investigación mediante la inclusión de materiales de cambio de fase (PCM) en generadores termoeléctricos. De esta forma, cuando la temperatura ambiente es superior a la temperatura de fusión del PCM, este material se funde, almacenando energía térmica. Por el contrario, cuando la temperatura ambiente desciende por debajo de la temperatura de fusión del PCM, este cristaliza y libera la energía térmica previamente almacenada. De esta forma se puede conseguir suministrar un gradiente térmico de manera constante al generador termoeléctrico para reconvertirlo en energía eléctrica útil. En el laboratorio, se ha desarrollado nanocápsulas de poliestireno con PCM en su interior y telas de fieltro recubiertas con estas nanocápsulas.

En general, creo que, para el desarrollo de generadores termoeléctricos portátiles, no solo debemos centrarnos en mejorar las propiedades termoeléctricas o la arquitectura del wTEG, sino también en la búsqueda de nuevos enfoques que aumenten el gradiente térmico a lo largo del wTEG y así maximizar su potencia de salida.